

# **Computer aided design, simulation and optimisation of the flux switching machine**

Thesis submitted for the degree of  
Doctor of Philosophy  
at the University of Leicester

by

**John Martin Reeve**

Department of Engineering  
University of Leicester

October 2002

UMI Number: U168763

All rights reserved

INFORMATION TO ALL USERS

The quality of this reproduction is dependent upon the quality of the copy submitted.

In the unlikely event that the author did not send a complete manuscript and there are missing pages, these will be noted. Also, if material had to be removed, a note will indicate the deletion.



UMI U168763

Published by ProQuest LLC 2013. Copyright in the Dissertation held by the Author.  
Microform Edition © ProQuest LLC.

All rights reserved. This work is protected against  
unauthorized copying under Title 17, United States Code.



ProQuest LLC  
789 East Eisenhower Parkway  
P.O. Box 1346  
Ann Arbor, MI 48106-1346

# SUMMARY

The flux switching machine is a relatively new class of reluctance machine in which power is converted mainly by changing mutual coupling between windings. This thesis develops the parameterised finite element analysis of this machine and introduces the 'flux map', an extension to the flux-mmf-position electromagnetic characterisation approach to fully account for mutual coupling between two phases. A dynamic simulation model of the flux switching machine and the flux switching motor including its drive and control are then developed based on this data. Comparison of experimental and simulated results shows good agreement in both cases and the effects of various factors on simulated output are examined.

A genetic algorithm system is integrated with parameterised finite element analysis and its operation demonstrated for design cases using flux switching and switched reluctance machines and it is shown that the system is applicable throughout the design and optimisation process. A simple image processing method for iron loss visualisation in electromagnetic devices is also developed and demonstrated for the flux switching motor.

The flux map is applicable to any reluctance machine where mutual coupling between two phases must be accounted for while the genetic algorithm system and iron loss visualisation technique may be applied to virtually any electromagnetic system which can be modelled in 2-dimensional finite element analysis.

# ACKNOWLEDGEMENTS

The author would like to acknowledge the support and guidance of Prof. Charles Pollock, without whom the work described in this thesis could not have taken place. The friendship, interest and encouragement of the staff and students with whom I have worked during this project is also greatly appreciated, as is the support offered by the various staff of companies within the Centre for Advanced Electronically Controlled Drives. I would also like to thank the support and development staff of Vector Fields Limited for their help and advice in the area of finite element modelling.

Outside of the laboratory I would like to thank the members of my family and friends who have always supported and encouraged me in my studies, in particular Samantha Dale for her help and support during the writing of this thesis.

John Reeve.

10th October 2002

# TABLE OF CONTENTS

<b>SUMMARY .....</b>	<b>I</b>
<b>ACKNOWLEDGEMENTS.....</b>	<b>II</b>
<b>TABLE OF CONTENTS.....</b>	<b>III</b>
<b>TABLE OF FIGURES.....</b>	<b>IX</b>
<b>TABLE OF MAIN SYMBOLS USED .....</b>	<b>XIX</b>
<b>1 INTRODUCTION.....</b>	<b>1</b>
1.1 OBJECTIVES OF RESEARCH .....	1
1.2 INTRODUCTION TO RELUCTANCE MACHINES .....	2
1.2.1 <i>General principle of operation.....</i>	<i>2</i>
1.2.2 <i>Switched reluctance and flux switching machines .....</i>	<i>6</i>
1.2.3 <i>Applications of the flux switching machine.....</i>	<i>6</i>
1.3 SIMULATION MODELS FOR RELUCTANCE MACHINES .....	8
1.3.1 <i>Machine models in the design process.....</i>	<i>9</i>
1.3.2 <i>Evaluation of switched reluctance machine models with respect to the flux switching machine.....</i>	<i>10</i>
1.4 METHODOLOGY OF THE SIMULATION MODEL DEVELOPED .....	13
1.5 CONTRIBUTION TO KNOWLEDGE.....	15
1.6 THESIS STRUCTURE .....	17
<b>2 CONSTRUCTION, OPERATION AND FINITE ELEMENT ANALYSIS OF THE FLUX SWITCHING MACHINE .....</b>	<b>19</b>
2.1 CONSTRUCTION OF THE FLUX SWITCHING MACHINE .....	19
2.2 METHOD OF OPERATION OF THE FLUX SWITCHING MACHINE .....	20
2.3 SIMPLE ANALYSIS OF THE FLUX SWITCHING MACHINE .....	24
2.4 SIMPLE ANALYSIS OF FLUX SWITCHING MACHINE INCLUDING MUTUAL EFFECTS ...	27
2.5 CALIBRATION OF SHAFT MOUNTED OPTICAL POSITION SENSOR .....	28
2.6 WINDING TECHNIQUES FOR THE FLUX SWITCHING MACHINE .....	29

2.7	PARAMETERISED FINITE ELEMENT ANALYSIS .....	31
2.8	PARAMETERISED FINITE ELEMENT ANALYSIS MODEL FOR THE FLUX SWITCHING MACHINE .....	34
2.9	EFFECTS OF FINITE ELEMENT MESHING .....	36
2.9.1	<i>Airgap region discretisation</i> .....	37
2.9.2	<i>Mesh gravity points in parameterised finite element analysis</i> .....	38
2.9.3	<i>Automatic mesh adaption</i> .....	40
2.10	POST PROCESSING TECHNIQUES .....	44
2.10.1	<i>Calculation of winding fluxes from 2-dimensional finite element analysis</i> .....	46
2.10.2	<i>Calculation of torque</i> .....	47
2.11	ANALYSIS OF FINITE ELEMENT ANALYSIS ERRORS .....	49
2.12	DEVELOPMENT OF GEOMETRICALLY ACCURATE AND FLEXIBLE PARAMETERISED FINITE ELEMENT ANALYSIS MODEL OF THE FLUX SWITCHING MACHINE .....	52
2.12.1	<i>Improvements in physical accuracy</i> .....	53
2.12.2	<i>Improvements in design flexibility</i> .....	55
2.13	SUMMARY AND CONCLUSIONS .....	58

### **3 ELECTROMAGNETIC CHARACTERISATION OF THE FLUX SWITCHING MACHINE.....59**

3.1	STRUCTURE AND PROPERTIES OF THE FLUX MAP .....	59
3.1.1	<i>Calculation of normalised magnetic quantities</i> .....	59
3.1.2	<i>Finite element solutions required for full characterisation of the flux switching machine</i> 60	
3.1.3	<i>Storage and manipulation of the flux map</i> .....	63
3.2	COMPUTATIONAL OVERHEAD REDUCTION.....	64
3.2.1	<i>Data set reduction by inspection</i> .....	65
3.2.2	<i>Data set reduction by interpolation</i> .....	66
3.2.3	<i>Maximum feasible number of finite element data points</i> .....	68
3.3	COMPARISON OF FLUX MAPS FROM FINITE ELEMENT ANALYSIS.....	70
3.3.1	<i>Effects of meshing and numerical accuracy</i> .....	72
3.3.2	<i>Effects of geometric accuracy</i> .....	74
3.3.3	<i>Effects of steel B-H characteristic</i> .....	77
3.3.4	<i>Comparison of results</i> .....	79
3.4	COMPARISON OF FINITE ELEMENT ANALYSIS AND EXPERIMENTALLY MEASURED FLUX LINKAGE DATA .....	80
3.4.1	<i>Method of comparison</i> .....	80
3.4.2	<i>Experimental conditions</i> .....	81
3.4.3	<i>Winding self inductances from finite element results</i> .....	82

3.4.4	<i>Winding effective inductances from simple time constant method</i> .....	84
3.4.5	<i>Accurate winding flux linkages from experiment</i> .....	87
3.4.6	<i>Winding inductances measured using a precision component analyser</i> .....	95
3.4.7	<i>Discussion</i> .....	98
3.5	SUMMARY AND CONCLUSIONS.....	99
<b>4</b>	<b>ELECTROMAGNETIC DATA STRUCTURE AND CONVERSION</b> .....	<b>100</b>
4.1	THE NEED FOR ELECTROMAGNETIC DATA CONVERSION.....	100
4.2	CONTOUR ANALYSIS OF THE FLUX MAP.....	103
4.2.1	<i>Obtaining <math>F_f(\Phi_f, \Phi_a, \theta)</math> and <math>F_a(\Phi_f, \Phi_a, \theta)</math></i> .....	104
4.2.2	<i>Obtaining <math>F_f(\Phi_f, F_a, \theta)</math> and <math>\Phi_a(\Phi_f, F_a, \theta)</math></i> .....	107
4.2.3	<i>Obtaining <math>F_a(F_f, \Phi_a, \theta)</math> and <math>\Phi_f(F_f, \Phi_a, \theta)</math></i> .....	108
4.2.4	<i>Numerical inaccuracy in positions of strong mutual coupling</i> .....	109
4.3	PRACTICAL IMPLEMENTATION OF DATA CONVERSION ALGORITHMS.....	111
4.3.1	<i>Interpolation of flux map data onto finer axes</i> .....	112
4.3.2	<i>Determination of independent flux axes</i> .....	115
4.3.3	<i>Calculation and reliability testing of contours</i> .....	116
4.3.4	<i>Interpolation of contour lines</i> .....	119
4.3.5	<i>Detection of contour intersections</i> .....	121
4.3.6	<i>Converted data numerical error estimation and reduction</i> .....	125
4.3.7	<i>Data conversion alternatives implemented</i> .....	131
4.4	RESULTS.....	131
4.4.1	<i>Typical converted data</i> .....	132
4.4.2	<i>Comparison of flux maps</i> .....	138
4.4.3	<i>Comparison of contour extrapolation methods</i> .....	145
4.4.4	<i>Comparison of contour interpolation methods</i> .....	146
4.5	SUMMARY AND CONCLUSIONS.....	150
<b>5</b>	<b>DYNAMIC SIMULATION MODEL FOR THE FLUX SWITCHING MACHINE</b> <b>151</b>	
5.1	INTRODUCTION.....	151
5.2	THEORETICAL DEVELOPMENT.....	152
5.2.1	<i>Denormalisation of flux map and derived data</i> .....	152
5.2.2	<i>Derivation of formulae for simulation</i> .....	154
5.2.3	<i>Gauss-Seidel solution of simultaneous non-linear equations</i> .....	156

5.2.4	<i>Results available from simulation</i> .....	161
5.3	IMPLEMENTATION OF DYNAMIC SIMULATION MODEL .....	161
5.3.1	<i>Simplification for static simulation</i> .....	161
5.3.2	<i>Choice of time step and convergence tolerance</i> .....	162
5.4	RESULTS .....	163
5.4.1	<i>Experimental conditions</i> .....	163
5.4.2	<i>Comparison of experimental and simulated results</i> .....	164
5.4.3	<i>Comparison of voltage and current source excitation</i> .....	168
5.4.4	<i>Effects of finite element data quality</i> .....	170
5.4.5	<i>Effects of data conversion methods</i> .....	177
5.4.6	<i>Effects of coil temperature and resistance estimate</i> .....	178
5.4.7	<i>Requirements for accurate dynamic simulation of the flux switching machine ...</i> .....	180
5.5	SUMMARY AND CONCLUSIONS .....	180

## **6 DYNAMIC SIMULATION MODEL FOR THE FLUX SWITCHING MOTOR INCLUDING POWER ELECTRONICS AND CONTROL STRATEGY..... 182**

6.1	INTRODUCTION.....	182
6.2	SYSTEM TO BE MODELLED.....	183
6.2.1	<i>Normal operation of the flux switching motor drive system</i> .....	185
6.2.2	<i>Transient start-up operation of the flux switching motor drive system</i> .....	186
6.3	MODEL DEVELOPMENT.....	187
6.3.1	<i>Position and optical sensor signal calibration of simulation model</i> .....	187
6.3.2	<i>Behaviour of the bifilar armature winding in the circuit</i> .....	188
6.3.3	<i>Adding external inductance to windings in the circuit</i> .....	199
6.3.4	<i>Switch control algorithms</i> .....	202
6.4	IMPLEMENTATION .....	204
6.4.1	<i>Complete system simulation model</i> .....	205
6.4.2	<i>Solution of complete system model</i> .....	209
6.5	RESULTS .....	209
6.5.1	<i>Experimental tests simulated</i> .....	209
6.5.2	<i>Comparison of experimental and simulated results</i> .....	211
6.5.3	<i>Effects of finite element data quality</i> .....	222
6.5.4	<i>Effects of winding resistances</i> .....	224
6.5.5	<i>Effects of contour interpolation methods during data conversion</i> .....	226
6.5.6	<i>Effects of switch operating positions</i> .....	228
6.5.7	<i>Effects of external inductances</i> .....	231
6.5.8	<i>Comparison of simulated torques</i> .....	235

6.5.9	<i>Requirements for accurate dynamic simulation of the flux switching motor, drive and control strategy</i> .....	246
6.6	SUMMARY AND CONCLUSIONS .....	247
<b>7</b>	<b>ELECTROMAGNETIC DESIGN AND OPTIMISATION USING A GENETIC ALGORITHM COUPLED WITH PARAMETERISED FINITE ELEMENT ANALYSIS .....</b>	<b>249</b>
7.1	INTRODUCTION .....	249
7.2	GENETIC ALGORITHMS FOR OPTIMISATION .....	251
7.2.1	<i>Background</i> .....	251
7.2.2	<i>Comparison of genetic algorithms with other optimisation techniques</i> .....	252
7.2.3	<i>Enabling technologies for electromagnetic design using a genetic algorithm and finite element analysis</i> .....	254
7.3	SIMPLE GENETIC ALGORITHM IMPLEMENTATION .....	255
7.3.1	<i>Encoding of individuals</i> .....	256
7.3.2	<i>Fitness evaluation of individuals</i> .....	258
7.3.3	<i>Genetic operators</i> .....	259
7.3.4	<i>Conditions for ending the genetic algorithm</i> .....	262
7.4	INTEGRATION OF THE GENETIC ALGORITHM WITH PARAMETERISED FINITE ELEMENT ANALYSIS .....	265
7.4.1	<i>Software control</i> .....	265
7.4.2	<i>Translation of decoded parameters into finite element models</i> .....	266
7.4.3	<i>Fitness evaluation using finite element analysis output</i> .....	266
7.4.4	<i>Progress logging</i> .....	268
7.5	RESULTS .....	269
7.5.1	<i>Effects of genetic algorithm parameter settings</i> .....	270
7.5.2	<i>Effects of population size and number of generations</i> .....	275
7.5.3	<i>Genetic algorithm applied to initial design</i> .....	279
7.5.4	<i>Summary of results</i> .....	282
7.6	SUMMARY AND CONCLUSIONS .....	283
<b>8</b>	<b>IMAGE PROCESSING METHOD FOR IRON LOSS VISUALISATION IN ELECTRICAL MACHINES .....</b>	<b>284</b>
8.1	INTRODUCTION .....	284
8.2	OBTAINING GRAPHICAL MAGNETIC FIELD DATA FROM FINITE ELEMENT ANALYSIS ... .....	288

8.3	IMAGE PROCESSING METHOD FOR OBTAINING MAGNETIC FIELD DATA FROM FINITE ELEMENT ANALYSIS .....	290
8.3.1	<i>Image generation in finite element analysis</i> .....	291
8.3.2	<i>Image conversion to bitmap format</i> .....	298
8.3.3	<i>Bitmap image to matrix conversion</i> .....	299
8.3.4	<i>Rotation of image matrices</i> .....	301
8.3.5	<i>Image matrix collation</i> .....	302
8.4	IMAGE MANIPULATION OPERATIONS FOR IRON LOSS VISUALISATION .....	303
8.4.1	<i>Image interpolation</i> .....	304
8.4.2	<i>Image operators for visualisation of iron loss distribution</i> .....	305
8.4.3	<i>Image results display</i> .....	306
8.5	RESULTS .....	307
8.5.1	<i>Results relating to hysteresis loss visualisation</i> .....	309
8.5.2	<i>Results relating to eddy current loss visualisation</i> .....	314
8.5.3	<i>Further results available</i> .....	316
8.5.4	<i>Application of data obtained to post-priori iron loss estimation formulae</i> ....	318
8.6	SUMMARY AND CONCLUSIONS .....	319
<b>9</b>	<b>CONCLUSIONS AND FURTHER WORK .....</b>	<b>320</b>
9.1	CONCLUSIONS .....	320
9.2	AREAS FOR FURTHER WORK.....	326
	<b>REFERENCES .....</b>	<b>329</b>

# TABLE OF FIGURES

FIGURE 1-1 SIMPLIFIED OPERATION OF A HYPOTHETICAL RELUCTANCE MACHINE.....	3
FIGURE 1-2 GENERAL SCHEMATIC ARRANGEMENT OF RELUCTANCE MOTOR, DRIVE AND CONTROL SYSTEM.....	5
FIGURE 1-3 NUMBER OF CANDIDATE SOLUTIONS AND MODEL ACCURACY DURING THE DESIGN PROCESS.....	9
FIGURE 1-4 METHODOLOGY ADOPTED FOR DYNAMIC SIMULATION MODEL OF THE FLUX SWITCHING MACHINE .....	14
FIGURE 1-5 STRUCTURE OF THE THESIS.....	18
FIGURE 2-1 SIMPLIFIED CONSTRUCTION OF A 4/2 FLUX SWITCHING MACHINE .....	19
FIGURE 2-2 SIMPLIFIED OPERATION OF FLUX SWITCHING AND SWITCHED RELUCTANCE MACHINES.....	22
FIGURE 2-3 SECTIONS OF AC AND DC BACK IRON FLUX IN FLUX SWITCHING AND SWITCHED RELUCTANCE MACHINES .....	24
FIGURE 2-4 IDEALISED OPERATION OF FLUX SWITCHING MACHINE OPERATING AS A MOTOR	26
FIGURE 2-5 IDEALISED FLUX LINKAGE-CURRENT LOCI FOR FLUX SWITCHING MACHINE OPERATING AS A MOTOR .....	27
FIGURE 2-6 EXPERIMENTAL WAVEFORM SHOWING OPTICAL POSITION SENSOR ALIGNMENT WITH ARMATURE INDUCED EMFS FOR DC FIELD EXCITATION .....	29
FIGURE 2-7 SCHEMATIC WINDING OPTIONS FOR ONE WINDING OF THE FLUX SWITCHING MOTOR.....	30
FIGURE 2-8 STAGES OF CONVENTIONAL FINITE ELEMENT ANALYSIS .....	32
FIGURE 2-9 STAGES OF PARAMETERISED FINITE ELEMENT ANALYSIS.....	33
FIGURE 2-10 COMPARISON OF FLUX SWITCHING MACHINE GEOMETRY AS DESIGNED AND AS MANUFACTURED.....	35
FIGURE 2-11 FINITE ELEMENT MESH USED DURING DESIGN OF 8/4 FLUX SWITCHING MACHINE .....	36
FIGURE 2-12 3- AND 5-LAYER AIRGAP DISCRETISATION IN FINITE ELEMENT ANALYSIS .....	38
FIGURE 2-13 EXAMPLE DISTRIBUTION OF ESTIMATED NUMERICAL ERROR IN THE SIMPLIFIED FINITE ELEMENT MODEL OF THE 8/4 FLUX SWITCHING MACHINE .....	39
FIGURE 2-14 EFFECT OF MESH GRAVITY POINTS ON FINITE ELEMENT DISCRETISATION .....	39
FIGURE 2-15 EFFECT OF AUTOMATIC MESH ADAPTION ON FINITE ELEMENT DISCRETISATION .....	41

FIGURE 2-16 ILLUSTRATION OF SOLUTION TIME SAVED BY REUSING PREVIOUSLY ADAPTED FINITE ELEMENT MESHES FOR GEOMETRICALLY IDENTICAL MODELS.....	43
FIGURE 2-17 EXAMPLE GRAPHICAL OUTPUT AVAILABLE FROM FINITE ELEMENT ANALYSIS.	45
FIGURE 2-18 SAMPLE EXTRACT FROM RESULTS FILE OBTAINED FROM PARAMETERISED FINITE ELEMENT ANALYSIS .....	45
FIGURE 2-19 SAMPLE EXPERIMENTAL RESULTS FOR SEPARATELY EXCITED 8/4 FLUX SWITCHING MOTOR.....	49
FIGURE 2-20 SAMPLE CONVERGENCE OF FLUX WITH FINITE ELEMENT SOLUTION ITERATIONS .....	51
FIGURE 2-21 COMPARISON OF EXPERIMENTALLY OBTAINED STEEL CHARACTERISTICS AT 20HZ AND 540HZ .....	52
FIGURE 2-22 EFFECTS OF FILLETING ON ESTIMATED NUMERICAL ERROR AND RELATIVE PERMEABILITY.....	54
FIGURE 2-23 COMPARISON OF SIMPLIFIED AND GEOMETRICALLY ACCURATE PARAMETERISED FINITE ELEMENT MODELS FOR THE 8/4 FLUX SWITCHING MACHINE .....	56
FIGURE 2-24 APPLICATION OF THE FLEXIBLE PARAMETERISED FINITE ELEMENT MODEL TO A NEW 8/4 FLUX SWITCHING MACHINE WITH RECTANGULAR STATOR AND FILLETING AT POLE ROOTS .....	57
FIGURE 3-1 DIFFERENT FIELD FLUX PATHS IN EACH INTERMEDIATE ROTOR POSITION .....	61
FIGURE 3-2 FIELD AND ARMATURE FLUXES IN AN ALIGNED POSITION OF NEGATIVE MUTUAL COUPLING .....	62
FIGURE 3-3 FIELD FLUX IN AN INTERMEDIATE POSITION SHOWING EFFECTS OF CROSS- SATURATION.....	63
FIGURE 3-4 ILLUSTRATION OF FLUX MAP STORAGE IN MULTI-DIMENSIONAL ARRAYS .....	64
FIGURE 3-5 ILLUSTRATION OF COMPUTATIONAL OVERHEAD REDUCTION BY INSPECTION OF THE FLUX MAP .....	65
FIGURE 3-6 ORIGINAL FLUX SURFACE FOR REFERENCE.....	66
FIGURE 3-7 EXAMPLE OF COMPUTATIONAL OVERHEAD REDUCTION BY INTERPOLATION .....	67
FIGURE 3-8 EFFECTS OF DATA POINT SPACING AND SMALL RANDOM ERROR ON INTERPOLATED DATA QUALITY .....	69
FIGURE 3-9 EXAMPLE OF FINITE ELEMENT ANALYSIS ERRORS IN SATURATED REGION OF THE FLUX MAP .....	70
FIGURE 3-10 FIELD AND ARMATURE FLUXES AT AN ALIGNED AND AN INTERMEDIATE POSITION.....	72
FIGURE 3-11 DIFFERENCES IN FLUX DUE TO FINITE ELEMENT MESHING AND NUMERICAL ACCURACY.....	73

FIGURE 3-12 DIFFERENCES IN FLUX DUE TO FINITE ELEMENT MODEL GEOMETRIC ACCURACY .....	74
FIGURE 3-13 DIFFERENCES IN FLUX DUE TO COIL SET-BACK IN THE FINITE ELEMENT MODEL .....	75
FIGURE 3-14 DIFFERENCES IN FLUX DUE TO FILLETING IN THE FINITE ELEMENT MODEL.....	76
FIGURE 3-15 DIFFERENCES IN FLUX DUE TO B-H CHARACTERISTICS USED IN THE FINITE ELEMENT MODEL .....	78
FIGURE 3-16 DEFINITIONS OF ABSOLUTE AND INCREMENTAL INDUCTANCE USED .....	81
FIGURE 3-17 COMPARISON OF INDUCTANCES OBTAINED FROM THE FLUX MAP FOR DIFFERENT B-H CHARACTERISTICS .....	83
FIGURE 3-18 TYPICAL CURRENT WAVEFORM FOR A LINEAR SERIES RL CIRCUIT.....	85
FIGURE 3-19 EXAMPLE OF MEASURED FLUX LINKAGES STARTING WITH POSITIVE AND NEGATIVE REMNANT FLUX .....	88
FIGURE 3-20 SCHEMATIC CIRCUIT USED FOR FLUX LINKAGE MEASUREMENT.....	89
FIGURE 3-21 EXAMPLE OF MEASURED FLUX LINKAGE DATA SMOOTHING USING A FITTED POLYNOMIAL .....	90
FIGURE 3-22 COMPARISON OF INDUCTANCES FROM EXPERIMENT AND FINITE ELEMENT ANALYSIS.....	92
FIGURE 3-23 EFFECT OF APPLIED VOLTAGE ON MEASURED FLUX LINKAGE AND INDUCTANCE .....	94
FIGURE 3-24 INDUCTANCES MEASURED USING PRECISION COMPONENT ANALYSER.....	96
FIGURE 4-1 EXAMPLE FLUX-MMF CHARACTERISTIC AND DATA CONVERSION FOR A SWITCHED RELUCTANCE MACHINE .....	101
FIGURE 4-2 FLUX SURFACES AT AN ALIGNED POSITION OF NEGATIVE MUTUAL COUPLING .	102
FIGURE 4-3 FLUX CONTOURS AT AN ALIGNED POSITION OF NEGATIVE MUTUAL COUPLING	104
FIGURE 4-4 EXAMPLE OF DATA CONVERSION PROCESS BY FINDING INTERSECTIONS OF FLUX CONTOURS .....	105
FIGURE 4-5 EXAMPLE OF FLUX SURFACES AND CONTOURS FOR A POSITION OF ZERO MUTUAL COUPLING .....	106
FIGURE 4-6 EXAMPLE OF OBTAINING FIELD MMF AND ARMATURE FLUX GIVEN KNOWN ARMATURE MMF AND FIELD FLUX.....	108
FIGURE 4-7 EXAMPLE OF OBTAINING ARMATURE MMF AND FIELD FLUX GIVEN KNOWN FIELD MMF AND ARMATURE FLUX.....	109
FIGURE 4-8 ERRORS IN CONTOUR INTERSECTION FOR POSITIONS OF ZERO AND STRONG MUTUAL COUPLING .....	110
FIGURE 4-9 EXAMPLE OF INCREASED CONTOUR DEFINING POINTS BY FINITE ELEMENT DATA INTERPOLATION.....	113

FIGURE 4-10 EXAMPLE OF FINITE ELEMENT DATA INTERPOLATION TO INCREASE FLUX DATA RESOLUTION .....	114
FIGURE 4-11 EXAMPLE OF NUMBER OF LINE SEGMENTS AS RELIABILITY TEST FOR FLUX CONTOURS .....	118
FIGURE 4-12 FLUX CONTOUR OSCILLATIONS DURING A COMPLETE ELECTRICAL CYCLE.....	122
FIGURE 4-13 EXAMPLE OF THE SEARCH PROCESS FOR FINDING A CONTOUR INTERSECTION	124
FIGURE 4-14 EXAMPLE DERIVED CONTOURS OF MMF AT AN ALIGNED AND AN INTERMEDIATE POSITION.....	126
FIGURE 4-15 EXAMPLE OF FLUX RECONSTRUCTION AS A NUMERICAL ERROR ESTIMATOR AT AN ALIGNED AND AN INTERMEDIATE POSITION.....	128
FIGURE 4-16 CHARACTERISTIC PATTERN IN DERIVED DATA INDICATING UNRELIABLE CONTOUR DATA .....	130
FIGURE 4-17 FIELD AND ARMATURE FLUX AS A FUNCTION OF FIELD AND ARMATURE MMFS FOR A COMPLETE ELECTRICAL CYCLE.....	134
FIGURE 4-18 FIELD AND ARMATURE MMF AS A FUNCTION OF FIELD AND ARMATURE FLUXES FOR A COMPLETE ELECTRICAL CYCLE.....	135
FIGURE 4-19 FIELD MMF AND ARMATURE FLUX AS A FUNCTION OF FIELD FLUX AND ARMATURE MMF FOR A COMPLETE ELECTRICAL CYCLE .....	136
FIGURE 4-20 FIELD FLUX AND ARMATURE MMF AS A FUNCTION OF FIELD MMF AND ARMATURE FLUX FOR A COMPLETE ELECTRICAL CYCLE .....	137
FIGURE 4-21 EFFECTS OF FINITE ELEMENT MODEL FORMULATION ON FIELD MMF AT AN ALIGNED POSITION.....	140
FIGURE 4-22 EFFECTS OF FINITE ELEMENT MODEL FORMULATION ON FIELD MMF AT AN INTERMEDIATE POSITION.....	141
FIGURE 4-23 COMPARISON OF FIELD NUMERICAL ERROR ESTIMATES FOR EACH FLUX MAP IN AN ALIGNED POSITION .....	143
FIGURE 4-24 COMPARISON OF FIELD NUMERICAL ERROR ESTIMATES FOR EACH FLUX MAP IN AN INTERMEDIATE POSITION .....	144
FIGURE 4-25 FIELD MMF ERRORS DUE TO POLYNOMIAL EXTRAPOLATION OF FLUX CONTOURS .....	146
FIGURE 4-26 EFFECT OF CONTOUR INTERPOLATION METHOD ON DERIVED FIELD MMF.....	147
FIGURE 4-27 EFFECT OF CONTOUR INTERPOLATION METHOD ON NUMERICAL ERROR ESTIMATE.....	149
FIGURE 5-1 GAUSS-SEIDEL ITERATIVE SOLUTION PROCESS AT EACH TIME STEP FOR BOTH WINDINGS CONNECTED.....	158
FIGURE 5-2 GAUSS-SEIDEL ITERATIVE SOLUTION PROCESS AT EACH TIME STEP FOR ARMATURE OPEN CIRCUIT .....	159

FIGURE 5-3 GAUSS-SEIDEL ITERATIVE SOLUTION PROCESS AT EACH TIME STEP FOR FIELD OPEN CIRCUIT .....	160
FIGURE 5-4 COMPARISON OF EXPERIMENTAL AND SIMULATED RESULTS FOR 8/4 FLUX SWITCHING MACHINE RUNNING AT 1094RPM WITH 1.02VDC FIELD EXCITATION AND ARMATURE OPEN CIRCUIT .....	165
FIGURE 5-5 COMPARISON OF EXPERIMENTAL AND SIMULATED RESULTS FOR 8/4 FLUX SWITCHING MACHINE RUNNING AT 1170RPM WITH 7.56VDC FIELD EXCITATION AND ARMATURE OPEN CIRCUIT .....	166
FIGURE 5-6 COMPARISON OF EXPERIMENTAL AND SIMULATED RESULTS FOR 8/4 FLUX SWITCHING MACHINE RUNNING AT 5008RPM WITH 0.94VDC FIELD EXCITATION AND ARMATURE OPEN CIRCUIT .....	166
FIGURE 5-7 COMPARISON OF EXPERIMENTAL AND SIMULATED RESULTS FOR 8/4 FLUX SWITCHING MACHINE RUNNING AT 4972RPM WITH 7.42VDC FIELD EXCITATION AND ARMATURE OPEN CIRCUIT .....	167
FIGURE 5-8 COMPARISON OF EXPERIMENTAL AND SIMULATED RESULTS FOR THE 8/4 FLUX SWITCHING MACHINE WITH VOLTAGE SOURCE AND CURRENT SOURCE FIELD EXCITATION SET TO EXPERIMENTAL MEAN VALUE.....	169
FIGURE 5-9 EFFECT OF FINITE ELEMENT MESH REFINEMENT ON SIMULATED RESULTS FOR THE 8/4 FLUX SWITCHING MACHINE WITH VOLTAGE SOURCE FIELD EXCITATION AND ARMATURE OPEN CIRCUIT AT CONSTANT SPEED .....	172
FIGURE 5-10 EFFECT OF FINITE ELEMENT MODEL GEOMETRIC ACCURACY ON SIMULATED RESULTS FOR THE 8/4 FLUX SWITCHING MACHINE WITH VOLTAGE SOURCE FIELD EXCITATION AND ARMATURE OPEN CIRCUIT AT CONSTANT SPEED.....	174
FIGURE 5-11 EFFECT OF FINITE ELEMENT ANALYSIS B-H CHARACTERISTIC ON SIMULATED RESULTS FOR THE 8/4 FLUX SWITCHING MACHINE WITH VOLTAGE SOURCE FIELD EXCITATION AND ARMATURE OPEN CIRCUIT AT CONSTANT SPEED.....	176
FIGURE 5-12 COMPARISON OF EXPERIMENTAL RESULTS AND SIMULATED RESULTS AT VARIOUS FIELD WINDING TEMPERATURES FOR THE 8/4 FLUX SWITCHING MACHINE WITH VOLTAGE SOURCE FIELD EXCITATION AND ARMATURE OPEN CIRCUIT AT CONSTANT SPEED.....	179
FIGURE 6-1 CIRCUIT DIAGRAM OF FLUX SWITCHING MOTOR AND DRIVE SYSTEM MODELLED .....	183
FIGURE 6-2 OPERATION OF FLUX SWITCHING MOTOR DRIVE SYSTEM IN NORMAL OPERATION .....	185
FIGURE 6-3 OPERATION OF FLUX SWITCHING MOTOR DRIVE SYSTEM FOR TRANSIENT START-UP CONDITIONS.....	186

FIGURE 6-4 EXAMPLE OF OPTICAL POSITION SENSOR SIGNAL CALIBRATION IN THE SIMULATION MODEL .....	188
FIGURE 6-5 BEHAVIOUR OF THE BIFILAR ARMATURE WINDING IN THE DRIVE CIRCUIT .....	189
FIGURE 6-6 DEFINITION OF BIFILAR ARMATURE CURRENTS AND DIRECTIONS.....	190
FIGURE 6-7 EXAMPLE IMPLEMENTATION OF SWITCH OPERATING POSITIONS FOR THE FLUX SWITCHING MOTOR .....	204
FIGURE 6-8 SIMPLIFIED CIRCUIT DIAGRAM FOR ANALYSIS WITH WINDINGS REPLACED BY 'BLACK-BOX' COMPONENTS.....	205
FIGURE 6-9 COMPARISON OF SIMULATED AND EXPERIMENTAL CURRENT WAVEFORMS FOR THE 8/4 FLUX SWITCHING MOTOR RUNNING AT 14,982RPM WITH NO EXTERNALLY APPLIED LOAD .....	213
FIGURE 6-10 COMPARISON OF SIMULATED AND EXPERIMENTAL CURRENT WAVEFORMS FOR THE 8/4 FLUX SWITCHING MOTOR RUNNING AT 15,022RPM WITH 0.5Nm EXTERNALLY APPLIED LOAD .....	214
FIGURE 6-11 COMPARISON OF SIMULATED AND EXPERIMENTAL CURRENT WAVEFORMS FOR THE 8/4 FLUX SWITCHING MOTOR RUNNING AT 8,075RPM WITH NO EXTERNALLY APPLIED LOAD.....	215
FIGURE 6-12 COMPARISON OF SIMULATED AND EXPERIMENTAL CURRENT WAVEFORMS FOR THE 8/4 FLUX SWITCHING MOTOR RUNNING AT 7,985RPM WITH 0.25Nm EXTERNALLY APPLIED LOAD .....	216
FIGURE 6-13 SAMPLE COMPREHENSIVE SET OF RESULTS FROM SIMULATION (PART 1 OF 3)	219
FIGURE 6-14 SAMPLE COMPREHENSIVE SET OF RESULTS FROM SIMULATION (PART 2 OF 3)	220
FIGURE 6-15 SAMPLE COMPREHENSIVE SET OF RESULTS FROM SIMULATION (PART 3 OF 3)	221
FIGURE 6-16 EFFECT OF FINITE ELEMENT MODEL ACCURACY ON SIMULATED CURRENT WAVEFORMS.....	223
FIGURE 6-17 EFFECT OF WINDING RESISTANCE ON SIMULATED CURRENT WAVEFORMS .....	225
FIGURE 6-18 EFFECT OF CONTOUR INTERPOLATION METHOD USED DURING DATA CONVERSION ON SIMULATED CURRENT WAVEFORMS.....	227
FIGURE 6-19 EFFECT OF SHIFTED SWITCH OPERATING POSITIONS ON SIMULATED CURRENT WAVEFORMS.....	229
FIGURE 6-20 EFFECT OF FIELD CURRENT USED FOR OPTICAL POSITION SENSOR SIGNAL CALIBRATION IN THE SIMULATION MODEL ON SIMULATED CURRENT WAVEFORMS.....	231
FIGURE 6-21 EFFECT OF EXTERNAL SERIES INDUCTANCES APPLIED TO BOTH WINDINGS ON SIMULATED CURRENT WAVEFORMS .....	233
FIGURE 6-22 EFFECT OF EXTERNAL SERIES INDUCTANCES APPLIED TO ONLY ONE WINDING ON SIMULATED CURRENT WAVEFORMS.....	234
FIGURE 6-23 FLUX LINKAGE-CURRENT LOCI AND INSTANTANEOUS TORQUE FOR THE 8/4 FLUX SWITCHING MOTOR RUNNING AT APPROX. 15,000RPM UNLOADED AND LOADED	237

FIGURE 6-24 FLUX LINKAGE-CURRENT LOCI AND INSTANTANEOUS TORQUE FOR THE 8/4 FLUX SWITCHING MOTOR RUNNING AT APPROX. 8,000RPM UNLOADED AND LOADED ..	238
FIGURE 6-25 ZOOMED FIELD FLUX LINKAGE-CURRENT LOCUS FOR THE 8/4 FLUX SWITCHING MOTOR RUNNING AT 14,982RPM WITH NO EXTERNALLY APPLIED LOAD .....	239
FIGURE 6-26 COMPARISON OF WINDING CURRENTS FOR THE 8/4 FLUX SWITCHING MOTOR RUNNING AT APPROX. 15,000RPM WITH AND WITHOUT 2 MECHANICAL DEGREE ADVANCE OF SWITCH OPERATING POSITIONS.....	242
FIGURE 6-27 COMPARISON OF FLUX LINKAGE-CURRENT LOCI AND INSTANTANEOUS TORQUE FOR THE 8/4 FLUX SWITCHING MOTOR RUNNING AT APPROX. 15,000RPM WITH AND WITHOUT 2 MECHANICAL DEGREE ADVANCE OF SWITCH OPERATING POSITIONS .....	243
FIGURE 7-1 GENERAL OPERATION OF A GENETIC ALGORITHM SYSTEM .....	252
FIGURE 7-2 ILLUSTRATIVE FITNESS LANDSCAPE WITH MULTIPLE LOCAL OPTIMA .....	253
FIGURE 7-3 SCHEMATIC OF GENETIC ALGORITHM/PARAMETERISED FINITE ELEMENT SYSTEM IMPLEMENTED .....	265
FIGURE 7-4 EVOLUTIONARY PROGRESS OF GENETIC ALGORITHM TESTS 1-3 .....	273
FIGURE 7-5 EVOLUTIONARY PROGRESS OF GENETIC ALGORITHM TESTS 4-6 .....	277
FIGURE 7-6 EVOLUTIONARY PROGRESS OF GENETIC ALGORITHM TEST 7 .....	280
FIGURE 8-1 EXAMPLE OF 8/4 FLUX SWITCHING MOTOR FLUX ORIENTATION AND CURRENTS DURING OPERATION.....	286
FIGURE 8-2 'TRADITIONAL' METHOD OF OBTAINING FINITE ELEMENT DATA FOR IRON LOSS ESTIMATION.....	287
FIGURE 8-3 EXAMPLE GRAPHICAL OUTPUT FROM FINITE ELEMENT ANALYSIS SHOWING SPATIAL DISTRIBUTION OF FLUX DENSITY.....	289
FIGURE 8-4 METHODOLOGY FOR IRON LOSS VISUALISATION METHOD DEVELOPED .....	290
FIGURE 8-5 DERIVATION OF POSITION INDEPENDENT FLUX COMPONENTS .....	291
FIGURE 8-6 COMPARISON OF CARTESIAN AND POLAR FLUX COMPONENTS .....	294
FIGURE 8-7 COMPARISON OF COLOUR AND GREYSCALE COMPONENT AXES.....	296
FIGURE 8-8 EXAMPLE OF DERIVING PIXEL DIMENSIONS BY INSPECTION OF THE BITMAP IMAGE.....	299
FIGURE 8-9 EXAMPLE OF FINDING REGION OF INTEREST WITHIN BITMAP IMAGE BY INSPECTION.....	301
FIGURE 8-10 EXAMPLE OF ROTOR IMAGE ROTATION AND CROPPING.....	302
FIGURE 8-11 COMPARISON OF GREYSCALE AND COLOUR AXES FOR DATA VISUALISATION	306

FIGURE 8-12 SPATIAL DISTRIBUTION OF MAXIMUM FLUX DENSITY IN THE STATOR OF THE 8/4 FLUX SWITCHING MOTOR OPERATING AT APPROX. 15,000RPM UNLOADED AND LOADED .....	310
FIGURE 8-13 SPATIAL DISTRIBUTION OF MEAN AND RANGE OF FLUX IN THE STATOR OF THE 8/4 FLUX SWITCHING MOTOR OPERATING AT APPROX. 15,000RPM UNLOADED AND LOADED .....	312
FIGURE 8-14 SPATIAL DISTRIBUTION OF MEAN AND RANGE OF FLUX IN THE ROTOR OF THE 8/4 FLUX SWITCHING MOTOR OPERATING AT APPROX. 15,000RPM UNLOADED AND LOADED .....	313
FIGURE 8-15 SPATIAL DISTRIBUTION OF MAXIMUM AND MEAN RATE OF CHANGE OF FLUX IN THE STATOR OF THE 8/4 FLUX SWITCHING MOTOR OPERATING AT APPROX. 15,000RPM UNLOADED AND LOADED .....	315
FIGURE 8-16 SPATIAL DISTRIBUTION OF MAXIMUM RATE OF CHANGE OF FLUX IN THE ROTOR OF THE 8/4 FLUX SWITCHING MOTOR OPERATING AT APPROX. 15,000RPM UNLOADED AND LOADED .....	315
FIGURE 8-17 EXAMPLE OF OSCILLATING FLUX IN REGIONS OF THE STATOR BACK IRON .....	317
FIGURE 8-18 EXAMPLE OF EDGE EFFECTS DUE TO BITMAP IMAGE DISCRETISATION AND INTERPOLATION .....	318

TABLE 2-1 MAIN SOURCES OF ERROR IN FINITE ELEMENT ANALYSIS.....	50
TABLE 3-1 SUMMARY OF FINITE ELEMENT MODELS USED TO CREATE EACH FLUX MAP FOR COMPARISON .....	71
TABLE 3-2 SUMMARY OF DIFFERENCES IN FLUXES DUE TO FINITE ELEMENT MODEL FORMULATION.....	80
TABLE 3-3 SUMMARY OF MEASURED AND CALCULATED INDUCTANCES OBTAINED BY THE SIMPLE TIME CONSTANT METHOD .....	86
TABLE 3-4 COMMUTATION FREQUENCIES FOR VARIOUS 8/4 FLUX SWITCHING MACHINE OPERATING SPEEDS.....	95
TABLE 3-5 COMPARISON OF INDUCTANCES OBTAINED FROM SIMPLE TIME CONSTANT METHOD AND COMPONENT ANALYSER.....	96
TABLE 4-1 SUMMARY OF STAGES FOR PRACTICAL IMPLEMENTATION OF THE DATA CONVERSION ALGORITHM .....	111
TABLE 4-2 OBJECTIVE FUNCTIONS TO BE SATISFIED AT POINTS OF INTERSECTION FOR DATA CONVERSION.....	124
TABLE 4-3 ALTERNATIVES IMPLEMENTED FOR EACH STAGE OF ELECTROMAGNETIC DATA CONVERSION.....	131
TABLE 4-4 SUMMARY OF FINITE ELEMENT MODELS USED FOR FLUX MAPS COMPARED .....	138
TABLE 5-1 PHYSICAL CHARACTERISTICS OF 8/4 FLUX SWITCHING MACHINE USED FOR MODEL VALIDATION .....	153
TABLE 5-2 FACTORS AFFECTING ACCURACY AND SOLUTION TIME OF DYNAMIC SIMULATION MODEL.....	162
TABLE 5-3 EXPERIMENTAL CONDITIONS FOR WHICH COMPARATIVE RESULTS ARE PRESENTED .....	164
TABLE 5-4 NUMERICAL COMPARISON BETWEEN EXPERIMENTAL AND SIMULATED RESULTS FOR THE 8/4 FLUX SWITCHING MACHINE WITH CONSTANT VOLTAGE FIELD EXCITATION AND ARMATURE OPEN CIRCUIT .....	167
TABLE 5-5 SUMMARY OF FINITE ELEMENT MODELS USED TO CREATE FLUX MAPS.....	170
TABLE 6-1 SUMMARY OF SYMBOLS USED DURING MODEL DERIVATION.....	184

TABLE 6-2 POSSIBLE OPERATING CONDITIONS FOR THE FLUX SWITCHING MOTOR WITH EFFECTIVE ARMATURE VOLTAGES AND CURRENTS.....	192
TABLE 6-3 SUMMARY OF EXPERIMENTAL CONDITIONS FOR WHICH EXPERIMENTAL RESULTS ARE COMPARED WITH SIMULATION.....	211
TABLE 6-4 SUMMARY OF FINITE ELEMENT MODELS USED TO CREATE FLUX MAPS.....	222
TABLE 6-5 COMPARISON OF MEAN TORQUE CALCULATED BY THE MAXWELL STRESS AND ENERGY CONVERSION LOOP METHODS.....	240
TABLE 6-6 COMPARISON OF MEAN TORQUE CALCULATED BY THE MAXWELL STRESS AND ENERGY CONVERSION LOOP METHODS FOR THE 8/4 FLUX SWITCHING MACHINE RUNNING AT APPROX. 15,000RPM WITH AND WITHOUT 2 MECHANICAL DEGREE ADVANCE OF SWITCH OPERATING POSITIONS .....	244
TABLE 7-1 EXAMPLE OF DECODING DESIGN PARAMETERS FROM A BINARY CHROMOSOME	257
TABLE 7-2 EXAMPLES OF SINGLE AND TWO POINT CROSSOVER OF BINARY CHROMOSOMES .....	260
TABLE 7-3 EXAMPLES OF SELECTION STRATEGIES FOR BREEDING.....	261
TABLE 7-4 EXAMPLE OF BITWISE MUTATION IN A BINARY CHROMOSOME.....	261
TABLE 7-5 EXAMPLE OF OBTAINING INDIVIDUAL FITNESS FROM FINITE ELEMENT ANALYSIS TEXT RESULTS FILE.....	267
TABLE 7-6 EXTRACT FROM FITNESS EVALUATION MODULE OUTPUT FILE .....	268
TABLE 7-7 DESIGN PARAMETERS AND DISCRETISATION FOR TESTS 1-3.....	271
TABLE 7-8 GENETIC ALGORITHM PARAMETERS USED FOR TESTS 1-3 .....	272
TABLE 7-9 COMPARISON OF PARAMETERS BETWEEN THE FITTEST INDIVIDUALS FOUND IN TEST 1 .....	274
TABLE 7-10 GENETIC ALGORITHM PARAMETERS USED FOR TESTS 4-6 .....	275
TABLE 7-11 POSITIONS OF FITTEST INDIVIDUALS IN EACH GENERATION OF TESTS 4-6.....	278
TABLE 7-12 GENETIC ALGORITHM PARAMETERS USED FOR TEST 7 .....	280
TABLE 7-13 POSITIONS OF FITTEST INDIVIDUALS IN EACH GENERATION OF TEST 7.....	281

## TABLE OF MAIN SYMBOLS USED

Symbol	Description	Units	
$B$	Magnetic flux density	Tesla	T
$C$	Capacitance	Farad	F
$e$	Electro motive force, emf	Volt	V
$F$	Magneto motive force, mmf	Ampere	A
$i$	Current (time varying)	Ampere	A
$k$	Constant		
$l$	Stack length	Metre	m
$L$	Inductance	Henry	H
$N$	Integer number		
$P^{(1)}$	Power	Watt	W
$P^{(2)}$	Parallel paths		
$q$	Electric charge	Coulomb	C
$R$	Resistance	Ohm	$\Omega$
$S$	Coils in series		
$t$	Time	Second	s
$T$	Torque	Newton metre	Nm
$v$	Voltage (time varying)	Volt	V
$V$	Voltage (time invariant)	Volt	V
$\Phi$	Magnetic flux	Weber	Wb
$\Psi$	Magnetic flux linkage	Volt seconds	Vs
$\theta$	Rotor angle	Degree	$^{\circ}$
$\omega$	Radian frequency	Radians per second	rads <sup>-1</sup>

### Subscripts

$f$	Field winding
$a$	Armature winding
$x$	Either winding
$s$	Stator
$r$	Rotor

---

# **Chapter 1**

Introduction

---

# 1 INTRODUCTION

## 1.1 Objectives of research

The primary objective of the project presented in this thesis was to research and develop a dynamic simulation model for the design of the flux switching machine, the construction and operating principles of which are presented in chapter 2. The model is intended for detailed design and development use and must fulfil several criteria. Firstly, it should be accurate, within acceptable bounds, up to and beyond the design operating speed including transient conditions. When the flux switching machine is operated as a motor, it should also be capable of modelling the interaction between the motor, the power electronic converter circuit and the switch control algorithm. To be of practical application the model should be rapid enough at the point of use that it can practicably be used within an iterative design process without requiring expensive computer hardware. The model developed is validated by comparison of results obtained by simulation and experiment.

In addition to the development of a dynamic simulation model for the flux switching machine, there were a number of secondary objectives of the project which facilitate the efficient implementation of the model developed and further assist in the design and analysis process. These include the development of an accurate 2-dimensional parameterised finite element model for the flux switching machine, the implementation of automated design and optimisation techniques and a simple method for visualisation of iron loss distribution. These secondary objectives add value within the design process and were implemented with a view to the future development of a more automated machine design process.

## 1.2 Introduction to reluctance machines

### 1.2.1 General principle of operation

Unlike most other types of electric machine, reluctance machines have no moving coils, permanent magnets or sliding contacts. Instead, the rotor consists of only steel and torque is produced by the tendency of the rotor to align itself with an applied magnetic field, thus minimising the reluctance of the magnetic circuit. Figure 1-1 illustrates the simplified operation of a hypothetical reluctance machine drawn schematically for clarity. Current in the coil gives rise to a magnetic flux,  $\phi$ , as denoted by the arrow, which links the coil. In Figure 1-1a the position of the rotor is such that if it is rotated clockwise the reluctance of the magnetic circuit decreases and a clockwise torque,  $T$ , is produced as shown until the rotor reaches the position shown in Figure 1-1b. In this position the reluctance of the magnetic circuit is at a minimum and a stable equilibrium is achieved. The rotor is then said to be in an aligned position.

If current in the coil is maintained then the rotor will eventually settle in the stable equilibrium position of Figure 1-1b after some overshoot and oscillation due to the inertia of the rotor. However, if current is removed from the coil while the rotor is still travelling in a clockwise direction then its momentum will carry it past this position towards the position shown in Figure 1-1c. This is an unstable equilibrium position where current applied to the coil will produce no net torque and the rotor is said to be in an unaligned position. If the momentum of the rotor is sufficient to carry it past this position then current applied to the coil thereafter will produce torque in the same direction as previously, shown in Figure 1-1d. Hence, by switching the coil current on and off at appropriate times, continuous rotation may be achieved or, if the rotor is driven by a prime mover, electrical power may be generated.

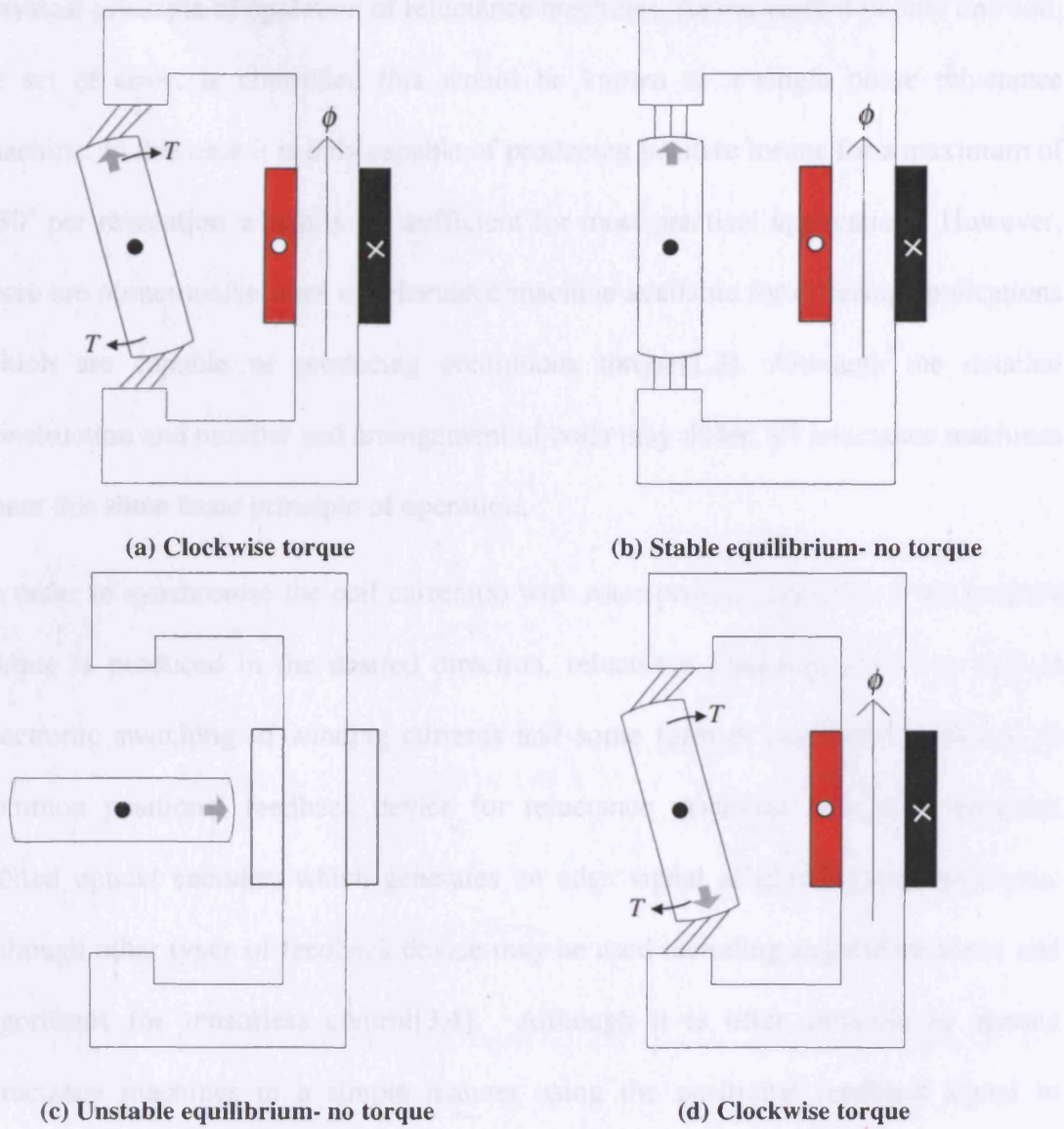
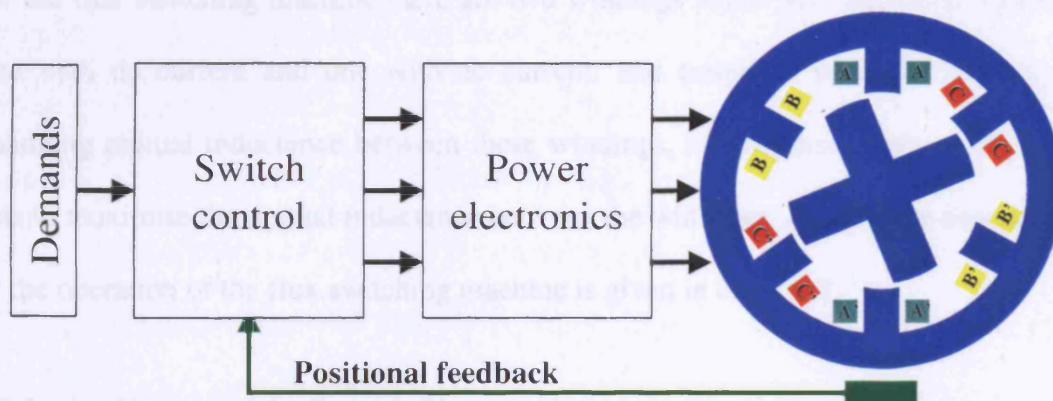


Figure 1-1 Simplified operation of a hypothetical reluctance machine

The hypothetical machine shown in Figure 1-1 gives a simple illustration of the physical principle of operation of reluctance machines. As the current in only one coil, or set of coils, is controlled this would be known as a single phase reluctance machine. In this case it is only capable of producing positive torque for a maximum of  $180^\circ$  per revolution which is not sufficient for most practical applications. However, there are numerous variants of reluctance machine available for differing applications which are capable of producing continuous torque[1,2]. Although the detailed construction and number and arrangement of coils may differ, all reluctance machines share this same basic principle of operation.

In order to synchronise the coil current(s) with rotor position such that a net positive torque is produced in the desired direction, reluctance machines generally require electronic switching of winding currents and some form of positional feedback. A common positional feedback device for reluctance machines is a shaft mounted slotted optical encoder, which generates an edge signal at specific rotor positions, although other types of feedback device may be used including angular resolvers and algorithms for sensorless control[3,4]. Although it is often possible to operate reluctance machines in a simple manner using the positional feedback signal to directly control the operation of the electronic switches in a similar way to the commutator of brushed dc machines, a microcontroller is generally used to enable increased performance.

Figure 1-2 illustrates the general arrangement of a 3-phase switched reluctance motor, drive and control system. In order to produce continuous rotation each of the three phases A, B and C are individually switched on in sequence, thus producing continuous torque in the manner described above. Performance demands such as speed are fed into the microcontroller which controls the switching sequence and timing. These low level outputs are used to control current in the motor windings via the power electronic switches while the control loop is closed by the position feedback signal, derived either from a shaft mounted encoder or by some other means, such as a position estimation observer.



**Figure 1-2** General schematic arrangement of reluctance motor, drive and control system

### ***1.2.2 Switched reluctance and flux switching machines***

The work of this thesis is based on the simulation and design of the flux switching machine [5] which produces torque by the same physical principle as the switched reluctance machine, i.e. the tendency of the steel rotor to align itself with an applied magnetic field. However, the method of controlling this applied magnetic field is different in each. For the switched reluctance machine, an example of which is shown in Figure 1-2, each winding is generally switched on individually in sequence and torque is produced mainly by changing self inductance, i.e. the movement of the rotor is such as to maximise the self inductance of the excited winding [1,6,7]. However, for the flux switching machine there are two windings which are controlled together, one with dc current and one with ac current, and torque is produced mainly by changing mutual inductance between these windings, i.e. the movement of the rotor acts to maximise the mutual inductance between the windings. A complete description of the operation of the flux switching machine is given in chapter 2.

### ***1.2.3 Applications of the flux switching machine***

In common with the switched reluctance machine the flux switching machine has no sliding contacts, moving windings or permanent magnets, leading to a simple and robust construction. Electronic commutation of winding currents is required for operation, although this is also required for variable speed operation of other motor types so is no longer considered an inherent disadvantage. Also in common with the switched reluctance machine, the flux switching machine produces significant amounts of pure tone acoustic noise which may be unacceptable in some applications.

The main performance advantages of the flux switching machine over the switched reluctance machine arise from the higher copper utilisation, theoretically 100% in the ideal case, and lower converter VA rating as magnetising energy need not pass back and forth through the power devices. However, in practice there is significant ripple in the output torque which would make the flux switching machine unsuitable for some applications.

In view of these advantages and disadvantages the main potential application areas of the flux switching motor are relatively high speed (between 6,000rpm and 26,000rpm) and low power (100W to 5kW) aimed at high volume, low cost product specific applications, e.g. fans, pumps, power tools. However, the flux switching machine also has the potential to be successfully applied at higher power levels, either as a motor, generator or combined system. There are also further potential applications in explosive atmospheres or applications requiring high reliability, such as gas turbine starter-generators, where the lack of moving contacts, windings or magnets and mechanical simplicity are advantages.

### 1.3 Simulation models for reluctance machines

Despite their simple construction and principle of operation reluctance machines are not generally straightforward to design and simulate as they often involve complex geometries and the steel is routinely driven well into saturation during operation. In fact, this saturation may be necessary to give acceptable performance under some circumstances [8,9]. There is a wide range of simulation models available for reluctance machines representing variations on several different overall approaches. However, although the physical principle of operation of switched reluctance and flux switching machines is similar in as much as the rotor always seeks to align itself with the applied magnetic field, design and simulation models for the switched reluctance machine are generally not directly applicable to the flux switching machine due to the dominance of changing mutual inductance in the flux switching machine.

Section 1.3.1 outlines the relationship between simulation model accuracy and complexity and the various stages in the design and optimisation process for a new machine. Section 1.3.2 then summarises the range of design and simulation models available for the switched reluctance machine and evaluates them with respect to the flux switching machine, showing the reasons why the development of the new simulation model detailed in this thesis was necessary for the detailed design and simulation of the flux switching machine.

### 1.3.1 Machine models in the design process

Figure 1-3 illustrates the relationship between number of potential candidate designs and accuracy of simulation model required during the various stages of the new machine design process. At the start of the design process there are a large number of potential candidate solutions which must be rapidly evaluated, most of which may be readily discarded, hence speed is generally more important than accuracy provided the results obtained represent the correct order of magnitude. However, as design progresses the number of candidate solutions is progressively decreased but the accuracy requirements, hence reasonable execution time, of the model used to evaluate them increases. As the design process converges towards a final design the simulation model used for evaluation must be accurate enough to give realistic results and make a correct comparison between possible solutions with minor changes in order to avoid over-design. However, to achieve this level of accuracy it is reasonable to expend more time in each simulation solution [10].

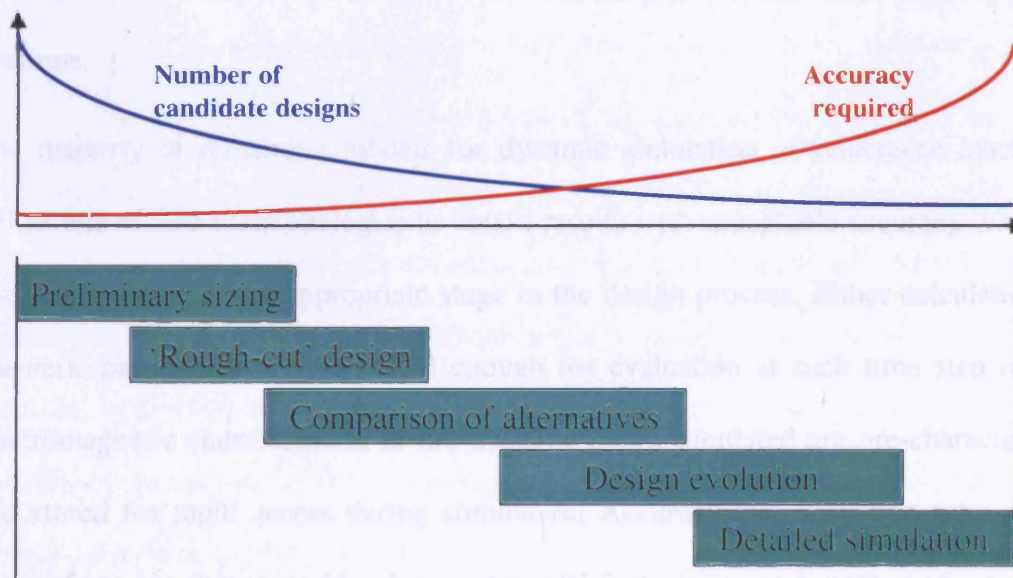


Figure 1-3 Number of candidate solutions and model accuracy during the design process

### ***1.3.2 Evaluation of switched reluctance machine models with respect to the flux switching machine***

The most potentially accurate method for simulating the dynamic performance of reluctance machines is time-stepping finite element analysis [11-13]. Given a finite element model of the machine being simulated and the external electrical circuit to which it is connected this method solves the system equations at every time step, including one or more non-linear finite element solutions. This method is potentially very accurate and is capable of accounting for eddy currents and dynamic effects in the steel for virtually any machine type and converter topology. Therefore, this simulation method is equally applicable to the switched reluctance and flux switching machines. However, it is expensive both in terms of computational time and the skilled user time required to formulate, run and analyse the model. Hence, it is currently only applicable for final detailed simulation where the expense is justified although it may be expected to become applicable progressively earlier in the design process if the current trends in affordable computing power and software ease of use continue.

The majority of remaining models for dynamic simulation of reluctance machines utilise one of two main strategies to obtain results with acceptable accuracy within a reasonable time for the appropriate stage in the design process. Either calculation of magnetic parameters is made rapid enough for evaluation at each time step or the electromagnetic characteristics of the machine being simulated are pre-characterised and stored for rapid access during simulation. Accuracy and execution time at the point of use are determined by the exact model formulation and method of magnetic parameter calculation used.

Analytic or linear models [14-19] are not generally applicable for detailed design of reluctance machines under practical operating conditions as the steel is generally driven well into saturation and specific regions, such as pole tips, experience extreme localised conditions. Furthermore, analytic models do not account well for complex geometries or magnetic flux fringing although some allowance can be made for this [15]. Hence, such models are only generally applicable during the very early stages of design for preliminary sizing calculations.

Several models for the switched reluctance machine explicitly assume that there is no mutual inductance between the phases [13,20-23], i.e. they assume that the flux linking a phase is due entirely to the current flowing in that phase, which is a reasonable assumption in many cases where there is little or no overlap of phase currents during operation. If such an assumption is made it is possible to fully characterise the magnetic properties of the lamination geometry by, for example, obtaining the magnetostatic flux-mmf (or flux linkage-current) relationships for one phase between the unaligned and aligned positions [7,24,25]. This magnetostatic data may itself be obtained either analytically [14,15,20], experimentally [26-28], or using finite element analysis [29,30] among other methods, and there are techniques available to reduce the amount of such data required without adversely affecting accuracy [31]. However, such models cannot be applied to the flux switching machine, regardless of the method by which the electromagnetic properties are derived, as torque in the flux switching machine is produced mainly by changing mutual inductance between two windings.

In practice, for switched reluctance motors where more than one phase is capable of producing positive torque simultaneously or when operating at high speed, there may be considerable overlap of phase currents [32-34] and it is not reasonable to completely neglect mutual coupling between phases. This is also the case for switched reluctance machines containing fully pitched windings [16,35-38]. However, as the main torque producing mechanism is still changing self inductance of the phases, some models include allowance for mutual inductance between phases by way of adjustments or correction factors applied to a predominantly non-coupled model. These methods can improve the accuracy of results obtained for the switched reluctance machine where phase current overlap is not negligible but they still do not fully model the effects of changing mutual inductance.

Magnetic equivalent circuit models are capable of application to mutually coupled reluctance machines and can be very rapid to execute [15,39]. However, the results obtained from such techniques can differ significantly from those obtained by finite element analysis and application to complex lamination geometries is difficult. Furthermore, the results obtained from magnetic equivalent circuit models are of the same type as finite element analysis, i.e. flux linkages as a function of currents and rotor position, but the solution is very rapid and a simulation model which includes mutual coupling is still required for predicting the dynamic performance of the machine. Hence, simulations based on data obtained using magnetic equivalent circuit models are most applicable during the iterative design evolution phase of design due to their speed but, due to their potentially limited accuracy, are not generally suitable for detailed optimisation.

## 1.4 Methodology of the simulation model developed

Although none of the existing models for the switched reluctance machine outlined in section 1.3 are directly applicable to simulation of the flux switching machine, the general methodologies remain valid. A rapid simulation model for the flux switching machine which is suitable for design iteration is already in existence [5] and has been applied to the design of new flux switching machines with some success. This model, which is described in chapter 2, is rapid at the point of use by using a limited number of simple non-linear finite element solutions to obtain the necessary data, which could similarly be obtained using a magnetic equivalent circuit method. However, it is not accurate enough for detailed simulation use and does not fully include the effects of mutual coupling between windings, the power electronic converter circuit or control strategy.

The dynamic simulation model for the flux switching machine developed in this thesis is intended for use during the detailed simulation phase of the design process, particularly for integration with the drive and control system. As such, accuracy of the simulated results is most important and significant computational effort to obtain them is acceptable, as introduced in Figure 1-3. However, in order to remain of practical use the model must be more rapid at the point of use by the end user and much less computationally expensive than time stepping finite element analysis. Therefore, the methodology adopted is based upon the flux-mmF characterisation of the switched reluctance machine [6,31], i.e. the electromagnetic properties of the lamination geometry are pre-characterised and stored for rapid access by the simulation model. However, as the flux switching machine is magnetically similar to a two-phase switched reluctance machine with strong mutual coupling, the technique has been extended to account for this.

Figure 1-4 illustrates the stages involved in implementation of the dynamic simulation model for the flux switching machine developed in this thesis. Firstly the lamination geometry is pre-characterised using finite element analysis and the data obtained is converted into the required format. This process need only be carried out once for each lamination geometry. Simulations may then be carried out using the data obtained without the need for further finite element analysis. Hence, by separating the lamination characterisation and design simulation stages the model remains relatively rapid at the point of use and the computational overhead involved in lamination characterisation can be quickly repaid.

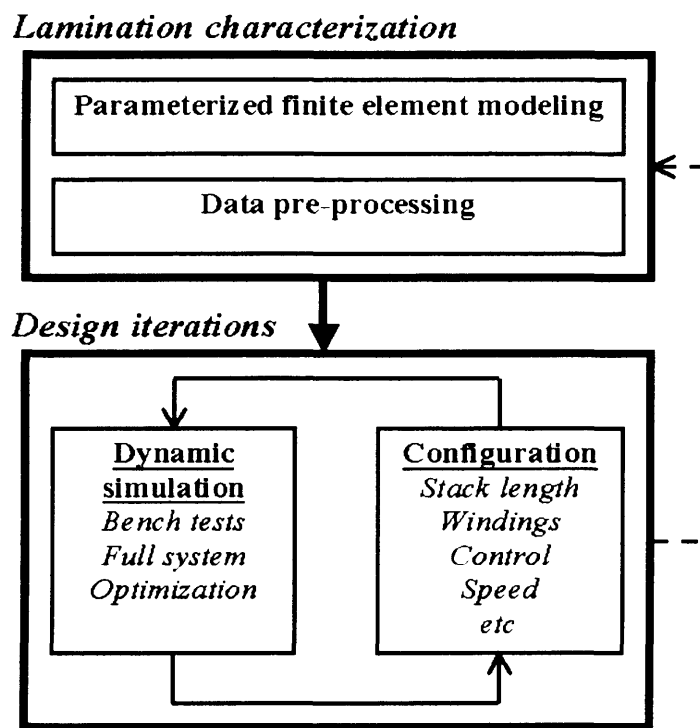


Figure 1-4 Methodology adopted for dynamic simulation model of the flux switching machine

## 1.5 Contribution to knowledge

Although the flux switching machine is similar in construction to previously known topologies [40,41,92], the use of power electronic commutation and its application as a continuous rotation motor [5] are new. Furthermore, despite some similarities in operation to the switched reluctance machine, existing models are not directly applicable to the dynamic simulation of the flux switching machine. Hence, a new dynamic simulation model, rapid enough to be used as part of the design process yet accurate enough for detailed simulation, was required.

The methodology adopted for this simulation model is well known and has been widely used for switched reluctance machines, i.e. the electromagnetic properties of the lamination geometry are pre-characterised using finite element analysis and this data is used as the basis for subsequent simulations without the need for further finite element solutions [7,31]. However, the technique has been extended to fully account for self and mutual coupling between two windings by means of the 'flux map' introduced in chapter 3 and the data conversion algorithm developed in chapter 4. Although applied throughout this thesis to the characterisation of the flux switching machine, the techniques developed are also applicable to the characterisation of other machine types where the self and mutual coupling of two windings must be fully accounted for, e.g. the switched reluctance machine operating in such a way that mutual coupling between adjacent phases may not reasonably be neglected [33].

The flexibility and computational efficiency of the electromagnetic characterisation process have also been improved by the development of a highly flexible yet accurate parameterised finite element model of the flux switching machine. Algorithms were also developed to reduce both the computation time required to solve a set of finite element models and the number of solutions required to yield a full characterisation without significant loss of accuracy, thus increasing the range of applications for which the flux map characterisation technique is practical.

The dynamic simulation model of the flux switching machine developed in chapter 5 demonstrates the effectiveness and applicability of the flux map as the basis for simulating the voltage driven flux switching machine including both self and mutual coupling effects which was not possible using existing dynamic simulation models, as detailed in section 1.3.2. The simulation model developed in chapter 6 for the flux switching motor, drive and control system further advances the field by modelling the flux switching motor in a novel drive topology, fully accounting for the effects of self and mutual coupling, the behaviour of the bifilar armature in the circuit and the effects of the switch control algorithm and yielding good agreement with experimental results up to design speed.

The integration of a genetic algorithm optimisation system with a commercially available parameterised finite element analysis package [47,48], as presented in chapter 8, advances the field by providing a generally applicable semi-automated design and optimisation system which can be applied to any system which may be modelled in 2-dimensional finite element analysis. The system developed requires no prior knowledge of the relationships between design parameters and performance and is, therefore, particularly applicable to the design of new machine types such as the flux switching machine where no large body of design experience exists.

Iron loss can form a significant proportion of losses from electrical machines but they are very difficult to model and quantify. However, the image processing method for iron loss visualisation developed in chapter 9 is simple and rapid in use but provides detailed visualisations to help the designer evaluate the relative distribution of such losses or as the basis for quantitative iron loss analysis. The technique is applicable to any machine which may be modelled in 2-dimensional finite element analysis and may be used in a wide range of situations where existing iron loss estimation techniques are not directly applicable, e.g. non-sinusoidal excitation, or too complex or costly to implement, e.g. initial design.

## **1.6 Thesis structure**

This thesis is structured into seven technical chapters, each of which introduces and develops a specific step in the implementation of the dynamic simulation model of the flux switching machine or a related area of research. Chapters 2-6 describe the operation of the flux switching machine and develop the stages necessary to characterise and simulate the operation of the flux switching machine on its own and the flux switching motor along with its power electronic drive and switch control algorithm. Chapters 7 and 8 introduce further optimisation and analysis methods which are more widely applicable, not just to the flux switching machine, but are facilitated by the techniques developed.

The various stages presented in chapters 2-6 combine to form a complete dynamic simulation system for the flux switching machine, specifically the flux switching motor, and are closely inter-related. Comparisons are made in each chapter between the intermediate results obtained for various conditions but it is the final results of the combined system which are of primary interest while the techniques developed in chapters 7 and 8 are facilitated by the processes implemented in chapters 2-6. Hence, results and observations are presented within each chapter but final conclusions are drawn in chapter 9 with reference to all the results presented in each chapter. This structure is summarised in Figure 1-5 for clarity.

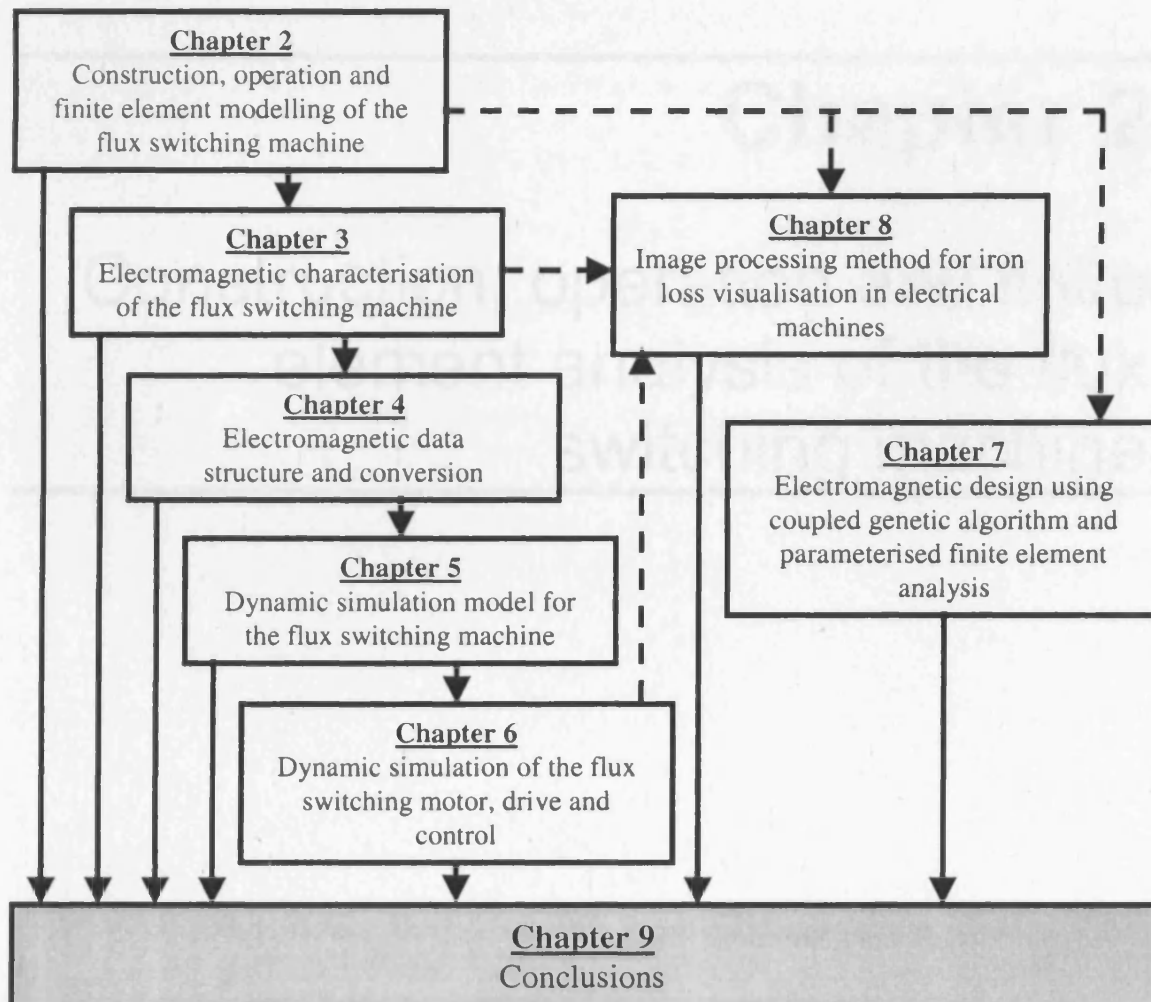


Figure 1-5 Structure of the thesis

---

# **Chapter 2**

Construction, operation and finite  
element analysis of the flux  
switching machine

---

## 2 CONSTRUCTION, OPERATION AND FINITE ELEMENT ANALYSIS OF THE FLUX SWITCHING MACHINE

### 2.1 Construction of the flux switching machine

The flux switching machine is similar in construction to the heteropolar inductor alternator [40,41] and the Law's relay limited motion actuator [92]. There are two fully pitched windings in slots on the salient pole stator, which are known as the field and armature, while the rotor is a simple reluctance rotor. As with all reluctance machines, motoring torque is produced by the tendency of the rotor to move in such a direction as to reduce the reluctance of the magnetic path for the flux created by current in the windings. Both stator and rotor are generally constructed from laminated steel. Figure 2-1 illustrates a simplified example of the construction of the flux switching machine in 4/2 configuration, i.e. 4 stator poles and 2 rotor poles. The two fully pitched windings are labelled F and A for field and armature respectively. In this case the fully pitched windings span 180 mechanical degrees across the stator.

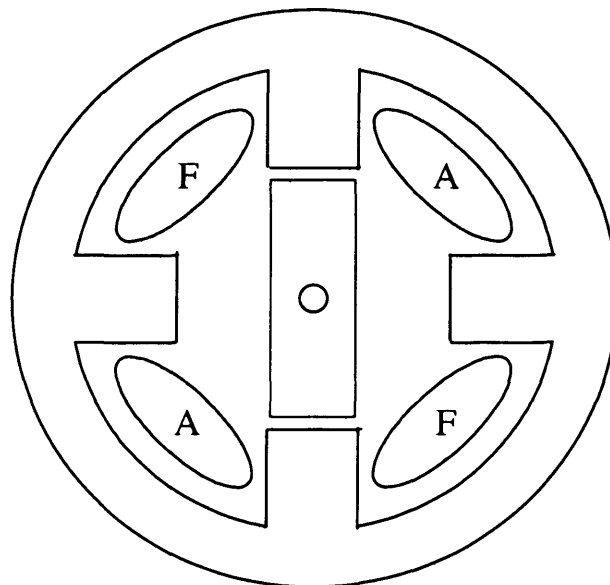


Figure 2-1 Simplified construction of a 4/2 flux switching machine

The field winding carries unipolar dc current while bipolar current is applied to the armature. This bipolar armature current may be obtained either by using an inverter circuit which is capable of reversing the current in a single strand winding or by applying unipolar current to either strand of a bifilar winding. Although the latter method can only utilise a maximum of 50% of the armature slot area per electrical cycle the power electronics are simpler, requiring only two ground-referenced switches, and hence cheaper. Therefore, in practice the field is generally single stranded and the armature is a bifilar winding.

## **2.2 Method of operation of the flux switching machine**

The field and armature winding current directions in Figure 2-2 are illustrated using the conventional dot and cross notation, i.e. current out of the page is represented by a dot and vice versa. In Figure 2-2a the field current gives rise to a magnetic flux in the south-westerly direction while the armature creates a magnetic flux in the south-easterly direction. Hence, the resultant magnetic flux is oriented in the southerly direction as if the top and bottom stator pole pair were energised by concentrated windings around the top and bottom poles as shown in Figure 2-2c. Thus, the rotor is pulled into alignment in the position shown.

Reversing the direction of the armature current while keeping field current the same, as shown in Figure 2-2b, similarly gives rise to a resultant flux in the westerly direction, pulling the rotor into alignment in the position shown. Therefore, by applying bipolar current to the armature winding while maintaining dc current in the field, the rotor can be made to rotate. As the direction of armature current is alternated the resultant flux switches between the two orientations shown and the momentum of the reluctance rotor keeps it rotating in the same direction. The constant dc excitation of the field maintains flux in the machine at all times while the orientation of armature current effectively controls, or switches, the path which this flux takes and, in turn, the stator pole pair with which the rotor aligns itself, hence the name flux switching machine. Hence, unlike the conventional switched reluctance machine, torque in the flux switching machine is produced mainly by changing mutual coupling between the field and armature [35,42,43].

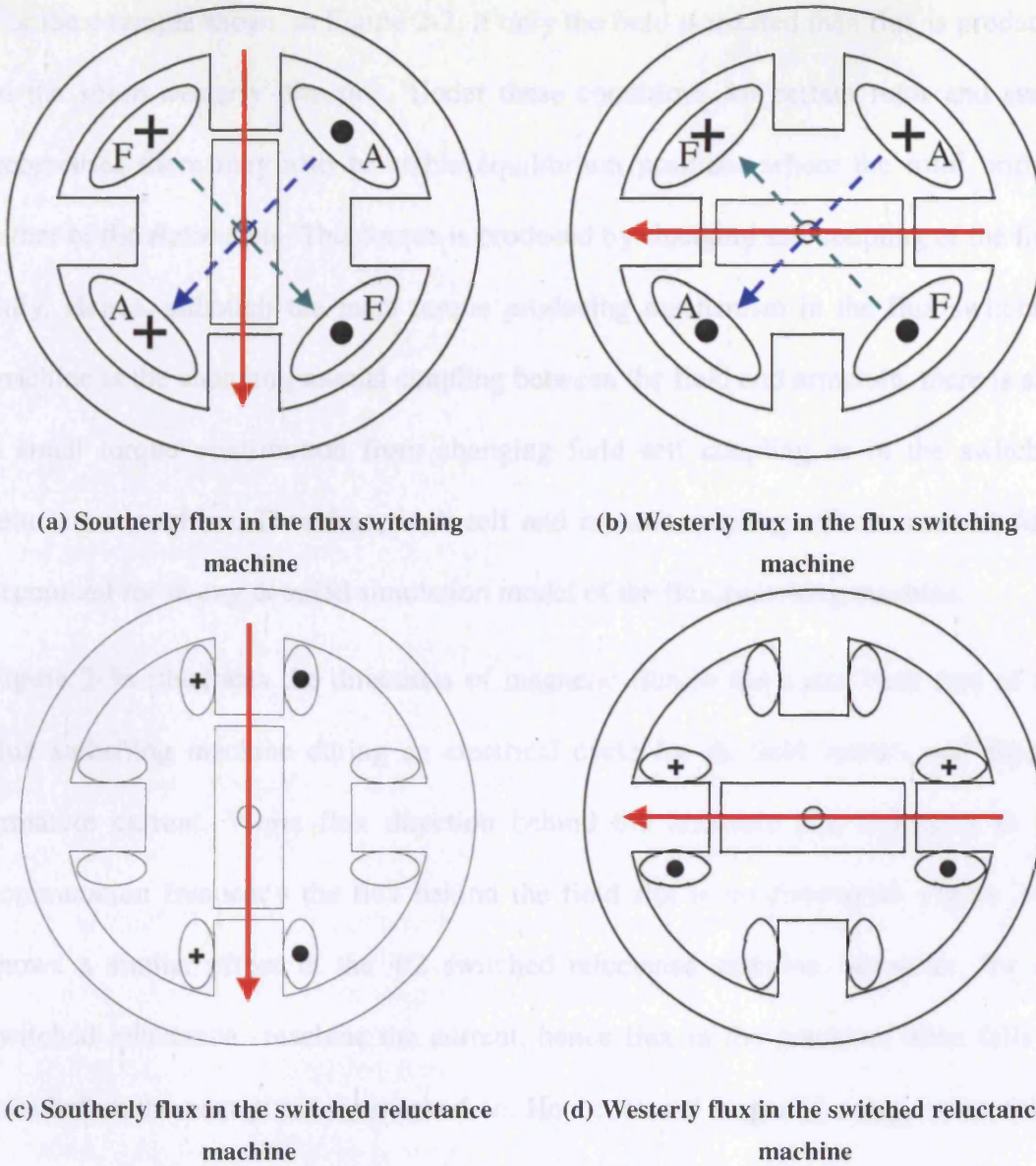
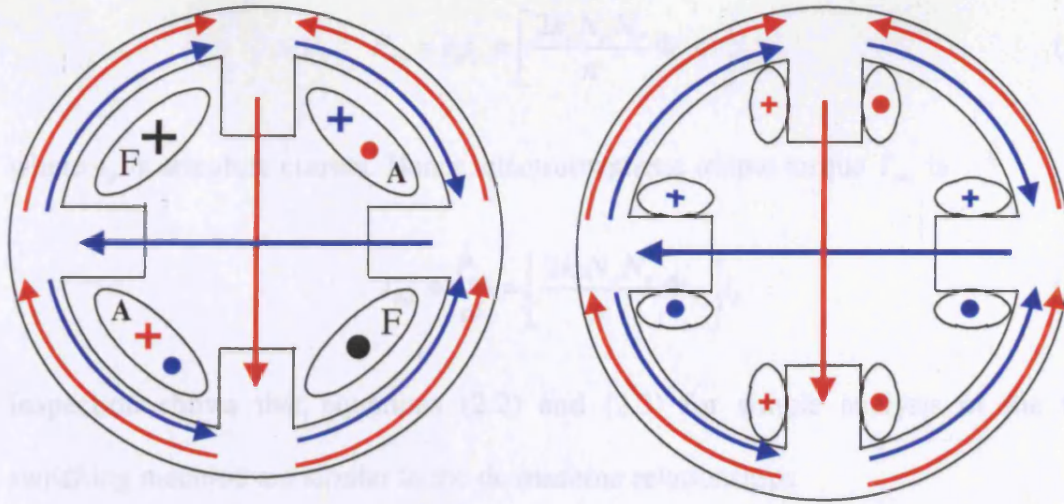


Figure 2-2 Simplified operation of flux switching and switched reluctance machines

For the example shown in Figure 2-2, if only the field is excited then flux is produced in the south-westerly direction. Under these conditions for certain rotor and stator geometries there may also be stable equilibrium positions where the rotor bridges either of the stator slots. This torque is produced by changing self coupling of the field only. Hence, although the main torque producing mechanism in the flux switching machine is the changing mutual coupling between the field and armature, there is also a small torque contribution from changing field self coupling as in the switched reluctance machine. Therefore, both self and mutual coupling effects must be fully accounted for in any detailed simulation model of the flux switching machine.

Figure 2-3a illustrates the directions of magnetic flux in the stator back iron of the flux switching machine during an electrical cycle for dc field current and bipolar armature current. While flux direction behind the armature slot alternates at the commutation frequency the flux behind the field slot is unidirectional. Figure 2-3b shows a similar effect in the  $4/2$  switched reluctance machine. However, for the switched reluctance machine the current, hence flux in the machine, often falls to zero before the next phase is switched on. Hence, stored magnetic energy must either be passed back to the supply through the power electronics or dissipated as heat and the sections of back iron with unipolar flux actually experience a rectified ac waveform. However, for the ideal flux switching machine dc current is present in the field at all times and the unipolar field in the back iron remains constant. Therefore, there is no need to recover or dissipate the stored magnetic energy and dynamic iron losses in these sections is ideally zero. This idealisation would require constant field reluctance. However, in practice there is some modulation of the flux in these sections.



(a) Directions of back iron flux in the flux switching machine      (b) Directions of back iron flux in the switched reluctance machine

Figure 2-3 Sections of ac and dc back iron flux in flux switching and switched reluctance machines

### 2.3 Simple analysis of the flux switching machine

Assuming constant dc field flux [5] as the rotor moves through a complete electrical cycle the field flux linking the armature varies linearly between positive and negative maximum values as shown in Figure 2-4a-c. To allow for some field flux which does not link the armature a coupling coefficient,  $k_c$  is used. This changing flux linking the armature induces an emf of magnitude

$$e_a = \frac{d\Psi_a}{dt} = \frac{2k_c N_a N_r}{\pi} \Phi_f \omega \quad (2.1)$$

where  $\Psi_a$  is armature flux linkage,  $N_a$  number of armature turns,  $N_r$  number of rotor poles,  $\Phi_f$  field flux and  $\omega$  is rotor speed in  $\text{rads}^{-1}$ . For electromechanical energy conversion to take place and produce a motoring torque, positive current must flow in the armature while mutual coupling is rising and vice versa. In the idealised case this is a square wave current synchronised with the armature induced emf as shown in Figure 2-4d. Under these conditions output power is given by the relationship

$$P_{em} = e_a i_a = \left[ \frac{2k_c N_a N_r}{\pi} \Phi_f \omega \right] i_a \quad (2.2)$$

where  $i_a$  is armature current. Hence, electromagnetic output torque  $T_{em}$  is

$$T_{em} = \frac{P_{em}}{\omega} = \left[ \frac{2k_c N_a N_r}{\pi} \Phi_f \right] i_a \quad (2.3)$$

Inspection shows that equations (2.2) and (2.3) for simple analysis of the flux switching machine are similar to the dc machine relationships

$$e = k\Phi\omega \quad (2.4)$$

and

$$T = k\Phi i_a \quad (2.5)$$

respectively where  $k$  is a constant of the dc machine which depends on its construction. However, unlike the dc machine, the flux switching machine has no brushes or rotor windings and requires electronic commutation. In equations (2.2) and (2.3), if the direction of armature current is changed then power  $P_{em}$  will be negative, meaning that the flux switching machine will act as a generator, converting mechanical input power to electrical output power.

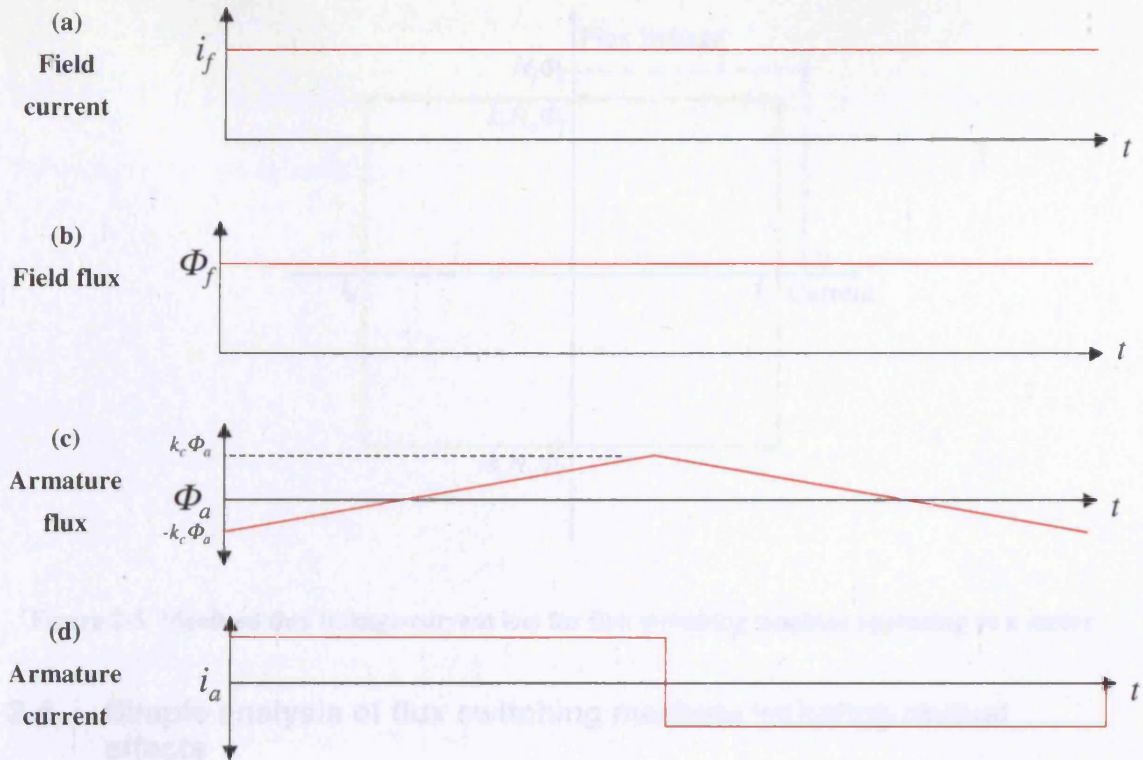


Figure 2-4 Idealised operation of flux switching machine operating as a motor

Simplified operation of the flux switching machine as a motor, as shown in Figure 2-4, gives rise to the idealised flux linkage-current loci over a complete electrical cycle shown in Figure 2-5. It can be seen that the field flux linkage and current remain constant and the locus is a single point, while the armature locus traces out a rectangle centred on the origin, the area of which yields the mechanical energy converted per electrical cycle. Hence, it can be clearly seen that in the ideal case no work is done by the field and all output torque is produced by the armature. Similarly, if the flux switching machine is operated as a generator then the same loci will be travelled but in the opposite direction, indicating that mechanical energy has been converted to electrical.

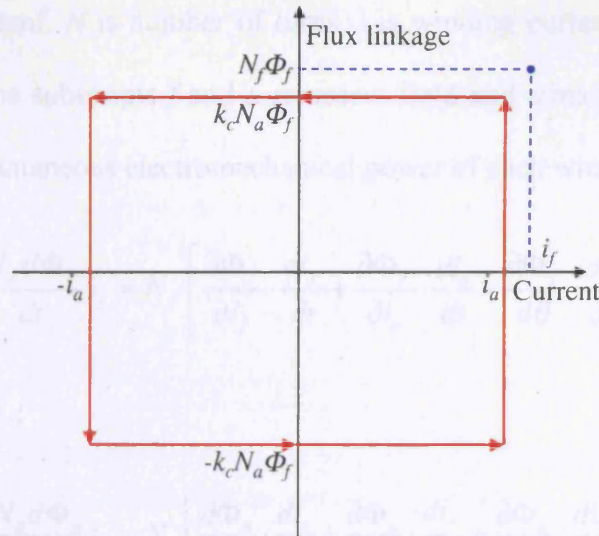


Figure 2-5 Idealised flux linkage-current loci for flux switching machine operating as a motor

## 2.4 Simple analysis of flux switching machine including mutual effects

The simplified analysis of section 2.3 is similar to the theory of dc machines and assumes that field flux is constant over the complete electrical cycle. However, in practice this is not the case and the field is modulated by changing reluctance of the flux path and changing mutual coupling with the armature as rotor position changes. Furthermore, in positions where there is magnetic coupling between the windings and current is changing there is transformer action between the windings. Hence, taking these factors into account the induced emfs for each winding may be expressed as

$$e_f = \frac{N_f d\Phi_f}{dt} = N_f \left[ \frac{\partial \Phi_f}{\partial i_f} \cdot \frac{di_f}{dt} + \frac{\partial \Phi_f}{\partial i_a} \cdot \frac{di_a}{dt} + \frac{\partial \Phi_f}{\partial \theta} \cdot \frac{d\theta}{dt} \right] \quad (2.6)$$

and

$$e_a = \frac{N_a d\Phi_a}{dt} = N_a \left[ \frac{\partial \Phi_a}{\partial i_a} \cdot \frac{di_a}{dt} + \frac{\partial \Phi_a}{\partial i_f} \cdot \frac{di_f}{dt} + \frac{\partial \Phi_a}{\partial \theta} \cdot \frac{d\theta}{dt} \right] \quad (2.7)$$

where  $e$  is induced emf,  $N$  is number of turns,  $i$  is winding current,  $\Phi$  is flux,  $\theta$  is rotor position and the subscripts  $f$  and  $a$  represent field and armature respectively. It follows that the instantaneous electromechanical power of each winding is given by

$$P_f = \frac{N_f d\Phi_f}{dt} i_f = N_f \left[ \frac{\partial \Phi_f}{\partial i_f} \cdot \frac{di_f}{dt} + \frac{\partial \Phi_f}{\partial i_a} \cdot \frac{di_a}{dt} + \frac{\partial \Phi_f}{\partial \theta} \cdot \frac{d\theta}{dt} \right] i_f \quad (2.8)$$

and

$$P_a = \frac{N_a d\Phi_a}{dt} i_a = N_a \left[ \frac{\partial \Phi_a}{\partial i_a} \cdot \frac{di_a}{dt} + \frac{\partial \Phi_a}{\partial i_f} \cdot \frac{di_f}{dt} + \frac{\partial \Phi_a}{\partial \theta} \cdot \frac{d\theta}{dt} \right] i_a \quad (2.9)$$

where winding fluxes are non-linear functions of current in both windings and rotor position. *Hence, for the general case where the rotor is moving and both currents are time varying torque is produced by both self and mutual coupling mechanisms.*

## 2.5 Calibration of shaft mounted optical position sensor

In common with the switched reluctance machine the flux switching machine requires feedback of rotational position for control of the switches and this commonly takes the form of a shaft mounted optical position sensor. The rising and falling edges of the signal obtained from this sensor are calibrated to known positions within the electrical cycle between which position may be inferred. For the flux switching machine this known position is defined as the zero crossing point of the induced armature emf for constant dc field excitation and both bifilar armature coils held open circuit. The bifilar armature coils may then be identified by the polarities of their induced emfs while the optical sensor signal is high. Figure 2-6 shows an example of armature induced emfs and the optical sensor calibrated such that its transitions coincide with the zero crossings of armature emf.

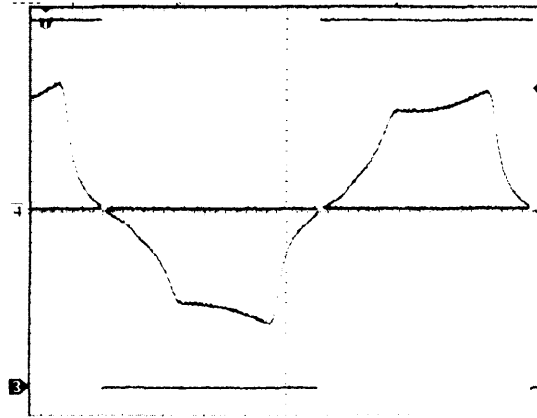


**Figure 2-6 Experimental waveform showing optical position sensor alignment with armature induced emfs for dc field excitation**

## 2.6 Winding techniques for the flux switching machine

Each winding of the flux switching machine may generally comprise a number of identical individual coils connected either in series or parallel. Provided the number of current carrying strands within each stator slot remains unchanged, the machine will appear identical for 2-dimensional analysis. However, behaviour and properties of the end windings and ease of manufacture are influenced by the method used to wind the coils. Figure 2-7 illustrates the main options for one winding in developed view. In each case a single line represents a coil of  $N$  strands and the direction of positive current  $i$  in each is indicated by an arrow. Hence, each case is electrically identical for 2-dimensional analysis with an mmf of  $2Ni$  present in each slot.

Options a and b represent the use of multiple coils which require internal connection to form a complete winding, the number of connections required rising with stator pole number. Options c and d represent the use of two or one large coils respectively which may be wound externally and drawn into the slots as shown, thus reducing the number of internal connections to one and none respectively, regardless of stator pole number.

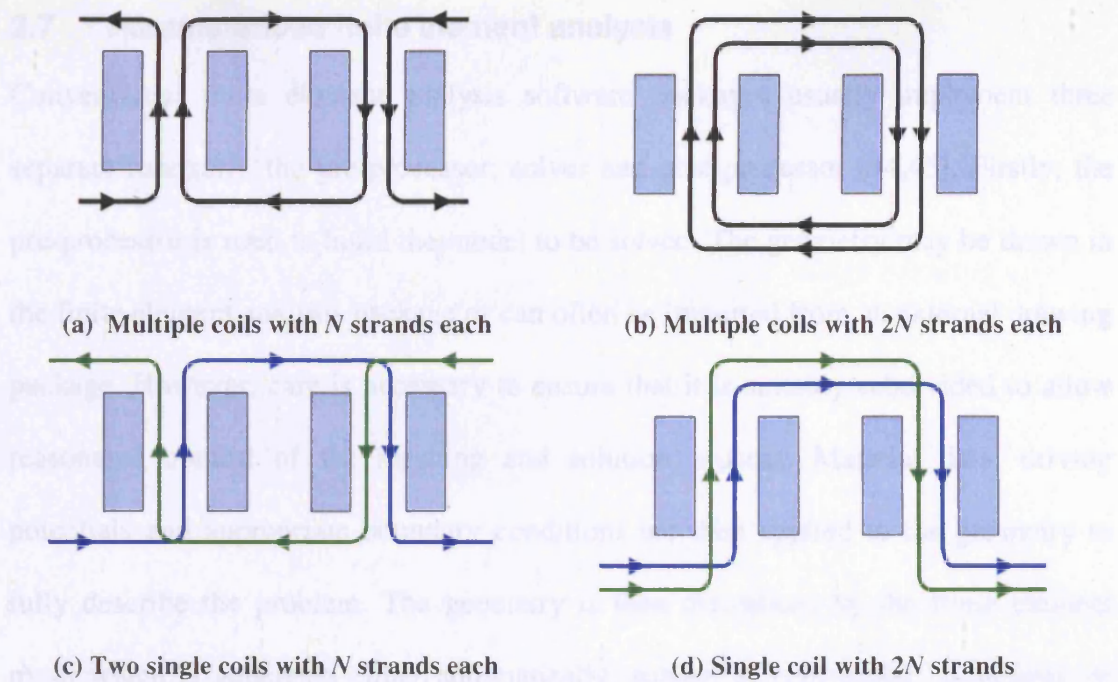


Figure 2-7 Schematic winding options for one winding of the flux switching motor

In general, options a and c are favourable for compact applications as they give a uniformly distributed end winding requiring minimum end clearance. For automated assembly option c and d are similar to a method in industrial use for machine winding of induction machine stators which may be applied to the flux switching machine.

Furthermore, reliability is potentially enhanced for options c and d by minimising the number of internal connections required, especially for high pole number machines.

## 2.7 Parameterised finite element analysis

Conventional finite element analysis software packages usually implement three separate functions, the pre-processor, solver and post-processor [44,45]. Firstly, the pre-processor is used to build the model to be solved. The geometry may be drawn in the finite element analysis package or can often be imported from an external drawing package. However, care is necessary to ensure that it is suitably subdivided to allow reasonable control of the meshing and solution process. Material data, driving potentials and appropriate boundary conditions are then applied to the geometry to fully describe the problem. The geometry is then discretised by the finite element mesh which is generated either automatically, subject to controlling constraints, or under the direct control of the user. The complete model generated is then solved by the finite element solver module, either on its own or as part of a larger set of such models. After each model has been solved, it must be post-processed to obtain the required results from it. This is often a manual process which entails the repetition of a number of steps for each solution, the number and complexity of these steps depending on the output results required.

Figure 2-8 illustrates this process and highlights the stages which require significant user involvement and expertise. Thus, conventional finite element analysis is not generally suitable for the creation and solution of large numbers of models during the early design stages of new machines, largely due to the amount of expert user time required.

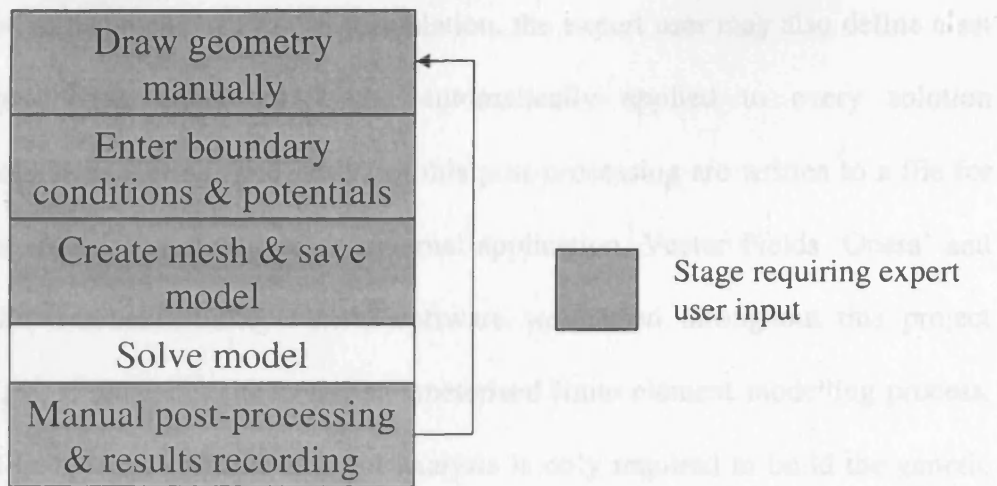


Figure 2-8 Stages of conventional finite element analysis

Two-dimensional parameterised finite element analysis [46-48] addresses this major drawback of conventional finite element analysis by vastly reducing the amount of user time and expertise required for the creation and solution of a large number of similar models. Firstly a flexible generic model is built by an expert user which sets the model structure in terms of machine type, topology, coil configuration, and mesh control etc. However, user definable parameters may be assigned to every aspect of the model in order to generate a wide range of alternatives based upon a common base. Examples of parameters which may be used to define a finite element model of the flux switching machine include

- Number of rotor and stator poles
- Radial and angular dimensions of poles and slots
- Coil currents and numbers of turns
- Rotor position

In addition to parameterised model formulation, the expert user may also define a set of post-processing operations to be automatically applied to every solution immediately after solving. The results of this post-processing are written to a file for inspection and/or importing into an external application. Vector Fields 'Opera' and 'Design Environment' finite element software were used throughout this project [44,45,47,48]. Figure 2-9 shows the parameterised finite element modelling process. Specialist knowledge of finite element analysis is only required to build the generic model while less specialist knowledge is required by the end user.

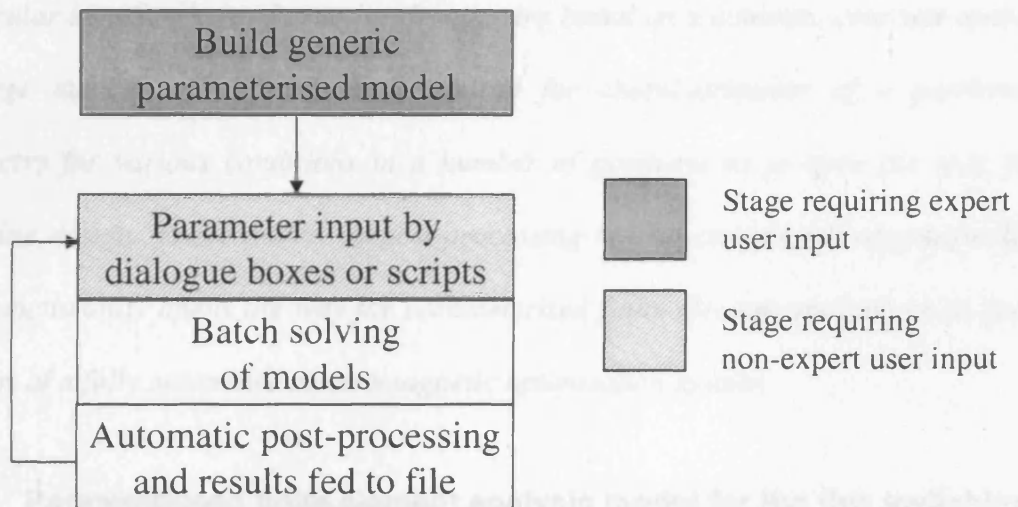
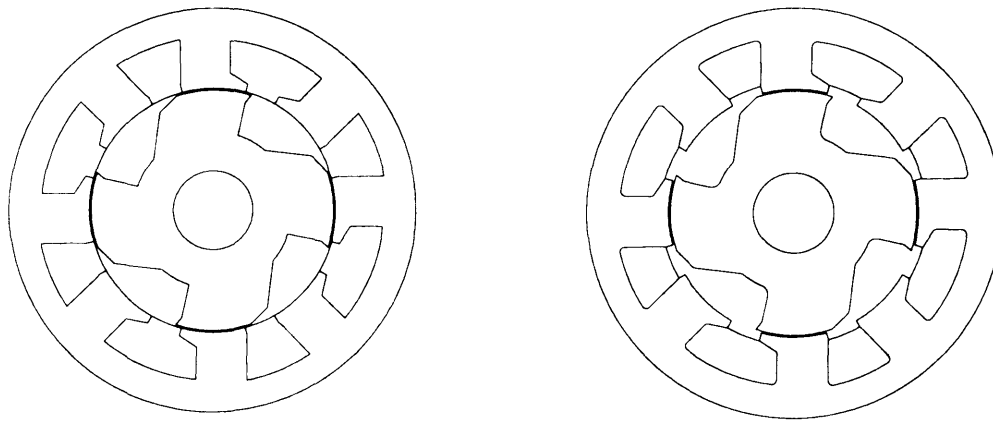


Figure 2-9 Stages of parameterised finite element analysis

Although the creation of a parameterised finite element model is generally more complex than a conventional finite element model, this initial investment is rapidly repaid in use. The user of the parameterised model is able to quickly create, solve and post-process large numbers of potentially very different models by simple dialogue box or script file input of the defined parameters. Furthermore, the level of finite element analysis expertise required of the end user is reduced as parameters to control automatic mesh generation are included in the generic model and reasonable discretisation is more assured. *Thus, parameterised finite element analysis is of particular benefit where alternative designs are based on a common structure and/or a large number of solutions are required for characterisation of a particular geometry for various conditions in a number of positions as is often the case for machine design. Furthermore, as post-processing is also carried out automatically, this functionality opens the way for parameterised finite element analysis to be used as part of a fully automated electromagnetic optimisation system.*

## **2.8 Parameterised finite element analysis model for the flux switching machine**

Figure 2-10 compares the lamination geometry of the 8/4 flux switching machine used throughout this thesis for experimental validation of results as it was modelled in finite element analysis during its design and the resulting lamination geometry as it was manufactured. For the 8/4 machine the coil end-windings now only span 90 degrees instead of 180 degrees for the 4/2 example introduced in section 2.2. In this design the field slots are deeper and narrower than the armature slots as the field back iron carries unipolar flux, hence less steel is required to obtain low iron losses.



(a) Simplified 8/4 flux switching machine geometry used during design

(b) 8/4 flux switching machine geometry with filleting as manufactured

Figure 2-10 Comparison of flux switching machine geometry as designed and as manufactured

While the main dimensions are identical in each case, filleting was added at manufacture to several corners, particularly at the pole roots. Hence, the geometry modelled in finite element analysis is a reasonable approximation to the manufactured geometry and in this case the filleting may be expected to improve performance slightly.

The field is a single strand winding and the armature comprises two bifilar coils wound two in hand. Therefore, it can be assumed to be close coupled, i.e. no magnetic flux links one half of the bifilar armature without also linking the other. Hence, it is modelled in finite element analysis as a single winding, the mmf of which is a superposition of the mmfs in the two bifilar halves.

Figure 2-11 shows the finite element mesh which was used during design and initial modelling of the flux switching machine of Figure 2-10. The discretisation is 'reasonable' for design use and represents a compromise between rapid solution time per model and sufficient numerical accuracy for design iteration. For such a finite element model of the flux switching machine all flux may be assumed to be contained within the machine, hence minimising the area which must be included in the finite element model. In general the amount of flux passing outside the laminations is small compared to the main flux and this is a reasonable assumption for design use.

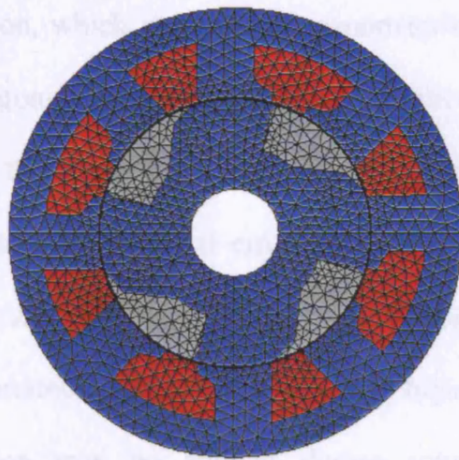


Figure 2-11 Finite element mesh used during design of 8/4 flux switching machine

## 2.9 Effects of finite element meshing

The numerical accuracy of finite element analysis solutions depends heavily on the mesh used to discretise the geometry of the model being solved [49-54]. In general, the best accuracy may be expected from models with a large number of small elements, thus making a good approximation to the real continuous field distribution. However, solution time is approximately proportional to the square of the number of elements in the model and may become unacceptable if the mesh is too fine. Hence, for each model a mesh is required which gives satisfactory numerical accuracy for a practical computation time.

For conventional finite element models it is usual for the user to check and control the generation of the mesh for each model individually. However, due to the flexibility of parameterised finite element analysis to create a wide range of models whose geometries are not known beforehand, particular attention is required to ensure an acceptable mesh is produced in each case.

Vector Fields 2-d finite element analysis software employs automatic triangular mesh generation[45]. Although the user cannot directly control the mesh generated the general distribution of elements is controlled by specifying the maximum element dimensions in each region, which may also be parameterised. While this method is acceptable for most regions of the flux switching machine, particular attention is required when meshing the airgap as it is of special interest for machine design as well as highly susceptible to numerical error caused by inadequate discretisation. Mesh gravity points may also be included in the parameterised finite element model to concentrate elements around points of potentially high numerical error while automatic mesh adaption may be applied during solution of each model to progressively add further elements to the finite element mesh in a targeted manner to reduce overall numerical error.

### ***2.9.1 Airgap region discretisation***

In common with most electrical rotating machines, the airgap of the flux switching machine is small by comparison to the overall machine dimensions. It is also a region of specific interest as it is where most torque is produced and post-processing operations are carried out in the airgap to obtain various results. However, elements in this region are also particularly susceptible to numerical errors due to the steel/air interfaces and rapid changes in the field [49]. Therefore, it is essential that the airgap region is properly discretised.

To satisfy this requirement in parameterised finite element analysis the airgap can be made up of a minimum of three thin regions, thus creating at least three layers of small elements spanning the airgap, as shown in Figure 2-12a. This ensures that post-processing operations in the centre of the airgap do not pass through any elements which border a change in material. Adding further layers of elements to the airgap, as shown in Figure 2-12b which has 5 layers, significantly increases computation time per solution and potentially leads to more numerically accurate results. However, the difference was found to be very small and the additional computational expense not justified.

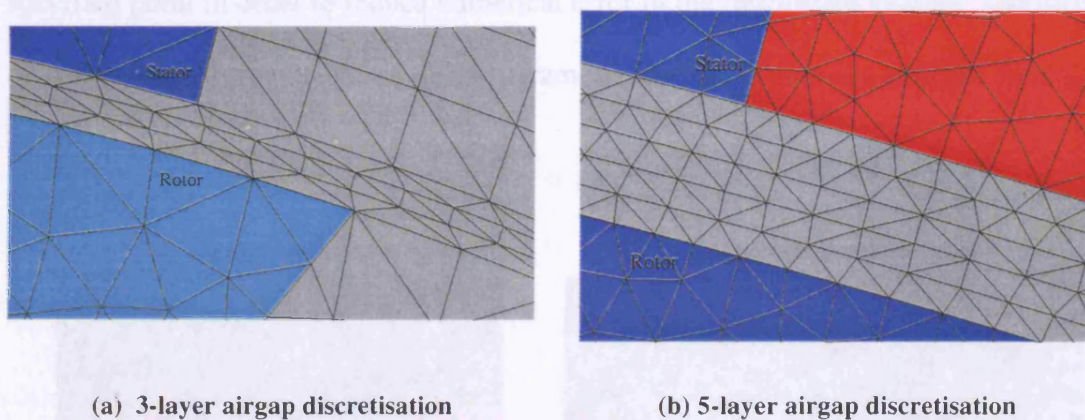
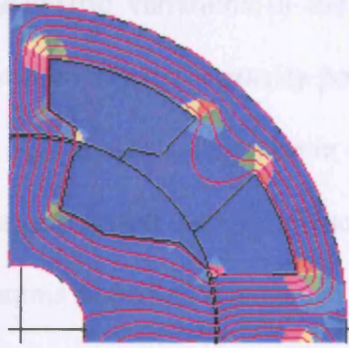


Figure 2-12 3- and 5-layer airgap discretisation in finite element analysis

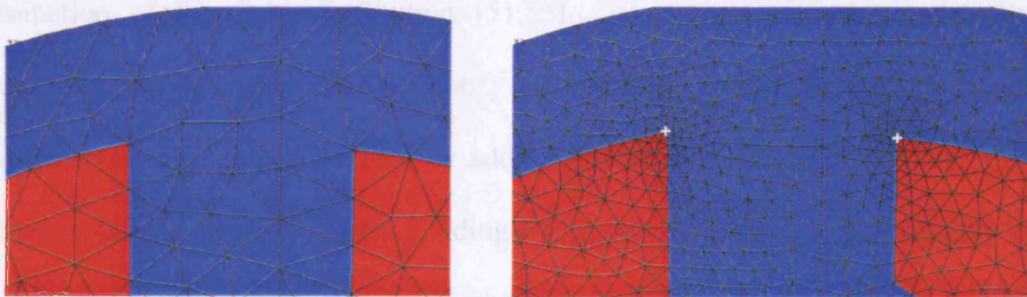
### 2.9.2 Mesh gravity points in parameterised finite element analysis

In addition to the airgap region, areas of the lamination where there is heavy saturation of the steel and/or the magnetic flux changes direction rapidly are also particularly susceptible to numerical errors. Such localised conditions may occur at several points within the flux switching machine during an electrical cycle, depending on geometry and excitation. Figure 2-13 shows the distribution of estimated numerical error for the 8/4 flux switching machine in an aligned position. In this case most numerical error is concentrated around the corners at the pole roots where there is localised saturation and a rapid change in flux direction.



**Figure 2-13 Example distribution of estimated numerical error in the simplified finite element model of the 8/4 flux switching machine**

Mesh gravity points [48] have the effect of concentrating small elements around the specified point in order to reduce numerical error in the immediate vicinity. The effect of adding mesh gravity points to the parameterised finite element analysis model is shown in Figure 2-14.



**(a) Initial mesh without gravity points at pole root in the 8/4 flux switching machine**      **(b) Mesh with gravity points added at marked corners**

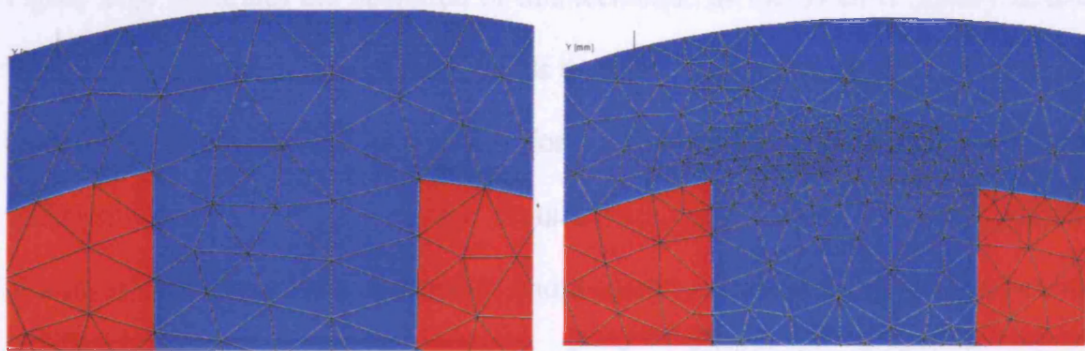
**Figure 2-14 Effect of mesh gravity points on finite element discretisation**

To allow for all possible geometric variations in the parameterised finite element model of the flux switching machine, a mesh gravity point would be required at every corner. However, this would also lead to a large rise in the number of elements for all models built using the parameterised model, hence increased solution times. Furthermore, mesh gravity points add small elements in every direction surrounding the specified point although inspection of Figure 2-13 shows that additional elements are only required in the steel. *Hence, although mesh gravity points may be used to ensure reasonable discretisation in key areas of the flux switching machine, they also tend to add unnecessary elements which increase computation time without yielding improved accuracy.*

### **2.9.3 Automatic mesh adaption**

Given a finite element solution it is possible to estimate the numerical error present by examination of the field distribution [51,55]. Using this information, the finite element solver can automatically identify regions with the largest numerical error estimate and further discretise them by adding further elements. The solution is then repeated using the improved mesh, yielding a more numerically accurate solution than the last. This process is repeated until either the maximum number of mesh adaption iterations is reached or the solution error estimate falls below a user defined limit, whichever occurs first [45].

Automatic mesh adaption places additional elements only in areas where they improve numerical accuracy and requires no prior knowledge of the geometry or excitation conditions being modelled. However, as the model is solved a number of times during the process with increasing numbers of elements, computation time may be greatly increased, the exact amount depending on the specified error limit and quality of initial mesh for each solution. Figure 2-15 shows an example of the outcome of automatic mesh adaption in the flux switching machine at the base of a stator tooth. Comparison with Figure 2-13 and Figure 2-15 shows that additional elements have been added only where necessary to improve numerical accuracy.



(a) Starting mesh at pole root in the 8/4 flux switching machine before adaption

(b) Final mesh after automatic mesh adaption to reduce estimated numerical error

Figure 2-15 Effect of automatic mesh adaption on finite element discretisation

Despite the advantages of automatic mesh adaption in terms of final solution accuracy and targeted mesh refinement, the large increase in average solution time due to the iterative process, potentially several multiples, is a drawback. Therefore, a technique was developed which retains the advantages for a much smaller increase in average solution time where a number of models are required for the same geometry with only differing excitation. Instead of using the same initial mesh for each solution, the adapted mesh from the previous solution is retained and used as the starting mesh for the present solution. Hence the number of mesh adaption iterations is greatly reduced or completely removed for subsequent models.

Figure 2-16 illustrates the operation of this technique as the mesh is rapidly adapted from the starting mesh to one which yields the specified numerical accuracy for every case. In the illustrative example shown, for the first solution the starting mesh is not sufficiently discretised to yield the required accuracy. Hence the mesh adaption process is carried out, adding elements and leading to a relatively long solution time. For subsequent solutions the most recent refined mesh is used as the initial mesh and gives sufficient accuracy until the seventh solution when further mesh adaption is required, leading again to a long solution time and additional elements. As the starting mesh for each solution now contains more elements the solution time of each model is increased but is still less than if the original mesh were adapted for each solution. The area of the shaded region above the solution times approximately represents the time saved by this technique compared to using automatic mesh adaption starting from the same original mesh for each solution.

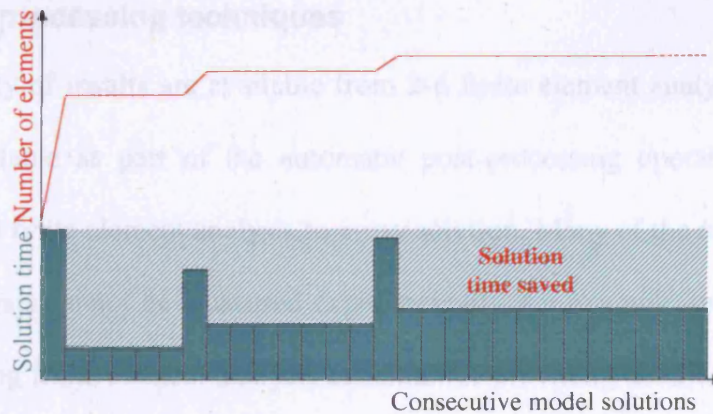


**Figure 2-16** Illustration of solution time saved by reusing previously adapted finite element meshes for geometrically identical models

In this way a detailed mesh is progressively built up for the geometry which will satisfy or exceed the specified accuracy in every subsequent case without further adaption. Although this mesh may be finer than is required for some cases, the additional computation time for each solution due to extra elements is generally more than repaid by not having to perform mesh adaption in most cases. Hence, more numerically accurate finite element solutions can be obtained for less computational cost. For a test set of 40 models based on the same flux switching machine geometry the technique reduced overall computation time by approximately 50% and yielded more numerically accurate solutions compared to the same model being solved using the same initial mesh in each case.

## 2.10 Post processing techniques

A wide variety of results are available from 2-d finite element analysis, all of which are also available as part of the automatic post-processing operations applied by parameterised finite element analysis to every solution. Many of the results from finite element analysis cannot be measured experimentally, for example spatial distribution of flux, making finite element analysis essential for providing detailed information on the operation of the flux switching machine. Furthermore, despite the implicit assumptions and approximations of a 2-dimensional finite element analysis model, it is repeatable and is not subject to experimental errors such as winding coil heating or mechanical movement which may be experienced during experimental tests.

The magnetostatic finite element solutions can be used as the input to further finite element simulation such as a mechanical solver to check for mechanical deformation and acoustic noise production or a thermal solver to investigate heat transfer within the machine. The main results of interest for simulation of the flux switching machine are winding fluxes and electromagnetic torque as a function of winding mmfs while additional graphical and numerical results potentially provide additional useful information.

Figure 2-17 shows examples of the main types of graphical results readily available from 2-dimensional finite element analysis. These types of results can be used to visualise the spatial and temporal variations of field quantities over a complete electrical cycle. Numerical results obtained automatically from parameterised finite element solutions are written sequentially to text files for collation and analysis. Figure 2-18 gives a sample extract from such a results file.

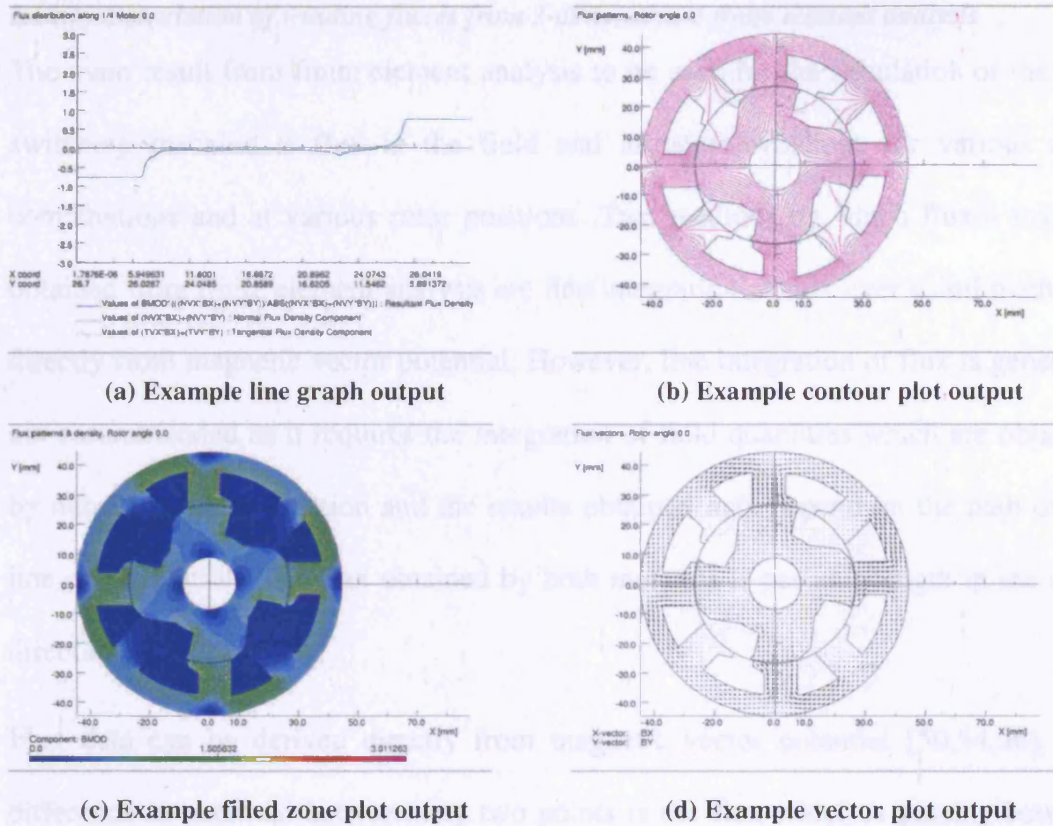


Figure 2-17 Example graphical output available from finite element analysis

Solution file: G006I0014\_1.ST  
 Rotor angle: 0  
 Field mmf: 349.645  
 Field flux: 0.0183486  
 Armature mmf: 0.0  
 Armature flux: 0.014938  
 Slot area: 80.0869

Solution file: G000I0014\_2.ST  
 Rotor angle: 45  
 Field mmf: 349.645  
 Field flux: 0.017532  
 Armature mmf: 0.0  
 Armature flux: -0.013324  
 Slot area: 80.0869

Figure 2-18 Sample extract from results file obtained from parameterised finite element analysis

### 2.10.1 Calculation of winding fluxes from 2-dimensional finite element analysis

The main result from finite element analysis to be used for the simulation of the flux switching machine is flux in the field and armature windings for various mmf combinations and at various rotor positions. Two methods by which fluxes may be obtained from finite element analysis are line integration of flux over a coil pitch and directly from magnetic vector potential. However, line integration of flux is generally not recommended as it requires the integration of field quantities which are obtained by numerical differentiation and the results obtained may depend on the path of the line of integration. The flux obtained by both methods is per unit length in the axial direction.

Flux data can be derived directly from magnetic vector potential [50,54,56]. The difference in potential between any two points is the flux which is passing between them, i.e.

$$\Phi_{12} = A_1 - A_2 \quad (2.10)$$

where  $\Phi_{12}$  is flux per unit stack length and  $A_1$  and  $A_2$  are magnetic vector potential at points 1 and 2 respectively. However, deriving flux from point values of potential in this way tends to make the result susceptible to error in the point potential values and, as for the line integration method, the choice of points 1 and 2 within the coil will affect the exact value of flux obtained. An improved method to obtain the flux passing through a given coil is to use the mean magnetic vector potential, i.e.

$$\Phi_{12} = \frac{\int_{Area1} Ads - \int_{Area2} Ads}{Area} \quad (2.11)$$

where  $\Phi_{12}$  is flux per unit stack length,  $\int_{AreaX} Ads$  is the area integral of potential in area

$X$  and  $Area_x$  is the area of each region where  $Area_1=Area_2$ . In this way localised random errors in  $A$  will tend to cancel while allowance is also made for flux which only partially links the coil. For the more general case where  $Area1 \neq Area2$  then equation (2.11) becomes

$$\Phi_{12} = \frac{\int_{Area1} Ads}{Area1} - \frac{\int_{Area2} Ads}{Area2} \quad (2.12)$$

### 2.10.2 Calculation of torque

Instantaneous torque may be obtained from a single finite element solution by integrating Maxwell stress in the airgap of the machine [45,56] and is often included as a standard operation in finite element post-processors. Hence, it is particularly suitable for evaluating the instantaneous torque of a machine for any given conditions. As with winding flux, the value of torque obtained from finite element analysis is per unit stack length. However, this method of torque computation is also sensitive to numerical errors and mesh quality in the airgap region. Hence, for this method to yield reliable results particular attention must be paid to discretisation of the airgap as shown in section 2.9.1.

The flux-mmF, or flux linkage-current, diagram is an established method for calculating average torque over a complete electrical cycle for the conventional switched reluctance machine [7,24,25,36] and it can also be applied to the flux switching machine. The area enclosed within the flux-mmF, or flux linkage-current, locus for a complete electrical cycle yields total energy converted in steady state operation while the rate of change of coenergy or other 'virtual work' methods may be used to obtain instantaneous torque over a small change in position [7,57], although this method is also sensitive to numerical errors [58].

Figure 2-19 shows winding currents and the flux linkage-current loci for the field and armature of the separately excited 8/4 flux switching motor from finite element analysis using experimentally measured current waveforms as inputs. Machine output is the sum of the area enclosed within the field and armature energy conversion loops. The asterisk shows the starting point of the flux linkage-current loci at an aligned position and direction of travel is from asterisk to cross. For the idealised case described in section 2.3, where field flux and current are constant, the field flux linkage-current locus would reduce to a point and, hence, enclose zero area. However, Figure 2-19c shows that, in practice, although the majority of output power is produced by the armature a small amount of work is done by the field.

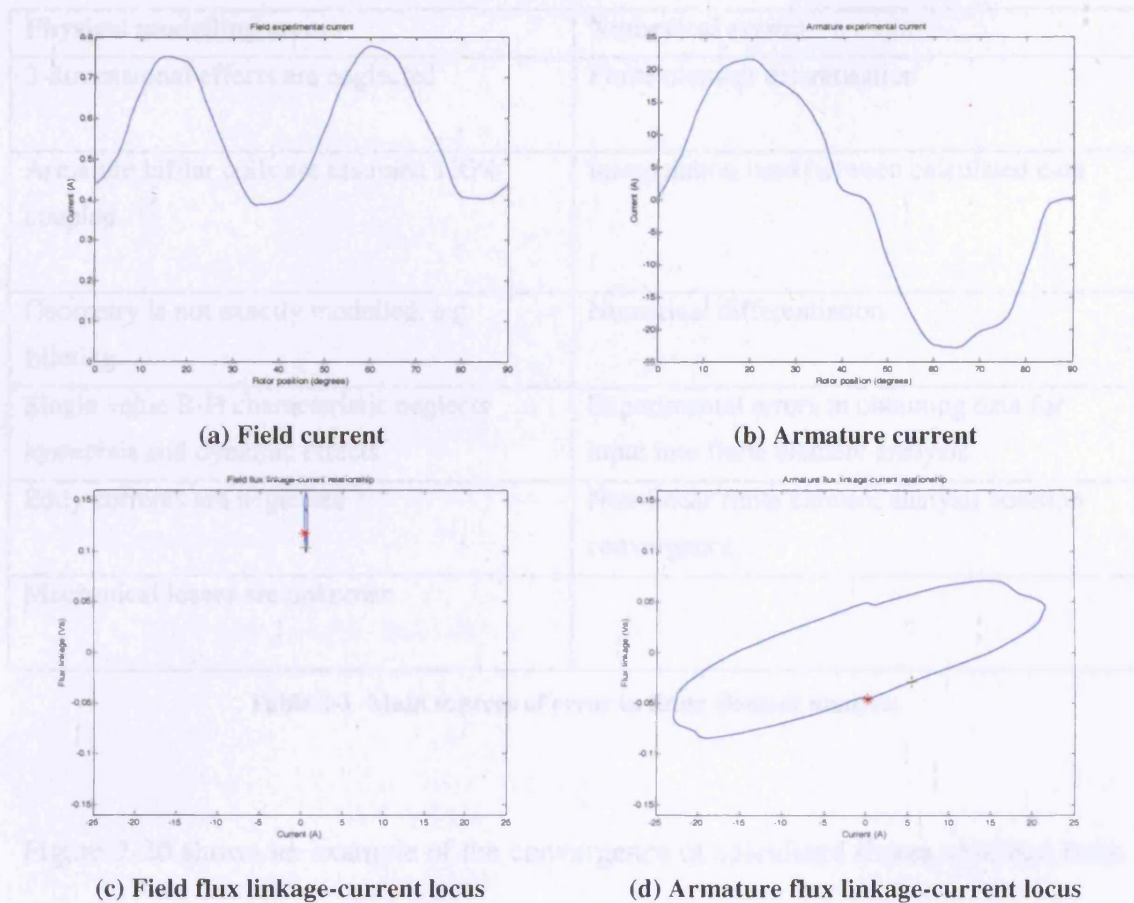


Figure 2-19 Sample experimental results for separately excited 8/4 flux switching motor

### 2.11 Analysis of finite element analysis errors

The sources of error between finite element and experimental results fall into two main categories- physical modelling errors and numerical errors. Table 2-1 summarises the main errors of each type. The physical modelling errors are the approximations and assumptions made in abstracting the physical system into a 2-dimensional magnetostatic finite element model while the numerical errors are introduced during calculations and may generally be reduced at the expense of increased computation time. However numerically accurate the solutions obtained from finite element analysis are, the solution will always be an approximation to the physical reality and increased computational effort in formulating and solving the finite element models does not necessarily lead to more physically accurate results.

<b>Physical modelling errors</b>	<b>Numerical errors</b>
3-dimensional effects are neglected	Finite element discretisation
Armature bifilar coils are assumed 100% coupled	Interpolation used between calculated data
Geometry is not exactly modelled, e.g. filleting	Numerical differentiation
Single value B-H characteristic neglects hysteresis and dynamic effects	Experimental errors in obtaining data for input into finite element analysis
Eddy currents are neglected	Non-linear finite element analysis solution convergence
Mechanical losses are unknown	

**Table 2-1 Main sources of error in finite element analysis**

Figure 2-20 shows an example of the convergence of calculated fluxes obtained from a finite element solution with increasing number of non-linear solver iterations. After 5 iterations there is still a large error in the solution but by the tenth iteration the calculated fluxes have reached their final value. This shows that to obtain fluxes accurately from finite element analysis a sufficiently small tolerance is required to ensure the solution has converged. However, if this tolerance is set too small the number of iterations, hence computational expense, is greatly increased but no benefit is gained from it.

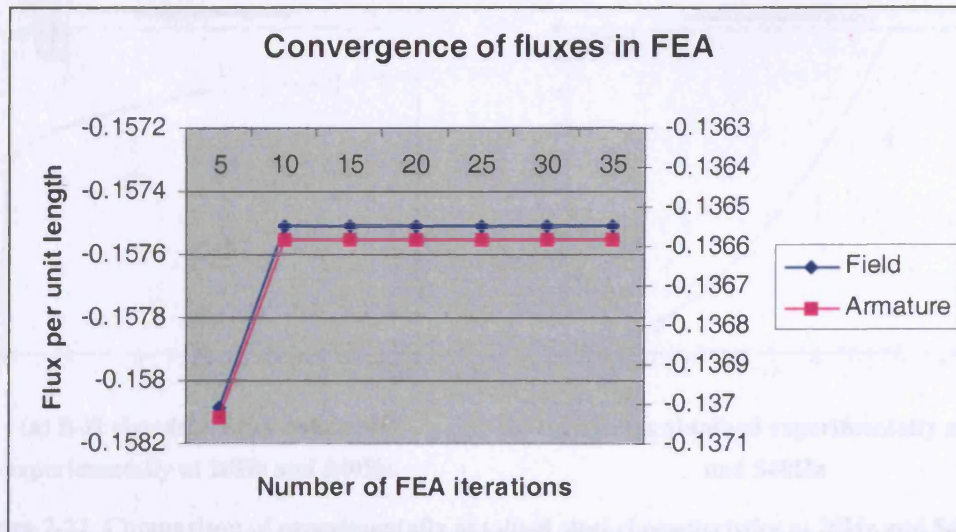


Figure 2-20 Sample convergence of flux with finite element solution iterations

To examine the effect of high frequency excitation on the steel flux-mmF relationship, B-H curves were obtained for the steel used [59] at a range of frequencies from 20Hz to 540Hz. The commutation frequency of the 8/4 flux switching motor running at 15000rpm is 1kHz but magnetic data was not available at that frequency. Figure 2-21a compares these B-H curves. As the single valued B-H characteristic is derived from the locus of the extreme points of major hysteresis loops [50] there is little difference in the characteristics obtained for the steel for 20Hz and 540Hz. However, Figure 2-21b shows the strong effect on power loss in the steel at 20Hz and 540Hz for varying peak flux density. Hence, although these two conditions are very different in practice, they appear similar in terms of magnetostatic finite element analysis.

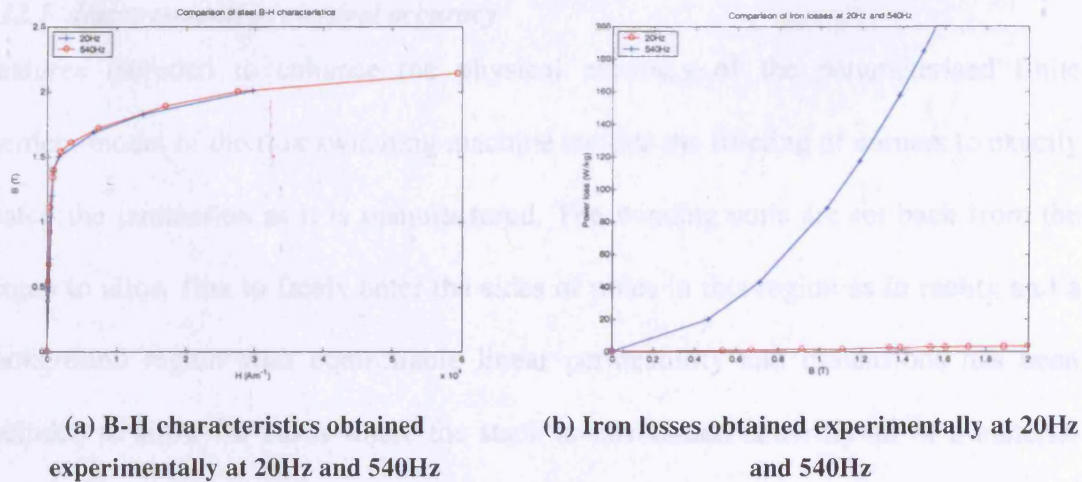


Figure 2-21 Comparison of experimentally obtained steel characteristics at 20Hz and 540Hz

## 2.12 Development of geometrically accurate and flexible parameterised finite element analysis model of the flux switching machine

Taking into account the main sources of finite element analysis error there is little merit in expending a large amount of computational effort in making a finite element analysis model more numerically accurate if it does not represent the physical system to a comparable accuracy. Hence, when formulating a finite element analysis model and during the manipulation and analysis of the data obtained from it a compromise is sought between model complexity, computational effort required for solution and the level of accuracy. Hence, a new parameterised finite element analysis model for the flux switching machine was developed which more precisely modelled the existing physical geometry of the 8/4 flux switching machine for detailed analysis while also improving flexibility for development of future flux switching machine designs.

### ***2.12.1 Improvements in physical accuracy***

Features included to enhance the physical accuracy of the parameterised finite element model of the flux switching machine include the filleting of corners to exactly match the lamination as it is manufactured. The winding coils are set back from the airgap to allow flux to freely enter the sides of poles in this region as in reality and a background region with controllable linear permeability and dimensions has been included to allow for cases where the stack is surrounded either by air or a material with relative permeability not equal to that of air.

Filleting of corners, particularly at pole roots, has a significant effect on the localised conditions. Sharp corners introduce a numerical singularity in the finite element solution and numerical errors due to the very rapid change in direction of the magnetic flux. In cases where there is a large flux the sharp corners also lead to extreme localised saturation in the finite element solution which is not present in practice. This in turn increases the reluctance of the magnetic circuit, potentially reducing calculated winding fluxes for given combination of mmfs.

Figure 2-22a and b show examples of the finite element analysis numerical error estimate and relative permeability distribution respectively for the rotor of the flux switching machine without filleting, i.e. as modelled during design. The high estimated error and extreme localised saturation at the root of the rotor pole are clear. Figure 2-22c and d shows the results for the same conditions using the improved finite element model with filleting as it was manufactured. The localised error estimate and localised saturation are both reduced, making the model more numerically as well as physically accurate.

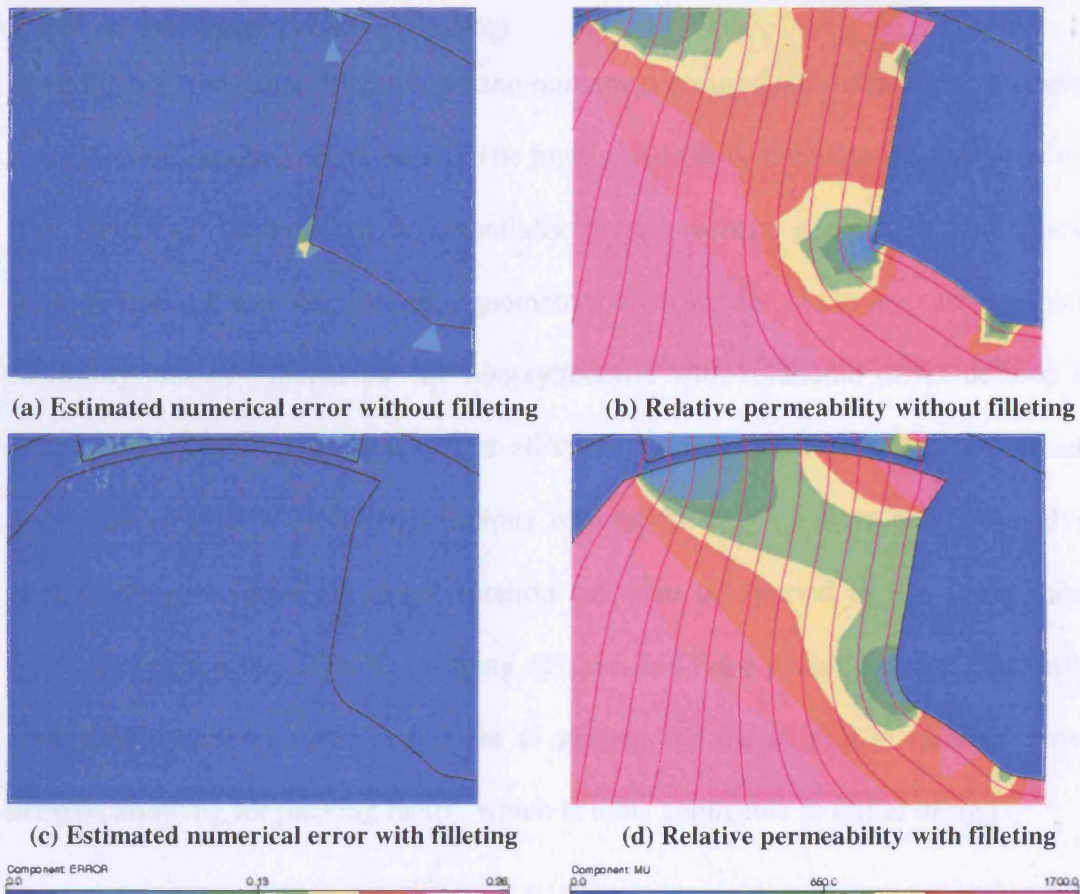


Figure 2-22 Effects of filleting on estimated numerical error and relative permeability

In general the windings do not completely fill the stator slots. However, it is common practice in finite element modelling to distribute coil mmf uniformly throughout the slots. However, for reluctance machines where a significant proportion of flux at unaligned positions may enter the stator pole via the side of the pole tips the calculated flux in such cases may be affected by the simplified coil distribution. Hence, the winding coils are set back from the airgap to more accurately approximate the practical distribution of mmf within the slots.

### ***2.12.2 Improvements in design flexibility***

In addition to the enhanced physical and numerical accuracy of the new parameterised model, it has also been formulated to be highly flexible to facilitate the design of new flux switching machines with potentially more complex geometries and quicker solution times. Extra parameterised geometry points are defined to increase geometric flexibility and slot shapes can be non-symmetric with rotational offset defined for each. Filleting is also implemented at all corners which can be enabled individually and/or globally to allow rapid solutions without filleting or more detailed analysis with filleting included. A global rotation can also be applied to the entire model without affecting the physical meaning of specified rotor position while mmf in the coils can be defined either as number of strands and the current in each or current density, allowing for packing factor, which is most applicable to initial design.

The model makes use of the ability of finite element analysis to solve a fraction of rotationally symmetric problems in order to greatly reduce solution times without affecting accuracy. For example, a 8/4 flux switching machine may be completely modelled in finite element analysis by a 90° section. However, in practice a 180° section is modelled for clarity. This is especially beneficial for machines with high pole numbers as solution time is approximately proportional to the square of the number of elements. A control parameter disables this property for cases where there is no rotational symmetry.

A global mesh density weighting factor allows discretisation of the model to be readily altered to suit either rapid and approximate solutions or a more accurate solution of the same geometry, as appropriate for the application. It is also possible to add a 'skin' of either fixed or parameterised dimensions to the stator back iron for cases where the stator outer dimensions are non-circular. Figure 2-23 shows the geometric differences between the new parameterised finite element model of the flux switching machine and the previous model used during design. It can be seen that, while the previous model was a reasonable approximation for design use, the improved model gives a more accurate representation of the physical system as it was actually manufactured.

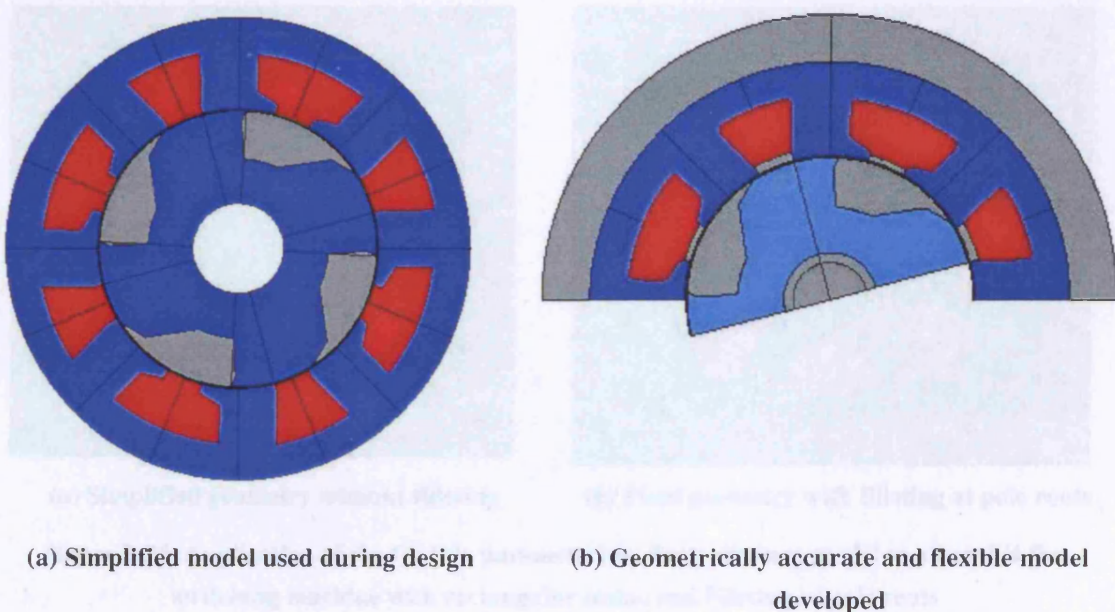


**Figure 2-23** Comparison of simplified and geometrically accurate parameterised finite element models for the 8/4 flux switching machine

Figure 2-24 shows an example of the new parameterised finite element model applied to the design of a new flux switching machine with rectangular outer dimensions which illustrates the addition of a steel 'skin' around the circular stator back iron. In this case the field slots are placed on the flat sides of the rectangle where the back iron is at its thinnest while the back iron is very thick behind the armature slots on the diagonals. Figure 2-24a shows the final candidate design without filleting as it was evolved from the iterative design process while Figure 2-24b shows the final optimised design with significant filleting applied all internal corners, thus reducing localised saturation and leading to performance improvements without significantly affecting the practical slot area available for windings.

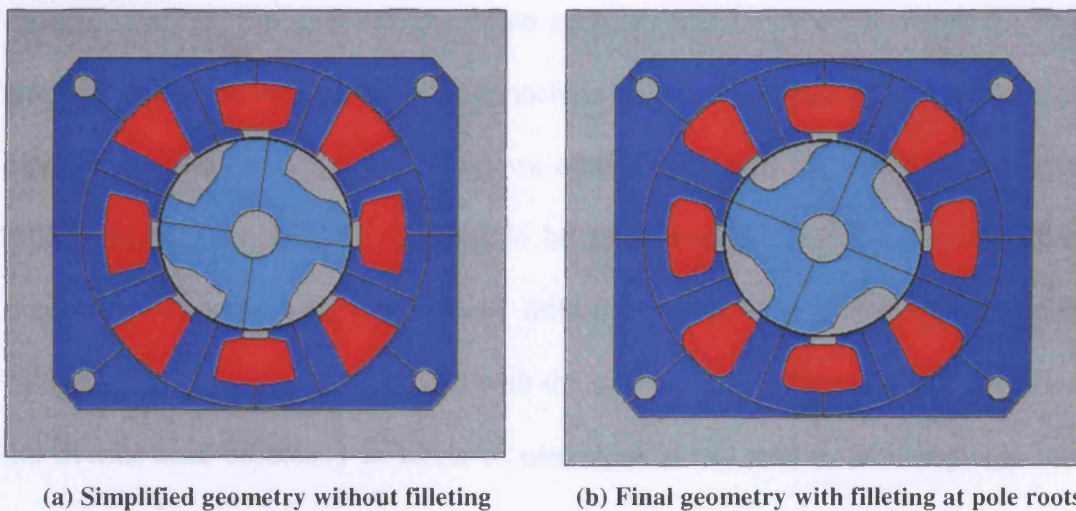


**Figure 2-24** Application of the flexible parameterised finite element model to a new  $8/4$  flux switching machine with rectangular stator and filleting at pole roots

### **2.13 Summary and conclusions**

This chapter has described the construction and method of operation of the flux switching machine and showed that its operation may be considered analogous to that of the brushed dc machine. Parameterised 2-dimensional finite element analysis of the finite element machine was introduced along with methods for ensuring numerical accuracy while reducing the associated computational expense. A new parameterised finite element model of the flux switching machine was also developed which is highly flexible for design and physically accurate for simulation.

In view of the modelling methodology adopted for dynamic simulation of the flux switching machine, i.e. a complete electromagnetic characterisation using finite element analysis, the development of an accurate and flexible parameterised finite element model for the flux switching machine is considered essential to making the method practical for design use. It allows a large number of different finite element models based on a common topology to be automatically created, solved and post-processed while requiring require very little user input. Hence, although the initial computational investment associated with the methodology adopted is still not trivial, the overall cost, especially in terms of user time, is reduced to an acceptable level while maintaining or improving accuracy.

---

# **Chapter 3**

Electromagnetic characterisation  
of the flux switching machine

---

## **3 ELECTROMAGNETIC CHARACTERISATION OF THE FLUX SWITCHING MACHINE**

### **3.1 Structure and properties of the flux map**

#### *3.1.1 Calculation of normalised magnetic quantities*

In a similar way to the flux-mmfs characteristics of the switched reluctance machine, the magnetostatic characteristics of any flux switching machine lamination geometry may be completely described by the relationship between field and armature flux per unit stack length and field and armature mmfs [60]. This complete characterisation is referred to as the “flux map.” These quantities may then be de-normalised to yield winding flux linkages for any combination of stack length, coil configuration and turns number. To use these 2-dimensional magnetostatic solutions as the basis for dynamic simulation requires that eddy currents, magnetic hysteresis and 3-dimensional effects, but not necessarily iron losses, are assumed negligible, as is also the case for the switched reluctance machine. Thus, caution is required when applying the finite element data that these assumptions remain acceptable, e.g. the stack is laminated, winding coils are stranded and the stack is long compared to its diameter etc.

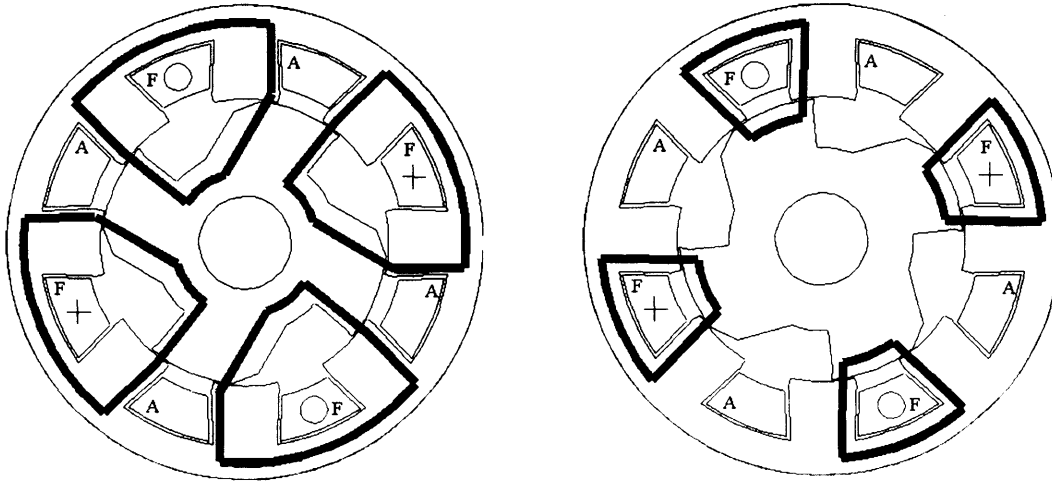
### 3.1.2 *Finite element solutions required for full characterisation of the flux switching machine*

For the conventional switched reluctance machine if no mutual coupling is assumed, any given geometry may be fully characterized by the family of curves giving the relationship

$$\Phi_x(F_x, \theta) \quad (3.1)$$

where  $\Phi$  is winding flux per unit stack length,  $F$  is winding mmf, the subscript  $x$  denotes any winding and  $\theta$  is rotor position generally spanning  $360/N_s$  degrees rotation, i.e. one stator pole pitch, or  $360/(2N_s)$  degrees, i.e. half a stator pole pitch, if both stator and rotor poles are symmetric, where  $N_s$  is the number of stator poles. Assuming that the stack is long enough to allow end-effects to be neglected, this data can be obtained from 2-d magnetostatic finite element analysis and used directly for dynamic simulation.

The flux passing through each winding of the flux switching machine is a non-linear function of mmf in both the field and armature and position over a complete electrical cycle. For the flux switching machine a full electrical cycle spans  $360/(N_s/2)$  degrees where  $N_s$  is the number of stator poles, i.e. 2 stator pole pitches. Figure 3-1 illustrates the field flux paths within the 8/4 flux switching machine with current in the field only for both intermediate positions in the electrical cycle. It can be seen that the flux path reluctance, hence field self inductance, is not equal in both cases while in both positions the armature flux, hence mutual inductance, is zero. This is the case whether or not the stator and/or rotor poles are symmetric. Hence, although it is necessary to compute the flux map over a complete electrical cycle there is no computational penalty incurred by including rotor and/or stator asymmetry as there is for the switched reluctance machine.



(a) Intermediate position with long flux paths (b) Intermediate position with short flux paths

Figure 3-1 Different field flux paths in each intermediate rotor position

The flux switching machine geometry can be fully characterized by a set of finite element solutions giving field and armature flux per unit stack length,  $\Phi$ , as a function of mmf in each winding,  $F$ , and rotor position,  $\theta$ . This data can then be de-normalized to represent any stack length for which it is reasonable to use 2-dimensional magnetostatic finite element analysis, and for windings with any number of turns, either series or parallel connected, making up each winding. Figure 3-2 shows the relationships

$$\Phi_f(F_f, F_a, \theta) \quad (3.2)$$

and

$$\Phi_a(F_f, F_a, \theta) \quad (3.3)$$

for the 8/4 flux switching machine at an aligned position where the field and armature are negatively coupled, i.e. positive current in the field leads to negative flux in the armature and vice versa, where the subscripts  $f$  and  $a$  represent field and armature respectively. The flux map is a family of such surfaces for each position modelled over a complete electrical cycle.

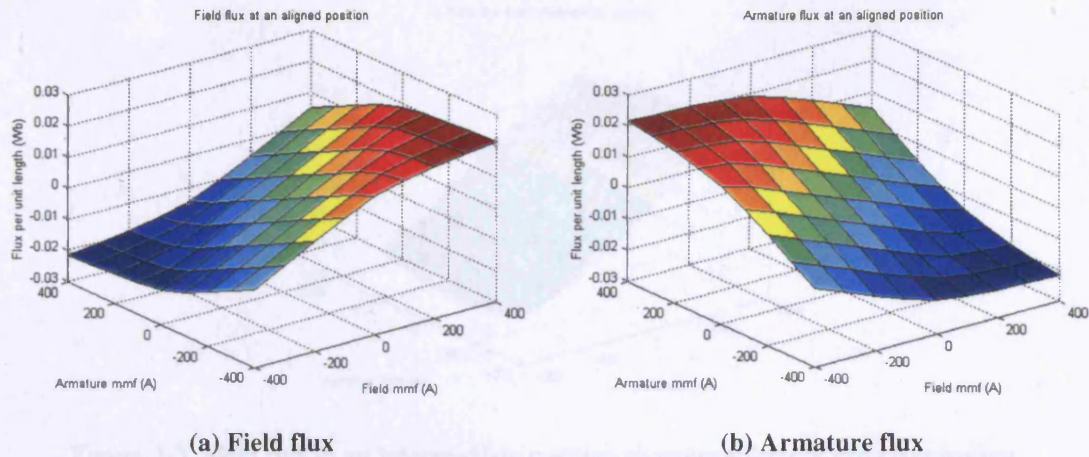
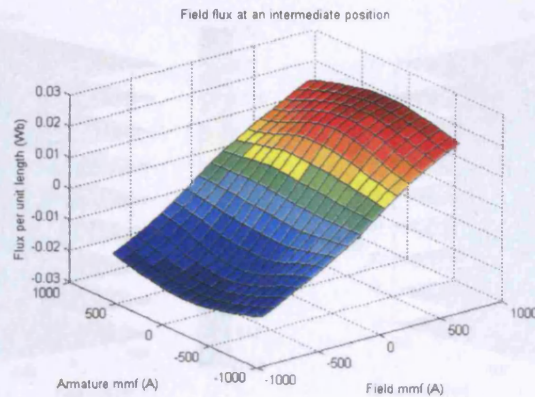


Figure 3-2 Field and armature fluxes in an aligned position of negative mutual coupling

The range of mmfs for which the flux map is calculated is determined by taking into account the available slot area, packing factor and maximum allowable current density of each coil, including foreseeable transient conditions.

Figure 3-3 illustrates the need to include a full range of mmf combinations at each position in the flux map. Cross-saturation effects become apparent in the flux switching machine at intermediate positions where the rotor is spanning a slot as in Figure 3-1. In the example shown, for small mmfs in both windings there is negligible mutual coupling and field flux is a function of field mmf only. However, for larger field mmf localized saturation occurs in parts of the steel which are shared by both field and armature fluxes. This leads to a reduction in field flux for any armature mmf, regardless of its polarity. Hence, the windings are effectively coupled under such conditions.



**Figure 3-3** Field flux in an intermediate position showing effects of cross-saturation

### 3.1.3 Storage and manipulation of the flux map

Field and armature flux are both non-linear functions of field mmf, armature mmf and rotor position, i.e. 3 independent variables and 2 dependent variables. This data is stored in two multi-dimensional arrays in MATLAB [61] with field mmf being the  $x$  axis, armature mmf the  $y$  axis, rotor position the  $z$  axis and the numerical value of flux per unit stack length stored in a corresponding array element for each modelled condition. Figure 3-4 illustrates this method of data storage. The magnitude of field and armature flux per unit stack length is visualised for each calculated mmf combination at a range of positions over a complete electrical cycle by colour. *Thus, the flux map completely characterises the electromagnetic properties of a given flux switching machine lamination geometry in a comparable way to the flux-mmf characteristic of the switched reluctance machine.*

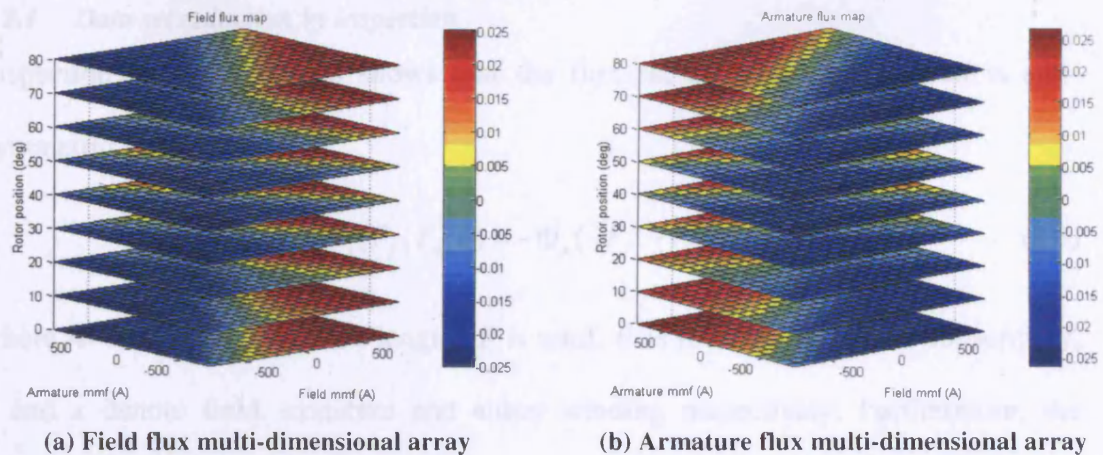


Figure 3-4 Illustration of flux map storage in multi-dimensional arrays

Using 3-dimensional interpolation the values of flux per unit stack length for any combination of mmfs and position within the range of the modelled mmf values may be inferred. Due to the non-linearity of the flux-mmfs relationships extrapolation outside of the modelled mmf range is generally not feasible.

### 3.2 Computational overhead reduction

The complete flux map presented above consists of one data point for each combination of 9 field mmfs, 9 armature mmfs and 18 rotor positions in order to fully characterise the electromagnetic properties of the lamination geometry over a complete electrical cycle. If each data point is calculated using finite element analysis this is a total of 1458 finite element solutions which, even considering the measures outlined in chapter 2 for reducing finite element analysis solution time, is a considerable computational investment. However, techniques have been developed to greatly reduce this computational overhead while maintaining acceptable accuracy.

### 3.2.1 Data set reduction by inspection

Inspection of the flux map shows that the flux surface for each position is anti-symmetric, i.e.

$$\Phi_x(F_f, F_a, \theta) = -\Phi_x(-F_f, -F_a, \theta) \quad (3.4)$$

where  $\Phi$  is flux per unit stack length,  $F$  is mmf,  $\theta$  is rotor angle and the subscripts  $f$ ,  $a$  and  $x$  denote field, armature and either winding respectively. Furthermore, the solution of

$$\Phi_x(F_f, F_a, \theta) \quad (3.5)$$

is trivial for  $F_f = F_a = 0$  at all positions  $\theta$ . Using these observations the number of finite element solutions required to construct a complete  $9 \times 9 \times 18$  flux map is reduced from 1458 to 720 with no deleterious effects on accuracy. Figure 3-5 illustrates the computational saving made for each position.

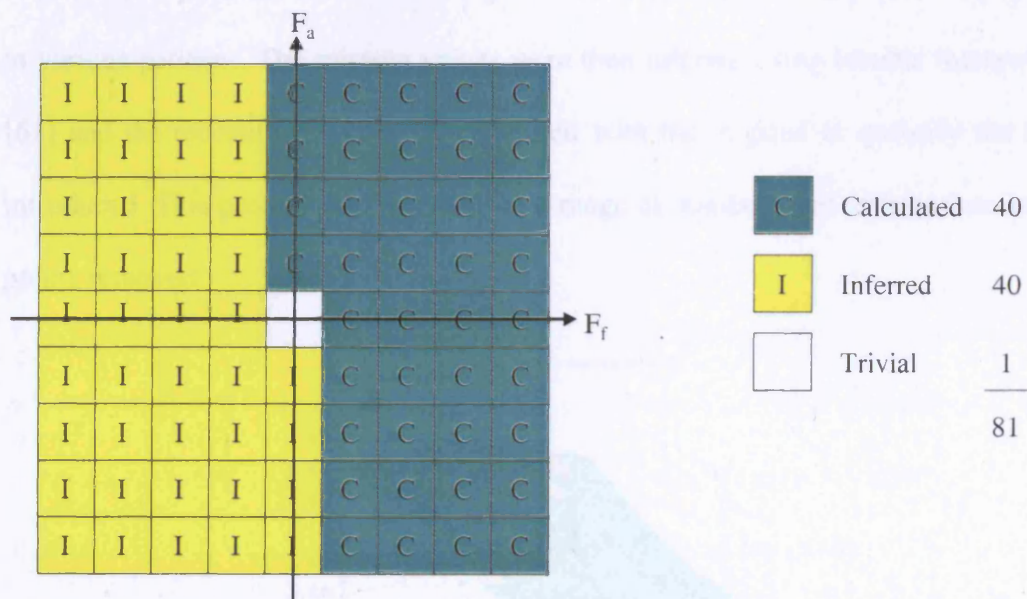


Figure 3-5 Illustration of computational overhead reduction by inspection of the flux map

### 3.2.2 Data set reduction by interpolation

In order to further reduce the number of finite element solutions required to produce a flux map of given resolution, interpolation may be used to produce substitute results to replace those removed. As an analytic solution is not readily obtainable for the relationship between winding mmfs, position and fluxes, interpolation of any sort will generally produce results that are different from those which would have been calculated using finite element analysis. Therefore, for comparison a simple measure of the errors introduced by such interpolation is the difference between the value inferred for a data point using interpolation and that obtained directly from finite element analysis. However, it must also be noted that finite element solutions also include small random errors and an interpolated result which differs slightly from that calculated by finite element analysis is not necessarily less correct in reality.

Starting with a flux surface where all values are obtained from finite element analysis at an aligned position, as shown in Figure 3-6, a number of data points were deleted in various patterns. The missing values were then inferred using bicubic interpolation [61] and the reconstituted data set compared with the original to quantify the errors introduced. This process was repeated for a range of numbers and distributions of data points removed.

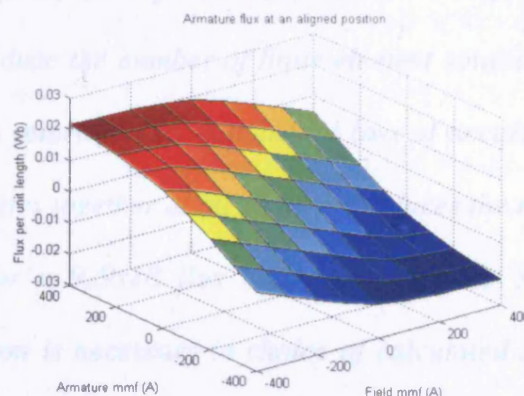
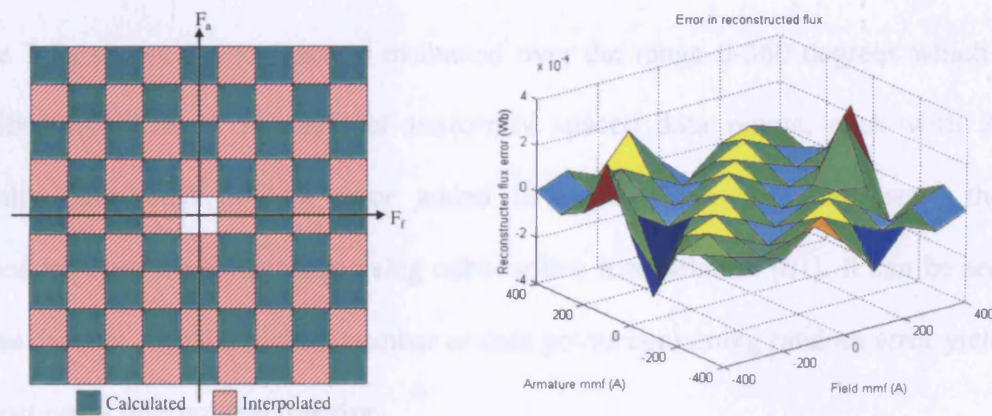


Figure 3-6 Original flux surface for reference

Figure 3-7 shows an example of an option which was found to offer a reasonable compromise between number of data points removed and accurate reconstruction of the underlying data in this position. In order to still take advantage of data set reduction by inspection the pattern of calculated data points must remain anti-symmetric. Using interpolation to reconstruct the missing data points introduces a mean norm error of  $4.66 \times 10^{-5}$  Wb and an RMS error of  $8.34 \times 10^{-5}$  Wb compared to the original, fully calculated data.



(a) Pattern of data points removed

(b) Error introduced into reconstructed data

**Figure 3-7 Example of computational overhead reduction by interpolation**

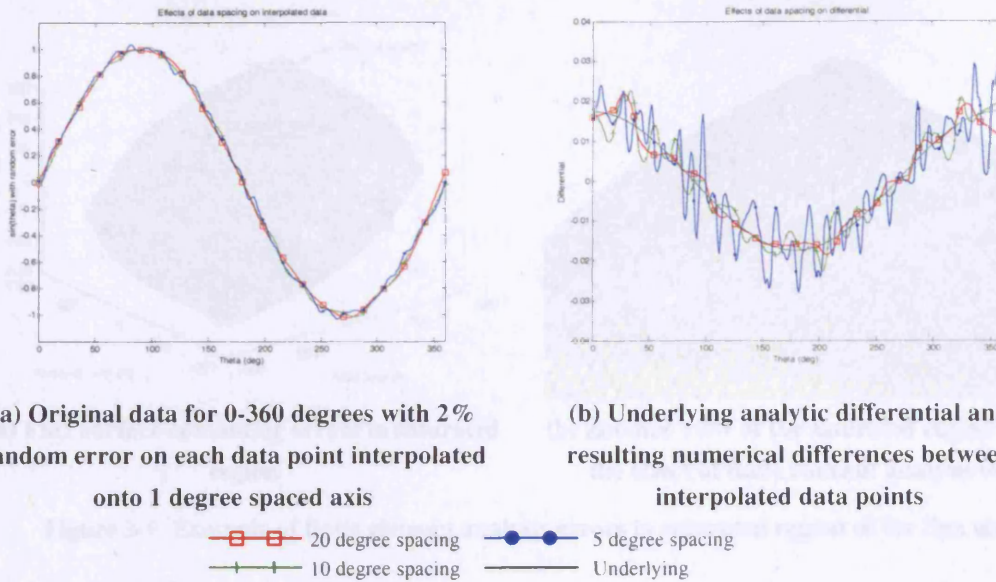
Hence, using this method, in conjunction with data set reduction by inspection, it is possible to further reduce the number of finite element solutions required to create a complete flux map in return for some potential loss of accuracy. Implementing both data reduction strategies together at all positions reduces the number of finite element solutions required for a  $9 \times 9 \times 18$  flux map from 1458 to 360, a saving of 75%. However, some caution is necessary in choice of calculated data points to maintain necessary data accuracy if the interpolation method is used.

### 3.2.3 *Maximum feasible number of finite element data points*

Intuitively the more flux map data points are calculated, the better the accuracy of any simulation model based upon it should be as the data obtained more closely resembles a continuum and interpolation errors are reduced. However, in the extreme this analysis requires that there are no random numerical errors in the calculated finite element analysis model solutions, otherwise discontinuities will arise. In finite element analysis these errors are not always negligible and if data points containing random error are too closely spaced this leads to a noisy data set which is difficult to interpolate reliably.

Figure 3-8a shows a sine function evaluated over the range 0-360 degrees which is described by different numbers of uniformly spaced data points, each with 2% normally distributed random error added to them. These data sets were then interpolated onto the same range using cubic spline interpolation [61]. It can be seen that the data set with the highest number of data points containing random error yields the most noisy interpolated function.

Figure 3-8b shows the derivative of each of the interpolated functions along with the underlying derivative. Due to the tendency of numerical differentiation to amplify the effect of random errors it can be seen that the data defined by the most points gave rise to the worst 'quality' interpolated data. *Hence, although enough data points must be calculated to adequately describe the complete flux map, there is a practical limit beyond which more closely spaced data points, hence more computational effort, yield no further benefit and, in practice, have a deleterious effect on the quality of the flux map.*



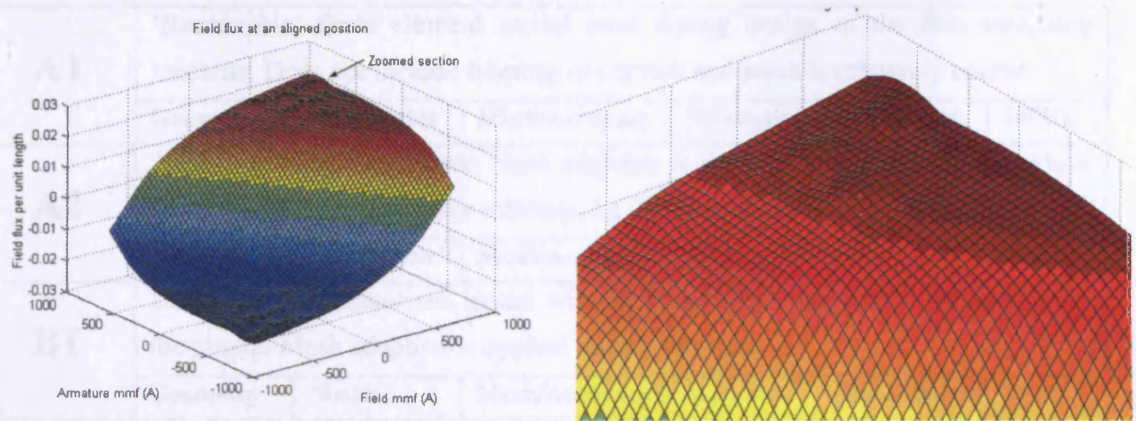
(a) Original data for 0-360 degrees with 2% random error on each data point interpolated onto 1 degree spaced axis

(b) Underlying analytic differential and resulting numerical differences between interpolated data points

■ 20 degree spacing    ● 5 degree spacing  
+ 10 degree spacing    — Underlying

Figure 3-8 Effects of data point spacing and small random error on interpolated data quality

This effect is particularly pronounced in regions of the flux map where there is extreme saturation and for a given change in applied mmf there is very little corresponding change in flux. Figure 3-9 shows an example of such a region of the flux map. As applied mmfs are increased the differences in calculated flux values between adjacent finite element solutions decrease due to magnetic saturation while random numerical errors in the finite element analysis solutions tend to be greatest under such conditions. Thus, in regions of the flux map where numerical errors approach a similar order of magnitude as the expected change in flux there is no benefit gained from calculating a large number of closely spaced data points.



(a) Flux surface containing errors in saturated region

(b) Zoomed view of the saturated region showing the effect of finite element analysis errors

Figure 3-9 Example of finite element analysis errors in saturated region of the flux map

### 3.3 Comparison of flux maps from finite element analysis

For direct comparison between finite element models several complete flux maps for the 8/4 flux switching machine were calculated. Each flux map was calculated for identical mmf and position combinations. The only differences between these finite element models are the meshing, numerical accuracy, i.e. solution error estimate, and/or frequency at which the steel B-H characteristic was obtained. The flux maps compared are referred to by name and are summarised in Table 3-1.

<b>A1</b>	'Reasonable' finite element model used during design of the flux switching machine. Does not include filleting of corners and mesh is relatively coarse.					
	<b>Geometry</b>	'Reasonable'	<b>Mesh/Accuracy</b>	'Reasonable'	<b>Steel B-H</b>	540Hz
<b>A2</b>	As A1 model but automatic mesh adaption is applied during solution to reduce finite element solution error estimate, i.e. increase numerical accuracy.					
	<b>Geometry</b>	'Reasonable'	<b>Mesh/Accuracy</b>	Accurate	<b>Steel B-H</b>	540Hz
<b>B1</b>	Using new parameterised model without filleting but with coils set back from the airgap. Mesh adaption is applied during solution.					
	<b>Geometry</b>	'Better'	<b>Mesh/Accuracy</b>	Accurate	<b>Steel B-H</b>	540Hz
<b>B2</b>	As B1 with filleting added to precisely model the manufactured lamination geometry.					
	<b>Geometry</b>	Precise	<b>Mesh/Accuracy</b>	Accurate	<b>Steel B-H</b>	540Hz
<b>B3</b>	As B2 but using 20Hz steel B-H characteristic					
	<b>Geometry</b>	Precise	<b>Mesh/Accuracy</b>	Accurate	<b>Steel B-H</b>	20Hz

**Table 3-1 Summary of finite element models used to create each flux map for comparison**

For comparison between these flux maps the difference between the flux surfaces at each modelled position is examined. The effects of meshing and numerical accuracy, geometric accuracy and steel B-H characteristic on the calculated fluxes in finite element analysis are each examined individually. However, as the finite element model used to calculate 'B2' most closely models the actual manufactured geometry, includes a high frequency derived steel B-H characteristic and is the most numerically accurate, it is reasonable to assume that it is the most accurate of the finite element models. In each case results for an aligned and an intermediate position are presented to show the range of differences. In the aligned position presented the field and armature are negatively mutually coupled and in the intermediate position presented the rotor is bridging the armature slot. The field and armature flux surfaces for these positions obtained from B2 are shown in Figure 3-10 for reference.

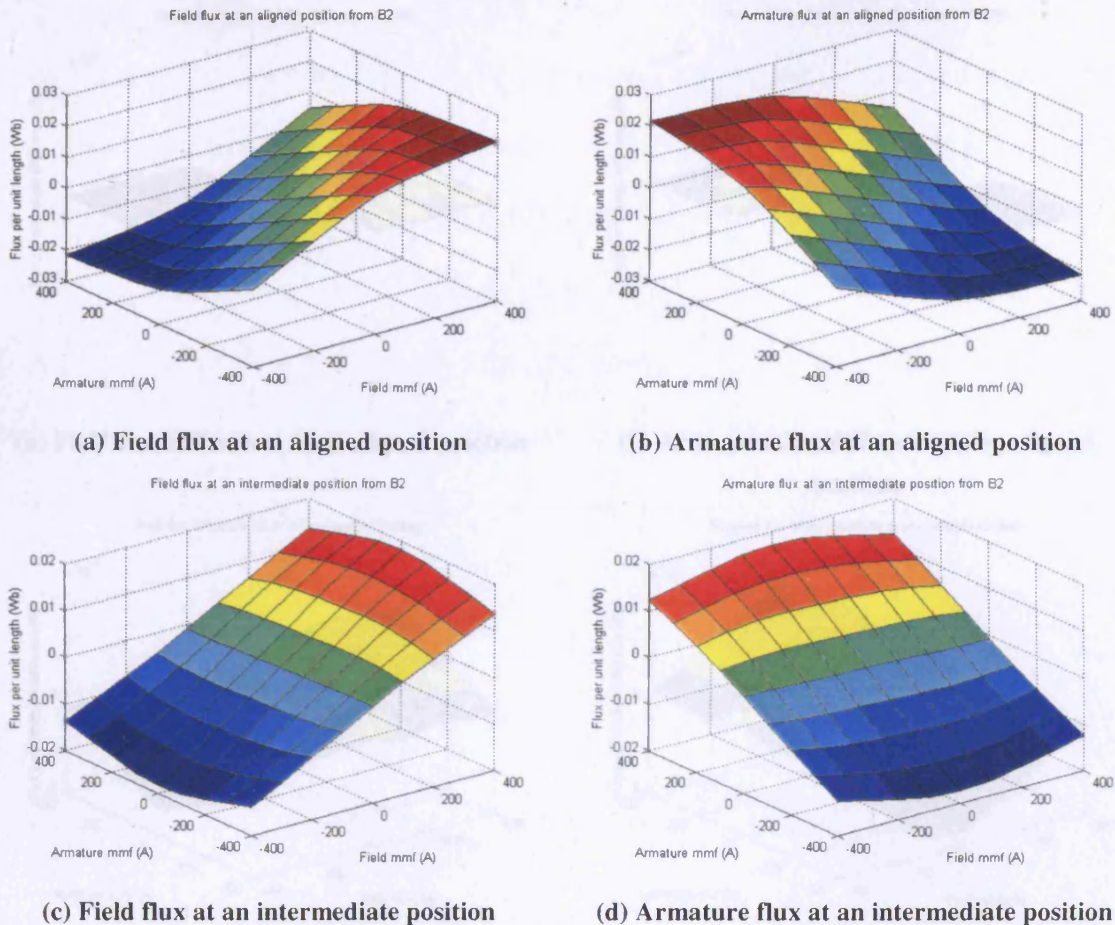


Figure 3-10 Field and armature fluxes at an aligned and an intermediate position

### 3.3.1 Effects of meshing and numerical accuracy

The effects of meshing and numerical accuracy may be isolated by comparing the results obtained for A1 and A2 flux maps. Both are solved from identical model formulations but A1 is solved normally without mesh adaption while A2 is solved using double precision arithmetic and automatic mesh adaption to achieve a much reduced numerical error estimate. Hence, differences between A1 and A2 flux maps are primarily due to the effects of meshing and numerical accuracy. Figure 3-11 shows the differences between the flux surfaces obtained for aligned and intermediate positions.

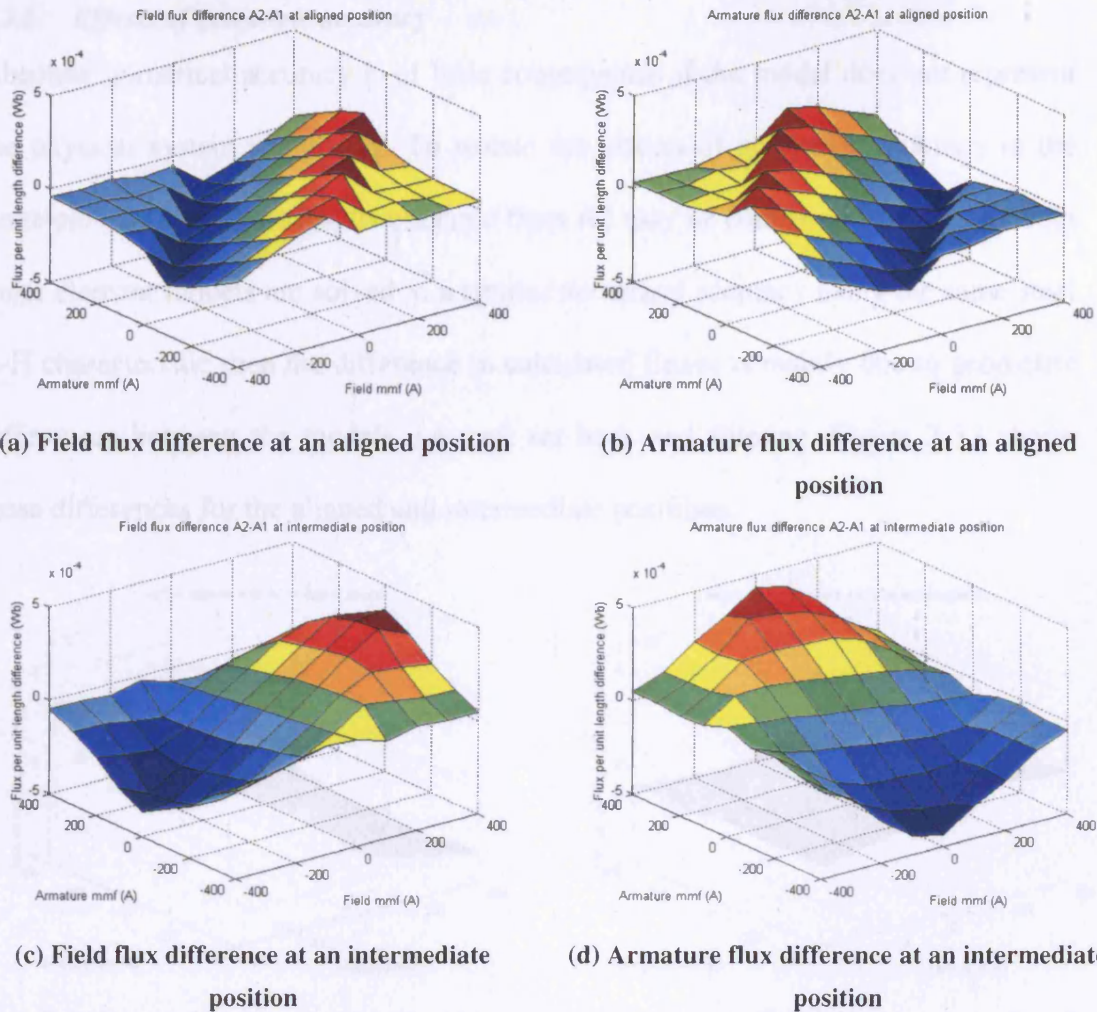
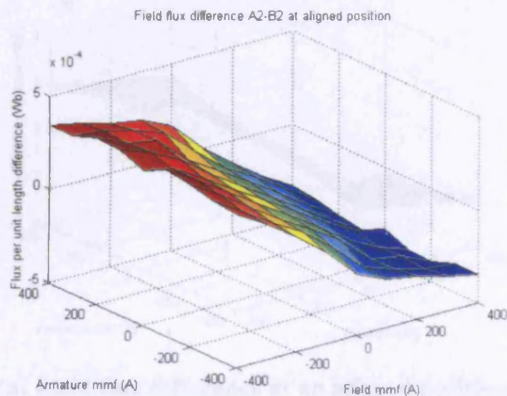


Figure 3-11 Differences in flux due to finite element meshing and numerical accuracy

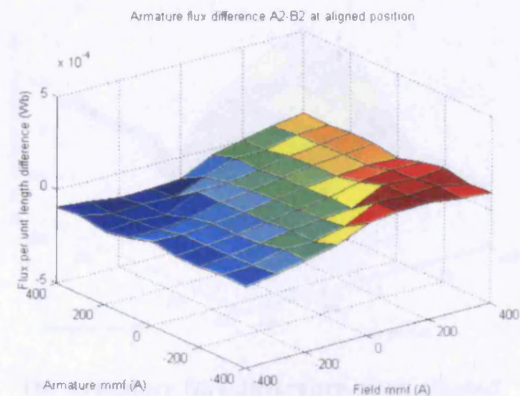
In both aligned and intermediate positions the magnitude of difference between the A1 and numerically more accurate A2 flux maps is small compared to the calculated flux. These differences are mainly due to insufficient meshing in areas of high localised saturation around sharp corners as introduced in chapter 2. *However, as A2 is some 5 times more computationally expensive than the A1 flux map, the limited benefit in accuracy obtained for this large additional investment may not be considered efficient use of resources in many cases.*

### 3.3.2 Effects of geometric accuracy

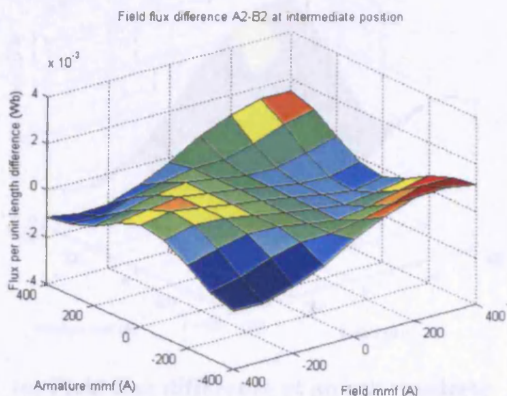
Absolute numerical accuracy is of little consequence if the model does not represent the physical system adequately. To isolate the effects of geometric accuracy in the finite element model the results obtained from A2 may be compared with B2. As both finite element models are solved to a similar numerical accuracy using the same steel B-H characteristic then the difference in calculated fluxes is mainly due to geometric differences between the models, i.e. coil set back and filleting. Figure 3-12 shows these differences for the aligned and intermediate positions.



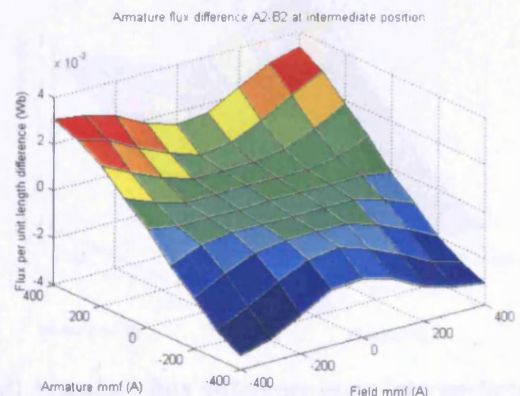
(a) Field flux difference at an aligned position



(b) Armature flux difference at an aligned position



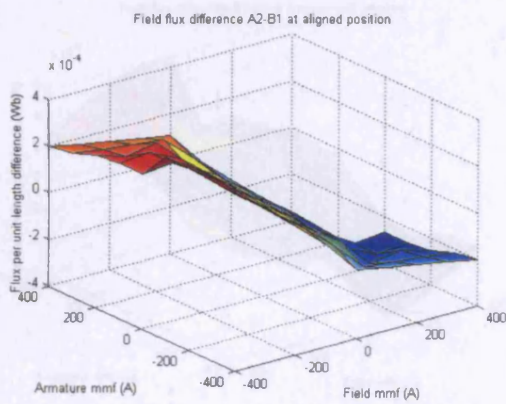
(c) Field flux difference at an intermediate position



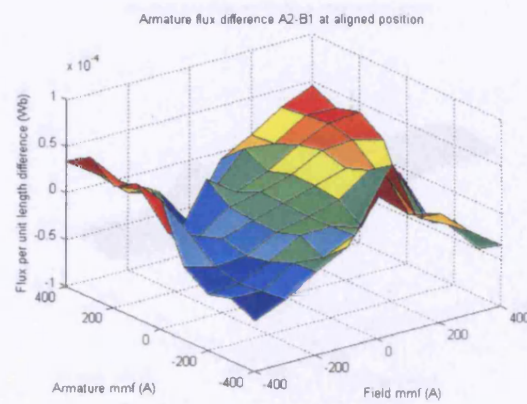
(d) Armature flux difference at an intermediate position

Figure 3-12 Differences in flux due to finite element model geometric accuracy

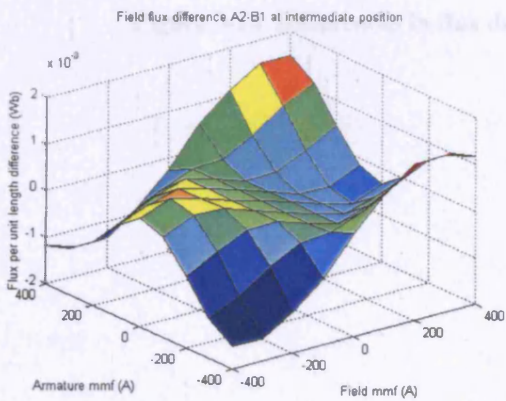
Comparing the differences between A2 and B2 it can be seen that the peak differences in the intermediate position are an order of magnitude greater than those in an aligned position and those due to numerical accuracy. To determine how much of the difference between A2 and B2 is due to setting the coils back from the airgap and how much is due to filleting, Figure 3-13 shows the differences between A2 and B1, i.e. mainly due to coil set-back only. The differences which are mainly due to filleting are shown in Figure 3-14 which compares the calculated fluxes using B1 and B2.



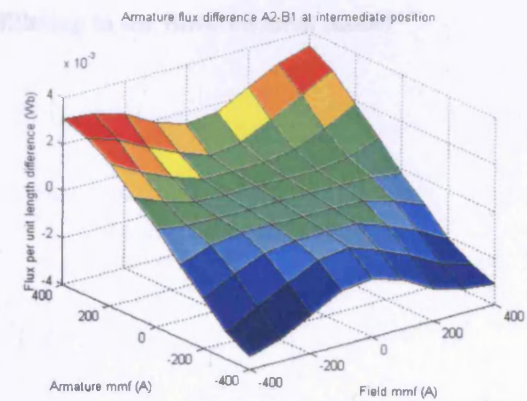
(a) Field flux difference at an aligned position



(b) Armature flux difference at an aligned position



(c) Field flux difference at an intermediate position



(d) Armature flux difference at an intermediate position

Figure 3-13 Differences in flux due to coil set-back in the finite element model

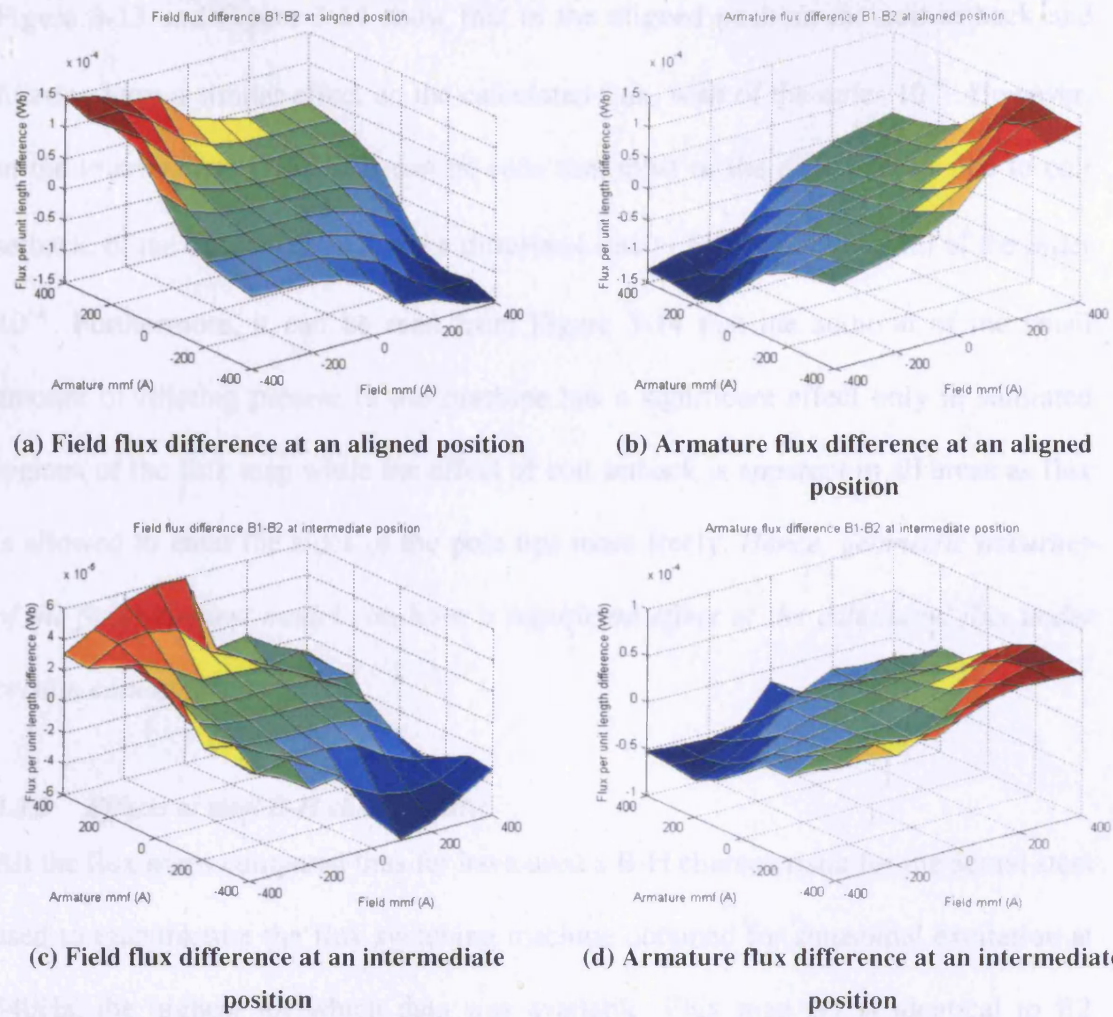
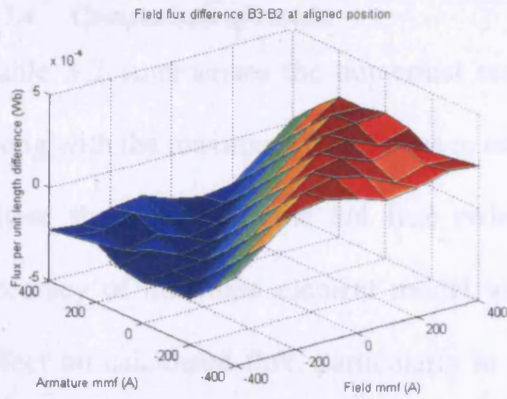


Figure 3-14 Differences in flux due to filleting in the finite element model

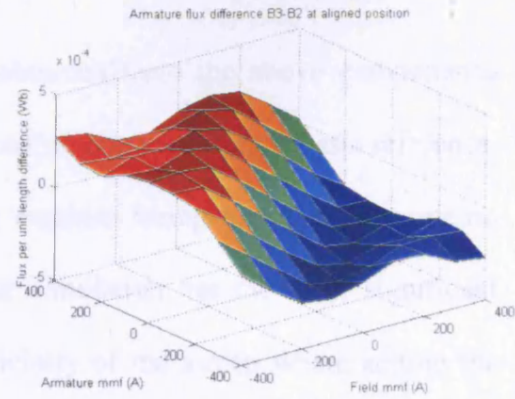
Figure 3-13 and Figure 3-14 show that in the aligned position the coil setback and filleting have a similar effect on the calculated flux, both of the order  $10^{-4}$ . However, in the intermediate position it can be seen that most of the difference is due to coil setback, of the order  $10^{-3}$ , while the difference due to filleting only is still of the order  $10^{-4}$ . Furthermore, it can be seen from Figure 3-14 that the addition of the small amount of filleting present in the machine has a significant effect only in saturated regions of the flux map while the effect of coil setback is apparent in all areas as flux is allowed to enter the sides of the pole tips more freely. *Hence, geometric accuracy of the finite element model can have a significant effect of the calculated flux under certain conditions.*

### **3.3.3 Effects of steel B-H characteristic**

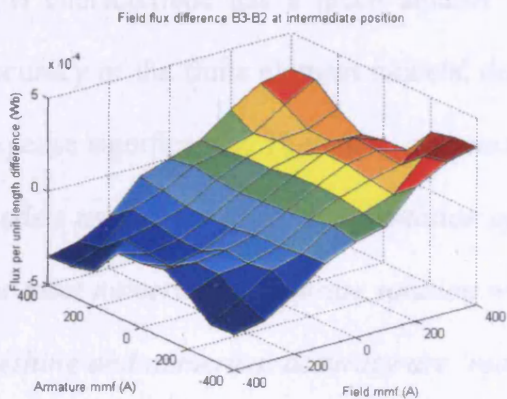
All the flux maps compared thus far have used a B-H characteristic for the actual steel used to manufacture the flux switching machine obtained for sinusoidal excitation at 540Hz, the highest for which data was available. Flux map B3 is identical to B2 including filleting, coil setback and mesh adaption, the only difference being that the B-H characteristic for the steel used was obtained at 20Hz, the lowest available. Hence, the differences between these flux maps are primarily due to the differing non-linear magnetisation characteristics used for the steel. Figure 3-15 shows the differences obtained for the aligned and intermediate positions.



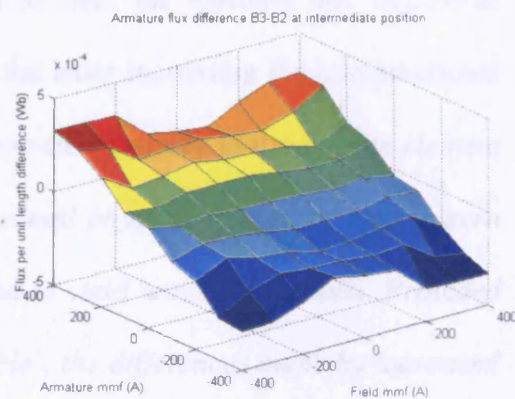
(a) Field flux difference at an aligned position



(b) Armature flux difference at an aligned position



(c) Field flux difference at an intermediate position



(d) Armature flux difference at an intermediate position

Figure 3-15 Differences in flux due to B-H characteristics used in the finite element model

It can be that the differences in flux data obtained using different BH characteristics are similar, of the order  $10^{-4}$ , in both aligned and intermediate positions. Although the area enclosed within major B-H hysteresis loops increases with frequency, the locus through the extrema of these loops, which is generally used in finite element analysis [50], does not change greatly. Hence, provided a representative B-H characteristic for the actual steel is used, the frequency at which it is obtained is of less importance. This is especially true considering that each region within the flux switching machine is subject to flux waveforms of widely differing amplitude and frequency.

### 3.3.4 Comparison of results

Table 3-2 summarises the numerical results obtained from the above comparisons along with the maximum flux values in each position obtained from B2 as a reference. These show that, for the 8/4 flux switching machine being examined, geometric accuracy of the finite element model used for simulation has the most significant effect on calculated flux, particularly in the vicinity of the airgap where setting the coils back from the airgap had the greatest effect. By comparison, the choice of steel B-H characteristic has a much smaller effect as does the meshing and numerical accuracy of the finite element models, despite the latter increasing the computational expense significantly. *Therefore, it is most important to ensure that the finite element models used are a good representation of the actual physical system, otherwise even the most numerically accurate solution will tend to yield unreliable results. Provided meshing and numerical accuracy are 'reasonable', the differences made by increased numerical accuracy are smaller and may not justify the additional computational expense.*

	Maximum norm difference ( $10^{-3}$ Wb)				RMS difference ( $10^{-3}$ Wb)			
	Aligned		Intermediate		Aligned		Intermediate	
	Field	Arm.	Field	Arm.	Field	Arm.	Field	Arm.
<i>B2</i> <i>maximum</i> <i>(reference)</i>	21.35	21.62	18.27	17.29				
Coarse meshing (A2-A1)	0.232	0.222	0.368	0.437	0.114	0.111	0.180	0.194
Simplified geometry (A2-B2)	0.396	0.130	1.50	3.40	0.254	0.070	0.669	1.60
Low freq. BH data (B3-B2)	0.285	0.295	0.349	0.330	0.210	0.207	0.184	0.169

Table 3-2 Summary of differences in fluxes due to finite element model formulation

### 3.4 Comparison of finite element analysis and experimentally measured flux linkage data

#### 3.4.1 Method of comparison

In order to quantify the differences between finite element analysis and experimentally obtained data the flux linkages of each winding with only that winding excited were compared for a range of positions spanning a complete electrical cycle, i.e. the self inductance characteristics of the windings. This measure of comparison was chosen as it is readily available, both experimentally and from finite element analysis, and can be expected to clearly show the differences between the two methods. While the finite element results are 2-d magnetostatic based on a single valued B-H characteristic, the experimental results include dynamic magnetic effects and 3-dimensional effects, both of which are neglected in finite element analysis. The experimental results obtained by different methods are also compared.

There are a variety of different definitions used to describe 'inductance' for different applications. In the context of this comparison absolute and incremental inductances are defined as in Figure 3-16 where  $\Psi$  is flux linkage,  $i$  is current and subscript  $x$  denotes either field or armature.

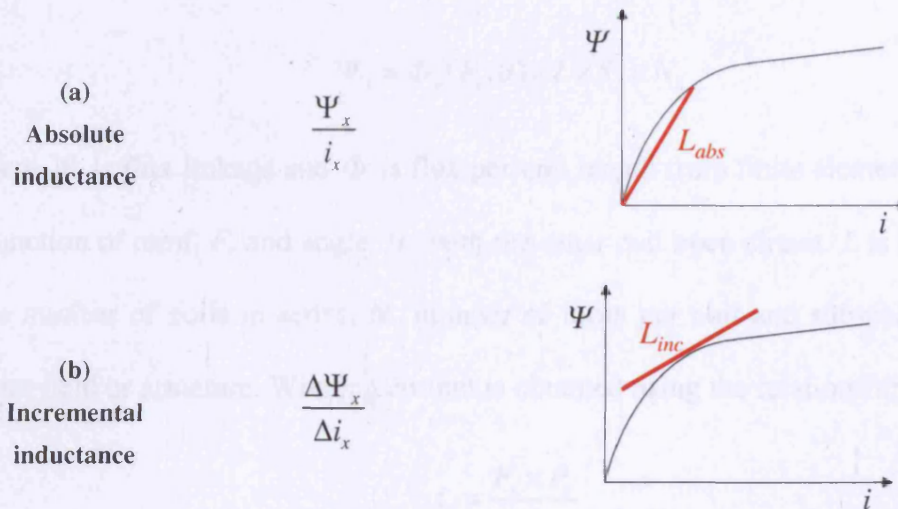


Figure 3-16 Definitions of absolute and incremental inductance used

### 3.4.2 Experimental conditions

The shaft mounted optical position sensor of the 8/4 flux switching machine was calibrated, as described in chapter 2, and the machine was then mounted onto a static test rig with precision dividing head. The precision dividing head allows accurate and repeatable positioning of the rotor relative to a rising edge of the position sensor signal, which is defined as zero degrees rotor angle. A similar process was carried out using the flux map data obtained from finite element analysis to provide correlation between experimental and finite element results in each position.

### 3.4.3 Winding self inductances from finite element results

For each position within the electrical cycle the field and armature flux linkage-current relationships are obtained directly from the finite element data contained in the flux map. Winding flux linkages for the machine being tested are obtained from the flux map using the relationship

$$\Psi_x = \Phi_x(F_x, \theta) \times L \times S_x \times N_x \quad (3.6)$$

where  $\Psi$  is flux linkage and  $\Phi$  is flux per unit length from finite element analysis as a function of mmf,  $F$ , and angle,  $\theta$ , with the other coil open circuit.  $L$  is stack length,  $S$  is number of coils in series,  $N$  number of turns per coil and subscript  $x$  denotes either field or armature. Winding current is obtained using the relationship

$$i_x = \frac{F_x \times P_x}{N_x} \quad (3.7)$$

where  $i$  is current, and  $P$  is number of parallel coils. Using the values obtained both absolute and incremental self inductances are readily obtained using the definitions given in Figure 3-16.

The results for two different flux maps, B2 and B3, are obtained and compared, the only difference between them being the steel B-H characteristics used during simulation. B2 was calculated using B-H data for the actual steel obtained for 540Hz sinusoidal excitation while B3 was calculated using the B-H characteristic obtained for 20Hz. Figure 3-17 compares the absolute and incremental inductance relationships obtained from flux maps B2 and B3 over a complete electrical cycle

The linear range of inductances for low currents is evident as the flat top of the inductance surfaces where there is little change in the value of inductance calculated with increasing winding current. In this region absolute and incremental inductances are similar. Beyond this region the effects of magnetic saturation become apparent and absolute inductance decreases with further increasing winding current while incremental inductance decreases more rapidly. The effects of differing magnetic path reluctance in each half of the electrical cycle, introduced in section 3.1.2, are also evident, i.e. although the shape of inductance relationships with position are similar for 0-45degrees and 45-85degrees the numerical values are not identical.

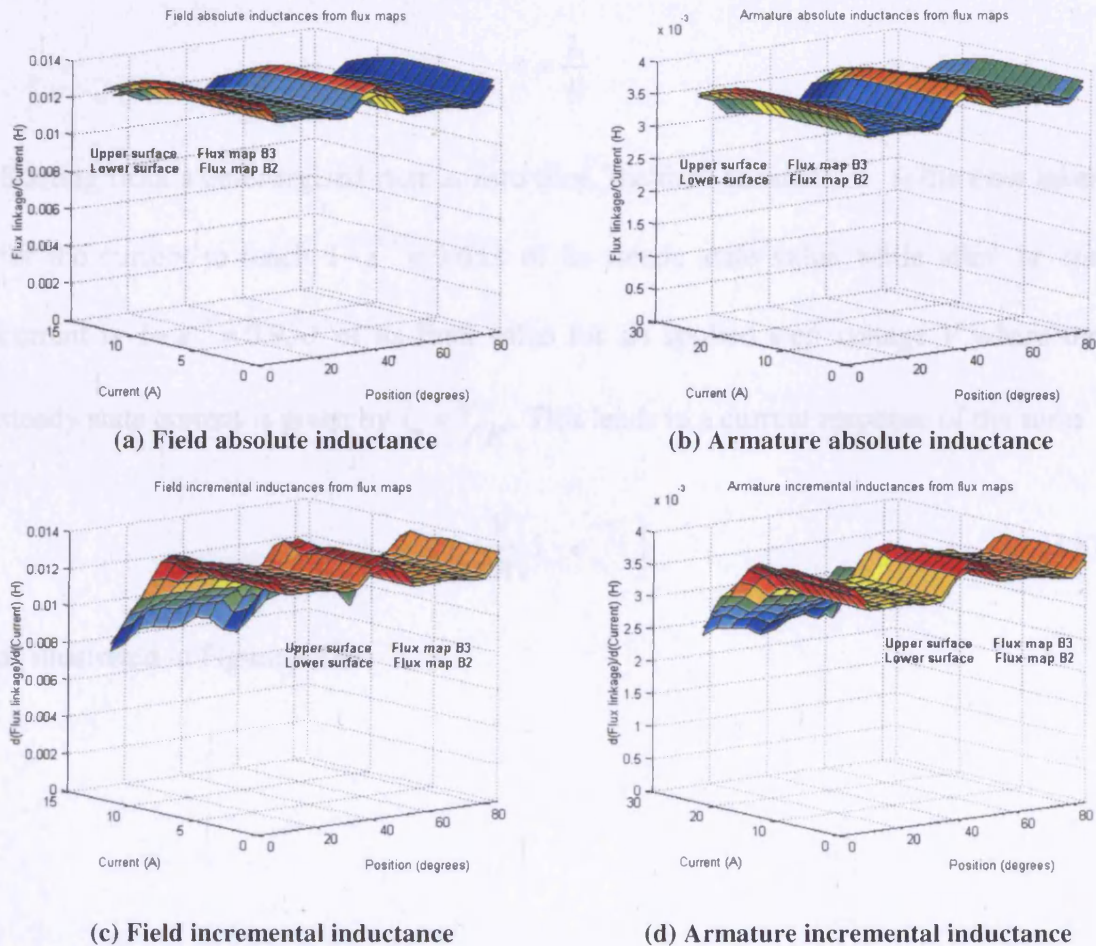


Figure 3-17 Comparison of inductances obtained from the flux map for different B-H characteristics

Comparing the inductances for both flux maps it can be seen that the values obtained from B3 are generally higher than those obtained from B2. Although the difference is not negligible it is relatively small compared to the magnitudes of calculated inductance. However, using the higher frequency B-H characteristic B2 more closely resembles the operating conditions of the flux switching machine, hence comparison of experimental results will be made with the values derived from B2.

#### ***3.4.4 Winding effective inductances from simple time constant method***

Given a linear inductor  $L$  and resistor  $R$  in series the time constant  $\tau$  of the system in seconds is given by the equation

$$\tau = \frac{L}{R}$$

Starting from a de-energised state at zero time, the time constant,  $\tau$ , is the time taken for the current to reach  $1 - e^{-1} = 0.632$  of its steady state value while after  $3\tau$  the current is  $1 - e^{-3} = 0.950$  of its final value for an applied step voltage  $V$  where the steady state current is given by  $i_{\infty} = V/R$ . This leads to a current response of the form

$$i = \frac{V}{R} \left[ 1 - e^{-tR/L} \right] \quad (3.8)$$

as illustrated in Figure 3-18.

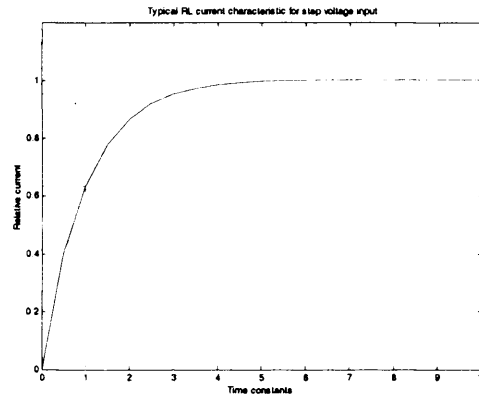


**Figure 3-18** Typical current waveform for a linear series RL circuit

Hence, linear inductance apparent at the terminals may be obtained by applying a step voltage to an initially de-energised winding and measuring the time taken for the winding current to reach 0.632 of its steady state value,  $t_{0.632}$ . Assuming that this current is within the linear inductance range, the measured time is the time constant of the series RL circuit representing the winding, i.e.  $t_{0.632} = \tau$ . Using a measured value of dc resistance the effective linear inductance may then be obtained using  $L = \tau R$ . The time taken for current to reach 0.950, of its final value,  $t_{0.950}$  may also be measured as a comparison. If there is no magnetic saturation then  $t_{0.950} = 3t_{0.632}$ . This simple procedure was repeated for each winding in a variety of positions.

Table 3-3 summarises the results obtained for field and armature linear self inductances from flux map B2 and experimentally using the simple time constant method. Comparing these results shows that the inductances obtained from the flux map and are similar magnitude to those obtained experimentally. However, the experimental results would normally be expected to be higher than those derived from 2-dimensional magnetostatic finite element analysis with the difference due to end winding inductances etc. This implies that either the finite element model consistently overestimates winding fluxes or the simple experimental method used makes a consistent underestimate. Hence, a more thorough experimental investigation was carried out to investigate the reasons for this unexpected difference between experimental and finite element derived inductances.

<b>Rotor position</b>	<b>0 deg</b>	<b>22.5 deg</b>	<b>45 deg</b>	<b>67.5 deg</b>
<b>Field absolute inductance (FEA)</b>	13.7mH	12.8mH	13.6mH	12.3mH
<b>Field inductance (experimental)</b>	11.99mH	11.34mH	12.21mH	11.56mH
<b>Armature absolute inductance (FEA)</b>	3.80mH	3.43mH	3.85mH	3.59mH
<b>Armature inductance (experimental)</b>	2.90mH	2.96mH	2.87mH	3.22mH

**Table 3-3 Summary of measured and calculated inductances obtained by the simple time constant method**

### 3.4.5 Accurate winding flux linkages from experiment

#### 3.4.5.1 Experimental method

The flux linkage in a winding at time  $t$  is given by the general relationship

$$\Psi = \int_0^t (v - iR)dt + \Psi_0 \quad (3.9)$$

where  $\Psi$  is flux linkage,  $v$  is applied voltage,  $i$  is current,  $R$  is resistance,  $t$  is time and  $\Psi_0$  is the initial flux linkage at zero time. In general the value of  $\Psi_0$  is not usually known as the steel retains some remnant flux after excitation is removed, the magnitude and sense depending on the last excitation applied to the windings and time since it was removed. For good quality electrical steel this remnant flux is generally small compared to the working flux but it is not negligible.

In equation (3.9), current,  $i$ , is multiplied by resistance,  $R$ . Hence, as the current rises close to its steady state value any error in the value of  $R$  has the potential to greatly affect the accuracy of calculated flux linkage. Furthermore, it is difficult to accurately measure  $R$  as its value depends on temperature and is also dependent on rate of change of current. However, if  $v$  is very large compared to  $iR$  the effect of any error in  $R$  on calculated flux linkage is greatly reduced [62].

In practice, when applying a large terminal voltage the maximum current must be controlled by the duration for which it is applied. Furthermore, as the maximum current is reached more rapidly for a higher applied voltage, less heat is dissipated in the winding resistance, thus making  $R$  easier to measure accurately. It remains important, however, that  $R$  is measured as accurately as possible at the same point in the circuit as the applied voltage to ensure that external resistances are not incorrectly included or omitted.

The value of flux linkage obtained by experiment using an applied terminal voltage is, more precisely, the change in flux linkage from that which was present the instant before the terminal voltage was applied. Depending on the polarity of the last excitation the remnant flux linkage is

$$\pm \Psi_{rem} \quad (3.10)$$

where  $\Psi_{rem}$  is the magnitude of remnant flux after excitation to the given peak magnitude. Hence, to obtain an accurate single valued flux linkage-current relationship it is necessary to conduct the test starting from both positive and negative initial conditions. The mean of the results is then taken, having defined the starting flux to be zero in each case. Figure 3-19 shows an example of the difference in experimental results obtained for the cases of positive and negative remnant flux and the mean value obtained.

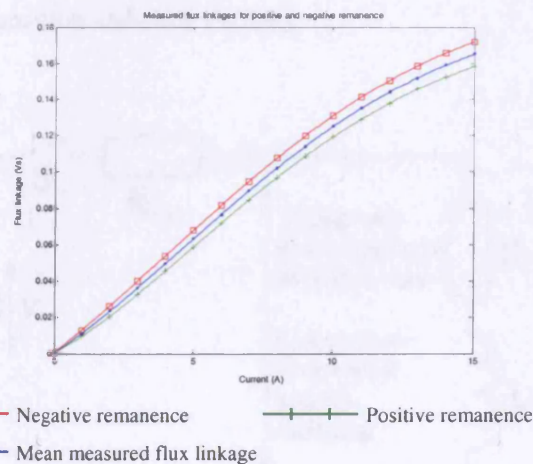


Figure 3-19 Example of measured flux linkages starting with positive and negative remnant flux

To ensure that remnant flux in the machine is of the correct polarity and magnitude for each test, the circuit of Figure 3-20 was used. The terminal connections to the winding are reversible to allow the polarity of excitation to be changed while an optional external forcing resistor,  $R_{ext}$ , could be added to further increase the rate of rise of current for a given applied voltage. Using this circuit the following procedure was implemented for each rotor position. By applying identical current pulses in either direction the magnitude of remnant flux linkage is made the same in each case.

1. Move rotor into desired position using dividing head
2. Switch polarity of excitation to positive
3. Apply 3 positive excitation pulses to ensure positive remnant flux linkage
4. Use 4th positive pulse to obtain flux linkage-current (positive remnant flux linkage)
5. Reverse polarity of excitation to negative
6. Apply 3 negative excitation pulses to ensure negative remnant flux linkage
7. Reverse polarity of excitation back to positive
8. Use 1st positive pulse to obtain flux linkage-current (negative remnant flux linkage)
9. Take average of flux linkages for positive and negative remnant flux linkage cases
10. Repeat for each position and each winding

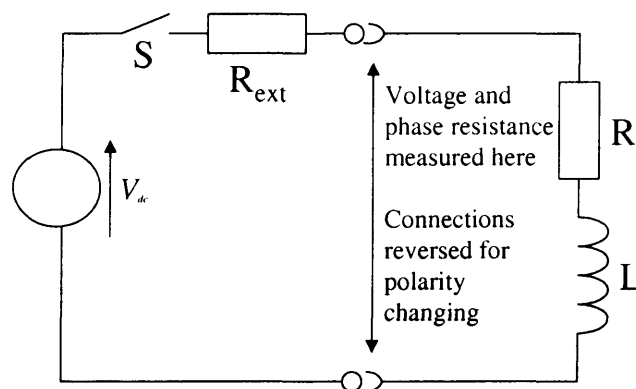
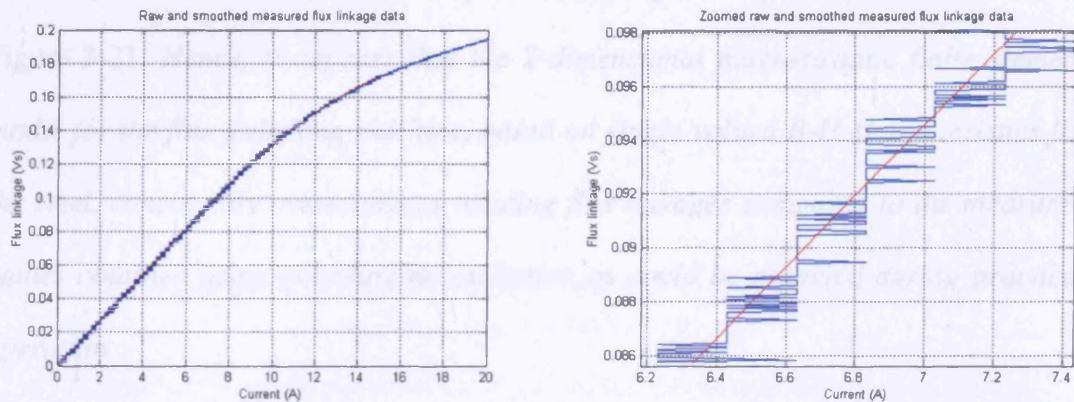


Figure 3-20 Schematic circuit used for flux linkage measurement

The voltages applied to the winding and its resistance were measured at the same point in the circuit and applied voltage and current were recorded using a digital storage oscilloscope. Using this data the flux linkage change from initial conditions as a function of current can be readily calculated. To obtain a smooth relationship free from quantisation noise introduced by the digital oscilloscope, a fifth order polynomial with zero intercept was fitted to the calculated data using the least squares method. Figure 3-21 shows an example of the flux linkage results obtained using the quantised oscilloscope data and the fitted polynomial, showing that it is a good fit to the data.



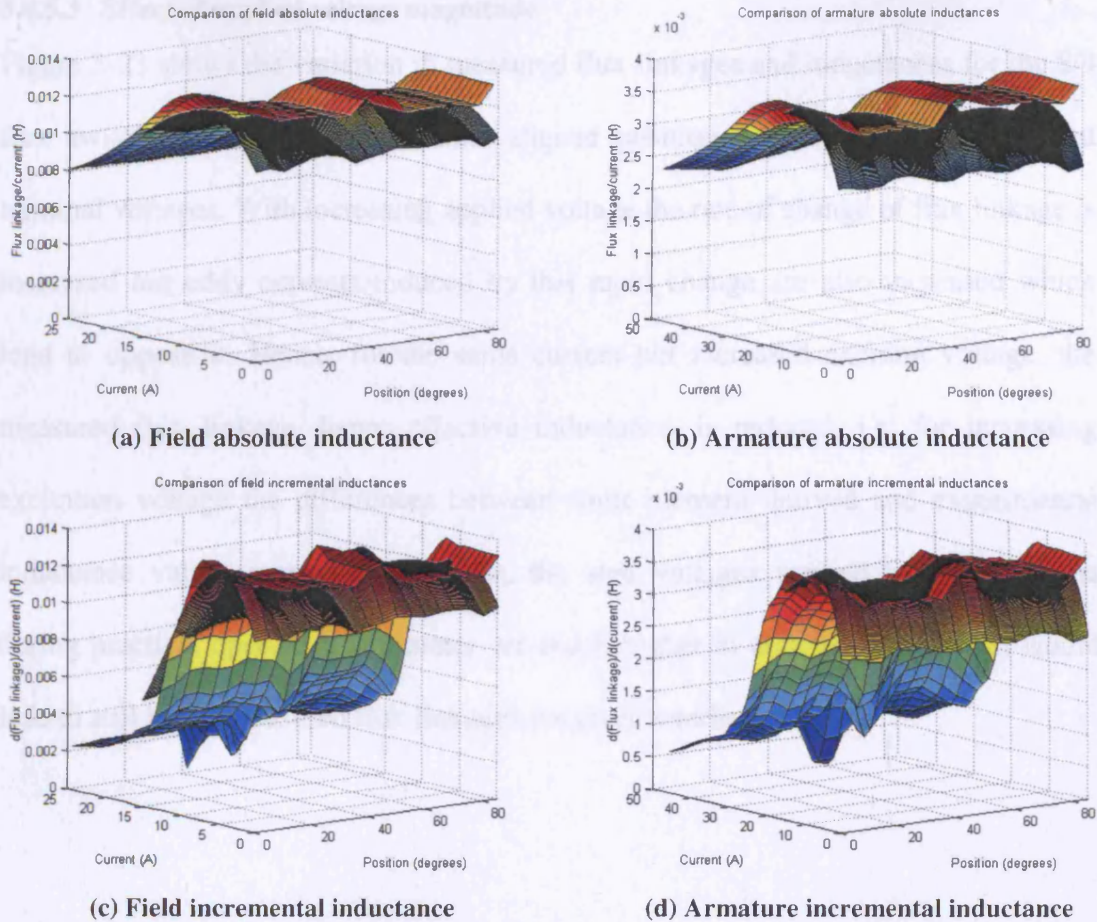
(a) Measured flux linkage data and polynomial smoothing

(b) Zoomed view of measured flux linkage data and polynomial smoothing

Figure 3-21 Example of measured flux linkage data smoothing using a fitted polynomial

### 3.4.5.2 Experimental results

Figure 3-22 shows a comparison between both absolute and incremental inductances obtained experimentally by the measurement of flux linkage/current characteristics and those derived from flux map B2. The experimental absolute inductance surfaces remain below the finite element derived inductances for all current and position combinations while incremental inductance values do exceed those derived from finite elements for some conditions although these surfaces are also generally below those obtained from finite elements. The curved shapes of the incremental inductances are due to the shape of the flux linkage-current relationship for low currents as it follows part of a minor hysteresis loop before joining the major loop as can be seen in Figure 3-21. *Hence, it appears that the 2-dimensional magnetostatic finite element model for the flux switching machine, based on single-valued B-H characteristics for the steel, consistently overestimates winding flux linkages compared to the measured values obtained using pulsating dc excitation as could be expected during practical operation.*

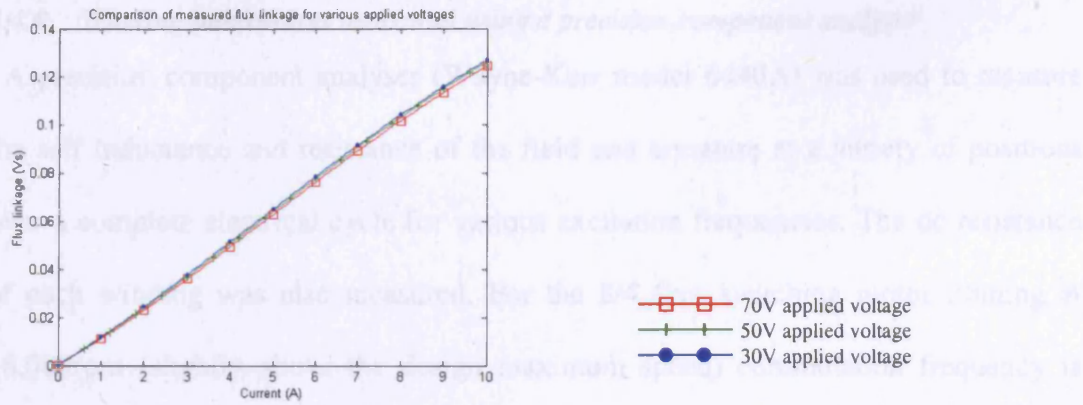


In each case the upper, flat, surfaces are obtained from finite element analysis and the lower, curved, surfaces from experimental results

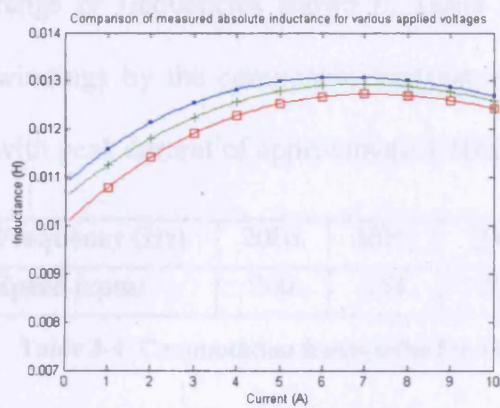
Figure 3-22 Comparison of inductances from experiment and finite element analysis

### 3.4.5.3 Effect of applied voltage magnitude

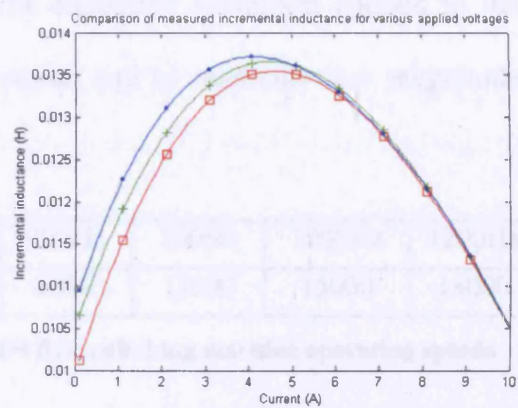
Figure 3-23 shows the variation in measured flux linkages and inductances for the 8/4 flux switching machine in the same aligned position but using different applied terminal voltages. With increasing applied voltage the rate of change of flux linkage is increased but eddy currents induced by this rapid change are also increased which tend to oppose it. Hence, for the same current but increased exciting voltage, the measured flux linkage, hence effective inductance, is reduced, i.e. for increasing excitation voltage the differences between finite element derived and experimental inductance values increases. However, the step voltages applied to the windings during practical operation as a motor are much higher at around 300V which would lead to still lower measured flux linkages for given winding currents.



(a) Effect of applied voltage on measured flux linkage



(b) Effect of applied voltage on measured absolute inductance



(c) Effect of applied voltage on measured incremental inductance

Figure 3-23 Effect of applied voltage on measured flux linkage and inductance

### 3.4.6 Winding inductances measured using a precision component analyser

A precision component analyser (Wayne-Kerr model 6440A) was used to measure the self inductance and resistance of the field and armature at a variety of positions over a complete electrical cycle for various excitation frequencies. The dc resistance of each winding was also measured. For the 8/4 flux switching motor running at 18,000rpm (slightly above the design maximum speed) commutation frequency is 1200Hz. Hence, the winding self inductances were measured in each position for the range of frequencies shown in Table 3-4. The excitation waveform applied to the windings by the component analyser is sinusoidal and of relatively low magnitude with peak current of approximately 100mA.

<b>Frequency (Hz)</b>	20Hz	50Hz	200Hz	400Hz	800Hz	1000Hz	1200Hz
<b>Speed (rpm)</b>	300	750	3000	6000	12000	15000	18000

**Table 3-4 Commutation frequencies for various 8/4 flux switching machine operating speeds**

Figure 3-24 shows the variation in measured inductance for each position and frequency. As expected the value of measured inductance in each position decreases as frequency is increased while the general shape of the inductance profile with varying position is also broadly as expected. However, the magnitude of measured inductance using the component analyser is much lower in all positions than that obtained by any other method examined.

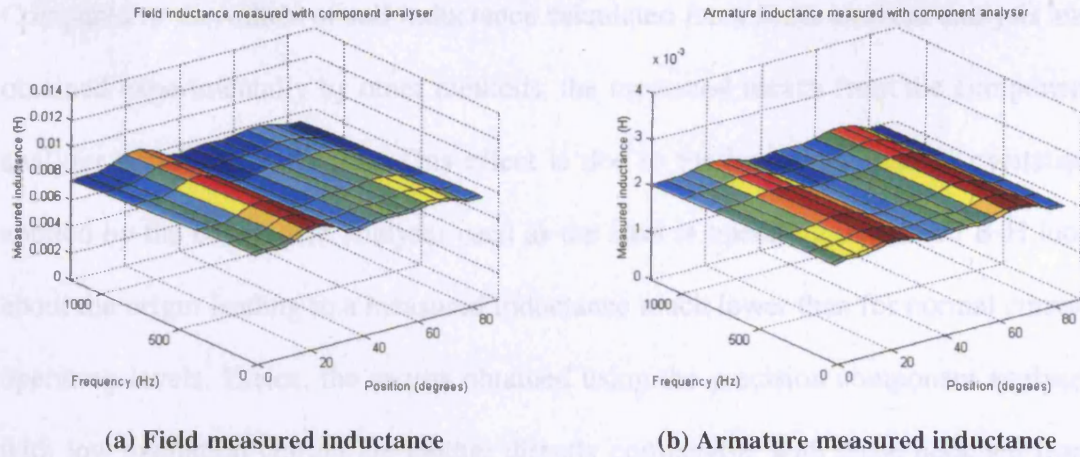


Figure 3-24 Inductances measured using precision component analyser

Table 3-5 compares the measured inductance values using the component analyser to those obtained from finite element analysis and experimentally using the simple time constant method for aligned and intermediate positions.

	0 deg	22.5 deg	45 deg	67.5 deg
<b>Field absolute inductance (FEA)</b>	13.7mH	12.8mH	13.6mH	12.3mH
<b>Field experimental from simple method</b>	11.99mH	11.34mH	12.21mH	11.56mH
<b>Field from component analyser at 20Hz</b>	8.16mH	8.9mH	8.10mH	8.39mH
<b>Armature absolute inductance (FEA)</b>	3.80mH	3.43mH	3.85mH	3.59mH
<b>Arm. experimental from simple method</b>	2.90mH	2.96mH	2.87mH	3.22mH
<b>Arm. from component analyser at 20Hz</b>	2.12mH	2.25mH	2.12mH	2.25mH

Table 3-5 Comparison of inductances obtained from simple time constant method and component analyser

Compared to the values of self inductance calculated from finite element analysis and obtained experimentally by other methods, the measured results from the component analyser are consistently low. This effect is due to the low magnitude of excitation applied by the component analyser used as the steel is operating in a small B-H loop about the origin leading to a measured inductance much lower than for normal current operating levels. Hence, the results obtained using the precision component analyser with low excitation current are neither directly comparable with those obtained from finite element analysis nor representative of normal operating conditions. *Hence, if a component analyser is to be used for measuring the winding inductances of a flux switching machine then it must incorporate a power amplifier stage which is capable of delivering peak current levels comparable to those encountered during operation at the desired frequency.*

### 3.4.7 Discussion

Using 2-dimensional magnetostatic finite element analysis to model a 3-dimensional system could generally be expected to produce an underestimate of flux linkage for given winding currents. In particular, neither end winding flux which does not cross the airgap nor additional flux in the steel end laminations due to coil overhang are included. Comparison of winding self inductances from finite element analysis and experiment has, however, shown that for the flux switching machine being tested finite element analysis yields consistently higher flux linkages than experimental measurements for given currents. Given that the 2-dimensional finite element model is geometrically accurate and numerically accurate, the main reason for this difference is the B-H characteristic used to describe the magnetic properties of the steel which is generally derived from the locus of the extrema of major hysteresis loops for sinusoidal excitation at a given frequency. Although it is a reasonable characterisation of the steel characteristics for many applications this B-H curve does not represent the behaviour of the steel in all conditions. For example the steel behind the field slots experiences only minor loop excitation with dc offset while the armature back iron and all parts of the rotor experience ac flux. Furthermore, under working conditions both windings are generally energised leading to extreme localised conditions and mutual coupling effects which cannot be readily obtained experimentally. Furthermore, the methods used to obtain winding self inductances were relatively simple and more satisfactory results may be obtained if a more rigorous method is employed [93]. *Hence, the simple experimental measurements of winding self inductances described have been shown to be generally unsuitable for calibration and correction of 2-dimensional magnetostatic finite element data for 3-dimensional effects.*

### 3.5 Summary and conclusions

The 'flux map' developed in this chapter is a coupled extension to the flux-mmF characterisation of switched reluctance machines, where mutual coupling is neglected, and fully describes the electromagnetic characteristics a given flux switching machine lamination geometry. Two methods were introduced for reducing the number of solutions required to obtain the flux map by finite element analysis, potentially reducing the computational overhead by 75%.

The differences between various finite element models were compared and it was shown that physical and geometric accuracy of the finite element model made more difference to the results obtained than increasing numerical accuracy of the solution. However, the differences are relatively small in each case. Hence, it is implied that, provided the finite element models are 'reasonable' and properly formulated then there is little benefit obtained by increasing model complexity, hence also computational expense.

A comparison was also made between winding self inductances obtained from finite element analysis and experimentally in order to try to quantify three-dimensional effects which are not included in 2-dimensional finite element analysis. However, it was shown that in this case it was not appropriate to use the experimental results obtained to calibrate the flux map in this way.

---

# **Chapter 4**

Electromagnetic data structure  
and conversion

---

## 4 ELECTROMAGNETIC DATA STRUCTURE AND CONVERSION

### 4.1 The need for electromagnetic data conversion

Finite element analysis calculates flux per unit stack length as a non-linear function of applied mmf, thus mmf is the independent variable and flux the dependent variable, from which flux linkage may be obtained as a function of current. However, the flux switching machine is generally voltage fed causing flux linkage to vary according to the applied terminal voltage while current follows as a result. Hence, as the basis for simulation of such conditions flux is required to be the independent variable with mmf the dependent variable. For the case of the switched reluctance machine where mutual coupling is neglected this conversion is simple as illustrated in Figure 4-1. Given the relationship

$$\Phi(F, \theta) \tag{4.1}$$

from finite element analysis where  $\Phi$  is flux per unit stack length,  $F$  is winding mmf and  $\theta$  is position, shown by the large arrows, the inverse relationship

$$F(\Phi, \theta) \tag{4.2}$$

required for voltage driven simulation is similarly obtained by interpolation as shown by the smaller arrows.

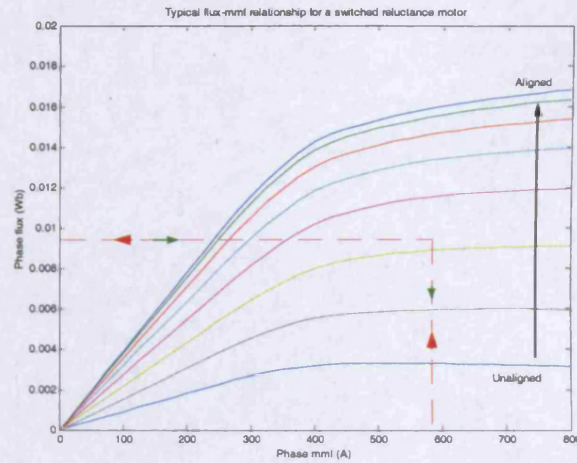


**Figure 4-1 Example flux-mmf characteristic and data conversion for a switched reluctance machine**

However, for the flux switching machine, or the switched reluctance machine where it is necessary to include the effects of mutual coupling, the flux in each winding is a non-linear function of mmf in both windings and position, thus finite element analysis gives the relationships

$$\Phi_f(F_f, F_a, \theta) \quad (4.3)$$

and

$$\Phi_a(F_f, F_a, \theta) \quad (4.4)$$

where the subscripts  $f$  and  $a$  represent field and armature respectively. Figure 4-2 shows an example of this relationship at an aligned position of negative mutual coupling. The conversion of fluxes from dependent into independent variables required a new technique to be developed.

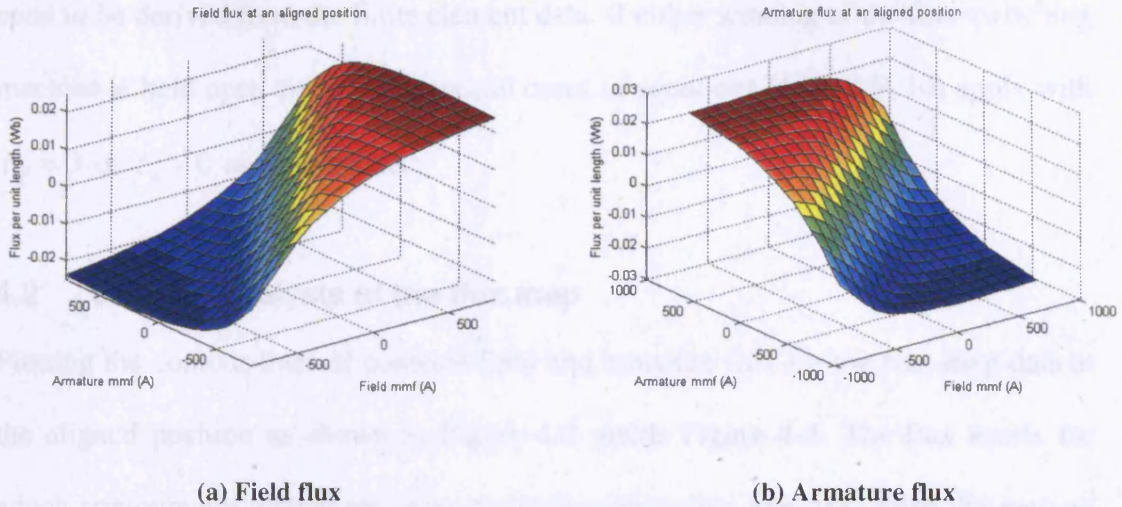


Figure 4-2 Flux surfaces at an aligned position of negative mutual coupling

Given the mutual coupling between windings it is possible to derive the flux or mmf of either field or armature given the other quantity for that winding and either quantity for the other winding, e.g. armature mmf may be derived as  $F_a(\Phi_f, \Phi_a, \theta)$  or  $F_a(F_f, \Phi_a, \theta)$ . Thus, to fully describe the electromagnetic properties of the flux switching machine in every case, the relationships

$$F_f(\Phi_f, \Phi_a, \theta) \tag{4.5}$$

$$F_a(\Phi_f, \Phi_a, \theta) \tag{4.6}$$

$$\Phi_f(F_f, \Phi_a, \theta) \tag{4.7}$$

$$F_a(F_f, \Phi_a, \theta) \tag{4.8}$$

$$F_f(\Phi_f, F_a, \theta) \tag{4.9}$$

$$\Phi_a(\Phi_f, F_a, \theta) \tag{4.10}$$

need to be derived from the finite element data. If either winding of the flux switching machine is held open circuit then special cases of equations (4.7) to (4.10) apply with  $F_f = 0$  or  $F_a = 0$  as appropriate.

## 4.2 Contour analysis of the flux map

Plotting the contour lines of constant field and armature flux for the flux map data at the aligned position as shown in Figure 4-2 yields Figure 4-3. The flux levels for which contours are plotted are to be the independent flux axes for which the derived quantities are calculated. Each contour line represents the continuum of field and armature mmf combinations which may be applied to the windings in order to give rise to the specified amount of flux in that winding. If a level of flux is chosen that is outside the range of values obtained from finite element data in that position then no contour will exist for that flux while the contour for zero flux will always pass exactly through the origin, i.e.  $F_f = F_a = 0$ .

The two strands of the bifilar armature winding are assumed to be 100% coupled, i.e. all flux which links one strand of the winding also links the other, and the flux calculated from finite element analysis and used in the flux map is that which passes through them both. Hence, calculated armature mmf is a superposition of the mmfs in each strand of the winding, i.e.  $F_a = F_{a1} + F_{a2}$  where  $F_a$  is resultant armature mmf and  $F_{a1}$ ,  $F_{a2}$  are the mmfs in each strand of the bifilar armature.

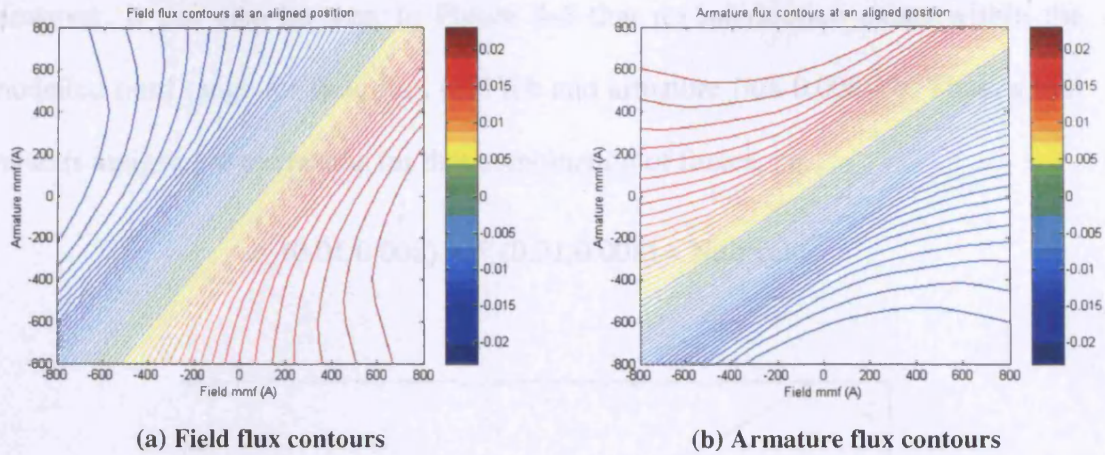


Figure 4-3 Flux contours at an aligned position of negative mutual coupling

#### 4.2.1 Obtaining $F_f(\Phi_f, \Phi_a, \theta)$ and $F_a(\Phi_f, \Phi_a, \theta)$

Given contours of specified constant flux for both field and armature, the combination of field and armature mmfs required to give rise to both desired fluxes simultaneously occurs at the intersection of these contour lines. However, in positions of strong mutual coupling there are a number of field and armature flux combinations which are not feasible and for which no such intersection of contours exists. This process is illustrated in Figure 4-4. In the example shown the rotor is in an aligned position of negative mutual coupling. The contours of field flux 0.01Wb and armature flux -0.005Wb intersect at the point (301.3,129.1) which corresponds to the field and armature mmfs respectively which give rise to this combination of fluxes. Hence,

$$F_f(0.01, -0.005, \theta) = 301.3A$$

and

$$F_a(0.01, -0.005, \theta) = 129.1A$$

where  $F_f$  and  $F_a$  are field and armature mmfs respectively and  $\theta$  is rotor position.

However, it can also be seen in Figure 4-4 that no intersection exists within the modelled mmf range for field flux 0.01Wb and armature flux 0.008Wb. Thus, a null value is assigned to the results for that combination of fluxes, i.e.

$$F_f(0.01,0.008) = F_a(0.01,0.008) = \text{Null value}$$

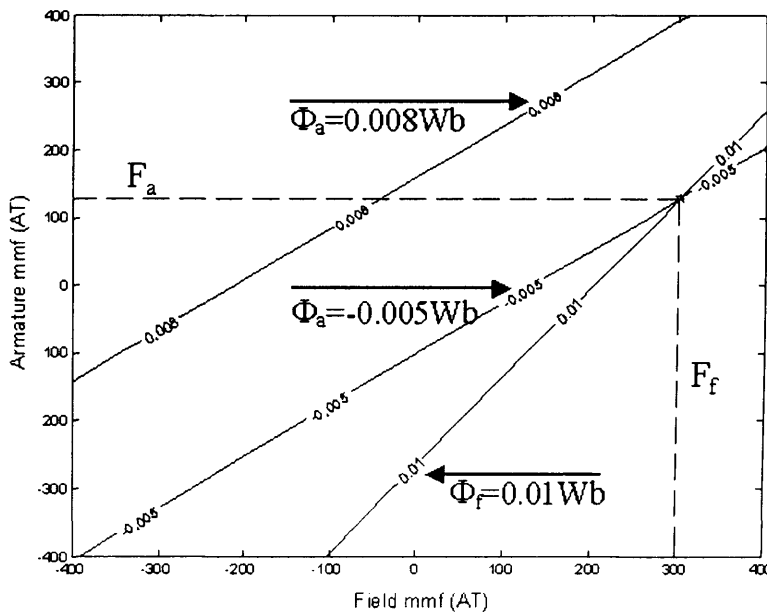


Figure 4-4 Example of data conversion process by finding intersections of flux contours

Figure 4-5 shows an example of the field and armature flux surfaces for an idealised case of zero mutual coupling. In this case all flux contours are straight lines parallel to the mmf axes, the intersections of which may be readily obtained. In the event that all the flux linking one winding also links the other in either positive or negative sense, i.e.  $\pm 100\%$  mutual coupling or  $\Phi_a = \pm \Phi_f$ , the contours for field and armature flux would become collinear and no unique solution would exist for the winding mmfs required to give rise to that flux. In such a case field and armature mmfs superimpose and the continuum of feasible solutions would be a straight line of the form

$$F_f + F_a = \text{constant} \tag{4.11}$$

where  $F_f$  and  $F_a$  are field and armature mmfs respectively. However, this condition does not generally arise in practice for the flux switching machine and in practical flux switching machine designs mutual coupling does not generally exceed 80%

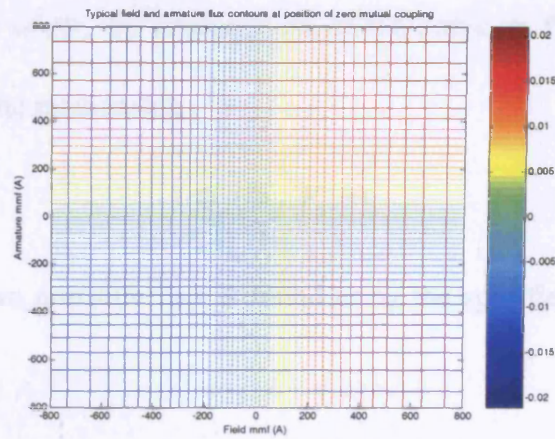
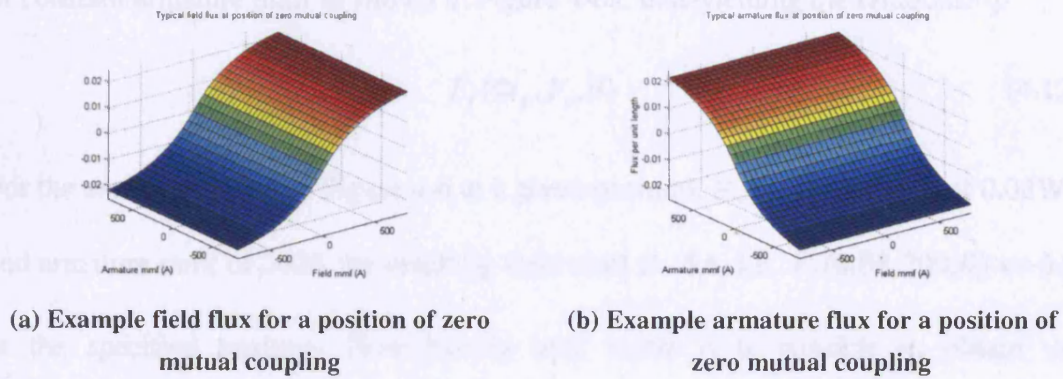


Figure 4-5 Example of flux surfaces and contours for a position of zero mutual coupling

Thus, by obtaining the intersections of contours of constant flux at each position winding mmfs are obtained as a function of winding fluxes and position. This conversion process is carried only once on the flux map data as it is obtained from finite element analysis for each lamination geometry.

### 4.2.2 Obtaining $F_f(\Phi_f, F_a, \theta)$ and $\Phi_a(\Phi_f, F_a, \theta)$

Given independent values for  $\Phi_f$  and  $F_a$  the unique value of  $F_f$  which gives rise to this condition occurs at the intersection of the contour of constant field flux and line of constant armature mmf as shown in Figure 4-6a, thus yielding the relationship

$$F_f(\Phi_f, F_a, \theta) \quad (4.12)$$

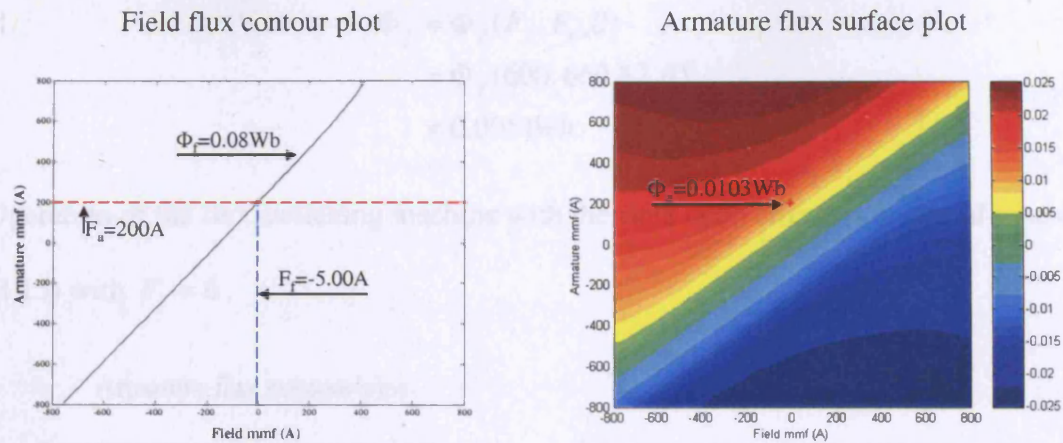
For the example shown in Figure 4-6 at a given position,  $\theta$ , for a field flux of 0.08Wb and armature mmf of 200A the resulting field mmf is -5A, i.e.  $F_f(0.08, 200, \theta) = -5A$  in the specified position. Now having both mmfs it is possible to obtain the corresponding value of  $\Phi_a$  by interpolation of the armature flux data as shown in Figure 4-6b to give the relationship

$$\Phi_a(\Phi_f, F_a, \theta) \quad (4.13)$$

In the example shown armature flux is found using the specified armature mmf and derived field mmf

$$\begin{aligned} \Phi_a &= \Phi_a(F_f, F_a, \theta) \\ &= \Phi_a(-5, 200, \theta) \\ &= 0.0103Wb \end{aligned}$$

Operation of the flux switching machine with the armature open circuit is a special case of (4.13) with  $F_a = 0$ .



(a) Example of finding field mmf by intersection of field flux contour and line of constant armature mmf

(b) Example of finding corresponding armature flux given known armature mmf and derived field mmf

Figure 4-6 Example of obtaining field mmf and armature flux given known armature mmf and field flux

### 4.2.3 Obtaining $F_a(F_f, \Phi_a, \theta)$ and $\Phi_f(F_f, \Phi_a, \theta)$

In a similar manner to obtaining  $F_f(\Phi_f, F_a, \theta)$  and  $\Phi_a(\Phi_f, F_a, \theta)$  detailed above, given independent values for  $F_f$  and  $\Phi_a$  the unique value of  $F_a$  which gives rise to this condition occurs at the intersection of the contour of constant armature flux and line of constant field mmf, thus yielding the relationship

$$F_a(F_f, \Phi_a, \theta) \tag{4.14}$$

and the corresponding value of

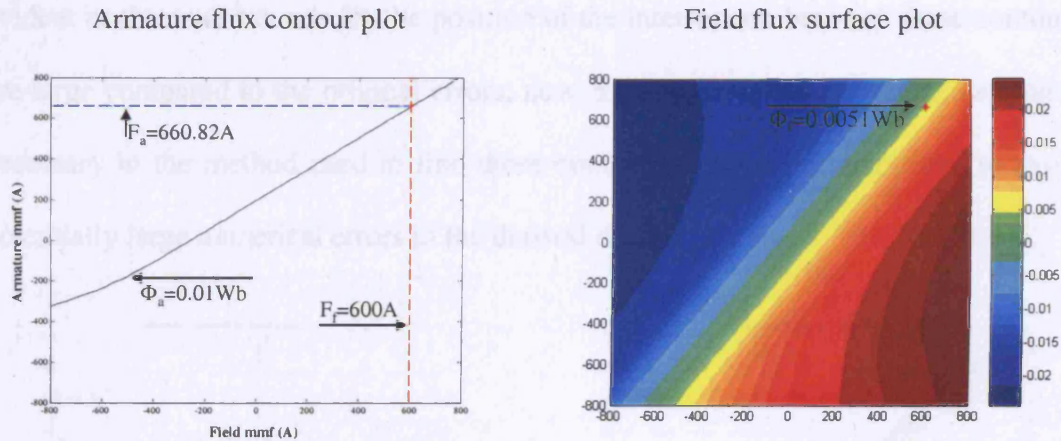
$$\Phi_f(F_f, \Phi_a, \theta) \tag{4.15}$$

is obtained using the derived value of  $F_a$ .

For the example shown in Figure 4-7 for a armature flux of 0.01Wb and field mmf of 600A the resulting armature mmf is -660.82A, i.e.  $F_a(600, 0.01, \theta) = -660.82A$  and derived armature mmf is

$$\begin{aligned}\Phi_f &= \Phi_f(F_f, F_a, \theta) \\ &= \Phi_f(600, 660.82, \theta) \\ &= 0.0051 \text{ Wb}\end{aligned}$$

Operation of the flux switching machine with the field open circuit is a special case of (4.15) with  $F_f = 0$ .



(a) Example of finding armature mmf by intersection of armature flux contour and line of constant field mmf

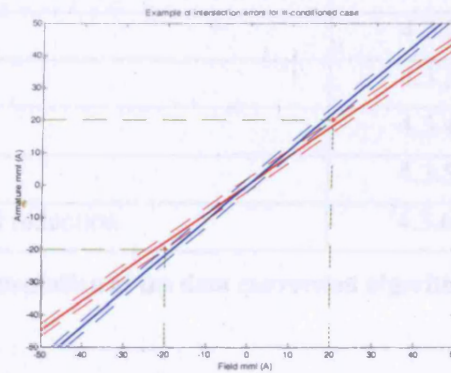
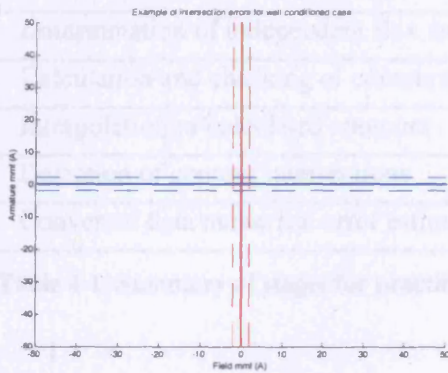
(b) Example of finding corresponding field flux given known field mmf and derived armature mmf

Figure 4-7 Example of obtaining armature mmf and field flux given known field mmf and armature flux

#### 4.2.4 Numerical inaccuracy in positions of strong mutual coupling

In positions where the windings are strongly mutually coupled in either sense, i.e. most of the flux linking one winding also links the other, the contour lines of constant winding fluxes are close to alignment and the data conversion process becomes numerically ill-conditioned, i.e. small errors in the input data may cause large errors in the output.

In Figure 4-8a a pair of hypothetical flux contours which represent a position of zero mutual coupling are shown with error bounds of  $\pm 2A$ . For this case the maximum potential error in contour intersection point is also  $\pm 2A$  on each axis. Figure 4-8b shows hypothetical flux contours representing a position of strong mutual coupling also with  $\pm 2A$  error bounds. For this case the effects of numerical ill-conditioning are evident as the error bounds for the position of the intersection between these contours are large compared to the original errors, now  $\pm 20A$  on each axis. Hence, caution is necessary in the method used to find these contours and their intersections to avoid potentially large numerical errors in the derived data.



(a) Error bounds of intersection for contours with small error at a position of zero mutual coupling

(b) Error bounds of intersection for contours with small error at a position of strong mutual coupling

————— Contour line    - - - - -  $\pm 2A$  error bounds

Figure 4-8 Errors in contour intersection for positions of zero and strong mutual coupling

### 4.3 Practical implementation of data conversion algorithms

The algorithms described in the previous section to obtain the complete set of relationships which describe the electromagnetic characteristics of the lamination geometry have been implemented in the MATLAB programming environment [61]. To implement the developed data conversion algorithm for practical data a number of processes are required to check and condition the input data, perform the conversion process and check the output data. Table 4-1 summarises the main steps carried out for practical implementation which are detailed individually.

<b>Implementation stage</b>	<b>Section</b>
1 Interpolation of flux map data	4.3.1
2 Determination of independent flux axes	4.3.2
3 Calculation and checking of contours	4.3.3
4 Interpolation of calculated contours	4.3.4
5 Detection of contour intersections	4.3.5
6 Converted data numerical error estimation and reduction	4.3.6

**Table 4-1 Summary of stages for practical implementation of the data conversion algorithm**

### 4.3.1 Interpolation of flux map data onto finer axes

1	Interpolation of flux map data
2	Determination of independent flux axes
3	Calculation and checking of contours
4	Interpolation of calculated contours
5	Detection of contour intersections
6	Converted data numerical error estimation and reduction

As the number of finite element solutions used to generate the flux map is kept to a minimum to limit computational cost and the effects of small random errors, the flux data available is on relatively coarse mmf axes. However, contour lines obtained from MATLAB are in the format of a number of points, each where the contour line crosses an axis value [61]. Figure 4-9a shows an example of a set of flux contours and the points which define them for an aligned position using flux map data with mmf ranges from  $-800\text{A}$  to  $800\text{A}$  at  $100\text{A}$  intervals. Figure 4-9b shows the contours obtained for the same flux surface which has been interpolated onto finer mmf axes with  $25\text{A}$  spacing, showing the corresponding increase in number of defining points for each contour. Interpolating the flux map data onto finer mmf axes prior to conversion slightly increases the computational investment required for conversion but can reduce the amount of interpolation required, hence execution time, at the point of use for simulation and also makes contour interpolation more reliable as will be shown in section 4.3.3.

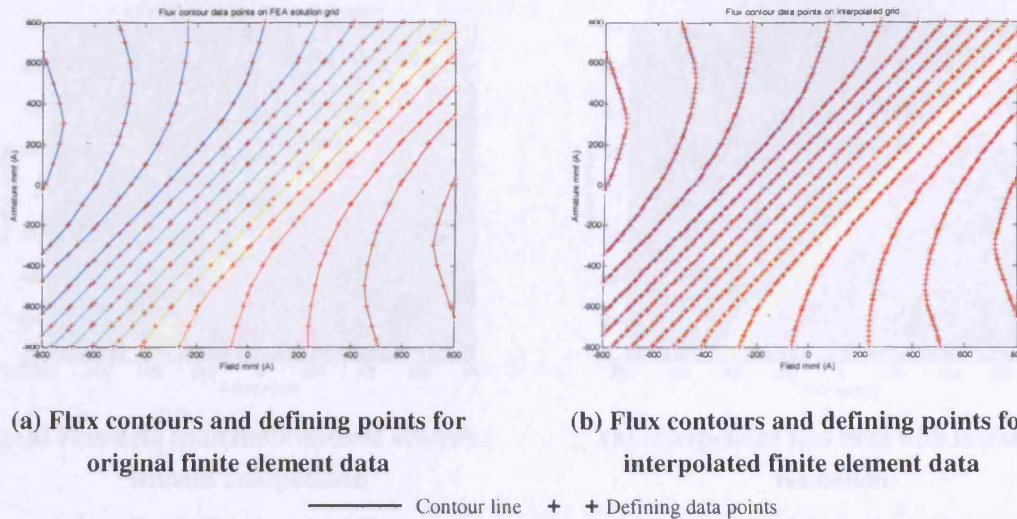
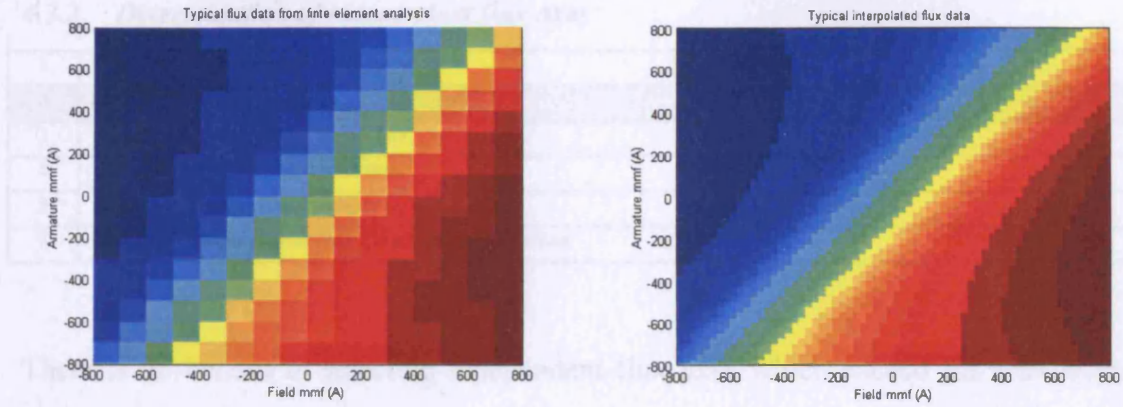


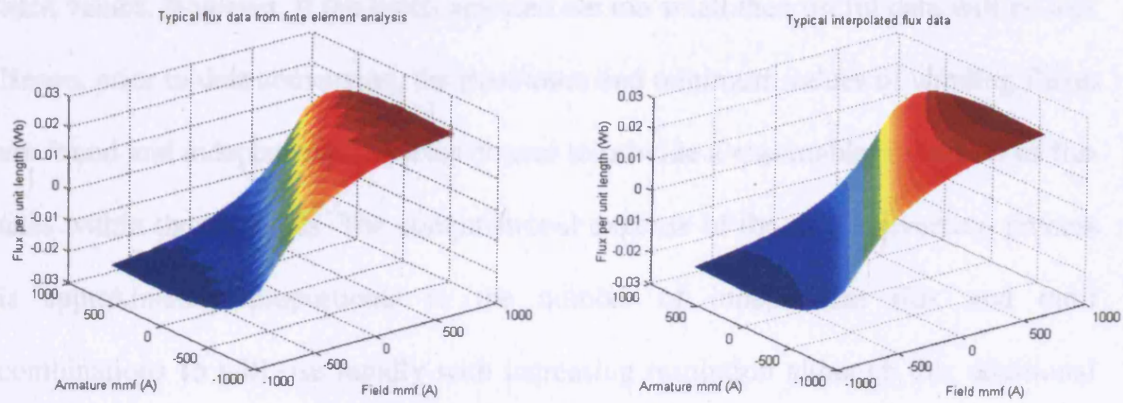
Figure 4-9 Example of increased contour defining points by finite element data interpolation

A number of 2-dimensional interpolation algorithms are available in MATLAB and 2 were examined, linear and bi-cubic. Linear interpolation is the simplest type and computationally least demanding but, due to the non-linear nature of the flux data, is not suitable for this application. Bi-cubic interpolation [61] was found to perform well as it is capable of smoothing the interpolated data without overshoot while passing exactly through all finite element data points. Figure 4-10 shows an example of a the grid of mmf values defining a typical flux surface and the resulting flux surface for an aligned position before and after interpolation. The number points defining the flux surface is far greater after interpolation and such an increase in the number of finite element solutions would be neither computationally efficient nor necessarily lead to increased accuracy as discussed in chapter 3.



(a) Flux data from finite element analysis without interpolation

(b) Interpolated flux data with increased resolution



(c) Flux data from finite element analysis without interpolation

(d) Interpolated flux data with increased resolution

Figure 4-10 Example of finite element data interpolation to increase flux data resolution

### 4.3.2 Determination of independent flux axes

1	Interpolation of flux map data
2	Determination of independent flux axes
3	Calculation and checking of contours
4	Interpolation of calculated contours
5	Detection of contour intersections
6	Converted data numerical error estimation and reduction

There is no benefit in selecting independent flux axes which exceed the maximum flux present in the finite element data as contours of constant flux will not exist for such values. However, if the limits selected are too small then useful data will be lost. Hence, prior to data conversion, the maximum and minimum values of winding fluxes are found and independent flux axes chosen to provide a reasonable resolution of flux axes within these bounds. The computational expense of the data conversion process is approximately proportional to the number of independent flux and mmf combinations so will rise rapidly with increasing resolution although this additional investment may be repaid by simpler interpolation at the point of use.

### 4.3.3 Calculation and reliability testing of contours

1	Interpolation of flux map data
2	Determination of independent flux axes
3	Calculation and checking of contours
4	Interpolation of calculated contours
5	Detection of contour intersections
6	Converted data numerical error estimation and reduction

Contour line data is obtained as a series of data points where the line of constant flux crosses each axis value. Hence, interpolating the finite element flux data onto fine mmf axes before evaluating contours yields contour lines each with more defining points as introduced in section 4.3.1. This effect is particularly important for flux values near to the maximum flux value present in each position where the number of points defining such contour lines would otherwise be very low, thus allowing reliable use of that contour for data conversion.

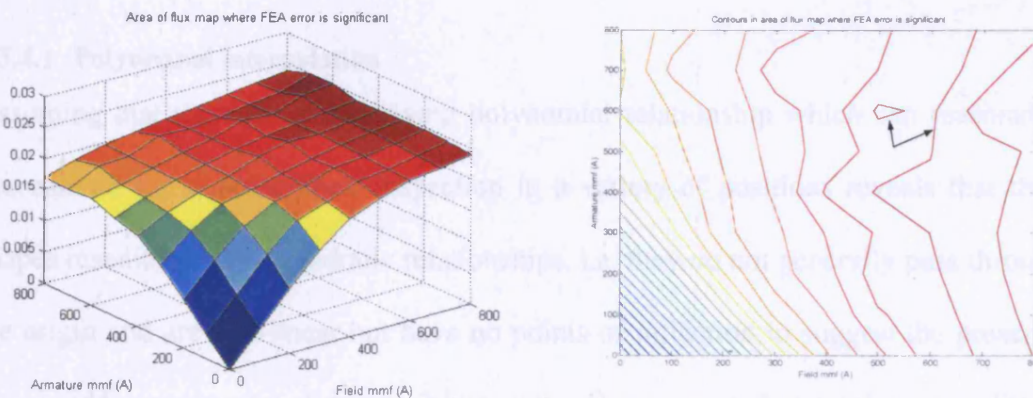
Simple checks can be made to detect contour lines which are definitely not reliable and should not be used for conversion. Any contour which does not meet all of the criteria for reliability cannot reasonably be used for data conversion as this would lead to potentially very unreliable results. Hence, when a contour fails any test it is removed and set to an empty state to be treated by all subsequent operations as though it had never existed. In this way a small amount of useful information may be lost from the converted data but confidence in the quality of converted data is increased as a consequence, even at its extremes.

#### 4.3.3.1 Number of points

If a contour line has only a small number of points defining it then it may be unreliable as there is not enough information to reasonably predict its behaviour. This is particularly important if a polynomial function is to be fitted to the contour line as, in general, for a fitted polynomial of degree  $n$  an absolute minimum of  $n+1$  points are required in order to properly describe it. However, if extrapolation is also to be performed using this fitted polynomial then a much higher number of data points are required to maintain reliability. Hence, by interpolating the flux surfaces at each position onto finer mmf axes as described in section 4.3.1, the number of points defining each contour are increased and several contour lines which would otherwise have been defined by too few points to be reliably used may now be included in the conversion process with some confidence. Hence, during the data conversion process every contour line must be defined by a specified minimum number of data points. A high limit means that more useful information is potentially discarded but also more confidence may be placed in the converted data.

### 4.3.3.2 Number of line segments

It has been noted in chapter 3 that under conditions of heavy saturation the data obtained from finite element analysis can become unreliable as numerical errors become comparable to the difference between adjacent solutions, producing a 'bumpy' flux surface as shown in Figure 4-11a. For large flux values where this effect becomes apparent such surface characteristics lead to multiple contour lines for the same flux value as shown in Figure 4-11b. Thus, the finite element data in these regions is unreliable and the affected contours cannot be meaningfully interpolated. Therefore, any flux contour comprising more than one line segment is rejected. Furthermore, it can also be seen that the contours in this region are jagged which also indicates that there is significant error present although this is more difficult to reliably detect automatically.



(a) Example region of the flux map where finite element analysis error is significant (b) Flux contours for the same region showing multiple line segments for one flux value

Figure 4-11 Example of number of line segments as reliability test for flux contours

#### 4.3.4 Interpolation of contour lines

1	Interpolation of flux map data
2	Determination of independent flux axes
3	Calculation and checking of contours
4	Interpolation of calculated contours
5	Detection of contour intersections
6	Converted data numerical error estimation and reduction

As the contours of constant flux have the format of a series of data points the underlying function for the behaviour of the contour in between these points is not known. Hence, in order to search for intersections of contour lines, they must be interpolated and the intersections of the resulting functions found. There are a number of alternative interpolation algorithms available and, in order to quantify the effects of this choice two different types have been implemented for comparison- quadratic polynomial and piecewise cubic hermite interpolating polynomial (PCHIP) [61].

##### 4.3.4.1 Polynomial interpolation

Assuming that there is an underlying polynomial relationship which can reasonably describe all the contour lines, inspection in a variety of positions reveals that their shapes resemble that of quadratic relationships, i.e. they do not generally pass through the origin and are non-linear but have no points of inflection to suggest the presence of any odd power terms of degree 3 or greater. Hence, a quadratic polynomial fitting function of the form

$$ax^2 + bx + c \quad (4.16)$$

may be used where  $x$  is the independent axis variable and the coefficients  $a-c$  are calculated to provide a least squared error fit of the fitting polynomial to the contour line data points.

The fitted polynomial is not constrained to pass directly through contour data points. Hence, the effects of small random errors caused by both finite element analysis and contour line evaluation on the fitted polynomial and, in turn, converted data are potentially reduced. This property provides potential benefit in cases of heavy saturation where finite element analysis numerical errors compared to the difference between solutions, hence resulting random errors in contour line data, are largest. By applying a line of best fit through such points the fitted polynomial can be a reasonable fit to the actual contour, although numerical errors in such regions make the data potentially less reliable than that in the rest of the flux map.

Furthermore, as the fitted polynomials are continuous analytic functions, it is possible to evaluate them for values beyond the finite element analysis modelled limits. Therefore, assuming that the fitted polynomials reasonably describe the contour lines within the modelled region and that enough data points have been specified to adequately define the behaviour of the polynomial, it is possible to search for intersections of extrapolated polynomials, thus extending the effective range of data available for some conditions.

#### **4.3.4.2 PCHIP interpolation**

In contrast to least squared error polynomial interpolation, piecewise cubic hermite interpolating polynomial (PCHIP) interpolation operates by fitting a number of cubic functions to each section of the data which join together to form a continuous fitted waveform which passes exactly through all data points. This is similar to spline interpolation [61] but the fitting polynomials are selected in order to maintain the monotonicity and local extrema of the data, i.e. PCHIP interpolation will not result in overshoot of the fitted function.

It is not possible to extrapolate PCHIP fitted functions, thus requiring that the flux map must include the full extent of mmf ranges which are required to be simulated. However, the interpolated function passes directly through all finite element data points and no prior knowledge is required of the form of analytic function which reasonably fits the contour data. In heavily saturated regions, where finite element analysis error is largest compared to the difference between solutions, unreliable contour lines must be reliably detected and rejected. If they are not, then PCHIP interpolation will fit a function exactly through the contour data points and erroneous intersection points will be obtained.

#### 4.3.5 Detection of contour intersections

1	Interpolation of flux map data
2	Determination of independent flux axes
3	Calculation and checking of contours
4	Interpolation of calculated contours
5	Detection of contour intersections
6	Converted data numerical error estimation and reduction

An inspection of the contour lines of equal flux for each winding over a complete electrical cycle shows that they behave in an oscillatory manner between positions of positive and negative mutual coupling as shown in Figure 4-12.

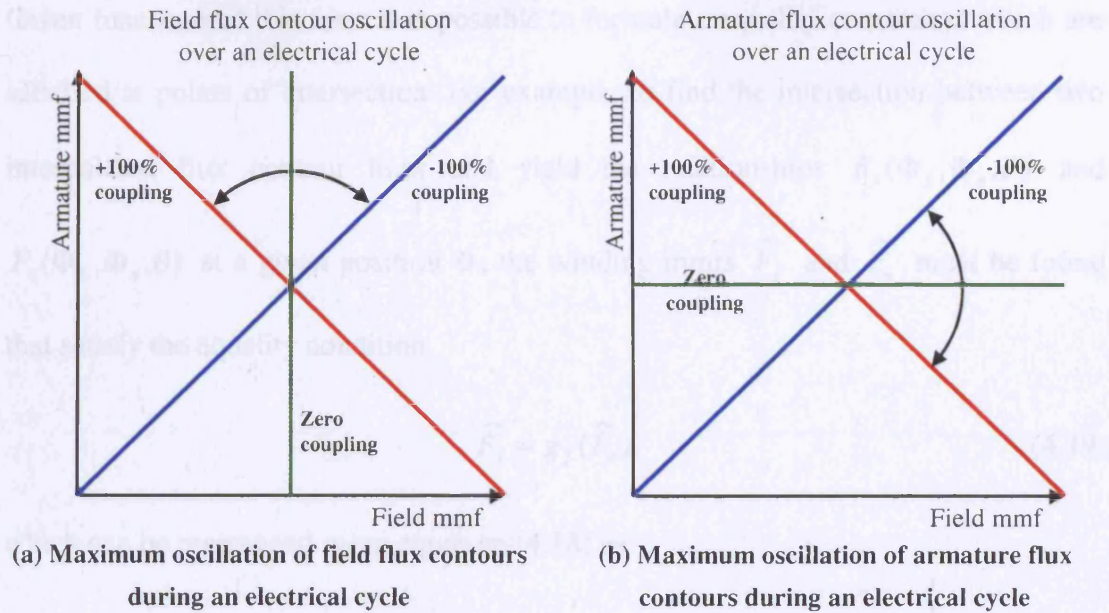


Figure 4-12 Flux contour oscillations during a complete electrical cycle

Hence, in order to interpolate the contour data points using functions of the form  $y = f(x)$ , where  $x$  is the independent mmf axis variable and  $y$  is the fitted contour line, contours of constant field flux must be interpolated in the form

$$F_f = g_f(F_a) \quad (4.17)$$

while armature flux contours must be interpolated in the form

$$F_a = g_a(F_f) \quad (4.18)$$

where  $F$  is mmf, subscripts  $f$  and  $a$  refer to field and armature,  $g_f$  and  $g_a$  are contour interpolating functions for field and armature respectively obtained using either interpolation method described in section 4.3.4.

Given functions of this form it is possible to formulate equality constraints which are satisfied at points of intersection. For example, to find the intersection between two interpolated flux contour lines and yield the relationships  $F_f(\Phi_f, \Phi_a, \theta)$  and  $F_a(\Phi_f, \Phi_a, \theta)$  at a given position  $\theta$ , the winding mmfs  $\widehat{F}_f$  and  $\widehat{F}_a$  must be found that satisfy the equality condition

$$\widehat{F}_f = g_f(\widehat{F}_a) \quad (4.19)$$

which can be rearranged using equation (4.18) as

$$\widehat{F}_f = g_f \{g_a(\widehat{F}_f)\} \quad (4.20)$$

the solution to which may be found using a numerical search method and  $\widehat{F}_a$  readily obtained using equation (4.18). The same results may also be obtained by a similar process, finding  $\widehat{F}_a$  by numerical search instead. Figure 4-13 illustrates this process. In Figure 4-13a the estimate of field mmf,  $F_f$ , is too low and the equality requirement of equation (4.20) is not met. However, in Figure 4-13b where  $F_f = \widehat{F}_f$  the equality requirement is met, indicating that an intersection has been found.

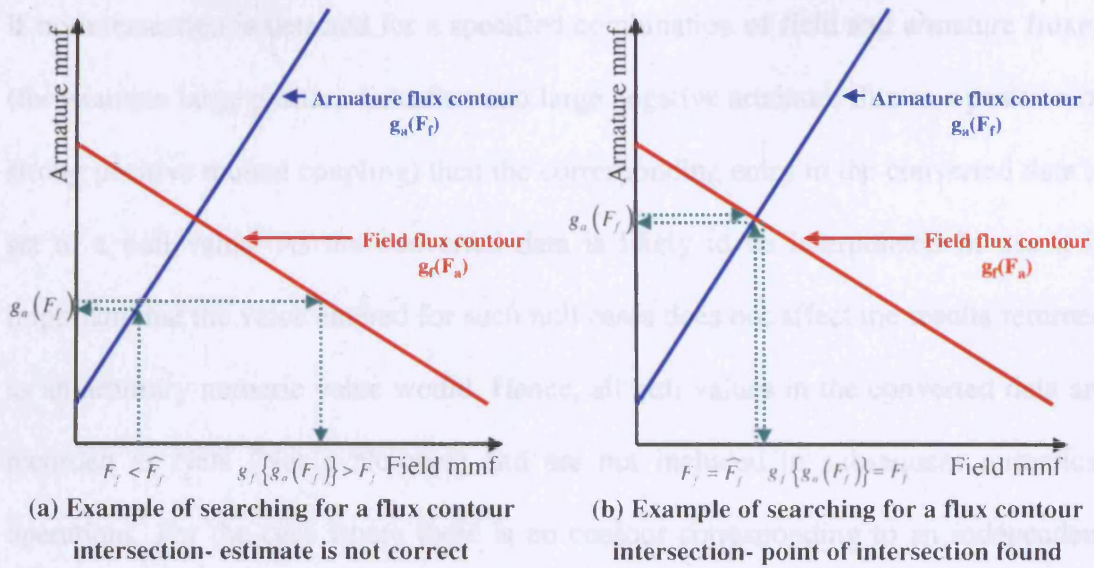


Figure 4-13 Example of the search process for finding a contour intersection

The entire set of relationships which describe the electromagnetic properties of the lamination may be found using a similar process to find the required intersections. Table 4-2 summarises the equality constraints to be satisfied in each case at the intersection and the function used to obtain the remaining required value.

Converted data	Equality constraint
$F_f(\Phi_f, \Phi_a), F_a(\Phi_f, \Phi_a)$	$F_f = g_f \{g_a(F_f)\}$ at intersection, $F_a = g_a(F_f)$
$F_f(\Phi_f, F_a), \Phi_a(\Phi_f, F_a)$	$F_f = g_f(F_a), \Phi_a = \Phi_a(F_f, F_a)$
$F_a(F_f, \Phi_a), \Phi_f(F_f, \Phi_a)$	$F_a = g_a(F_f), \Phi_f = \Phi_f(F_f, F_a)$

Table 4-2 Objective functions to be satisfied at points of intersection for data conversion

If no intersection is detected for a specified combination of field and armature fluxes (for example large positive field flux and large negative armature flux in a position of strong positive mutual coupling) then the corresponding entry in the converted data is set to a null value. As the converted data is likely to be interpolated in use it is important that the value entered for such null cases does not affect the results returned as an arbitrary numeric value would. Hence, all null values in the converted data are recorded as NaN (Not a Number) and are not included in subsequent numerical operations. For the case where there is no contour corresponding to an independent flux level then by inspection all converted data entries corresponding to that value of flux are set to NaN.

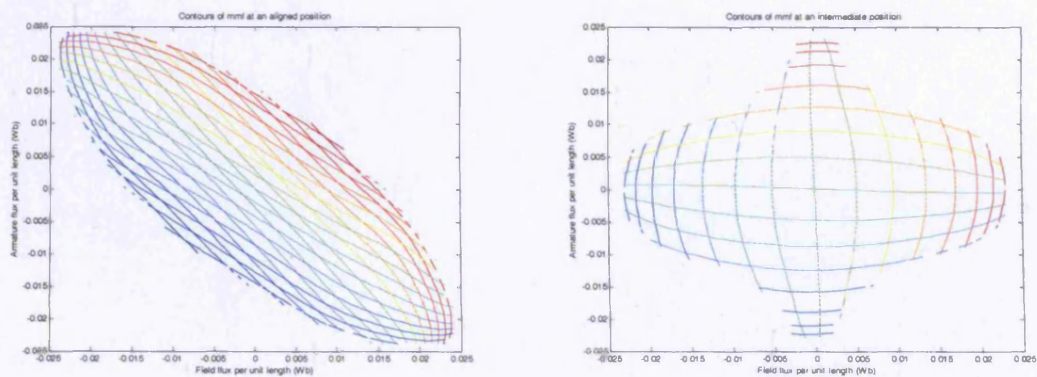
#### 4.3.6 *Converted data numerical error estimation and reduction*

1	Interpolation of flux map data
2	Determination of independent flux axes
3	Calculation and checking of contours
4	Interpolation of calculated contours
5	Detection of contour intersections
6	Converted data numerical error estimation and reduction

Due to the amount of interpolation used during the data conversion process it is reasonable to assume that a degree of numerical error is introduced into the converted data. The main factors affecting the amount of such error are the resolution of the flux map mmf axes and choice of interpolation methods used. Hence, a method has been developed for estimating the degree of numerical error introduced by the data conversion process, without recourse to further finite element analysis, along with a method of reducing the potential effects.

#### 4.3.6.1 Numerical error estimation algorithm

The transformation of winding mmfs from dependent into independent variables has been carried out by searching for intersections of contours of constant flux as detailed in sections 4.2.1 and 4.3.5, making winding fluxes the dependent variables. As noted above this process is likely to have introduced some degree of numerical error into the converted data. However, the same process may be repeated using the contours of constant winding mmf to transform winding mmfs back into independent variables, with fluxes dependent, i.e. returning to the original data format. Figure 4-14 shows examples of the contours of constant winding mmfs obtained for an aligned and an intermediate position. Not all of the original finite element data can be retrieved due to some contours being rejected as potentially unreliable during both conversion processes. However, a comparison of this reconstructed data with the original flux map data gives a reasonable measure of the numerical errors introduced by the conversion process largely independently of the original flux map used.



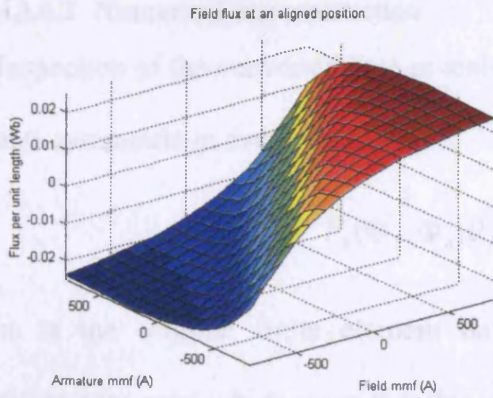
(a) Contours of mmf for an aligned position of negative mutual coupling

(b) Contours of mmf for an intermediate position of minimum mutual coupling

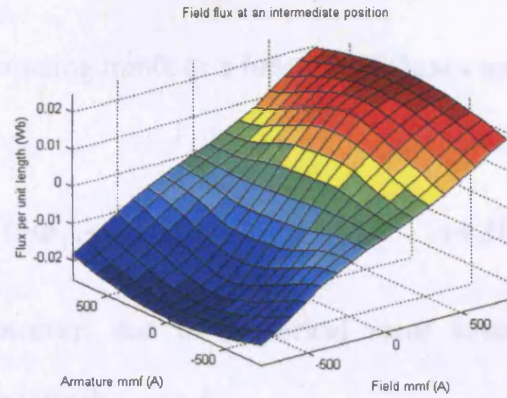
Figure 4-14 Example derived contours of mmf at an aligned and an intermediate position

In positions of strong mutual coupling where the flux contours are numerically ill-conditioned, the mmf contours are also ill-conditioned and vice-versa. Hence, similar numerical errors are introduced twice, once during each conversion process, and the resulting error estimate gives a reasonable comparison between the errors introduced by the process in each position.

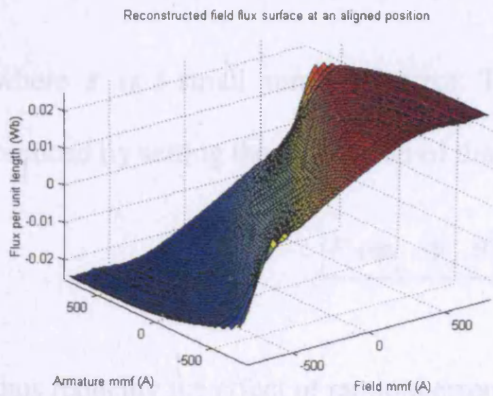
Figure 4-15 shows an example of the original field flux surface, the reconstructed field flux surface and numerical error estimate, i.e. the difference between them, for an aligned and an intermediate position using quadratic polynomial interpolation of contours. Comparison of the two shows that the conversion process at the aligned position has introduced larger estimated errors due to numerical ill-conditioning as expected. The larger estimated errors around the periphery of the mmf range in both positions is mainly due to less reliable interpolation of the flux contours in these regions which are defined by fewer points.



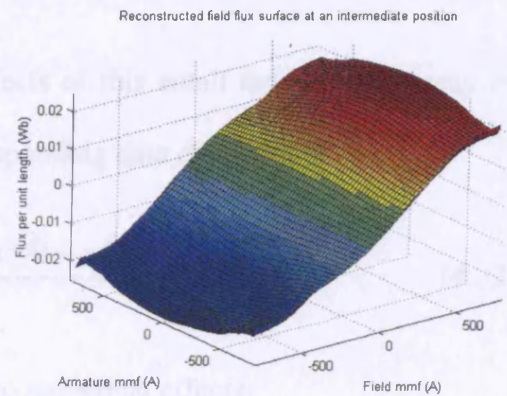
(a) Field flux from finite element analysis at an aligned position



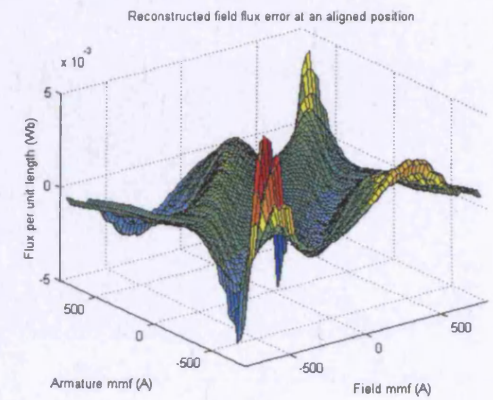
(b) Field flux from finite element analysis at an intermediate position



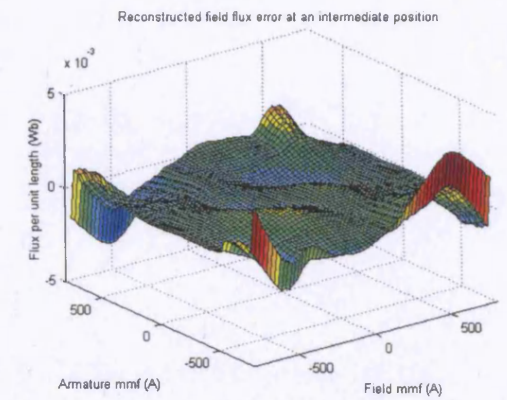
(c) Reconstructed field flux at an aligned position



(d) Reconstructed field flux at an intermediate position



(e) Error in reconstructed field flux at an aligned position



(f) Error in reconstructed field flux at an intermediate position

Figure 4-15 Example of flux reconstruction as a numerical error estimator at an aligned and an intermediate position

#### 4.3.6.2 Numerical error reduction

Inspection of the converted data reveals that winding mmfs as a function of fluxes are anti-symmetric in every position, i.e.

$$F_x(\Phi_f, \Phi_a, \theta) = -F_x(-\Phi_f, -\Phi_a, \theta) \quad (4.21)$$

as is the original finite element data. However, due to numerical error small differences exist which mean that this is not exactly the case, i.e.

$$F_x(\Phi_f, \Phi_a, \theta) + F_x(-\Phi_f, -\Phi_a, \theta) = \varepsilon \quad (4.22)$$

where  $\varepsilon$  is a small numerical error. The effects of this small random error may be reduced by setting the magnitude of the corresponding data entries to be

$$\frac{|F_x(\Phi_f, \Phi_a, \theta)| + |F_x(-\Phi_f, -\Phi_a, \theta)|}{2} \quad (4.23)$$

thus reducing the effect of random errors due to numerical effects.

4.3.6.3 Detection of unreliable contour interpolation and extrapolation

As noted in section 4.3.4 a certain amount of contour extrapolation is possible if polynomial contour fitting is used. However, this process becomes rapidly less reliable with increasing distance outside the actual modelled mmf range and with decreasing number of data points defining the contour. Such definitely unreliable extrapolation manifests itself as adjacent contour lines intersecting, which represents a physically impossible situation. Figure 4-16 shows an example of the characteristic pattern of numerical values in the converted data at a given position which arises as a result of such unreliable extrapolation. The adjacent numerical value to the left of the highlighted entries may also be unreliable although this is less certain. Such entries may be detected and deleted from the converted data. However, as they are bounded by null values, interpolation in these regions will generally return a null result, which is the correct outcome, even if they are not deleted. Hence, the presence of some such errors may be tolerated without having a deleterious effect on the reliability of the converted data at the point of use.

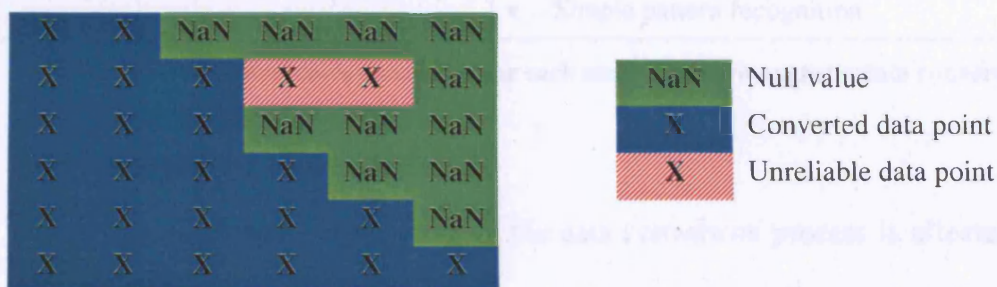


Figure 4-16 Characteristic pattern in derived data indicating unreliable contour data

### 4.3.7 Data conversion alternatives implemented

In order to examine the effects of the various interpolation and numerical processing options for the data conversion process a number of alternative methods have been used during each stage of the data conversion algorithm. Table 4-3 summarises the main processes which have been examined and implemented at each stage for reference.

Implementation stage	Methods implemented
1 Interpolation of flux map data	<ul style="list-style-type: none"> <li>• Linear interpolation</li> <li>• Bi-cubic interpolation</li> </ul>
2 Determination of independent flux axes	<ul style="list-style-type: none"> <li>• Range of calculated fluxes</li> </ul>
3 Calculation and checking of contours	<ul style="list-style-type: none"> <li>• Number of defining points</li> <li>• Number of line segments</li> </ul>
4 Interpolation of calculated contours	<ul style="list-style-type: none"> <li>• Quadratic polynomial</li> <li>• PCHIP</li> </ul>
5 Detection of contour intersections	<ul style="list-style-type: none"> <li>• Using interpolated contours</li> </ul>
6 Converted data numerical error estimation and reduction	<ul style="list-style-type: none"> <li>• Reconstruction of original data</li> <li>• Averaging</li> <li>• Simple pattern recognition</li> </ul>

Table 4-3 Alternatives implemented for each stage of electromagnetic data conversion

## 4.4 Results

The accuracy of results obtained from the data conversion process is affected by the quality of finite element data used to build the flux map being converted and the methods used to implement the data conversion algorithms. Each of the methods has potential advantages and disadvantages compared to the others and the final choice of which to use will depend upon the exact application, quantity and quality of finite element data and computing resources available.

Firstly some typical results are presented for the various derived quantities and their variation over a complete electrical cycle. The effect on the derived data of the various flux maps is then compared using the quadratic polynomial contour interpolation method to quantify the net effect of finite element data quality. Extrapolation using quadratic polynomial interpolation is then compared to the results obtained using the same methods for directly calculated finite element data to show the applicability and limitations of such extrapolation. Finally, using a larger flux map data set the results of each contour interpolation method are compared to quantify the effects of each.

#### ***4.4.1 Typical converted data***

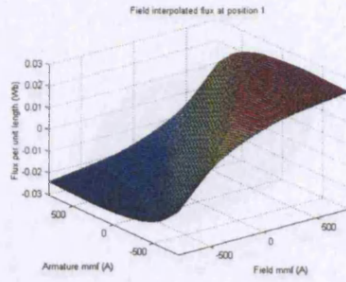
The typical converted data presented here is obtained using the second order polynomial contour interpolation method from the B2 flux map data set, i.e. the most complete and accurate finite element data available. Each of the derived quantities is shown for four positions spanning a complete electrical cycle. Position 1 is an aligned position of negative mutual coupling and position 3 is an aligned position of positive mutual coupling between field and armature. Positions 2 and 4 are intermediate positions between positions 1&3 and 3&1 respectively in the direction of normal rotation.

Figure 4-17 shows the interpolated flux map data for positions 1 to 4. The B2 flux map was used based on field and armature mmf ranges  $-800\text{A}$  to  $800\text{A}$  in  $100\text{A}$  steps. In each position the winding fluxes were interpolated onto the same mmf range with  $25\text{A}$  steps using the bi-cubic method to increase resolution with consequent benefits during the conversion process as discussed in section 4.3.

Figure 4-18 shows the variation of the relationships  $F_f(\Phi_f, \Phi_a, \theta)$  and  $F_a(\Phi_f, \Phi_a, \theta)$  over an electrical cycle. In each case the regions where the relationship appears to be incomplete correspond to combinations of winding fluxes for which no contour intersection was found for one of the reasons described in section 4.3.3. The range of independent fluxes,  $-0.03\text{Wb}$  to  $0.03\text{Wb}$  in  $0.001\text{Wb}$  increments, was selected after inspection of the flux map to include the full range of fluxes present and provide good resolution of the independent flux axes.

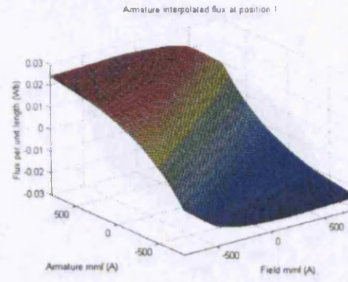
The relationships  $F_f(\Phi_f, F_a, \theta)$  and  $\Phi_a(\Phi_f, F_a, \theta)$  are shown in Figure 4-19 and the relationships  $F_a(F_f, \Phi_a, \theta)$  and  $\Phi_f(F_f, \Phi_a, \theta)$  are shown in Figure 4-20 over an electrical cycle. It can be seen that the oscillatory behaviour observed in the flux map over an electrical cycle is also evident in all the data derived from it.

$$\Phi_f(F_f, F_a, \theta)$$



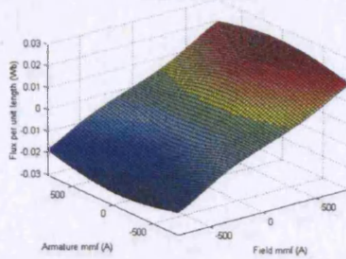
(a) Field flux at position 1

$$\Phi_a(F_f, F_a, \theta)$$



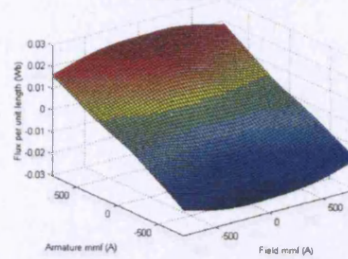
(b) Armature flux at position 1

Field interpolated flux at position 2



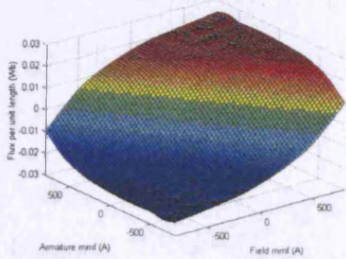
(c) Field flux at position 2

Armature interpolated flux at position 2



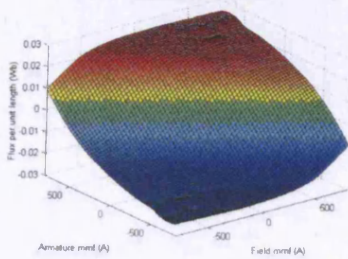
(d) Armature flux at position 2

Field interpolated flux at position 3



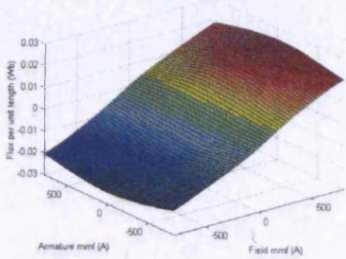
(e) Field flux at position 3

Armature interpolated flux at position 3



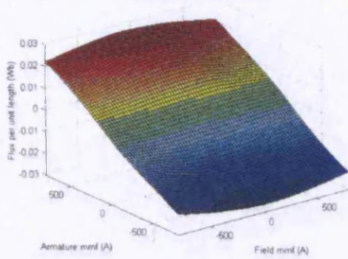
(f) Armature flux at position 3

Field interpolated flux at position 4



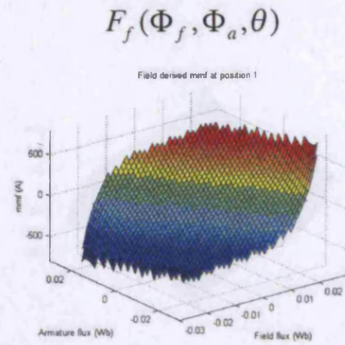
(g) Field flux at position 4

Armature interpolated flux at position 4

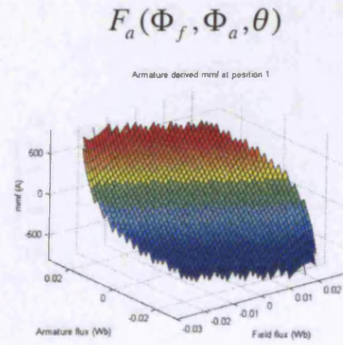


(h) Armature flux at position 4

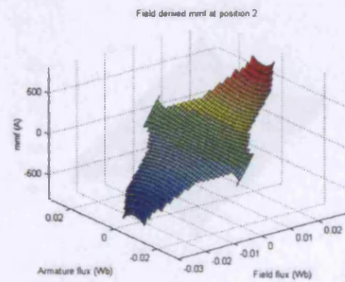
Figure 4-17 Field and armature flux as a function of field and armature mmfs for a complete electrical cycle



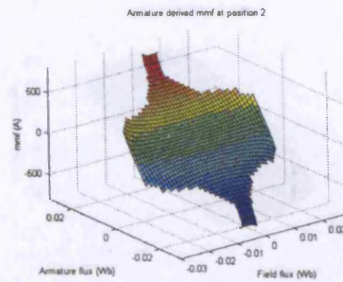
(a) Field mmf at position 1



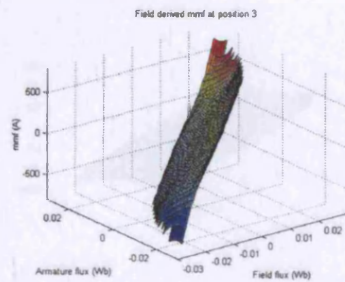
(b) Armature mmf at position 1



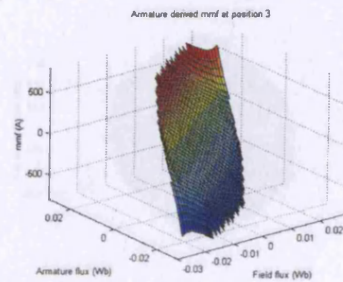
(c) Field mmf at position 2



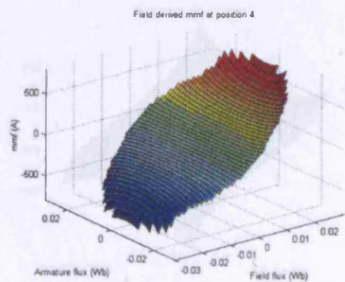
(d) Armature mmf at position 2



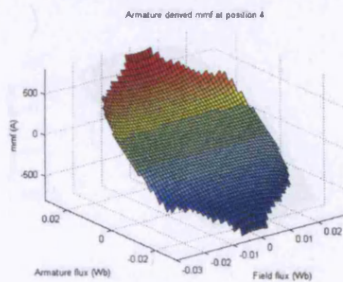
(e) Field mmf at position 3



(f) Armature mmf at position 3

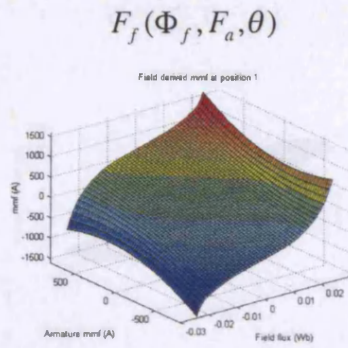


(g) Field mmf at position 4

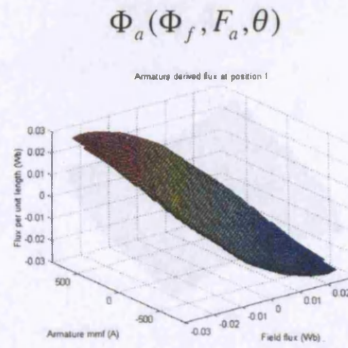


(h) Armature mmf at position 4

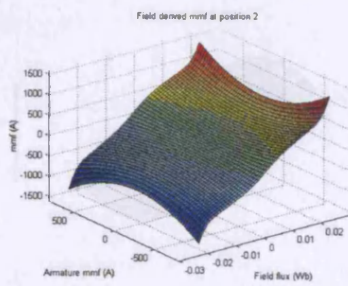
Figure 4-18 Field and armature mmf as a function of field and armature fluxes for a complete electrical cycle



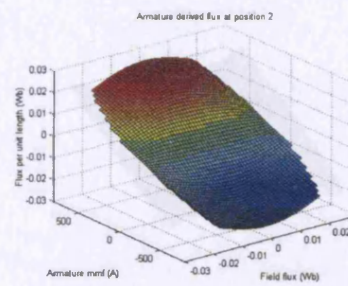
(a) Field mmf at position 1



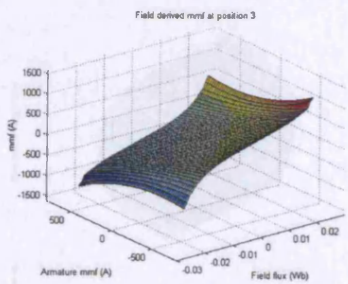
(b) Armature flux at position 1



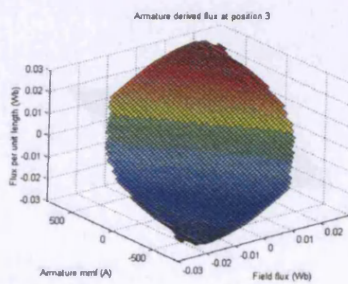
(c) Field mmf at position 2



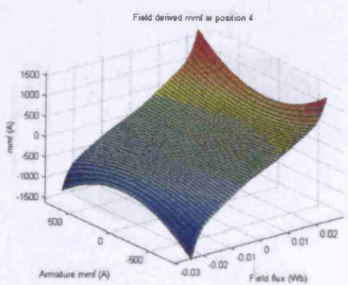
(d) Armature flux at position 2



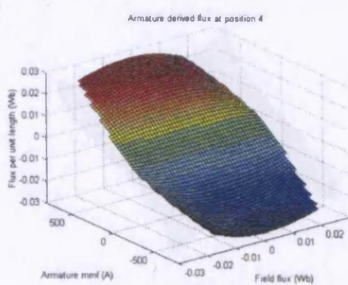
(e) Field mmf at position 3



(f) Armature flux at position 3



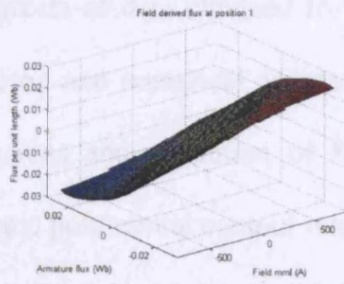
(g) Field mmf at position 4



(h) Armature flux at position 4

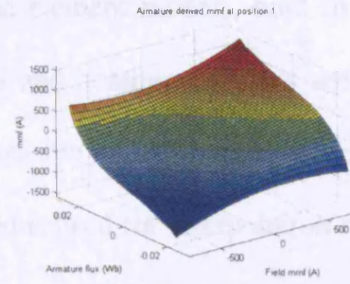
Figure 4-19 Field mmf and armature flux as a function of field flux and armature mmf for a complete electrical cycle

$$\Phi_f(F_f, \Phi_a, \theta)$$



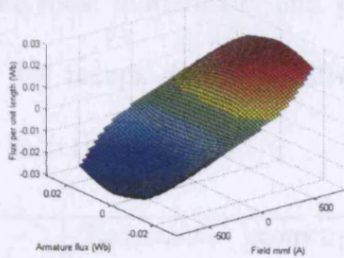
(a) Field flux at position 1

$$F_a(F_f, \Phi_a, \theta)$$



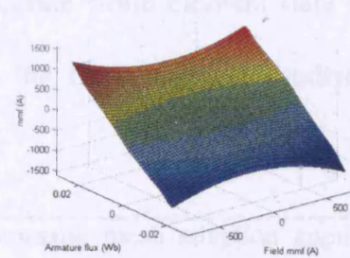
(b) Armature mmf at position 1

Field derived flux at position 2



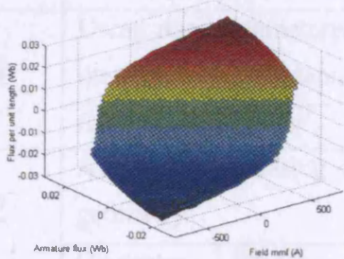
(c) Field flux at position 2

Armature derived mmf at position 2



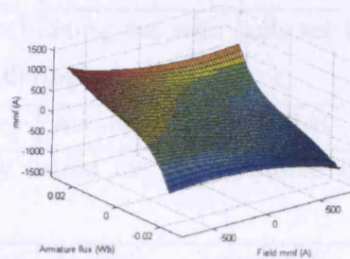
(d) Armature mmf at position 2

Field derived flux at position 3



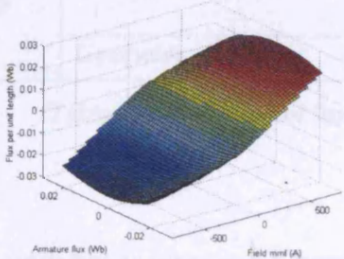
(e) Field flux at position 3

Armature derived mmf at position 3



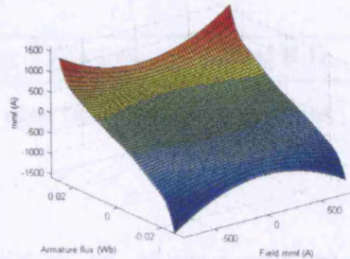
(f) Armature mmf at position 3

Field derived flux at position 4



(g) Field flux at position 4

Armature derived mmf at position 4



(h) Armature mmf at position 4

Figure 4-20 Field flux and armature mmf as a function of field mmf and armature flux for a complete electrical cycle

#### 4.4.2 Comparison of flux maps

The effects of data obtained from differing finite element models, both in terms of geometric and numerical accuracy, are evaluated and compared in this section. The dimensions and resolution of flux map used are the same in each case and the quadratic polynomial contour interpolation method is used for interpolation of contour lines. Data derived from the B2 flux map is taken as the datum for this comparison as it is the most numerically and geometrically accurate finite element data available. Table 4-4 recaps the main differences between the finite element models used to create each flux map.

<b>A2</b>	'Reasonable' geometric model with automatic mesh adaption applied during solution to yield good numerical accuracy					
	<b>Geometry</b>	'Reasonable'	<b>Mesh/Accuracy</b>	Accurate	<b>Steel B-H</b>	540Hz
<b>B1</b>	Using new parameterised model without filleting but with coils set back from the airgap. Mesh adaption is also applied during solution.					
	<b>Geometry</b>	'Better'	<b>Mesh/Accuracy</b>	Accurate	<b>Steel B-H</b>	540Hz
<b>B2</b>	As B1 with filleting added to precisely model the manufactured lamination geometry.					
	<b>Geometry</b>	Precise	<b>Mesh/Accuracy</b>	Accurate	<b>Steel B-H</b>	540Hz
<b>B3</b>	As B2 but using 20Hz steel B-H characteristic					
	<b>Geometry</b>	Precise	<b>Mesh/Accuracy</b>	Accurate	<b>Steel B-H</b>	20Hz

**Table 4-4 Summary of finite element models used for flux maps compared**

The comparisons presented here are for the field in an aligned and intermediate position, positions 1 and 2 as defined above in section 4.4.1, for the derived quantities

$$F_f(\Phi_f, \Phi_a, \theta) \quad (4.24)$$

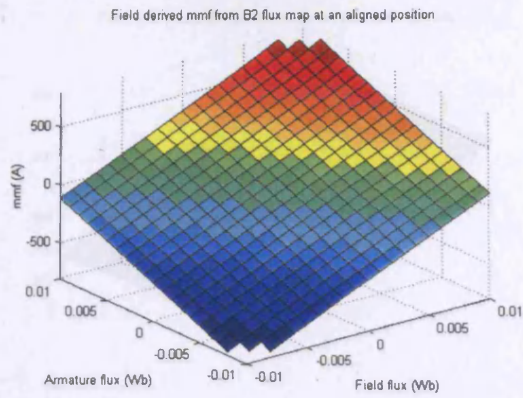
which requires the intersection between two interpolated contour lines to be found, thus introducing the largest potential errors and

$$\Delta F_f(\Phi_f, \Phi_a, \theta) \quad (4.25)$$

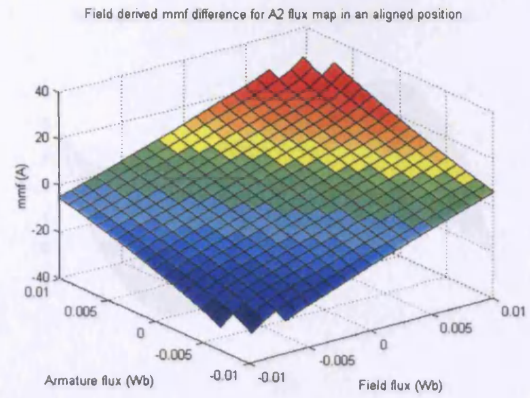
where  $\Delta F_f$  is the error estimate obtained by using the data conversion algorithm to reconstruct the original data.

As the converted data and contour lines become less reliable for all flux maps towards the extremes of the finite element data the comparisons shown are all made in the central region of the derived data for clarity.

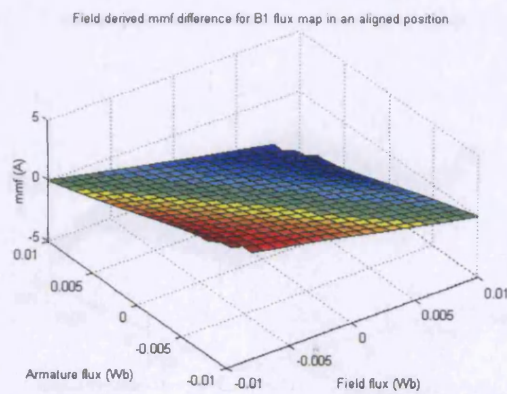
Figure 4-21 compares the differences in derived field mmf at an aligned position for the A2, B1 and B3 flux maps to the datum data derived from B2 while Figure 4-22 shows the same comparisons for an intermediate position. Comparison with A2 isolates the effects of geometric accuracy of the finite element model while comparison with B1 isolates the effects of filleting and comparison with B3 shows the effects of steel B-H characteristic used in finite element analysis. *It can be seen that geometric accuracy of the finite element model, i.e. coil geometry and filleting, has the largest effects in both positions on derived mmf, particularly in the aligned position. The choice of steel B-H characteristic in the finite element model also has greatest effect in the aligned position where bulk saturation of the steel occurs.*



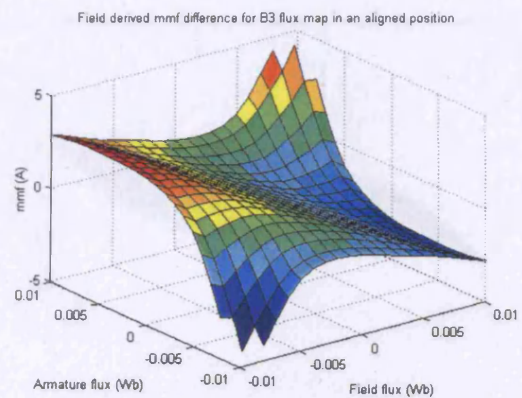
(a) Field mmf for flux map B2 at an aligned position



(b) Difference in field mmf for flux map A2 in an aligned position

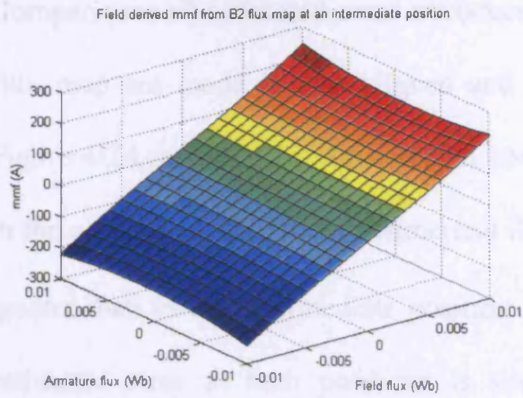


(c) Difference in field mmf for flux map B1 in an aligned position

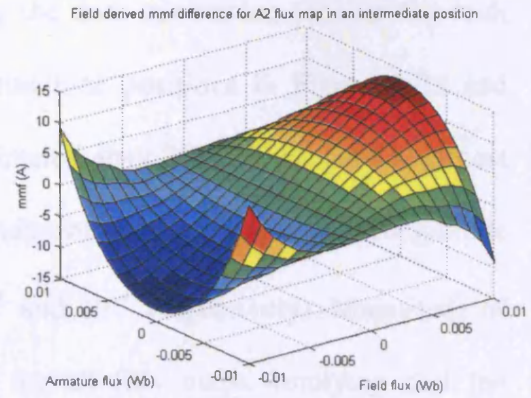


(d) Difference in field mmf for flux map B3 in an aligned position

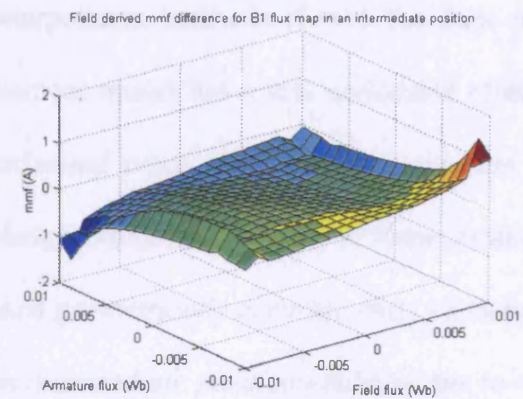
Figure 4-21 Effects of finite element model formulation on field mmf at an aligned position



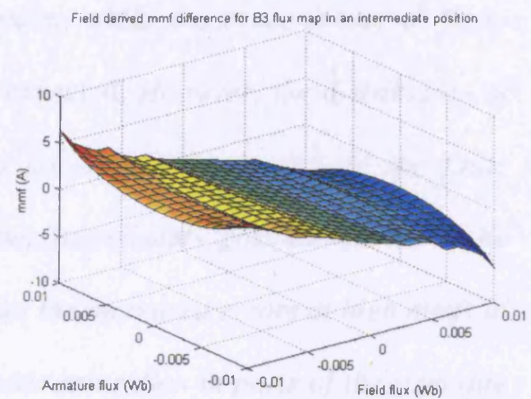
(a) Field mmf for flux map B2 at an intermediate position



(b) Difference in field mmf for flux map A2 in an intermediate position



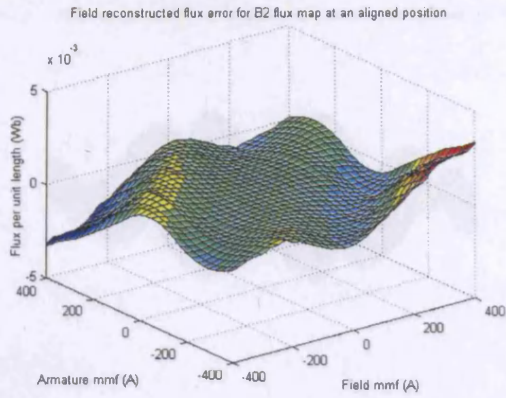
(c) Difference in field mmf for flux map B1 in an intermediate position



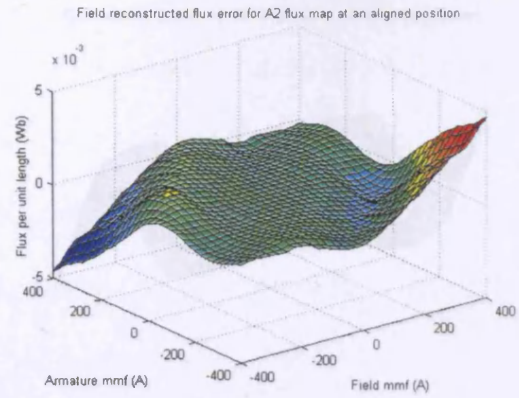
(d) Difference in field mmf for flux map B3 in an intermediate position

Figure 4-22 Effects of finite element model formulation on field mmf at an intermediate position

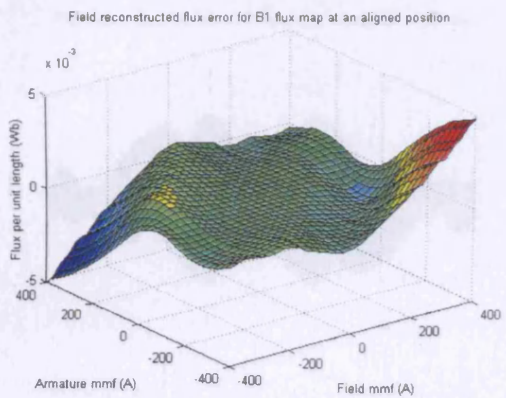
Comparisons of estimated error introduced by the data conversion process for each flux map are made for the aligned and intermediate positions in Figure 4-23 and Figure 4-24 respectively. As expected, the estimated error for all flux maps is largest in the aligned position due to numerical ill-conditioning, being an order of magnitude greater than in the intermediate position ( $10^{-3}$  and  $10^{-4}$  respectively). Magnitude of estimated error in both positions is similar for all flux maps, implying that the estimated errors are mainly systematic and arise due to the flux and contour interpolation methods chosen for data conversion, while the exact choice of finite element model has a less noticeable effect as expected. *However, the distribution of estimated error in the aligned position does not appear to depend on the finite element model but it does to some extent in the intermediate position. As A2 is the least geometrically accurate finite element model the increased errors at high mmfs in an intermediate position could be due to magnetic saturation in parts of the steel due to the simplified geometry affecting the bulk results.*



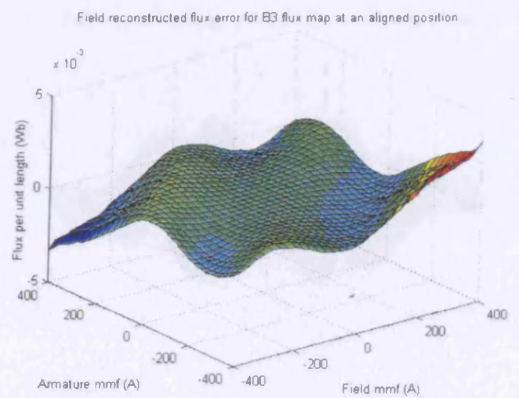
(a) Field numerical error estimate for flux map B2 in an aligned position



(b) Field numerical error estimate for flux map A2 in an aligned position

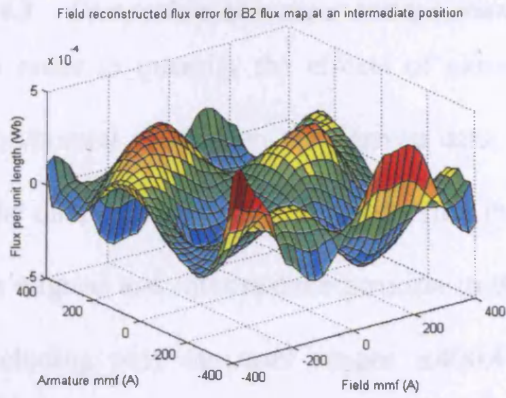


(c) Field numerical error estimate for flux map B1 in an aligned position

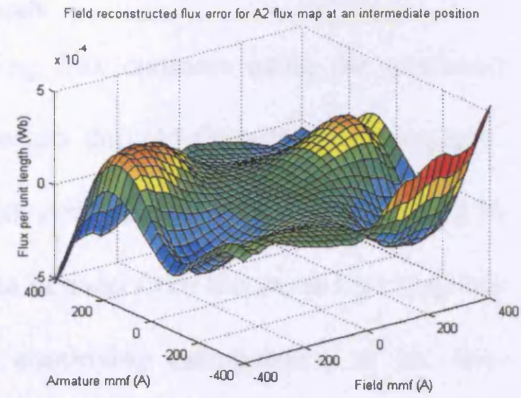


(d) Field numerical error estimate for flux map B3 in an aligned position

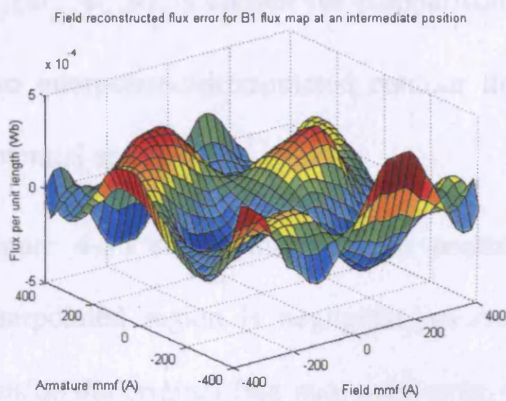
Figure 4-23 Comparison of field numerical error estimates for each flux map in an aligned position



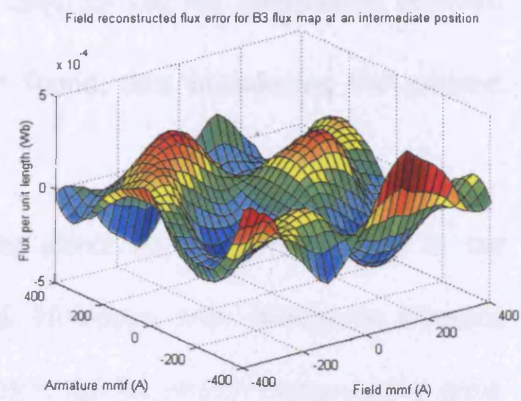
(a) Field numerical error estimate for flux map B2 in an intermediate position



(b) Field numerical error estimate for flux map A2 in an intermediate position



(c) Field numerical error estimate for flux map B1 in an intermediate position



(d) Field numerical error estimate for flux map B3 in an intermediate position

Figure 4-24 Comparison of field numerical error estimates for each flux map in an intermediate position

#### 4.4.3 Comparison of contour extrapolation methods

In order to quantify the effects of extrapolating flux contours using the quadratic polynomial method on the derived data, the results derived from B2 are compared. The data derived from a complete flux map with mmf ranges  $\pm 800A$  is compared in an aligned and intermediate position to the data derived from the same flux map but including only the mmf ranges  $\pm 400A$  and employing extrapolation of the flux contours to estimate the derived data in the range  $\pm 800A$ . The derived quantity  $F_f(\Phi_f, \Phi_a, \theta)$  is chosen for comparison as it requires that the intersection between two interpolated/extrapolated contour lines be found, thus introducing the greatest potential error.

Figure 4-25 shows that in both positions the effect on the derived data in the interpolated region is negligible, as expected. However, with increasing distance outside the original flux map mmf range the errors due to contour extrapolation grow rapidly, particularly for flux values whose contours are defined by the least number of data points. *Hence, extrapolation may only be applied with caution and the quadratic fitting polynomial leads to reasonably predictable, if not completely accurate, derived data in the extrapolated region.*

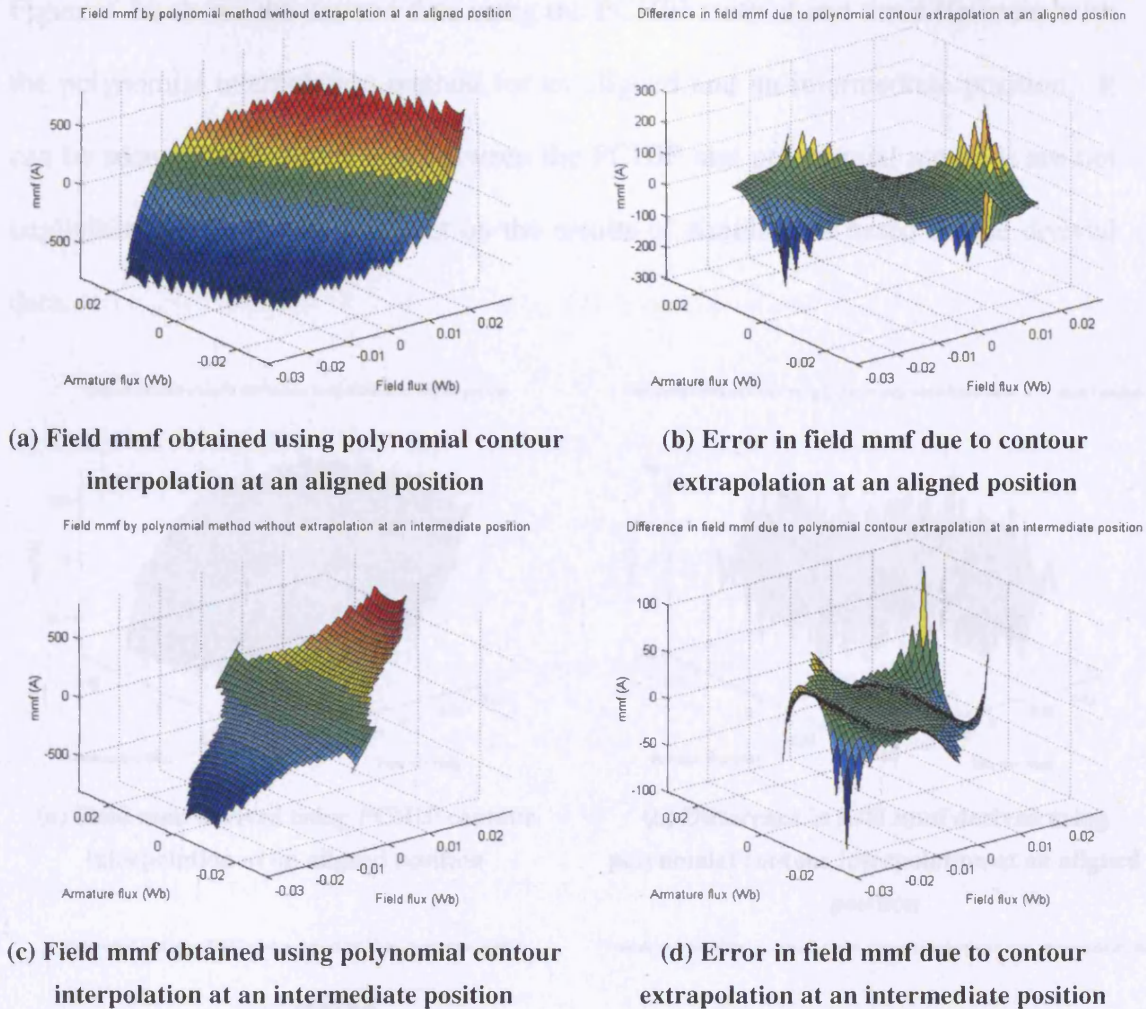


Figure 4-25 Field mmf errors due to polynomial extrapolation of flux contours

#### 4.4.4 Comparison of contour interpolation methods

For comparison between contour interpolation methods the derived relationship  $F_f(\Phi_f, \Phi_a, \theta)$  is evaluated at an aligned and an intermediate position using the PCHIP method and B2 flux map. The PCHIP interpolation method is used as the datum for comparisons as the interpolant passes directly through each data point defining the contour line and B2 is the most complete and accurate flux map available.  $F_f(\Phi_f, \Phi_a, \theta)$  is chosen for comparison as it requires the intersection between two contours to be found, thus introducing the greatest potential difference between techniques while estimated error is compared to evaluate the relative magnitude of numerical errors introduced by each method.

Figure 4-26 shows the derived data using the PCHIP method and the differences with the polynomial interpolation method for an aligned and an intermediate position. It can be seen that the differences between the PCHIP and polynomial methods are not negligible and may have an effect on the results of simulations based on the derived data.

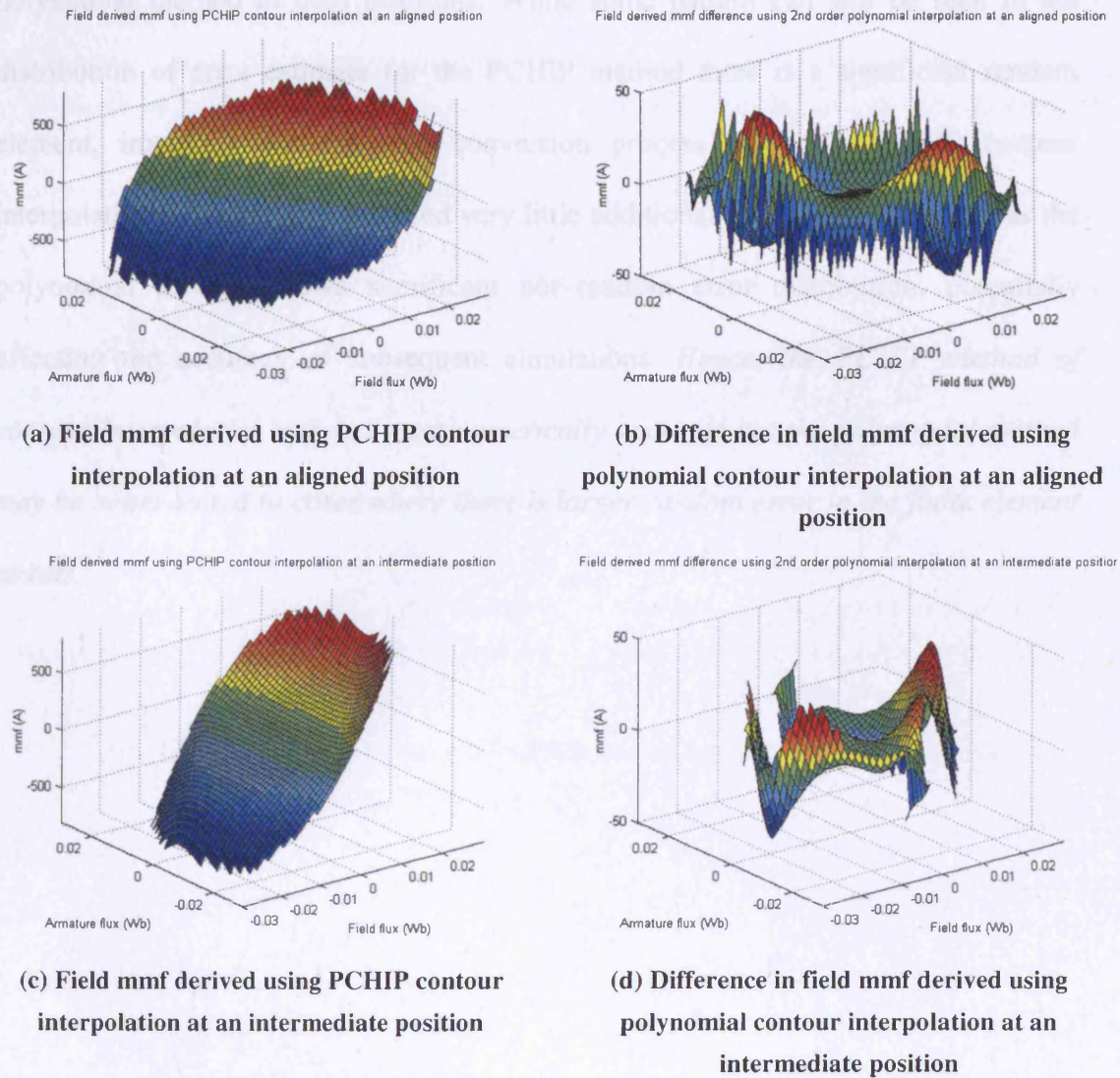
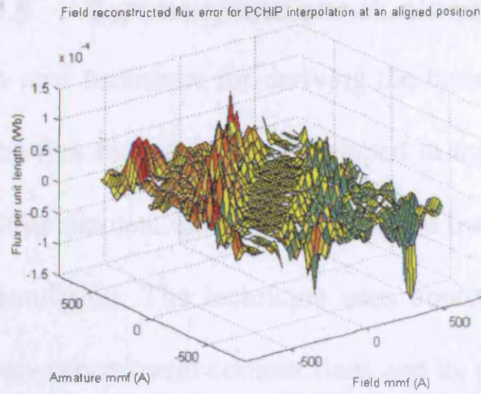
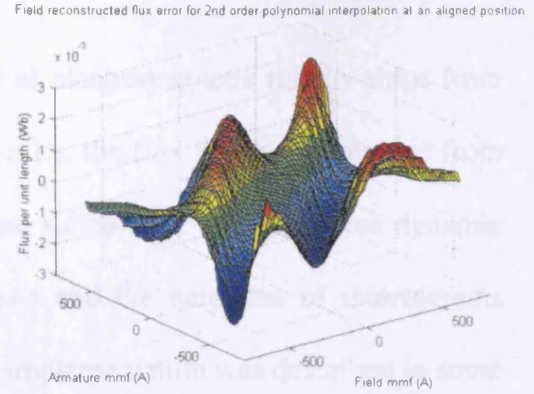


Figure 4-26 Effect of contour interpolation method on derived field mmf

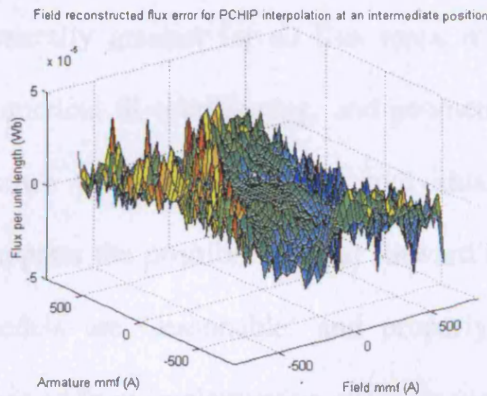
Comparing the estimated error introduced by each contour interpolation method, shown in Figure 4-27 for an aligned and an intermediate position, it can be seen that, for both interpolation methods, estimated errors in the aligned position are greater than for the intermediate position due to numerical ill-conditioning. Estimated error for the PCHIP method is also at least an order of magnitude smaller than the polynomial method in both positions. While some pattern can still be seen in the distribution of error estimate for the PCHIP method there is a significant random element, implying that the data conversion process using the PCHIP contour interpolation method has introduced very little additional numerical error whereas the polynomial method shows significant non-random error distribution, potentially affecting the accuracy of subsequent simulations. *Hence, the PCHIP method of contour interpolation appears most numerically accurate but the polynomial method may be better suited to cases where there is larger random error in the finite element results.*



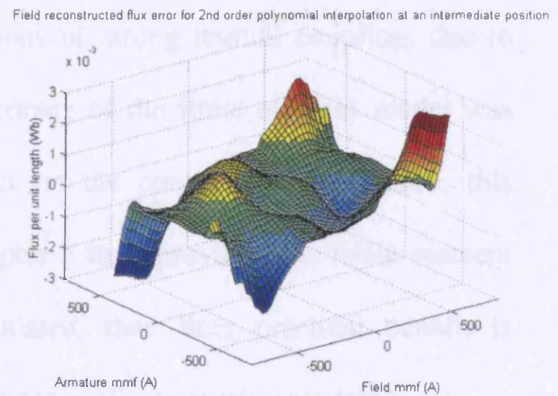
(a) Field numerical error estimate using PCHIP contour interpolation at an aligned position



(b) Field numerical error estimate using polynomial contour interpolation at an aligned position



(c) Field numerical error estimate using PCHIP contour interpolation at an intermediate position



(d) Field numerical error estimate using polynomial contour interpolation at an intermediate position

Figure 4-27 Effect of contour interpolation method on numerical error estimate

## **4.5      Summary and conclusions**

A new technique for deriving the complete set of electromagnetic relationships from the flux map data was developed in this chapter, i.e. the flux map data obtained from finite element analysis is converted into a format suitable for voltage driven dynamic simulation. The technique uses contour analysis and the detection of intersections between relevant contour lines and its practical implementation was described in some detail. An algorithm was also developed for estimating and reducing the numerical error introduced during the data conversion process. It was shown that errors are generally greatest for all flux maps in positions of strong mutual coupling, due to numerical ill-conditioning, and geometric accuracy of the finite element model was shown to have the greatest individual effect on the converted data. Hence, this supports the position first put forward in chapter 3 that, provided the finite element models are 'reasonable' and properly formulated, then little practical benefit is derived from implementing complex and computationally expensive models.

---

# **Chapter 5**

Dynamic simulation model for the  
flux switching machine

---

## **5      DYNAMIC SIMULATION MODEL FOR THE FLUX SWITCHING MACHINE**

### **5.1      Introduction**

This chapter presents a voltage driven model for the flux switching machine either stationary or rotating at constant speed which utilises the flux map and derived data as developed in chapters 3 and 4. Given the speed of rotation and arbitrary terminal voltages, the behaviour of winding flux linkages and currents can be simulated. Such simulations are comparable to the initial experimental tests which are carried out on a prototype machine such as static testing of self and mutual coupling and constant speed back emf testing. In addition the simulations can return quantities such as flux linkage, instantaneous torque and visualisations from finite element analysis which cannot generally be obtained experimentally. The results of such simulations are also repeatable and directly comparable as the simulation conditions can be exactly specified, which is not always the case for experimental tests. The simulation is relatively rapid at the point of use, using the previously obtained flux map and derived data to characterise the machine geometry without the need for further finite element analysis while retaining flexibility for detailed winding design and optimisation, i.e. the methodology is similar to the use of the flux-mmF characterisation of the switched reluctance machine as discussed in chapter 2.

The finite element modelling, simplified analysis, electromagnetic characterisation and data conversion processes presented in chapters 3 to 4 are generally applicable to the flux switching machine, whether it is to operate in motoring or generating modes. Furthermore, the electromagnetic characterisation, data structure and processing are applicable to any two-phase mutually coupled reluctance machine. The technique developed may also be applicable to multi-phase reluctance machines where mutual coupling need only be considered between two phases at any instant. However, the research presented in this thesis is focused on the flux switching motor and, while the dynamic simulation model developed in this chapter is also applicable to the flux switching generator, it is experimentally validated using the 8/4 flux switching machine which was designed to be a motor.

## 5.2 Theoretical development

### 5.2.1 Denormalisation of flux map and derived data

The flux map and data derived from it contain normalised data which is capable of describing any stack length or common winding configuration based upon the characterised lamination geometry for which 2-dimensional assumptions are valid. Prior to use as the basis for simulation the data must be denormalised to describe the actual machine being simulated. Neglecting end effects, assuming that all coils comprising each winding are identical and that eddy currents may be neglected, winding flux linkage is given by

$$\Psi_x = \Phi_x \times N_x \times l \times S_x \quad (5.1)$$

where  $\Psi$  is flux linkage,  $\Phi$  is flux linkage per turn per unit stack length,  $N$  is number of turns per coil,  $l$  is stack length,  $S$  is number of coils in series comprising the winding and subscript  $x$  denotes either field or armature. Similarly, winding current is obtained from

$$i_x = (F_x \times P_x) / N_x \quad (5.2)$$

where  $i$  is winding current,  $F$  is mmf,  $P$  is number of parallel paths comprising the winding,  $N$  is number of turns per coil and subscript  $x$  denotes either winding. The quantities  $\Psi$  and  $i$  are now those which would be measured at the terminals of the machine being modelled. The above relationships do not require that each half of the bifilar armature be identical although in practice this would generally be the case. For the 8/4 flux switching machine being modelled the characteristics summarised in Table 5-1 apply.

		Field	Armature
Number of turns per coil	$N_x$	32	17
Number of coils in series	$S_x$	4	4
Number of parallel paths	$P_x$	1	1
Stack length	$l$	65mm	

Table 5-1 Physical characteristics of 8/4 flux switching machine used for model validation

In the more general case where the flux linking each series connected coil comprising a winding is not identical, for example if the rotor is eccentric, then equation (5.1) becomes

$$\Psi_x = \sum_{p=1}^{S_x} (\Phi_{xp} \times N_x \times l) \quad (5.3)$$

while equation (5.2) becomes

$$i_x = F_x / N_x \quad (5.4)$$

This assumes that all coils comprising the winding are physically identical, i.e. the same number of turns each, and that they are connected in series, hence the current in each must be identical. If the coils are not physically identical but are connected in series then a new set of finite element solutions is required to reflect the unbalanced mmfs in each coil while if there is more than one parallel path the current will not necessarily divide equally between them and further finite element solutions and data processing would be required in order to account for every likely combination, thus requiring the data conversion techniques presented in this thesis to be further extended for machines with more than two mutually coupled windings.

### 5.2.2 Derivation of formulae for simulation

For a single voltage driven winding the relationship

$$\Psi = \int_0^t (v - iR) dt + \Psi_0 \quad (5.5)$$

always applies where  $\Psi$  is flux linkage,  $v$  is applied winding terminal voltage,  $i$  is current,  $R$  is resistance measured at the terminals,  $t$  is time and  $\Psi_0$  is flux linkage at time zero. For the case of the flux switching machine current in each winding is a non-linear function of flux linkage in both windings and position

$$i_x(\Psi_f, \Psi_a, \theta) \quad (5.6)$$

where  $i$  is current,  $\Psi$  is flux linkage,  $\theta$  is position and the subscripts  $f$ ,  $a$ , and  $x$  denote field, armature and either winding respectively. Applying equation (5.5) to the flux switching machine with both windings connected yields

$$\Psi_f = \int_0^t \{v_f - i_f(\Psi_f, \Psi_a, \theta)R_f\}dt + \Psi_0 \quad (5.7)$$

and

$$\Psi_a = \int_0^t \{v_a - i_a(\Psi_f, \Psi_a, \theta)R_a\}dt + \Psi_0 \quad (5.8)$$

Rearranging equations (5.7) and (5.8) into discrete time form, and assuming that the time step is small yields the equations

$$\Psi_{f(n+1)} = \Psi_{f(n)} + \left( v_{f(n)} - \frac{i_{f(n)} + i_{f(n+1)}(\Psi_{f(n+1)}, \Psi_{a(n+1)}, \theta_{(n+1)})}{2} R_f \right) \Delta t \quad (5.9)$$

and

$$\Psi_{a(n+1)} = \Psi_{a(n)} + \left( v_{a(n)} - \frac{i_{a(n)} + i_{a(n+1)}(\Psi_{f(n+1)}, \Psi_{a(n+1)}, \theta_{(n+1)})}{2} R_a \right) \Delta t \quad (5.10)$$

where subscript  $(n)$  denotes present values and  $(n+1)$  denotes new values after time interval  $\Delta t$  with constant terminal voltages  $v_f$  and  $v_a$  applied during that time to the field and armature respectively. Due to the mutual coupling between windings, equations (5.9) and (5.10) must be solved simultaneously at each time step.

If either winding is open circuit, for example simulating a back emf test, then its current and applied voltage are both constrained to be zero at all times and its flux linkage is obtained directly from denormalised flux map data. The current in the connected winding is then obtained using the flux linkage of that winding only with the other mmf constrained to be zero. If the armature is open circuit, field current is obtained using the relationship

$$i_f(\Psi_f, i_a, \theta) \quad (5.11)$$

while armature flux linkage is obtained directly from the denormalised flux map data

$$\Psi_a(i_f, i_a, \theta) \quad (5.12)$$

for  $i_a = 0$  in both cases. Similarly, if the field is open circuit the relationships

$$i_a(i_f, \Psi_a, \theta) \quad (5.13)$$

and

$$\Psi_f(i_f, i_a, \theta) \quad (5.14)$$

are used with  $i_f = 0$  in both cases.

### 5.2.3 Gauss-Seidel solution of simultaneous non-linear equations

The non-linear equations given in section 5.2.2 are solved simultaneously at each time step using the Gauss-Seidel iterative technique [63]. This technique was selected as it requires no knowledge of the analytic form of the non-linear relationships or their derivatives. It also has the potential to converge quicker than some other techniques as, at each stage in the iteration process, the most recent estimate for every quantity is used.

For each time step an initial estimate must be made for the solution at the next time step in order to begin the iteration technique. As time steps are small this first estimate for the state at the next time instant is the same as the present instant, i.e.

$$\Psi_{f(n+1)} = \Psi_{f(n)}, \quad \Psi_{a(n+1)} = \Psi_{a(n)}, \quad i_{f(n+1)} = i_{f(n)} \quad \text{and} \quad i_{a(n+1)} = i_{a(n)}. \quad \text{Thus, the initial}$$

estimate can always be expected to be close to the actual solution, potentially minimising the number of iterations required. If the system is in dc steady state equilibrium then this initial estimate will be correct and no iterations necessary.

Theoretically, after a number of iterations the estimate for the solution at the next time step will reach a steady state and will not change, regardless of further iterations. When this condition has been reached the solution has fully converged. However, in practice due to numerical errors the solution may not become completely static and a convergence tolerance must be defined. If the magnitude of change between successive solution estimates for all calculated quantities is below the convergence tolerance specified for each then the solution is deemed to have converged and the most recent estimate for each quantity is taken to be the solution. For the case where the numerical system is unstable or the convergence tolerance is set too small a maximum number of iterations is also specified which, if exceeded, terminates the simulation at that point, thus avoiding the possibility of an infinite loop. Figure 5-1 to Figure 5-3 show the Gauss-Seidel iterative solution process for the flux switching machine which is carried out at every time step for both windings connected, armature open circuit and field open circuit respectively.

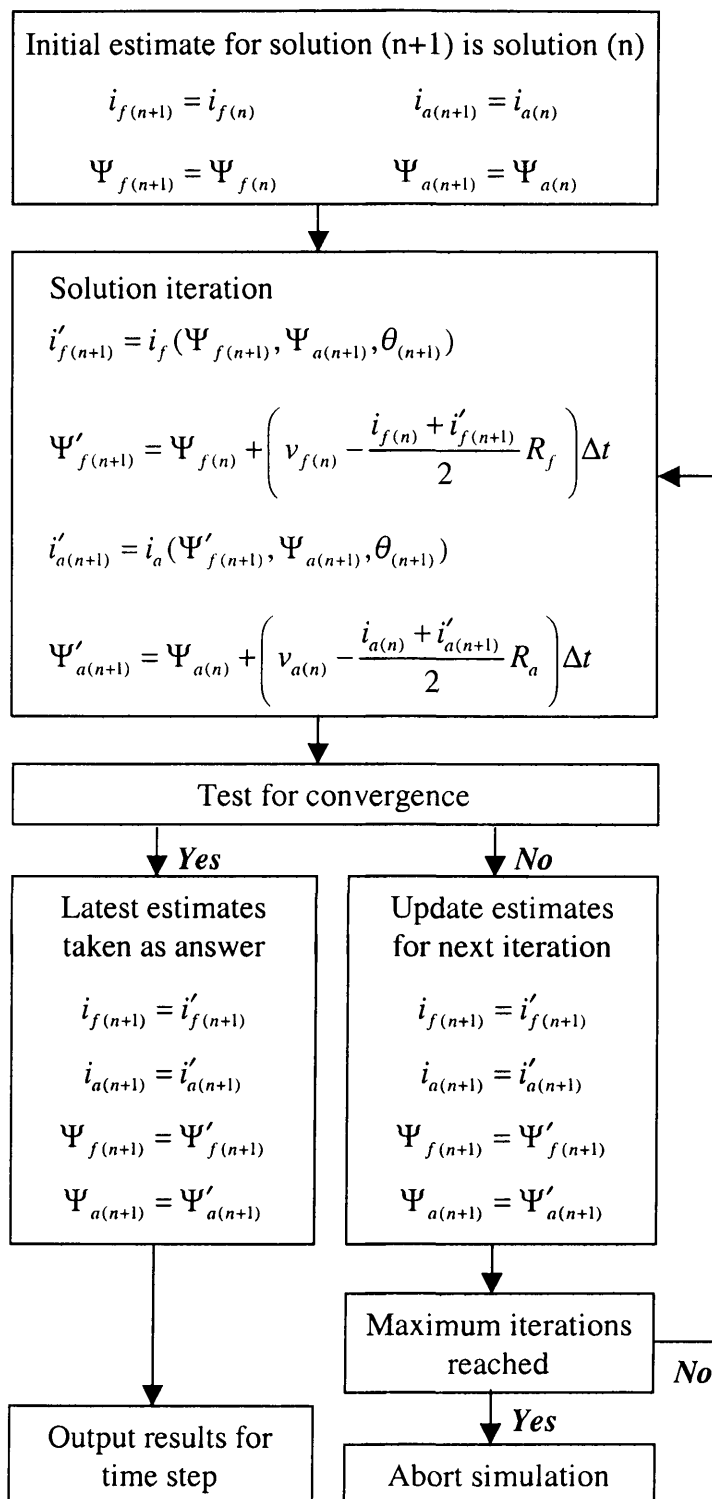


Figure 5-1 Gauss-Seidel iterative solution process at each time step for both windings connected

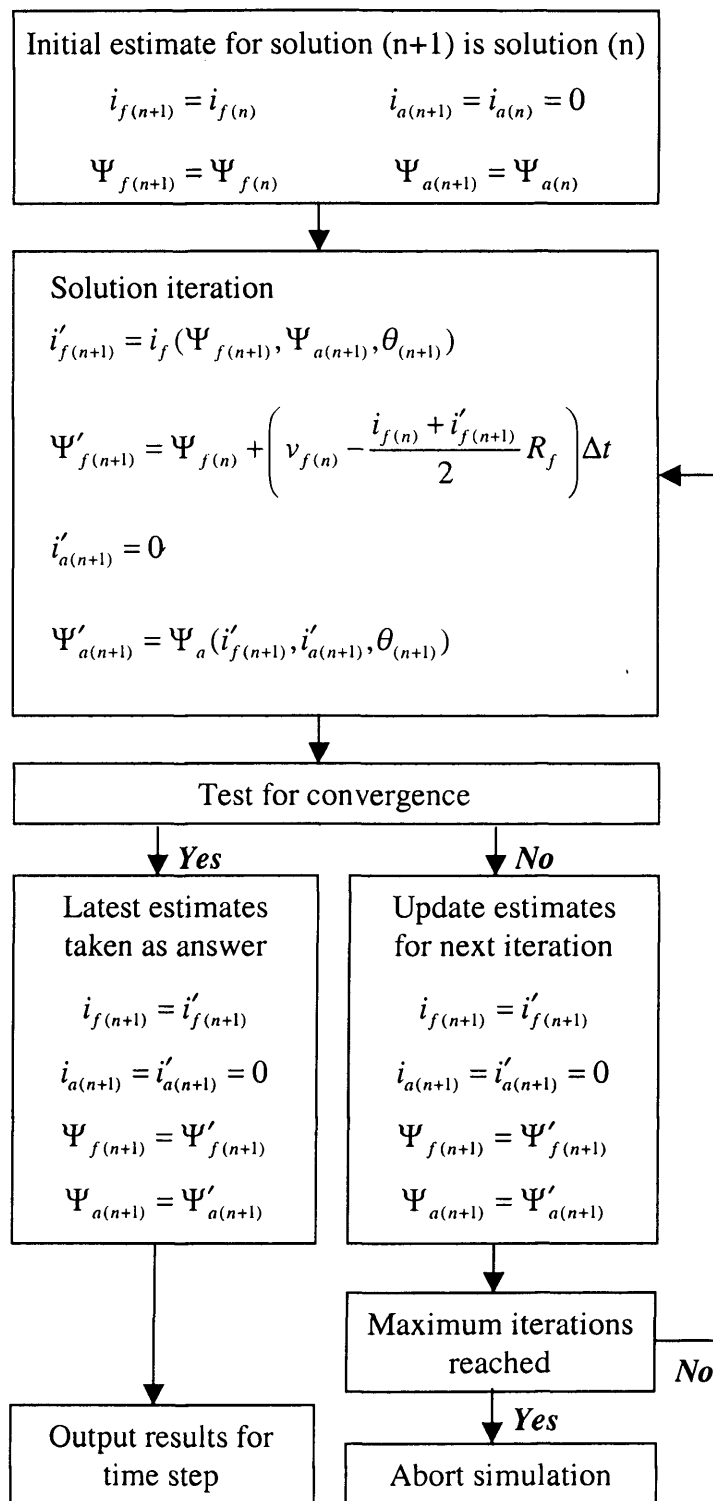


Figure 5-2 Gauss-Seidel iterative solution process at each time step for armature open circuit

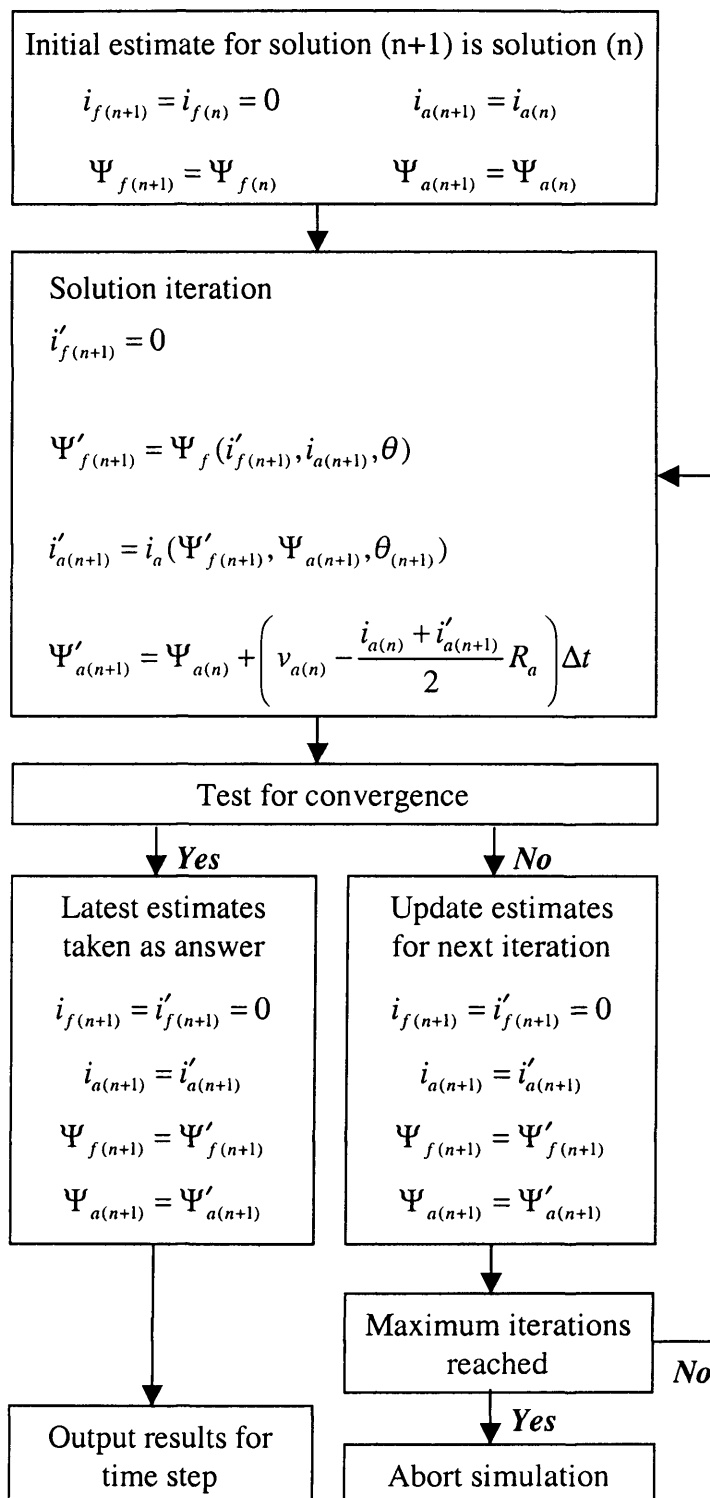


Figure 5-3 Gauss-Seidel iterative solution process at each time step for field open circuit

#### **5.2.4 Results available from simulation**

The simulation results provide winding flux linkages and currents directly. As the finite element and converted data upon which the simulation is based includes the effects of saturation, including cross-saturation, and changing self and mutual coupling with position these effects are all accounted for within the simulation results. Corresponding electromagnetic torque may be obtained either from interpolation of finite element results, i.e. using the Maxwell Stress method, or by evaluating the area enclosed by the flux linkage-current loci for each winding over a complete cycle as described in chapter 2. Further results available include graphical results which are also obtained from finite element analysis, potentially using image processing and interpolation methods for visualisation of flux density distribution or post-priori iron loss estimation as described in chapter 8.

### **5.3 Implementation of dynamic simulation model**

#### **5.3.1 Simplification for static simulation**

If only a static simulation is required then position,  $\theta$ , is constant for all time. Hence, the position term may be removed from all equations solved and only the data pertaining to this constant position need be stored and interpolated during simulation, i.e. 2-dimensional instead of 3-dimensional interpolation, thus reducing execution time without affecting the accuracy of results.

### 5.3.2 *Choice of time step and convergence tolerance*

The validity of the assumption that time step is small enough to assume a linear change in current and flux linkage between time steps is crucial to the accuracy of the flux switching machine simulation presented. Furthermore, the effects of time step, rotation speed, applied voltages and convergence tolerances are all inter-related, for example if the time step is very small and/or voltage is very low then the change in solution between time steps will be very small. If convergence tolerance is of a similar magnitude to this change then the iteration process will terminate too early, having incorrectly detected convergence of the solution, yielding inaccurate results. Further, if the time step is large and/or rotational speed is high then the differences between solutions may be too large for the assumptions to hold, leading to errors in the solution. However, if the convergence tolerance is too small then the iterative solution process may fail to converge, causing the simulation to abort unnecessarily. Thus, time step, convergence tolerance and maximum number of iterations must be selected to give the solution a 'reasonable' chance of convergence while maintaining acceptable accuracy. Table 5-2 summarises the main requirements to achieve such a compromise between accuracy and solution time.

- |  |
|--|
| <ul style="list-style-type: none"><li>• Time step must be small compared to electrical time constants of system</li><li>• Rotational angle between time steps must be small compared to the electrical cycle</li><li>• Convergence tolerances must be small compared to expected changes between time steps</li><li>• Smaller convergence tolerance generally leads to better accuracy but increased number of iterations and possible non-convergence if too small</li><li>• Maximum iterations set to allow 'reasonable' chance of convergence at each time step</li></ul> |
|--|

**Table 5-2 Factors affecting accuracy and solution time of dynamic simulation model**

## 5.4 Results

### 5.4.1 *Experimental conditions*

The flux switching machine was mounted onto a test rig such that it could be driven in its normal direction of operation by a coupled dc motor whose speed could be controlled up to approximately 5000rpm. A flywheel with inertia much larger than the machine rotor was mounted onto the shaft between the driving motor and the flux switching machine to stabilise speed during tests and minimise any speed fluctuation within each electrical cycle of the flux switching machine due to pulsating torque. The field winding was excited from a high current laboratory power supply with regulated voltage output and both halves of the bifilar armature were held open circuit. Field resistance was measured at ambient temperature at the same point in the circuit as field voltage was measured. The temperature was also measured using embedded thermocouples immediately after each test to allow correction of field resistance for operating temperature.

The driving motor was used to rotate the flux switching machine at the specified speed and a constant dc voltage was applied to the field. The field current, both bifilar armature induced emfs and shaft mounted optical sensor signal were recorded using a digital storage oscilloscope and field voltage was measured using a digital volt meter. The speed of rotation was obtained from the frequency of the optical sensor signal from the flux switching machine.

The constant speed back emf test is selected for comparison because it is widely used during the initial testing of machines and is readily reproducible, both experimentally and in simulation. Calculation of the armature induced emf also involves numerical differentiation of the simulated armature flux linkage which will tend to amplify the effect of any errors. Hence, it provides a reasonable test of simulation accuracy in addition to its practical application.

#### 5.4.2 Comparison of experimental and simulated results

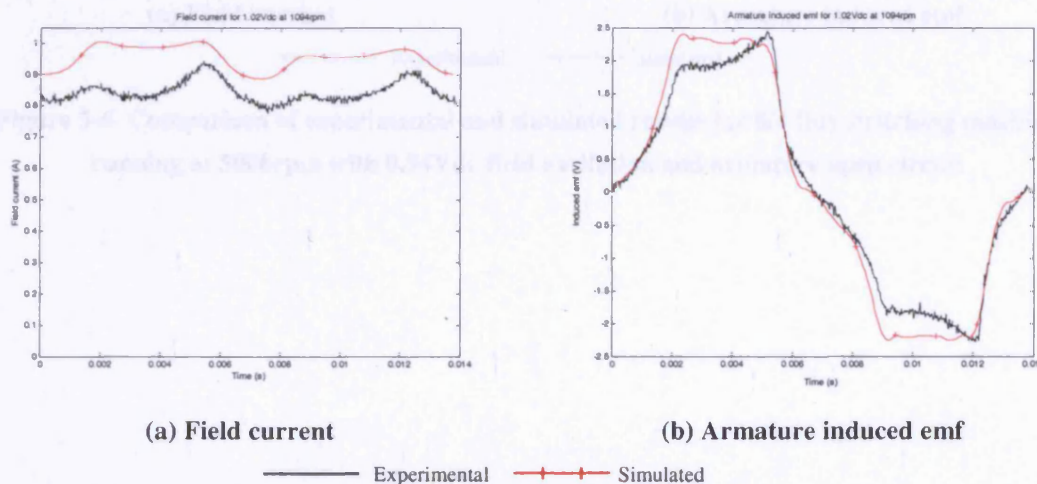
Experimental results are compared to simulation for a variety of speeds and field excitation voltages. The experimental results were obtained first and then the simulations carried out for identical conditions with field resistance corrected using measured coil temperature. The simulations presented were carried out using data derived from the B2 flux map, as this is the most complete and accurate finite element data available, using the PCHIP contour interpolation method which was shown in chapter 4 to introduce the least numerical error into the converted data. Table 5-3 summarises the comparisons shown in Figure 5-4 to Figure 5-7 and their descriptions by which they will be referred to in later sections.

Speed (rpm)	Field voltage (V)	Description	Figure
1094	1.02	Low speed, low voltage	Figure 5-4
1170	7.56	Low speed, high voltage	Figure 5-5
5008	0.94	High speed, low voltage	Figure 5-6
4972	7.42	High speed, high voltage	Figure 5-7

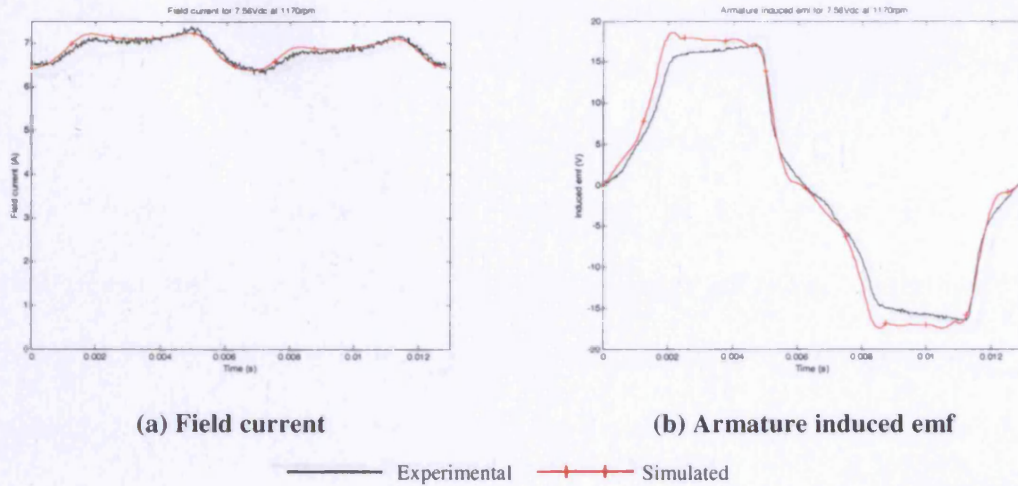
**Table 5-3 Experimental conditions for which comparative results are presented**

Figure 5-4 to Figure 5-7 show that in general the dynamic simulation model for the flux switching machine accounts well for the modulation of the field current due to changing flux path reluctance over the electrical cycle. The electrical asymmetry introduced by asymmetric rotor and stator poles is evident in the slightly differing results for each half of the electrical cycle. While armature induced emf generally agrees for the majority of the electrical cycle and the magnitudes are similar there is a clear difference in the shape of the waveforms which is common to all the operating conditions compared. Table 5-4 summarises the numerical results, comparing mean field current and RMS armature induced emf for each condition modelled.

For both low field voltage conditions the simulated field current is noticeably higher than that obtained experimentally despite the field resistance being corrected for temperature. The difference in shape between experimental and simulated armature induced emf, which is apparent for each modelled condition, appears to be a systematic difference, possibly due to a dynamic or an end effect not accounted for in the data derived from 2-dimensional magnetostatic finite element analysis.



**Figure 5-4 Comparison of experimental and simulated results for 8/4 flux switching machine running at 1094rpm with 1.02Vdc field excitation and armature open circuit**



**Figure 5-5 Comparison of experimental and simulated results for 8/4 flux switching machine running at 1170rpm with 7.56Vdc field excitation and armature open circuit**

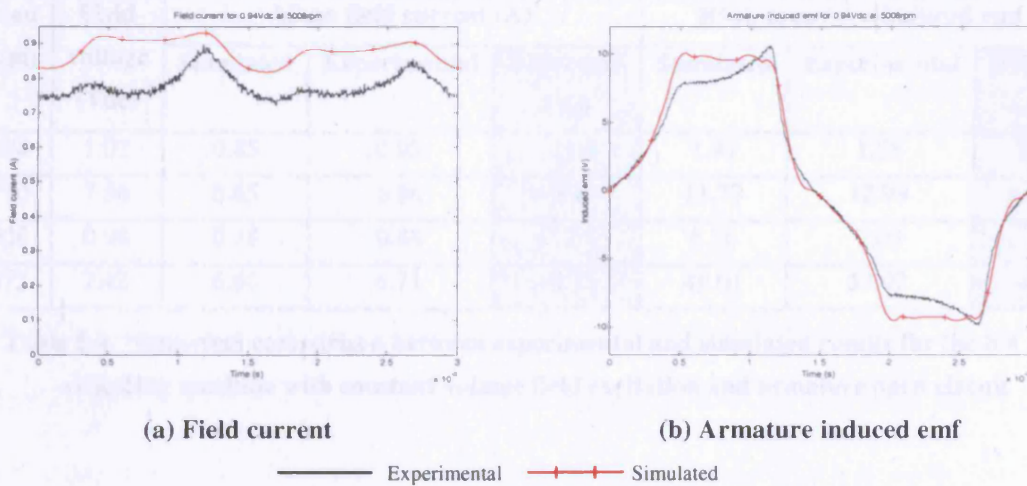
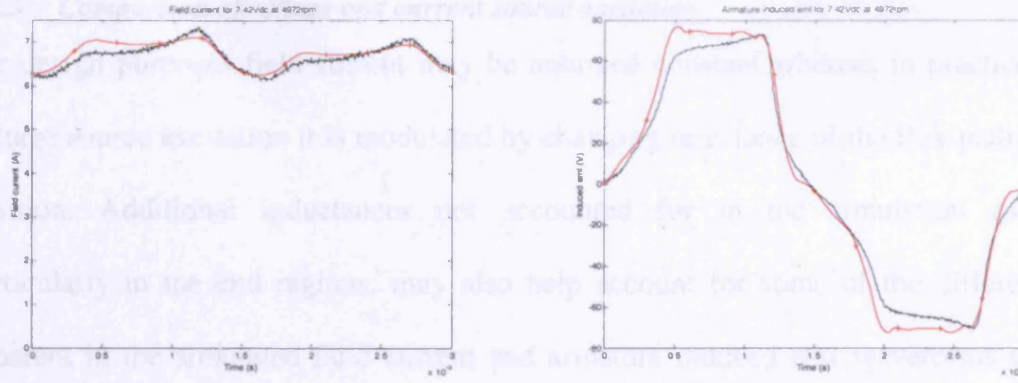


**Figure 5-6 Comparison of experimental and simulated results for 8/4 flux switching machine running at 5008rpm with 0.94Vdc field excitation and armature open circuit**



(a) Field current

(b) Armature induced emf

— Experimental —+— Simulated

Figure 5-7 Comparison of experimental and simulated results for 8/4 flux switching machine running at 4972rpm with 7.42Vdc field excitation and armature open circuit

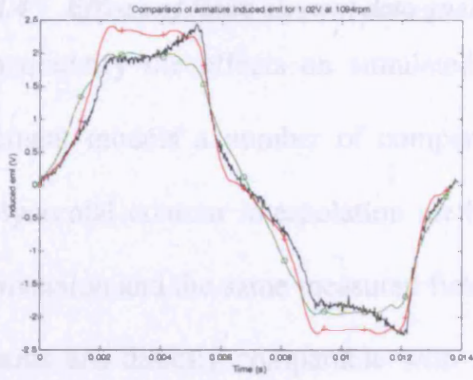
Speed (rpm)	Field voltage (Vdc)	Mean field current (A)			RMS armature induced emf (V)		
		Simulated	Experimental	Difference (%)	Simulated	Experimental	Difference (%)
1094	1.02	0.85	0.95	+11.8	1.49	1.68	+12.8
1170	7.56	6.85	6.86	+0.15	11.79	12.99	+10.2
5008	0.94	0.78	0.88	+12.8	6.36	7.09	+11.5
4972	7.42	6.66	6.71	+0.75	49.01	53.92	+10.0

Table 5-4 Numerical comparison between experimental and simulated results for the 8/4 flux switching machine with constant voltage field excitation and armature open circuit

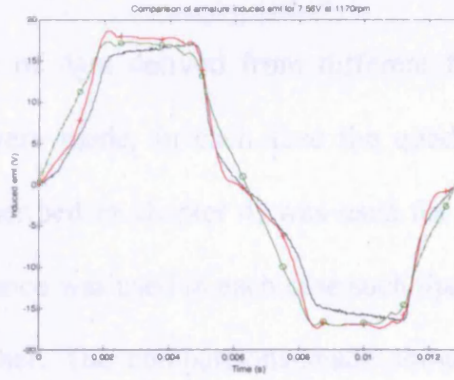
### 5.4.3 Comparison of voltage and current source excitation

For design purposes field current may be assumed constant whereas in practice for voltage source excitation it is modulated by changing reluctance of the flux path with position. Additional inductances not accounted for in the simulation model, particularly in the end regions, may also help account for some of the differences apparent in the simulated field current and armature induced emf waveforms when compared with experimental results. Imposing a constant current on the field has the same effect as adding an external inductor of infinite value connected in series, such that the rate of change of current is always constrained to be zero. Hence, if the differences were mainly due to external inductances then it may be expected that the simulated armature induced emf waveform for constant current excitation would more closely match the experimental results than that calculated using constant voltage source excitation.

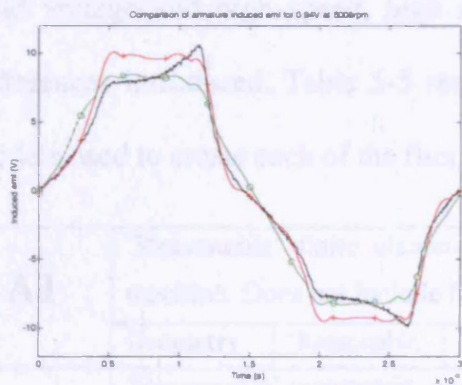
Figure 5-8 shows the simulated armature induced emf waveforms obtained for constant voltage field excitation, as above, and a constant field current set to the mean value of the experimentally recorded current waveform. The B2 flux map was used in both cases. The armature induced emf for constant field current is significantly less than the experimental case and the shape does not closely resemble that obtained experimentally for constant voltage excitation. *Hence, the results of the voltage driven dynamic simulation model show significantly better agreement with experimental results than those obtained assuming constant field current.*



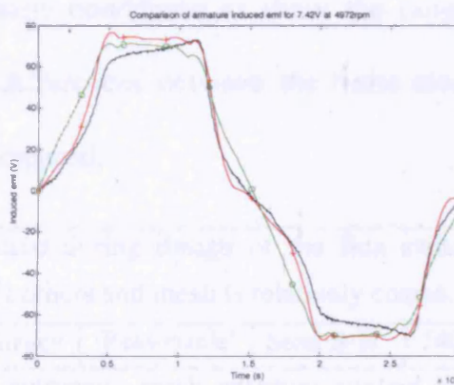
(a) Armature induced emf for 1.02V field excitation at 1094rpm



(b) Armature induced emf for 7.56V field excitation at 1170rpm



(c) Armature induced emf for 0.94V field excitation at 5008rpm



(d) Armature induced emf for 7.42V field excitation at 4972rpm

Experimental  
 Simulated (Voltage source)     Simulated (Current source)

**Figure 5-8 Comparison of experimental and simulated results for the 8/4 flux switching machine with voltage source and current source field excitation set to experimental mean value**

**5.4.4 Effects of finite element data quality**

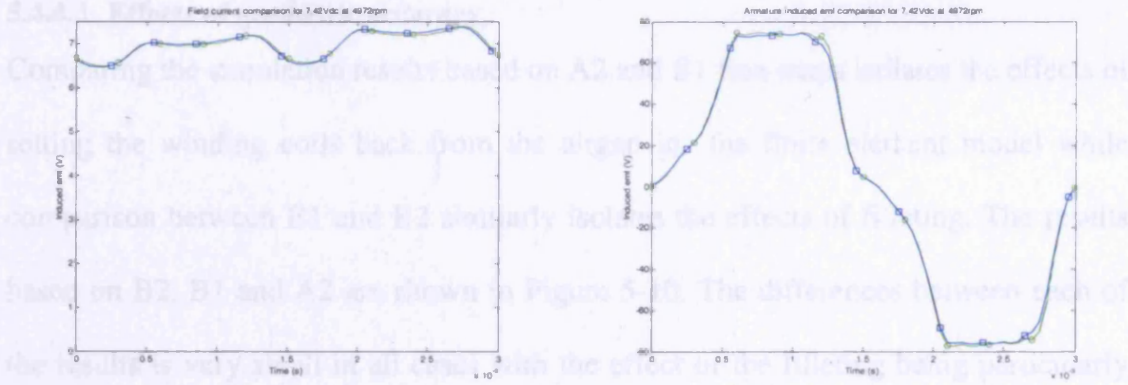
To quantify the effects on simulated results of data derived from different finite element models a number of comparisons were made. In each case the quadratic polynomial contour interpolation method, described in chapter 4, was used for data conversion and the same measured field resistance was used in each case such that the results are directly comparable with each other. The comparisons made show the differences in simulated field current and armature induced emf for low speed, low field voltage and high speed, high field voltage conditions to show the range of differences introduced. Table 5-5 recaps the differences between the finite element models used to create each of the flux maps compared.

<b>A1</b>	'Reasonable' finite element model used during design of the flux switching machine. Does not include filleting of corners and mesh is relatively coarse.					
	<b>Geometry</b>	'Reasonable'	<b>Mesh/Accuracy</b>	'Reasonable'	<b>Steel B-H</b>	540Hz
<b>A2</b>	'Reasonable' geometric model with automatic mesh adaption applied during solution to yield good numerical accuracy					
	<b>Geometry</b>	'Reasonable'	<b>Mesh/Accuracy</b>	Accurate	<b>Steel B-H</b>	540Hz
<b>B1</b>	Using new parameterised model without filleting but with coils set back from the airgap. Mesh adaption is also applied during solution.					
	<b>Geometry</b>	'Better'	<b>Mesh/Accuracy</b>	Accurate	<b>Steel B-H</b>	540Hz
<b>B2</b>	As B1 with filleting added to precisely model the manufactured lamination geometry.					
	<b>Geometry</b>	Precise	<b>Mesh/Accuracy</b>	Accurate	<b>Steel B-H</b>	540Hz
<b>B3</b>	As B2 but using 20Hz steel B-H characteristic					
	<b>Geometry</b>	Precise	<b>Mesh/Accuracy</b>	Accurate	<b>Steel B-H</b>	20Hz

**Table 5-5 Summary of finite element models used to create flux maps**

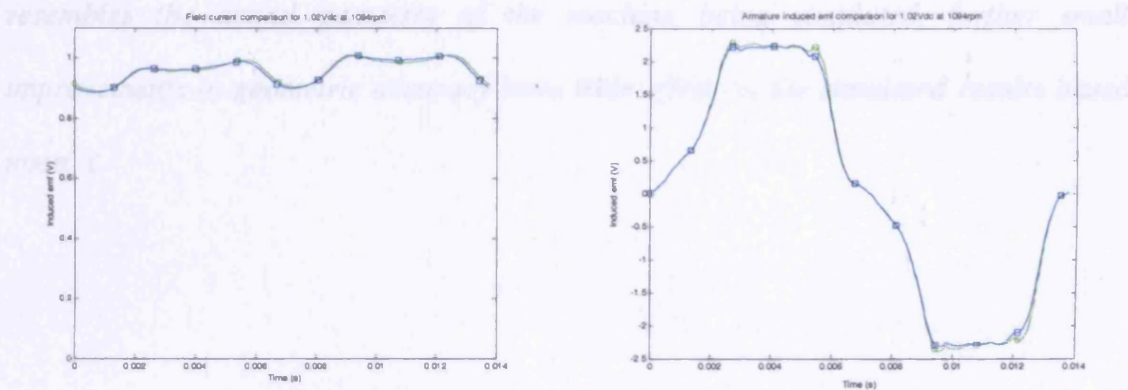
#### **5.4.4.1 Effects of finite element meshing and numerical accuracy**

Figure 5-9 shows a comparison between the simulated results obtained using flux map A1 and the A2 flux map. Thus the differences are almost entirely due to the effects of finite element model meshing and numerical accuracy. For both conditions the difference between the results is small. However, the A2 flux map was some five times more computationally expensive to create than A1. *Hence, provided that the finite element model is properly formulated with a 'reasonable' mesh then the addition of further elements has only a very small effect on the accuracy of simulations based upon it.*



(a) Field current for 7.42V field excitation at 4972rpm

(b) Armature induced emf for 7.42V field excitation at 4972rpm



(c) Field current for 1.02V field excitation at 1094rpm

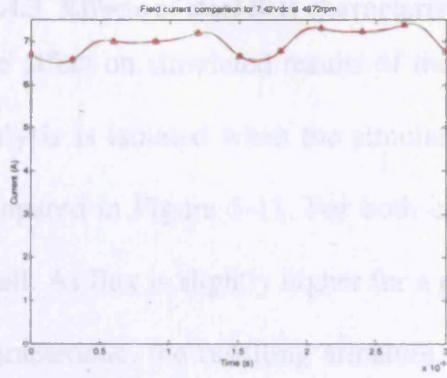
(d) Armature induced emf for 1.02V field excitation at 1094rpm

—■— 'Reasonable' mesh    —●— Refined mesh

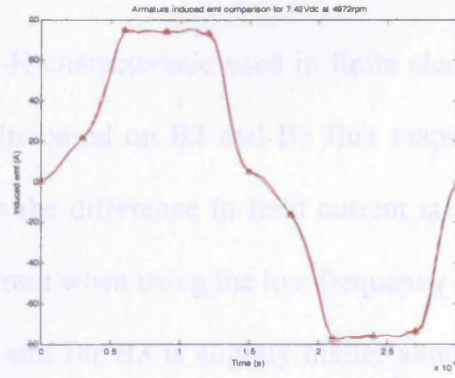
**Figure 5-9** Effect of finite element mesh refinement on simulated results for the 8/4 flux switching machine with voltage source field excitation and armature open circuit at constant speed

#### **5.4.4.2 Effects of geometric accuracy**

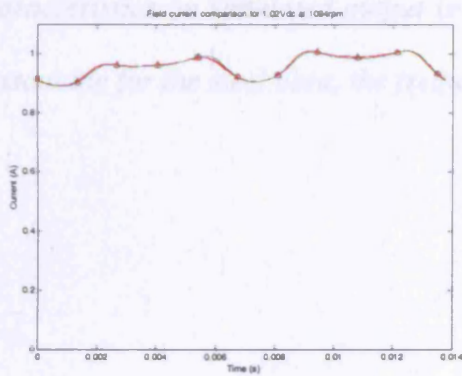
Comparing the simulation results based on A2 and B1 flux maps isolates the effects of setting the winding coils back from the airgap in the finite element model while comparison between B1 and B2 similarly isolates the effects of filleting. The results based on B2, B1 and A2 are shown in Figure 5-10. The differences between each of the results is very small in all cases with the effect of the filleting being particularly small. *These results imply that provided the finite element model reasonably resembles the actual geometry of the machine being simulated, further small improvements in geometric accuracy have little effect on the simulated results based upon it.*



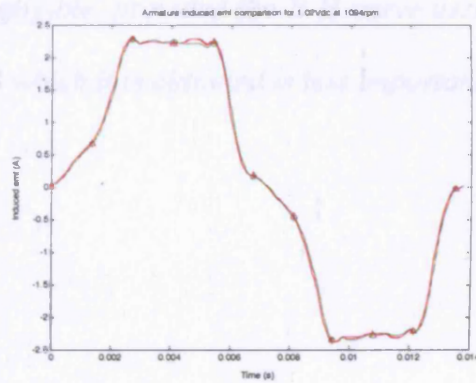
(a) Field current for 7.42V field excitation at 4972rpm



(b) Armature induced emf for 7.42V field excitation at 4972rpm



(c) Field current for 1.02V field excitation at 1094rpm



(d) Armature induced emf for 1.02V field excitation at 1094rpm

—○— 'Reasonable' geometry  
—△— Filletting and coil set-back —△— Coil set-back

Figure 5-10 Effect of finite element model geometric accuracy on simulated results for the 8/4 flux switching machine with voltage source field excitation and armature open circuit at constant speed

#### 5.4.4.3 Effects of steel B-H characteristic

The effect on simulated results of the steel B-H characteristic used in finite element analysis is isolated when the simulation results based on B2 and B3 flux maps are compared in Figure 5-11. For both conditions the difference in field current is very small. As flux is slightly higher for a given current when using the low frequency B-H characteristic, the resulting armature induced emf for B3 is slightly higher although the difference is still relatively small. *Hence, although the effect of B-H characteristics on simulated output is not negligible, provided the B-H curve used is reasonable for the steel used, the frequency at which it is obtained is less important.*



### 5.4.5 Effects of data conversion methods

#### 5.4.5.1 Effects of contour interpolation method

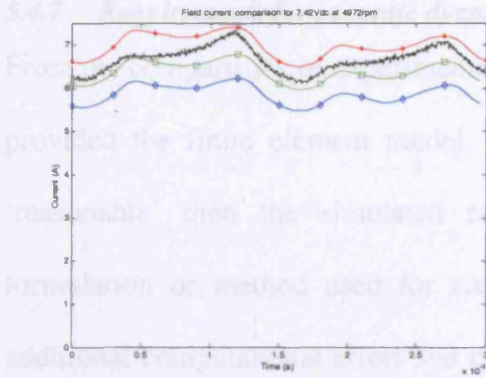
Simulation results based on data derived from the B2 flux map using the PCHIP and polynomial methods for contour interpolation were compared and found to be indiscernible from each other. *Hence, provided the flux map data is of 'reasonable' quality and the selected contour interpolation method provides a 'reasonable' fit to the underlying contours, then the exact method of contour interpolation during data conversion has little effect on the simulation results based on it.*

#### 5.4.5.2 Effects of contour extrapolation

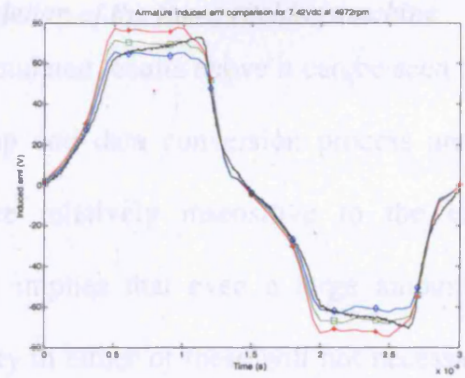
For simulated currents within the original data range the implementation of quadratic polynomial contour extrapolation has no discernable effect on simulated results, as expected. Results were not obtained in the extrapolated range for the back emf test because contour extrapolation does not extend the range of conditions which can be simulated with one winding open circuit in all positions. The extended data obtained using contour extrapolation only relates to certain operating conditions where high currents are expected in one or both windings at positions of strong mutual coupling. *Hence, unless such specific conditions are expected, implementation of contour extrapolation has no noticeable effect on simulated results in the interpolated region and does not necessarily extend the range of currents which may be simulated.*

#### 5.4.6 *Effects of coil temperature and resistance estimate*

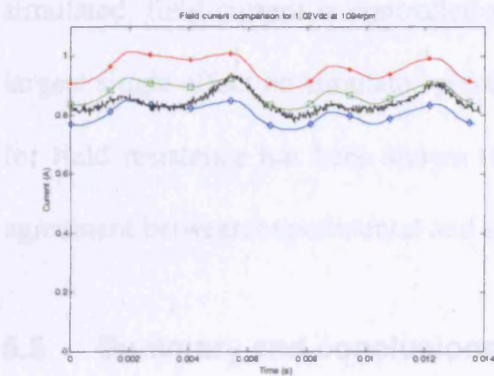
Experimental and simulated results using field resistance adjusted to  $25^{\circ}C$ ,  $50^{\circ}C$  and  $75^{\circ}C$  are compared in Figure 5-12. Although the shapes of each are similar, as temperature is increased so is the field resistance with a corresponding reduction in field current and armature induced emf. *The difference introduced by adjusting the winding resistance is much larger than that due to factors within the finite element model used to create the flux map. Hence, an accurate value for winding resistance is important, either measured if the machine exists or estimated if it does not, for the results of this type of simulation to be accurate.*



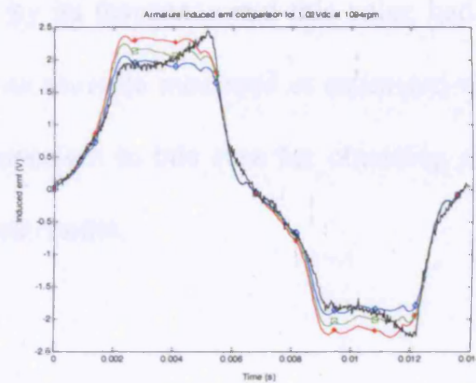
(a) Field current for 7.42V field excitation at 4972rpm



(b) Armature induced emf for 7.42V field excitation at 4972rpm



(c) Field current for 1.02V field excitation at 1094rpm



(d) Armature induced emf for 1.02V field excitation at 1094rpm

Experimental  
 25°C winding temperature  
 75°C winding temperature

**Figure 5-12 Comparison of experimental results and simulated results at various field winding temperatures for the 8/4 flux switching machine with voltage source field excitation and armature open circuit at constant speed**

#### **5.4.7    *Requirements for accurate dynamic simulation of the flux switching machine***

From the comparisons of experimental and simulated results above it can be seen that, provided the finite element model, flux map and data conversion process are all 'reasonable' then the simulated results are relatively insensitive to the exact formulation or method used for each. This implies that even a large amount of additional computational effort and complexity in either of these will not necessarily lead to more accurate simulated results. However, for the case of the back-emf test simulated, field current is controlled mainly by its resistance and this value had the largest single effect on simulated results and an accurate measured or estimated value for field resistance has been shown to be important in this case for obtaining close agreement between experimental and simulated results.

### **5.5    Summary and conclusions**

This chapter has developed a dynamic simulation model for the flux switching machine, either stationary or running at constant speed, with arbitrary voltage excitation on both windings or with one winding open circuit. Simulated and experimental results were compared for the 8/4 flux switching machine running at constant speed with steady dc voltage field excitation and the armature open circuit, i.e. a standard back-emf test.

Good agreement was shown between experimental and simulated results with winding resistance variation having the largest individual effect on simulated results. It was also shown that the simulated results are relatively insensitive to the exact geometric and numerical accuracy of the finite element model used to create the flux map and the techniques used during data conversion, provided 'reasonable' precautions are implemented at each stage. This further supports the position put forward previously that complex and computationally expensive models are not necessary for successful dynamic simulation of the flux switching machine. Furthermore, as the simulation model is rapid at the point of use, using the flux map and converted data, the initial computational investment is rapidly repaid, making the overall system efficient, both in terms of computational expense and user time, for practical design use.

---

# **Chapter 6**

Dynamic simulation model for the  
flux switching motor and drive  
system

---

## **6 DYNAMIC SIMULATION MODEL FOR THE FLUX SWITCHING MOTOR INCLUDING POWER ELECTRONICS AND CONTROL STRATEGY**

### **6.1 Introduction**

While the dynamic simulation model detailed in chapter 5 has been shown to work well for the flux switching machine in isolation from its power electronic drive, i.e. replicating simple experimental tests which are common to both flux switching motor and generator, for detailed design and optimisation of the flux switching motor and drive a complete system simulation model is developed which includes the power electronic circuit and control algorithm, both of which have a strong effect on overall system performance and characteristics. The system model presented in this chapter describes the complete drive system for the flux switching motor in the series connected configuration, as this has been found to be favourable in operation, running at constant speed with a specified power switch control algorithm. Hence, performance of the motor can be examined, component values selected and the control algorithm optimised for a variety of constant running speeds. The model developed also accounts for the behaviour of the bifilar armature winding in the electronic circuit and has been implemented in MATLAB [61].

## 6.2 System to be modelled

Figure 6-1 shows the motor and power electronic drive system which has been modelled. It is in the series connected configuration and represents the generic power electronic circuit which is generally used for operation of the flux switching motor with either field diode  $D_f$ , intermediate capacitor  $C$ , or both, being utilised depending on the application. Each winding is modelled as a resistance and inductance in series and the conventional dot notation indicates the orientation of each coil, showing the connections of the bifilar armature. External inductances and resistances are included in series with each winding to allow for lead resistance, end winding inductance etc. The armature external inductances are magnetically close coupled. Table 6-1 summarises the symbols used in Figure 6-1 to describe the drive system and their meanings.

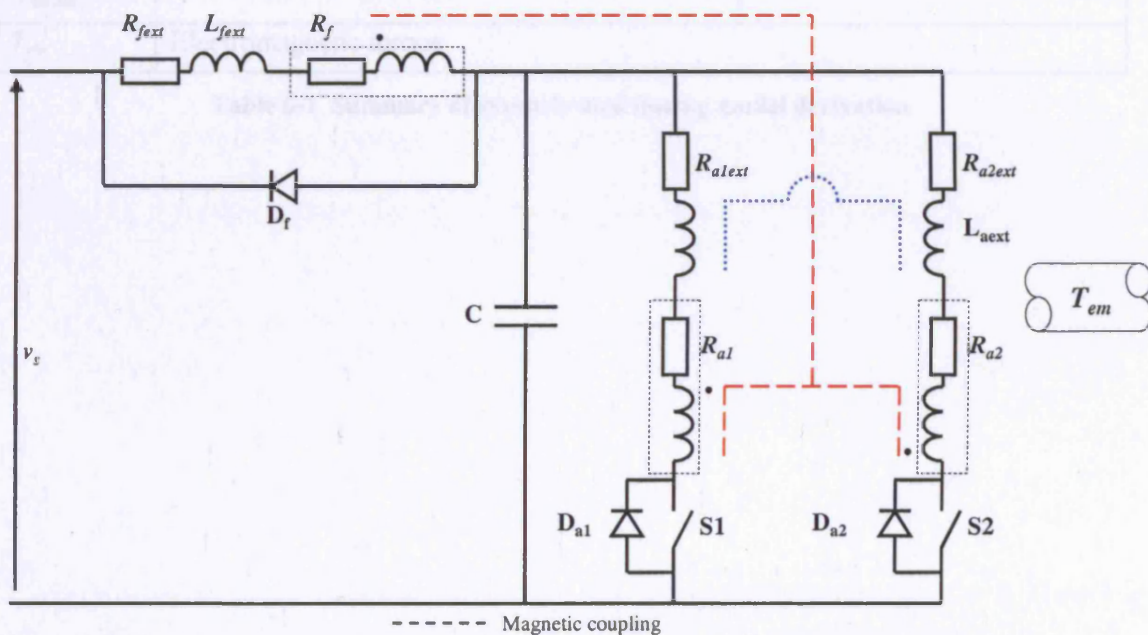


Figure 6-1 Circuit diagram of flux switching motor and drive system modelled

Symbol	Meaning
Field, f	Field winding described by the denormalised flux map and converted data
Armature, a1, a2, a	Armature winding described by the denormalised flux map and converted data. The coils of the bifilar winding are labelled 1 and 2.
$R_f, R_a$	Field and armature winding resistances respectively
$R_{fext}, R_{a1ext}, R_{a2ext}$	Field, armature 1 and armature 2 external resistances respectively
$L_{fext}, L_{aext}$	Field and armature external inductances respectively
S1, S2	Armature 1 and 2 switches respectively
$D_f$	Field diode (optional if capacitor C is present in the circuit)
$D_{a1}, D_{a2}$	Armature 1 and 2 and field diodes respectively.
C	Linear capacitor (optional if $D_f$ is present in the circuit)
$v_c$	Voltage across capacitor C
$V_s$	Voltage source supply from dc link, either constant or with ripple
$V_{dfon}$	Field diode forward bias voltage
$V_{da1on}, V_{da2on}$	Armature 1 and armature 2 diode forward bias voltages respectively
$T_{em}$	Electromagnetic torque

Table 6-1 Summary of symbols used during model derivation



Figure 6-2 Operation of flux switching motor drive system in normal operation

6.2.1 Normal operation of the flux switching motor drive system

During normal operation of the flux switching motor if switch S1 is switched on at a time when field current is non-zero, as is generally the case during normal operation, current rises in armature bifilar coil a1 driven by the voltage  $v_c$  which is maintained at  $v_s + V_{dfon}$  by the continuing field current as long as field current remains greater than armature current, as illustrated in Figure 6-2a. Although field current also increases during this time it is possible for armature current to become higher than field current, causing a drop in capacitor voltage  $v_c$ . When switch S1 is turned off current cannot continue to flow in the armature bifilar coil a1 and instantaneously transfers to coil a2 which is connected in opposition to a1, as illustrated in Figure 6-2b. Hence, if both a1 and a2 have identical number of turns then the current flowing into the armature leg of the circuit instantaneously changes direction but not magnitude. This current in a2 now falls rapidly as it is opposed by capacitor voltage,  $v_c$ , which is clamped to a maximum value of  $v_s + V_{dfon}$  by the presence of field diode  $D_f$ . A similar process takes place when switch S2 is operated. Thus, the behaviour of the bifilar winding in the circuit depends on both the state of the switches and the armature mmf at that time.

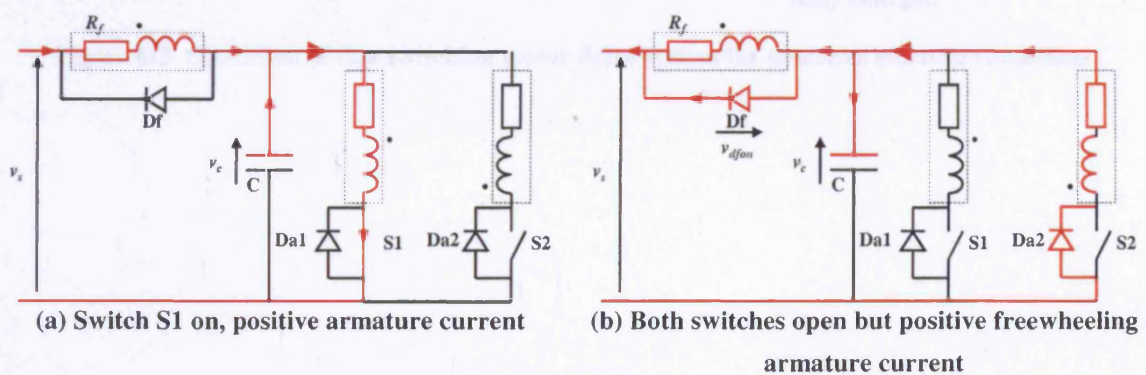


Figure 6-2 Operation of flux switching motor drive system in normal operation

6.2.2 Transient start-up operation of the flux switching motor drive system

Starting from a completely de-energised state and holding the rotor stationary, as supply voltage  $v_s$  is applied with neither switch on, current builds in the field driven by the difference between  $v_s$  and  $v_c$  until  $v_c$  reaches  $v_s + V_{dfon}$  where  $v_c$  is the voltage across capacitor C and  $V_{dfon}$  is the forward bias voltage of field diode  $D_f$  as illustrated in Figure 6-3a. As neither switch is on the armature is effectively open circuit and armature current remains zero, although there is an induced emf by transformer action, the magnitude of which depends on the field to armature turns ratio and rotor position. When  $v_c = v_s + V_{dfon}$  there is maximum current flowing in the field which must continue to flow, which it does by free-wheeling through  $D_f$  as in Figure 6-3b until a steady state is reached with zero field current and  $v_c = v_s + V_{dfon}$ .

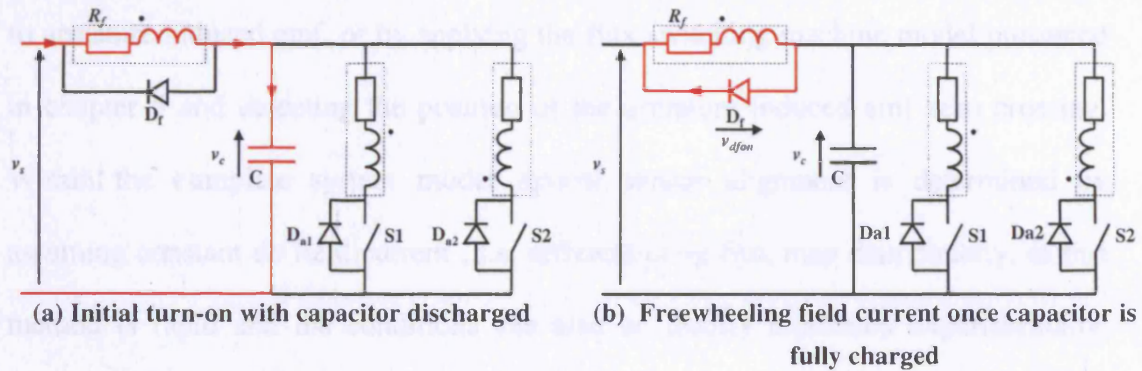


Figure 6-3 Operation of flux switching motor drive system for transient start-up conditions

## 6.3 Model development

### 6.3.1 *Position and optical sensor signal calibration of simulation model*

In practice, the state of the switches at a given instant is generally derived from the state of the shaft mounted optical sensor signal and a control algorithm such that the switches are switched on and off at specified positions in the electrical cycle. Position within the electrical cycle of the flux switching motor is defined in the direction of normal rotation relative to the zero crossing of armature induced emf for constant dc excited field. Hence, physical position and rotor angle in the finite element model are not generally the same and it is necessary to correlate them. This may be done by differentiating armature flux linkage from finite element data over a complete cycle for fixed field current and armature open circuit, yielding a waveform of similar shape to armature induced emf, or by applying the flux switching machine model presented in chapter 5 and detecting the position of the armature induced emf zero crossing. Within the complete system model optical sensor alignment is determined by assuming constant dc field current, i.e. differentiating flux map data directly, as this method is rapid and the conditions can also be readily replicated experimentally, either by using a regulated current power supply or placing a large inductance in series with the field to reduce current ripple.

Having obtained the positions of armature induced emf zero crossings the corresponding position within the electrical cycle and optical sensor signal can be derived, taking into account mechanical advance angle and duty cycle as illustrated in Figure 6-4 where  $\theta_{adv}$  is mechanical advance angle,  $\theta_{cycle}$  is the number of mechanical degrees per complete electrical cycle and duty cycle is  $\theta_{high}/\theta_{cycle}$ . The positional and optical sensor data generated can be used to aid visualisation and comparison of results and as inputs to switch control algorithms which are implemented during simulation.

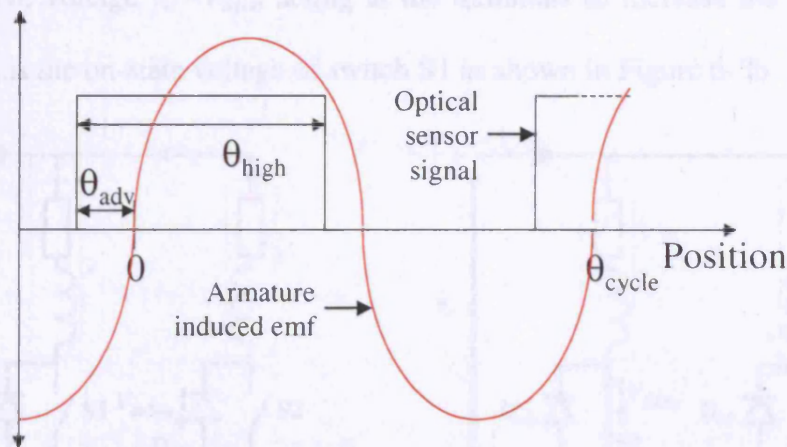


Figure 6-4 Example of optical position sensor signal calibration in the simulation model

### 6.3.2 Behaviour of the bifilar armature winding in the circuit

As described in section 6.2.1 the behaviour of the bifilar armature in the power electronic circuit depends on the state of the switches and the mmf in the armature. Mmf in the armature is a superposition of the mmf in both bifilar armature coils, i.e.

$$F_a = N_{a1}i_{a1} + N_{a2}i_{a2} \quad (6.1)$$

where  $F_a$  is armature resultant mmf,  $N$  is number of turns,  $i$  is current and the subscripts  $a1$  and  $a2$  denote the two bifilar coils of the armature. Positive current, hence mmf, acts to make armature flux linkage more positive. For example, if there is a positive mmf in the armature and both switches are open then this current must be free-wheeling in coil  $a2$  through diode  $D_{a2}$  and the effective voltage driving the flux linkage towards zero is  $-(v_c + V_{da2on})$  where  $v_c$  is capacitor voltage and  $V_{da2on}$  is the forward bias voltage of diode  $D_{a2}$  as illustrated in Figure 6-5a. However, given the same armature mmf but with switch S1 on then the current must be flowing in coil  $a1$  with effective voltage  $v_c - V_{S1on}$  acting at the terminals to increase the flux linkage, where  $V_{S1on}$  is the on-state voltage of switch S1 as shown in Figure 6-5b.

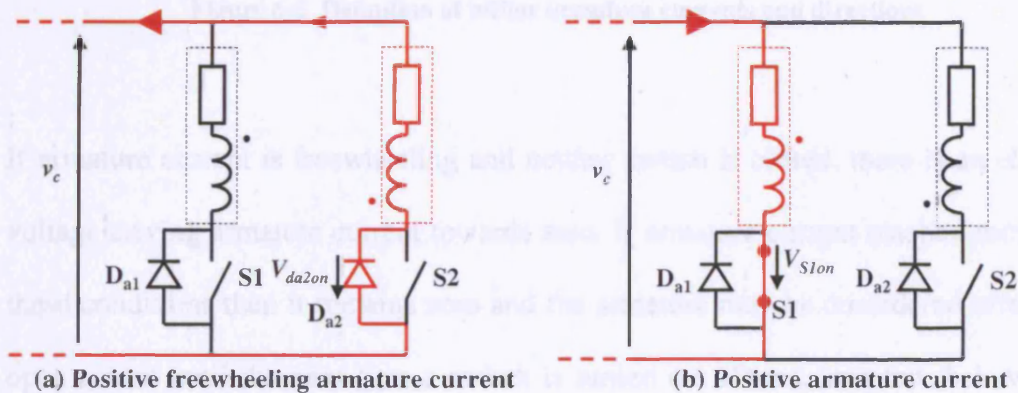


Figure 6-5 Behaviour of the bifilar armature winding in the drive circuit

Referring to the denormalised data derived from finite element analysis, closing switch S1 effectively applies a positive voltage to the armature, making armature flux linkage more positive, while closing S2 effectively applies a negative voltage to the armature, making armature flux linkage more negative, due to the orientation in which the two bifilar coils are connected. If the number of turns in each bifilar coil is identical, effective armature current is given by the relationship

$$i_a = i_{a1} + i_{a2} \quad (6.2)$$

and

$$i_{arm} = i_{a1} - i_{a2} \quad (6.3)$$

where  $i_{arm}$ ,  $i_{a1}$  and  $i_{a2}$  are defined in Figure 6-6 and  $i_a$  is effective armature current. Positive  $i_{a1}$  and  $i_{a2}$  are defined such that both make armature flux linkage more positive.

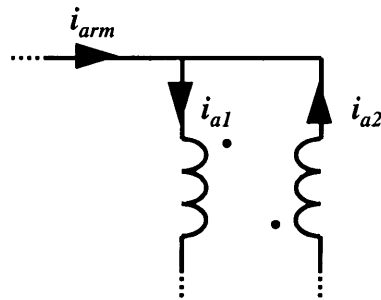


**Figure 6-6 Definition of bifilar armature currents and directions**

If armature current is freewheeling and neither switch is closed, there is an effective voltage driving armature current towards zero. If armature current reaches zero under these conditions then it remains zero and the armature may be considered effectively open circuit until the next time a switch is turned on. Hence, armature behaviour in simulation depends on current at the present and next time steps as well as switch states.

Table 6-2 summarises all the possible combinations of switch state, and armature current, at present and next time steps, along with the effective values assigned for them which are discussed in more detail below. Each case is given a unique number by which it will be referred to in the following discussion and *AOC* is a Boolean flag to indicate whether the armature is to be considered effectively open circuit.

S1	S2	$i_{a(n)}$	$v_{a(n)}$	$i_{a(n+1)}$	$i_{arm(n+1)}$	$i_{a1(n+1)}$	$i_{a2(n+1)}$	$AOC_{(n+1)}$	Case	Comment
Off	Off	<0	$\frac{v_{c(n)} + v_{c(n+1)}}{2} + V_{da1on}$	<0	$i_{a(n+1)}$	$i_{a(n+1)}$	0	No	1	Positive free-wheeling
				0	0	0	0	Yes	2	Positive free-wheeling ending
				>0	0	0	0	Yes	3	Positive free-wheeling ending
Off	Off	0	$\left( \frac{\Psi_{a(n+1)} - \Psi_{a(n)}}{\Delta t} \right) + \frac{v_{c(n)} + v_{c(n+1)}}{2} + V_{da1on}$	<0	$i_{a(n+1)}$	$i_{a(n+1)}$	0	No	4	Negative conduction starting due to armature induced emf
				0	0	0	0	Yes	5	Armature effectively open circuit
				$\frac{\Psi_{a(n+1)} - \Psi_{a(n)}}{\Delta t} - \left( \frac{v_{c(n)} + v_{c(n+1)}}{2} + V_{da2on} \right)$	>0	$-i_{a(n+1)}$	0	$i_{a(n+1)}$	No	6
Off	Off	>0	$-\left( \frac{v_{c(n)} + v_{c(n+1)}}{2} + V_{da2on} \right)$	<0	0	0	0	Yes	7	Negative free-wheeling ending
				0	0	0	0	Yes	8	Negative free-wheeling ending
				>0	$-i_{a(n+1)}$	0	$i_{a(n+1)}$	No	9	Negative free-wheeling
On	Off	<0	$\frac{v_{c(n)} + v_{c(n+1)}}{2} + V_{da1on}$	<0	$i_{a(n+1)}$	$i_{a(n+1)}$	0	No	10	Positive excitation
				0	$i_{a(n+1)}$	$i_{a(n+1)}$	0	No	11	Positive excitation
				>0	$i_{a(n+1)}$	$i_{a(n+1)}$	0	No	12	Positive excitation
On	Off	0	$\frac{v_{c(n)} + v_{c(n+1)}}{2} - V_{s1on}$	<0	$i_{a(n+1)}$	$i_{a(n+1)}$	0	No	13	Positive excitation
				0	$i_{a(n+1)}$	$i_{a(n+1)}$	0	No	14	Positive excitation
				>0	$i_{a(n+1)}$	$i_{a(n+1)}$	0	No	15	Positive excitation
On	Off	>0	$\frac{v_{c(n)} + v_{c(n+1)}}{2} - V_{s1on}$	<0	$i_{a(n+1)}$	$i_{a(n+1)}$	0	No	16	Positive excitation
				0	$i_{a(n+1)}$	$i_{a(n+1)}$	0	No	17	Positive excitation
				>0	$i_{a(n+1)}$	$i_{a(n+1)}$	0	No	18	Positive excitation

Table 6-2 (part 1 of 2)

Off	On	<0	$-\left(\frac{v_{c(n)} + v_{c(n+1)}}{2} - V_{S2on}\right)$	<0	$-i_{a(n+1)}$	0	$i_{a(n+1)}$	No	19	Negative excitation
				0	$-i_{a(n+1)}$	0	$i_{a(n+1)}$	No	20	Negative excitation
				>0	$-i_{a(n+1)}$	0	$i_{a(n+1)}$	No	21	Negative excitation
Off	On	0	$-\left(\frac{v_{c(n)} + v_{c(n+1)}}{2} - V_{S2on}\right)$	<0	$-i_{a(n+1)}$	0	$i_{a(n+1)}$	No	22	Negative excitation
				0	$-i_{a(n+1)}$	0	$i_{a(n+1)}$	No	23	Negative excitation
				>0	$-i_{a(n+1)}$	0	$i_{a(n+1)}$	No	24	Negative excitation
Off	On	>0	$-\left(\frac{v_{c(n)} + v_{c(n+1)}}{2} + V_{da2on}\right)$	<0	$-i_{a(n+1)}$	0	$i_{a(n+1)}$	No	25	Negative excitation
				0	$-i_{a(n+1)}$	0	$i_{a(n+1)}$	No	26	Negative excitation
				>0	$-i_{a(n+1)}$	0	$i_{a(n+1)}$	No	27	Negative excitation
On	On	<0	Not allowed	<0	N/A	N/A	N/A	N/A	28	Forbidden condition
		0		0	N/A	N/A	N/A	N/A	29	Forbidden condition
		>0		>0	N/A	N/A	N/A	N/A	30	Forbidden condition
On	On	<0	Not allowed	<0	N/A	N/A	N/A	N/A	31	Forbidden condition
		0		0	N/A	N/A	N/A	N/A	32	Forbidden condition
		>0		>0	N/A	N/A	N/A	N/A	33	Forbidden condition
On	On	<0	Not allowed	<0	N/A	N/A	N/A	N/A	34	Forbidden condition
		0		0	N/A	N/A	N/A	N/A	35	Forbidden condition
		>0		>0	N/A	N/A	N/A	N/A	36	Forbidden condition

Table 6-2 Possible operating conditions for the flux switching motor with effective armature voltages and currents

### 6.3.2.1 Assignment of effective applied armature voltage

Treating the bifilar armature mathematically as a single winding, its effective current,  $i_a$ , being a superposition of coil currents  $i_{a1}$  and  $i_{a2}$ , it is necessary to translate the effects of closing either switch or freewheeling current in either bifilar coil into an effective voltage acting on the armature to either increase or decrease the effective flux linkage, hence effective current. The effective voltage acting, which is assumed constant over the simulation time step, depends on the switch states, S1 and S2, and the armature current at the beginning of the time step,  $i_{a(n)}$ . Each possible combination summarised in Table 6-2 is discussed in turn.

#### Cases 1-3

If both switches are off but there is a negative effective armature current then it must be free-wheeling in coil a1 through diode  $D_{a1}$  with an effective voltage

$$\frac{v_{c(n)} + v_{c(n+1)}}{2} + V_{da1on} \quad (6.4)$$

acting to bring it towards zero, where  $V_{da1on}$  is the forward bias voltage of diode  $D_{a1}$ .

#### Cases 4-6

If both switches are off and there is no armature current flowing then in general there will be no effective voltage acting on the armature, i.e. it may be considered effectively open circuit (case 5). However, due to changing field current and changing mutual coupling with rotation, there is an emf induced in the armature which is given by

$$\frac{\Psi_{a(n+1)} - \Psi_{a(n)}}{\Delta t} \quad (6.5)$$

If this emf exceeds the maximum capacitor voltage available to oppose it then a current will begin to flow in the armature through one of the diodes, i.e. there is an effective voltage applied to the armature. Hence, if

$$\frac{\Psi_{a(n+1)} - \Psi_{a(n)}}{\Delta t} > \frac{v_{c(n)} + v_{c(n+1)}}{2} + V_{da2on} \quad (6.6)$$

where  $\Psi_{a(n)}$  and  $\Psi_{a(n+1)}$  are armature flux linkage at the beginning and end of the time step and  $\Delta t$  is the time step, then there is an effective voltage acting to make armature flux linkage more positive and give rise to positive armature current given by

$$\frac{\Psi_{a(n+1)} - \Psi_{a(n)}}{\Delta t} - \left( \frac{v_{c(n)} + v_{c(n+1)}}{2} + V_{da2on} \right) \quad (6.7)$$

(case 6). Similarly, if

$$\frac{\Psi_{a(n+1)} - \Psi_{a(n)}}{\Delta t} < - \left( \frac{v_{c(n)} + v_{c(n+1)}}{2} + V_{da1on} \right) \quad (6.8)$$

then there will be an effective voltage acting to make armature flux linkage more negative and give rise to negative armature current given by

$$\left( \frac{\Psi_{a(n+1)} - \Psi_{a(n)}}{\Delta t} \right) + \frac{v_{c(n)} + v_{c(n+1)}}{2} + V_{da1on} \quad (6.9)$$

(case 4).

This mechanism allows armature conduction to restart without either switch being closed and once this has occurred cases 1-3 or 7-9 will apply thereafter.

However, during simulation of the flux switching motor and drive the magnitude of induced emf is similar to the voltage available to oppose it. Under these conditions implementation of this mechanism can lead to numerical instability and oscillation of the solution and/or erroneous restarting of conduction due to the differentiation of armature flux linkages with random errors and small time step involved. Hence, for the flux switching motor, although this effect has been observed experimentally, it may reasonably be neglected without seriously affecting the results obtained. However, for the case of a flux switching generator, this effect may not be neglected but the induced armature emf will tend to be much larger than the voltage available to oppose it and such stability problems would be less likely to arise.

#### Cases 7-9

If both switches are off but there is a positive effective armature current then it must be free-wheeling in armature coil a2 with an effective voltage

$$-\left( \frac{v_{c(n)} + v_{c(n+1)}}{2} + V_{da2on} \right) \quad (6.10)$$

acting to bring it towards zero, where  $V_{da2on}$  is the forward bias voltage of diode  $D_{a2}$ .

#### Cases 10-18

If switch 1 is on and switch 2 is off then the effective voltage applied to the armature over the time step must be positive, acting to make armature flux linkage, hence current, more positive. If armature current is negative then it is still freewheeling in coil a1 through diode  $D_{a1}$  with an effective voltage

$$\frac{v_{c(n)} + v_{c(n+1)}}{2} + V_{da1on} \quad (6.11)$$

(cases 10-12), while if armature current  $i_a$  is zero or positive then it must be flowing in armature a1 through switch S1 with an effective applied voltage given by

$$\frac{v_{c(n)} + v_{c(n+1)}}{2} - V_{s1on} \quad (6.12)$$

(cases 13-18).

### Cases 19-27

If switch 1 is off and switch 2 is on then the effective voltage applied to the armature over the time step must be negative, acting to make armature flux linkage, hence current, more negative. If armature current is positive then it is still freewheeling in coil a2 through diode  $D_{a2}$  with an effective voltage

$$-\left( \frac{v_{c(n)} + v_{c(n+1)}}{2} + V_{da2on} \right) \quad (6.13)$$

(cases 25-27), while if armature current  $i_a$  is zero or negative then it must be flowing in armature a2 through switch S2 with an effective applied voltage given by

$$-\left( \frac{v_{c(n)} + v_{c(n+1)}}{2} - V_{s2on} \right) \quad (6.14)$$

(cases 19-24).

### Cases 28-36

If both switches are ever switched on simultaneously this will create a shoot-through condition in the armature immediately giving rise to extremely large currents which are controlled only by stray inductances which are not modelled. In practice, this leads to rapid failure of the switches. There would also be potentially very large circulating currents in the armature coils if they were non-identical. Hence, such a condition is forbidden and will cause the simulation to be aborted if it occurs at any time.

#### 6.3.2.2 Assignment of armature current to bifilar coils

Although total armature current cannot change instantaneously, the bifilar coil in which it flows, and hence the direction of current  $i_{arm}$  in the circuit, can. The coil in which armature current flows is determined by the polarity of the effective armature current and the switch states. Furthermore, if a freewheeling armature current falls to zero during a time step or armature current begins the time step at zero and neither switch is on nor conduction restarted due to induced emf, then it must be held at zero and the armature treated as effectively open circuit until the next time an effective voltage is applied, either due to a switch being turned on or induced emf. Hence, the assignment of armature current for the end of the time step being calculated ( $n+1$ ) depends on the switch states, polarity of effective applied voltage and polarity of current at the start of the time step ( $n$ ). Each of the possible combinations summarised in Table 6-2 is discussed below.

### Cases 1-3

If neither switch is on and there is a negative current at the beginning of the time step but a zero or positive current is estimated at the end then negative free-wheeling in armature coil  $a_1$  is ending and armature current must be held at zero (case 1). However, if neither switch is on but there is a negative armature current at both the beginning and end of the time step then current is continuing to free-wheel in armature coil  $a_1$  through diode  $D_{a1}$  (cases 2 and 3).

### Cases 4-6

If neither switch is on and current at the beginning of the time step is zero but current at the end is negative due to a negative effective voltage then free-wheeling conduction in armature coil  $a_1$  through diode  $D_{a1}$  is being started by induced emf (case 4). Similarly, if neither switch is on and current at the beginning of the time step is zero but current at the end is positive due to a positive effective voltage then free-wheeling conduction in armature coil  $a_2$  through diode  $D_{a2}$  is being started by induced emf (case 6). However, if neither switch is on and current is zero at the beginning and end of the time step then no effective voltage has been applied and the armature is effectively open circuit (case 5).

### Cases 7-9

If neither switch is on and there is a positive current at the beginning of the time step but a zero or negative current is estimated at the end then positive free-wheeling in armature coil  $a_2$  is ending and armature current must be held at zero (cases 7 and 8). However, if neither switch is on but there is a positive current flowing at both the beginning and end of the time step then current is free-wheeling normally in armature coil  $a_2$  through diode  $D_{a2}$  (case 9).

### Cases 10-18

If switch 1 is on and switch 2 is off and there is a positive armature current then this must be flowing in armature coil a1 through switch S1 (cases 11-12, 14-15, 17-18). However, if switch 1 is on and switch 2 is off while there is still negative armature current then it must still be free-wheeling in armature coil a1 through diode  $D_{a1}$  (cases 10, 13 and 16).

### Cases 19-27

If switch 1 is off and switch 2 is on and there is a negative armature current then this must be flowing in armature coil a2 through switch S2 (cases 19-20, 22-23, 25-26). However, if switch 1 is off and switch 2 is on while there is still positive armature current then it must still be free-wheeling in armature coil a2 through diode  $D_{a2}$  (cases 21, 24 and 27).

### Cases 28-36

As noted above, both switches being on simultaneously at any time will cause the simulation to abort.

#### 6.3.3 Adding external inductance to windings in the circuit

As given in chapter 5 the flux linkage of either winding at the end of the time step is given by the discrete time relationship

$$\Psi_{x(n+1)} = \Psi_{x(n)} + \left( v_x - \frac{i_{x(n)} + i_{x(n+1)} (\Psi_{f(n+1)}, \Psi_{a(n+1)}, \theta_{(n+1)})}{2} R_x \right) \Delta t \quad (6.15)$$

where  $\Psi$  is flux linkage,  $v$  is terminal voltage,  $i$  is winding current,  $\theta$  is position,  $R$  is winding resistance,  $\Delta t$  is time step. Subscripts  $f, a, x$  denote field, armature and either winding respectively and subscripts  $(n)$  and  $(n+1)$  represent the start and end of the time step (i.e. present and next values) respectively. However, in order to add some allowance in the simulation for end windings, leakage inductance and dynamic effects, all of which act to reduce the magnitude and/or rate of change of torque producing flux linkage a linear external inductance may be added in series with each winding which is not magnetically coupled with the main winding flux.

For a linear inductance,  $L$ , flux linkage is given by

$$\Psi_{xext} = Li_x \quad (6.16)$$

where subscript  $xext$  denotes 'external to either field or armature'. The voltage applied to the terminals of the winding acts to change the total flux linking that winding, including series external inductance. Hence, the effect of the applied voltage is effectively divided between changing the main winding flux linkage which crosses the airgap to produce torque, as derived from the flux map, and flux linking the external inductance. Thus, the effective voltage available to change the main torque producing flux is reduced leading to a lower rate of change of main flux linkage and current than without the external inductance.

Given the present current,  $i_{x(n)}$ , and an estimate for the current at the next time step,  $i_{x(n+1)}$ , the change in flux linkage of the external linear inductor over the time step is

$$\Delta\Psi_{xext} = (i_{x(n+1)} - i_{x(n)}) \times L_{xext} \quad (6.17)$$

where subscripts  $(n)$  and  $(n+1)$  denote present and next values respectively. This gives an emf in the external inductance of

$$e_{xext} = \frac{\Delta\Psi_{xext}}{\Delta t} \quad (6.18)$$

which acts in opposition to the rate of change of current. Hence, the remaining voltage available to change the main winding flux linkage is

$$v_{eff} - e_{xext} \quad (6.19)$$

where  $v_{eff}$  is the effective voltage at the winding terminals over the time step as derived in section 6.3.2. Using this relationship, flux linking the external inductance at the next time step is

$$\Psi_{xext(n+1)} = L_{xext} \times i_{x(n+1)} \quad (6.20)$$

and main flux linkage is found using the modified relationship

$$\Psi_{x(n+1)} = \Psi_{x(n)} + \left( \left\{ v_x - \frac{(i_{x(n+1)} - i_{x(n)}) \times L_{xext}}{\Delta t} \right\} - \frac{i_{x(n)} + i_{x(n+1)} (\Psi_{f(n+1)}, \Psi_{a(n+1)}, \theta_{(n+1)})}{2} R_x \right) \Delta t \quad (6.21)$$

where  $\Psi$  is flux linkage,  $i$  is winding current,  $v$  is applied terminal voltage,  $R$  is winding resistance,  $\Delta t$  is time step and the subscripts  $f$ ,  $a$ ,  $x$ ,  $(n)$ , and  $(n+1)$  denote field, armature and either winding, present value and next value respectively.

The external inductance added to the windings in this way is linear and lossless which is reasonable for adding some correction for end-winding inductance that is not included in 2-dimensional finite element analysis. However, eddy currents induced in the steel laminations also have the effect of limiting rate of change of flux linkage but are a loss mechanism converting electrical energy to heat. This loss is not modelled by adding an external inductance although its effect on current waveforms may be accounted for by adding a suitable value of external inductance. A non-linear and/or position dependent external inductance may be modelled in a similar way by defining the relationship

$$\Psi_{xex}(i_x, \theta) \quad (6.22)$$

#### 6.3.4 Switch control algorithms

In general the positions within the electrical cycle at which the switches must be turned on and off to achieve optimal performance are a function of speed and load conditions. Hence, the simulation model allows control algorithms to be flexibly specified to account for various conditions and allow rapid optimisation of the control algorithm. This functionality has been included in such a way that the switches can be controlled either by time, position within the electrical cycle, optical sensor signal, as discussed in section 6.3.1, or any combination of these. For example, the switches can be set to operate a specified time interval after a transition in the optical sensor signal as may be the case in practice.

To allow flexibility and rapid implementation of new control algorithms, the name of the control function to be used is specified in the simulation parameters. Inputs of optical sensor signal, position within the electrical cycle relative to armature emf zero crossing, mechanical degrees per cycle, simulated time and the last eight positive and negative going optical sensor transitions are passed to the switch control function which is a simple function that is called from the main simulation code. Using any combination of these inputs the states of the switches at every time step may be derived. For example, for optimisation of the control algorithm absolute position within the electrical cycle may be used while to accurately reproduce the operation of a control algorithm as implemented in a microcontroller a time delay since optical sensor transitions may be more appropriate. As in practice, care must be taken to ensure that at no time are both switches on simultaneously or else the simulation will abort.

Figure 6-7 shows an example of the implementation of a simple position controlled switch control algorithm. In the example shown a complete electrical cycle is 90 mechanical degrees and each switch is on for 30 mechanical degrees, advanced by 6 mechanical degrees. Thus S1 is on for  $\theta \leq 24$  and  $\theta \geq 84$ , S2 is on for  $39 \leq \theta \leq 69$  and for all other  $\theta$  both S1 and S2 are off. Position within the electrical cycle,  $\theta$ , is obtained for any position as the remainder from  $\alpha/\theta_{cycle}$  where  $\alpha$  is the position and  $\theta_{cycle}$  is the number of mechanical degrees per complete electrical cycle.

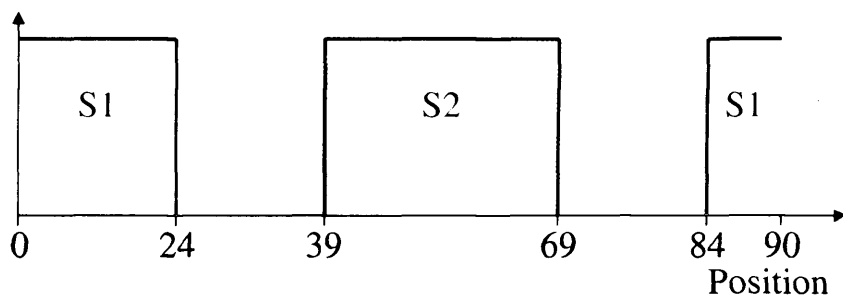


**Figure 6-7** Example implementation of switch operating positions for the flux switching motor

## 6.4 Implementation

Using the relationships developed to characterise the behaviour of the bifilar winding in the circuit, calibrate and control the switches it is possible to solve the electrical circuit system of Figure 6-1 with diode  $D_f$  and/or capacitor  $C$  present. The simulation model is developed initially for the general case where both are present and then the special cases where either is omitted are discussed.

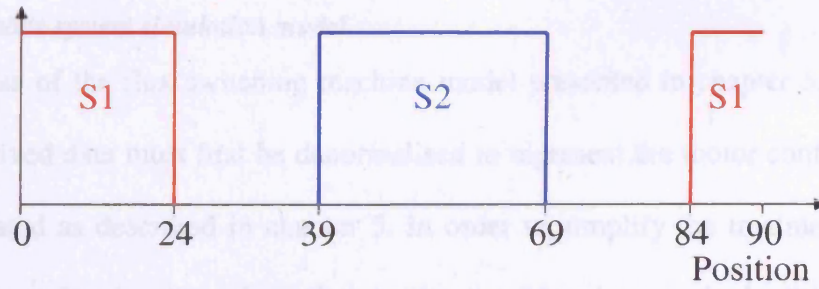


**Figure 6-7** Example implementation of switch operating positions for the flux switching motor

#### 6.4 Implementation

Using the relationships developed to characterise the behaviour of the bifilar winding in the circuit, calibrate and control the switches it is possible to solve the electrical circuit system of Figure 6-1 with diode  $D_f$  and/or capacitor  $C$  present. The simulation model is developed initially for the general case where both are present and then the special cases where either is omitted are discussed.



**Figure 6-8** Simplified circuit diagram for simulation

6.4.1 Complete system simulation model

As is the case of the flux switching machine model presented in chapter 5, the flux map and derived data must first be denormalised to represent the motor configuration being simulated as described in chapter 5. In order to simplify the treatment of the bifilar armature in circuit analysis it may be considered as a single ‘black box’ component comprising both bifilar windings, the power switches, free-wheel diodes and external resistance and inductance. The apparent behaviour of this system in the circuit depends on the voltage applied at its terminals, its current and the state of the switch control inputs. The field may also be considered a simple two terminal component for this analysis containing the main and external inductances and resistances. Figure 6-8 shows the simplified circuit to be analysed. The states for which the system will be solved are field flux linkage, armature effective flux linkage and capacitor charge.

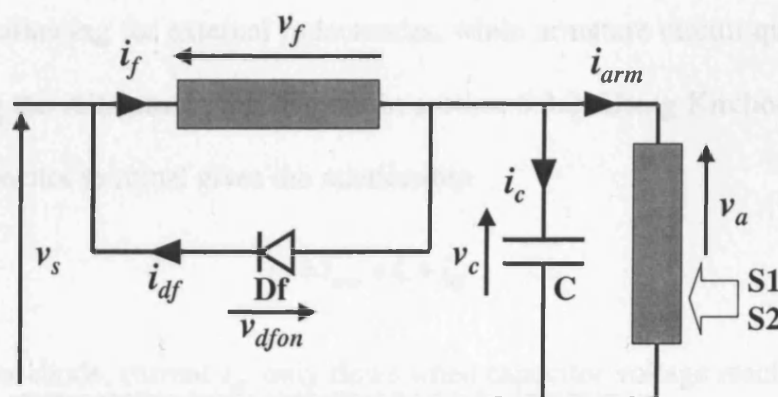


Figure 6-8 Simplified circuit diagram for analysis with windings replaced by ‘black-box’ components

Using Kirchoff's Laws to formulate the equations necessary for solution of the circuit it can be seen that field voltage is given by

$$v_f = v_s - v_c \quad (6.23)$$

where  $v$  is voltage and the subscripts  $f$ ,  $s$ , and  $c$  denote field, supply and capacitor respectively while armature voltage is given by

$$v_a = v_c \quad (6.24)$$

where subscript  $a$  denotes armature. The voltage across the linear capacitor  $C$  is given by

$$v_c = \frac{q}{C} \quad (6.25)$$

where  $q$  is stored charge and  $C$  is the value of the capacitance. Field and armature effective flux linkage and current are obtained from the relationships derived in section 6.3.3, allowing for external inductances, while armature circuit quantities are obtained using the relationships developed in section 6.3.2. Using Kirchoff's Current Law at the capacitor terminal gives the relationship

$$i_f = i_{arm} + i_c + i_{df} \quad (6.26)$$

As  $D_f$  is an ideal diode, current  $i_{df}$  only flows when capacitor voltage reaches

$$v_c = v_s + v_{dfon} \quad (6.27)$$

where  $v_{dfon}$  is the forward bias voltage of the diode  $D_f$ . Hence, when  $D_f$  is not conducting, current into capacitor  $C$  is given by

$$i_c = i_f - i_a \quad (6.28)$$

and when  $D_f$  is conducting capacitor C remains fully charged, hence

$$i_c = 0 \quad (6.29)$$

and

$$i_{df} = i_f - i_a \quad (6.30)$$

either allowing the field current to free-wheel or returning energy to the dc bus.

Therefore, capacitor charge cannot rise above a maximum value

$$q_{\max} = C \times (v_s + v_{dfon}) \quad (6.31)$$

at any time and excess charge must flow back to the supply through diode  $D_f$ . During a given time step the charge flowing into the capacitor if  $D_f$  is not conducting is

$$\Delta q = i_c \Delta t \quad (6.32)$$

where  $\Delta t$  is the time step and capacitor charge at the end of the time step is

$$q_{(n+1)} = q_{(n)} + \Delta q \quad (6.33)$$

where subscripts  $(n)$  and  $(n+1)$  denote the beginning and end of the time step respectively. If  $q_{(n+1)} > q_{\max}$  then

$$q_{(n+1)} = q_{\max} \quad (6.34)$$

and the surplus charge which cannot be stored in the capacitor

$$q_d = q_{(n+1)} - q_{\max} \quad (6.35)$$

must flow back to the supply through field diode  $D_f$ , giving a mean diode current during the time step of

$$i_{df(n+1)} = \frac{q_d}{\Delta t} \quad (6.36)$$

Hence, the general behaviour of the circuit is fully described and, with the addition of the previously derived relationships describing the behaviour of the windings under all conditions, the complete motor and power electronic system can be simulated.

#### 6.4.1.1 Simulation of circuit with capacitor only

If the circuit of Figure 6-1 is utilised without field diode  $D_f$  present, then there is no limit on the amount of charge which may be stored in the capacitor  $C$ . Hence, this special case may be simulated by setting  $v_{dfon}$  to infinity.

#### 6.4.1.2 Simulation of circuit with diode only

If the circuit of Figure 6-1 is implemented without the capacitor  $C$  present then there is no mechanism for electrical energy storage within the circuit. Hence, this case may be modelled by constraining capacitor voltage and current to be

$$v_c = v_s - v_f \quad (6.37)$$

and

$$i_c = 0 \quad (6.38)$$

respectively at all times where

$$v_f = \left( \frac{(\Psi_{f(n+1)} - \Psi_{f(n)}) + (\Psi_{fext(n+1)} - \Psi_{fext(n)})}{\Delta t} \right) + \left( \frac{i_{f(n)} + i_{f(n+1)}}{2} \cdot (R_f + R_{fext}) \right) \quad (6.39)$$

if  $i_f \leq i_{arm}$  or

$$v_f = -V_{dfon} \quad (6.40)$$

if  $i_f > i_{arm}$  to apply the correct terminal voltage to the armature as if the capacitor were not present.

### **6.4.2    *Solution of complete system model***

As with the dynamic model for the flux switching machine developed in chapter 5, the Gauss-Seidel method is used to solve the non-linear system of simultaneous equations which describe the complete flux switching motor and drive system. However, unlike the system of equations to be solved for the dynamic model of the flux switching machine on its own many of the relationships in the complete system model are conditional and discontinuous. This has the effect of making their solution generally more oscillatory for time steps where there is a discontinuous change, potentially leading to non-convergence in extreme cases. Results are returned at each time step for winding flux linkages, currents and circuit quantities from which the complete behaviour of the flux switching motor and drive circuit may be observed.

## **6.5    Results**

### **6.5.1    *Experimental tests simulated***

The flux switching motor was mounted onto a dynamometer test rig and connected to its power electronic circuit, including both capacitor and field diode, as described in section 6.2. The resistance of both windings was measured at ambient temperature and the temperature of each was also measured immediately after every test using thermocouples embedded in the coils to allow correction of winding resistances for running conditions. Dc link voltage, current, speed, electrical input and mechanical output power were recorded using a power analyser connected to the drive circuit and dynamometer while winding current waveforms and shaft mounted optical sensor signal were recorded using a digital storage oscilloscope.

During each test the motor was started and run in its direction of normal operation and the supply voltage adjusted to give the desired running speed with specified external load applied by the dynamometer. If running speed remains constant between tests then mechanical losses such as friction and windage, whose magnitude is not known and cannot easily be measured, may also reasonably be assumed constant. Hence, comparing results for the flux switching motor at the same running speed unloaded and with external load applied by the dynamometer, all differences may be reasonably assumed to be due to of the externally applied load and the accuracy of the simulation model for output torque prediction may be estimated.

For each comparison made, the experimental data was obtained first and the dynamic model for the flux switching motor used to simulate the operation of the motor for identical conditions. The shaft mounted optical sensor was aligned such that the rising edge of the output signal was aligned with the zero crossing point of the armature induced emf for dc field excitation, i.e. the physical zero datum for rotor angle, and the corresponding flux map zero position was similarly obtained by finding the zero crossing of the armature induced emf assuming constant dc field current of 5.8A. From inspection of the experimentally obtained armature current waveforms and the optical sensor signal, the rotor positions at which the armature switches were turned on and off were obtained for each condition and corresponding switch control functions were written to implement the same switching positions in the dynamic simulation model. Table 6-3 summarises the conditions for which experimental and simulated data were compared.

Speed (rpm)	External load (Nm)	Dc link voltage (V)
14,982	0.023 <sup>(1)</sup>	115.12
15,022	0.504	213.12
8,075	-0.003 <sup>(1)</sup>	76.526
7,985	0.253	122.86
<sup>(1)</sup> In these cases the dynamometer was set to zero load and the small readings are due to zero offset error in the load cell		

**Table 6-3 Summary of experimental conditions for which experimental results are compared with simulation**

### 6.5.2 Comparison of experimental and simulated results

To show the operation of the dynamic simulation model for the flux switching motor and drive under a range of operating conditions results are presented here for the motor with and without external load applied running at approximately 15,000rpm and 8,000rpm. In each case the simulated field and armature currents are compared with the corresponding experimental results. For the no load case at approximately 15,000rpm a more comprehensive examination is made of the simulation results obtained to illustrate the range of results which may be obtained from the simulation model, some of which cannot be readily measured experimentally. In this case electromagnetic data derived from the B2 flux map using the PCHIP contour interpolation method is used as it is the most complete and numerically accurate data available, as described in chapter 4.

#### 6.5.2.1 Comparison of simulated and experimental winding currents

Figure 6-9 to Figure 6-12a show comparisons between experimental and simulated field current waveforms for the flux switching motor with no external load at 14,982rpm, 0.5Nm external load at 15,022rpm, no load at 8,075rpm and 0.25Nm at 7,985rpm respectively. Figure 6-9 to Figure 6-12b show comparisons for experimental and simulated current in each half of the bifilar armature.

In each case it can be seen that the simulation underestimates the magnitude of both field and armature currents but the shape is well accounted for. The interaction of the field and armature is evident in the modulation of the field current due to changing self and mutual coupling with position. The behaviour of the bifilar armature is also modelled and is evident where each switch turns off as current instantaneously transfers from one bifilar coil into the other to freewheel.

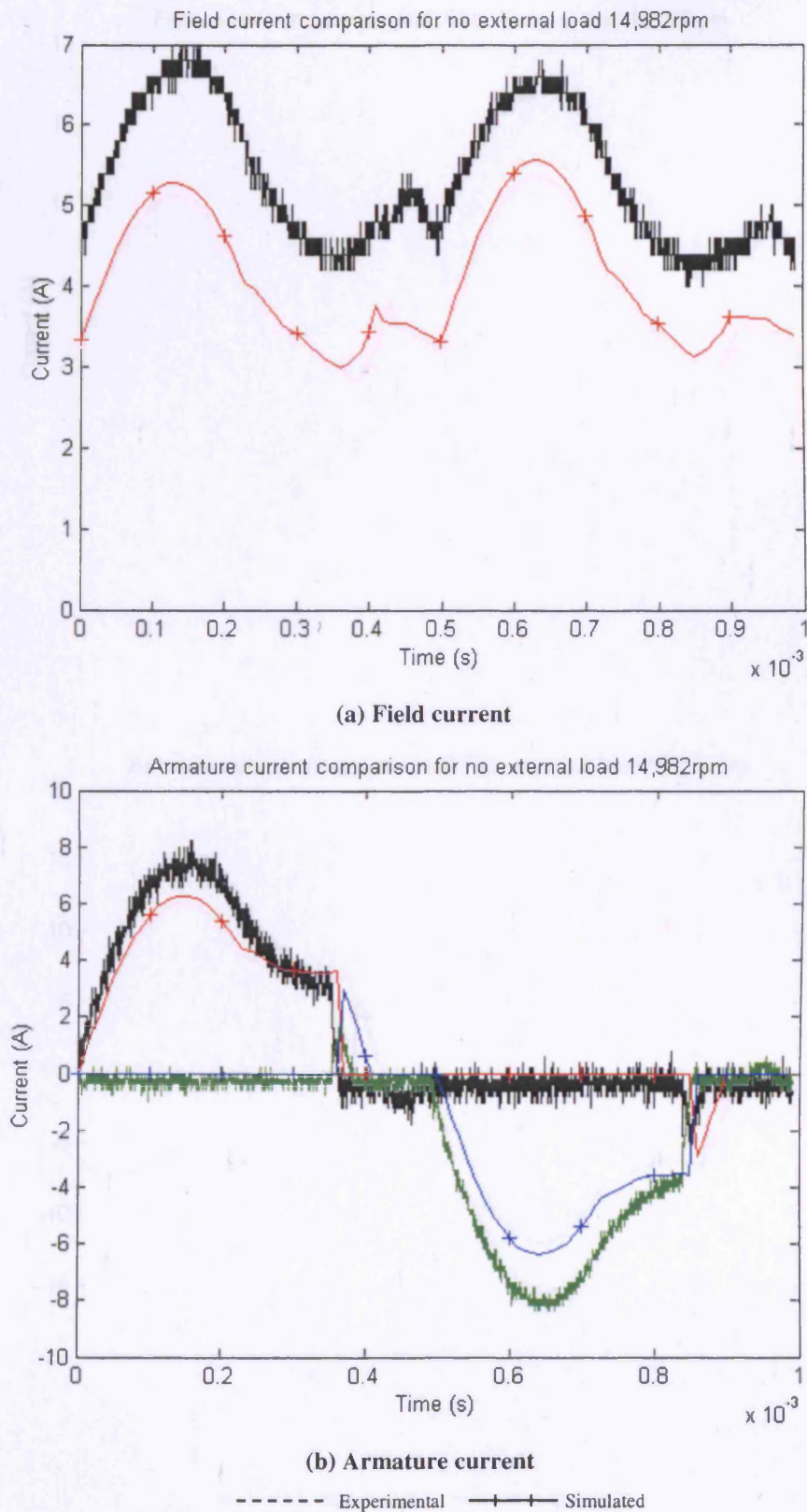
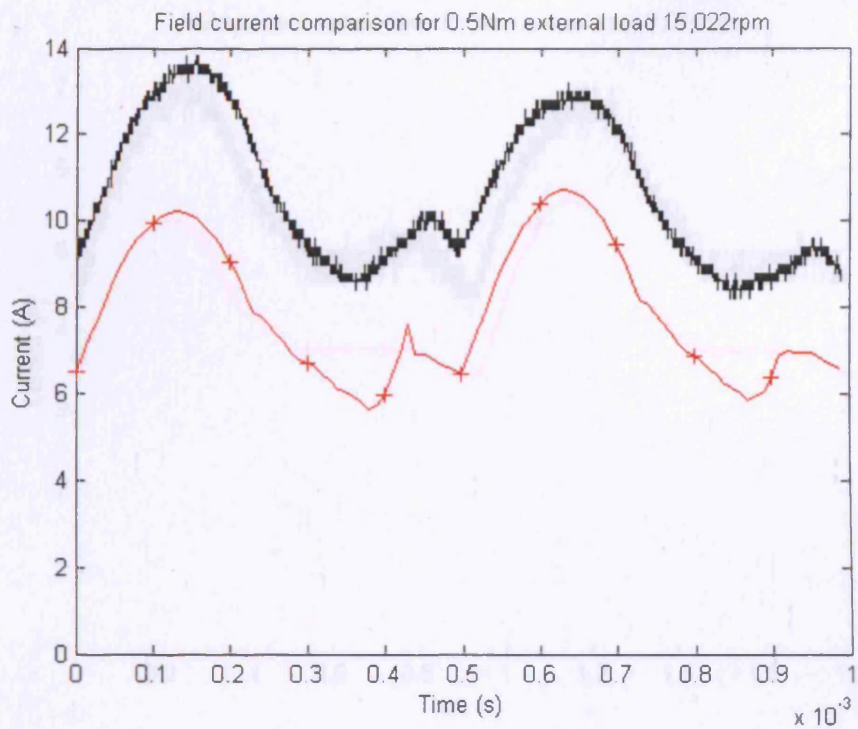
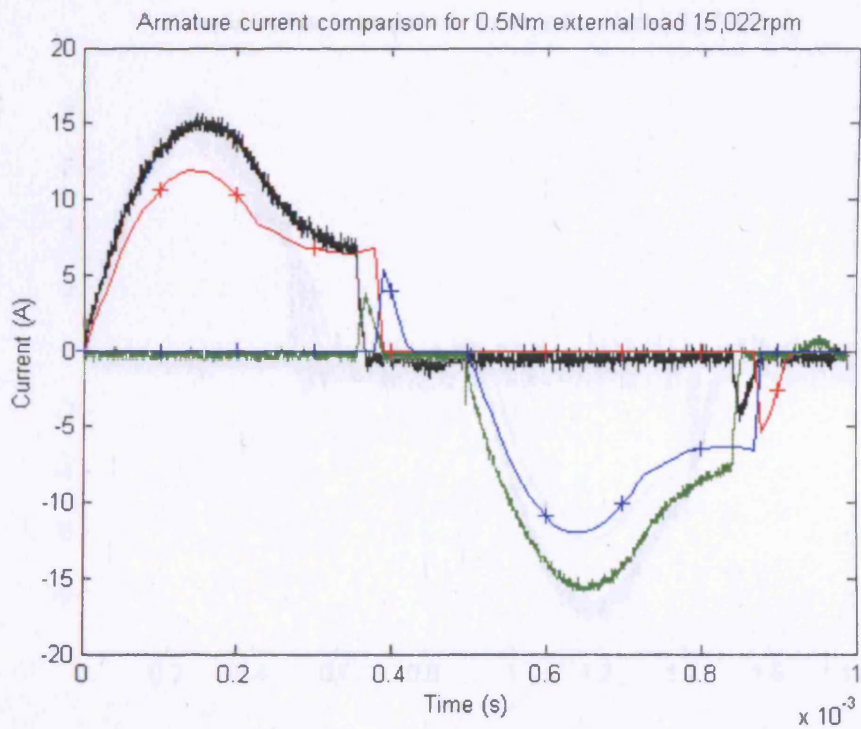


Figure 6-9 Comparison of simulated and experimental current waveforms for the 8/4 flux switching motor running at 14,982rpm with no externally applied load



(a) Field current



(b) Armature current

----- Experimental    —+— Simulated

Figure 6-10 Comparison of simulated and experimental current waveforms for the 8/4 flux switching motor running at 15,022rpm with 0.5Nm externally applied load

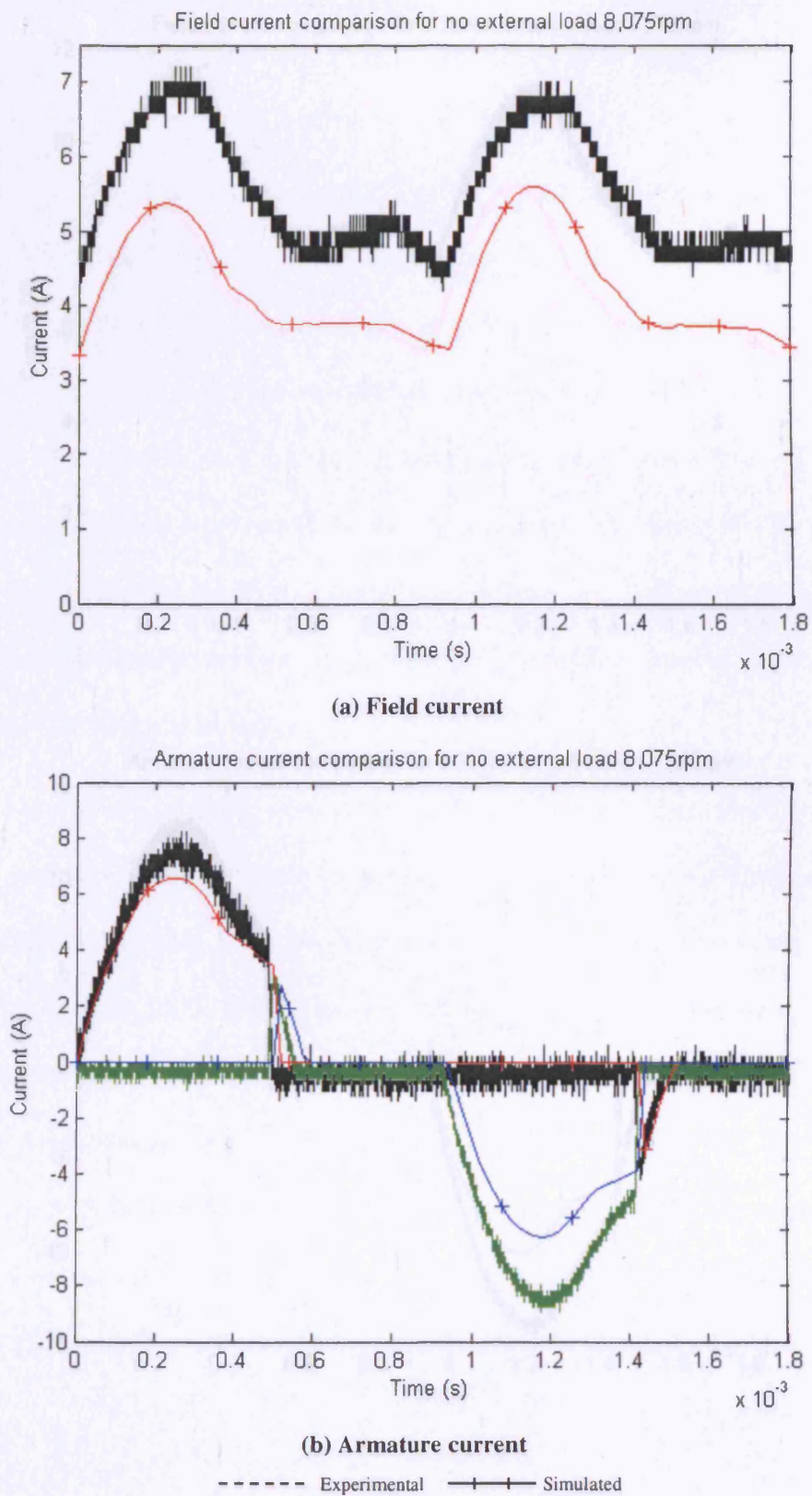
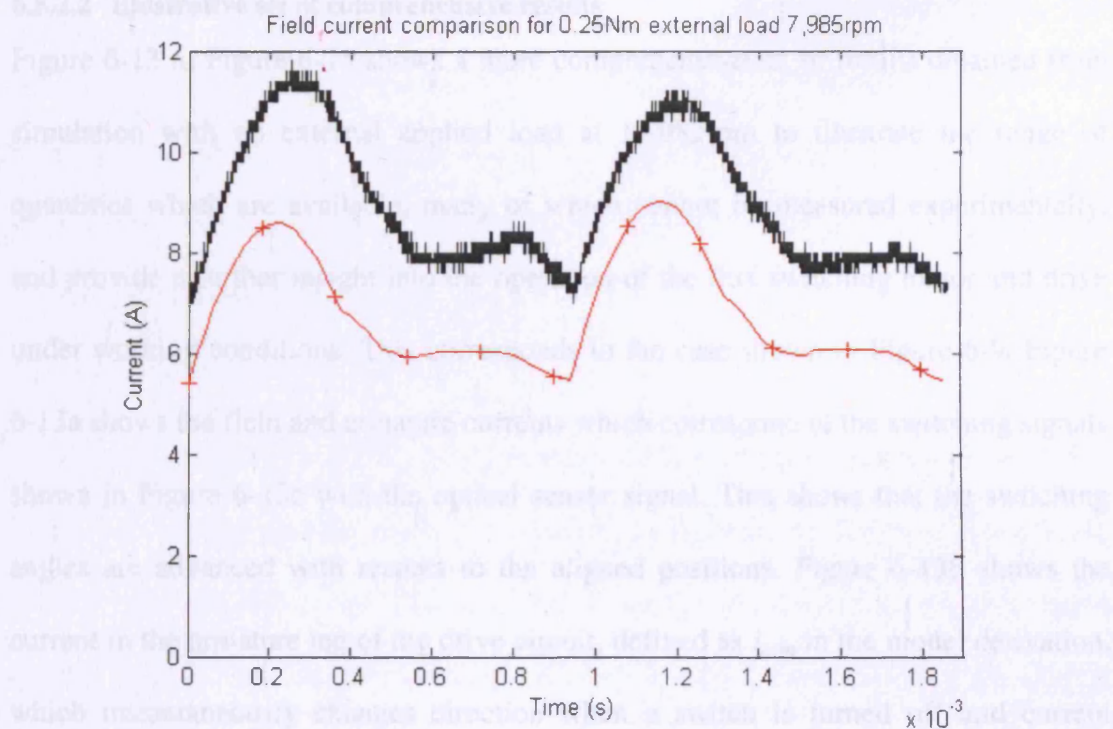
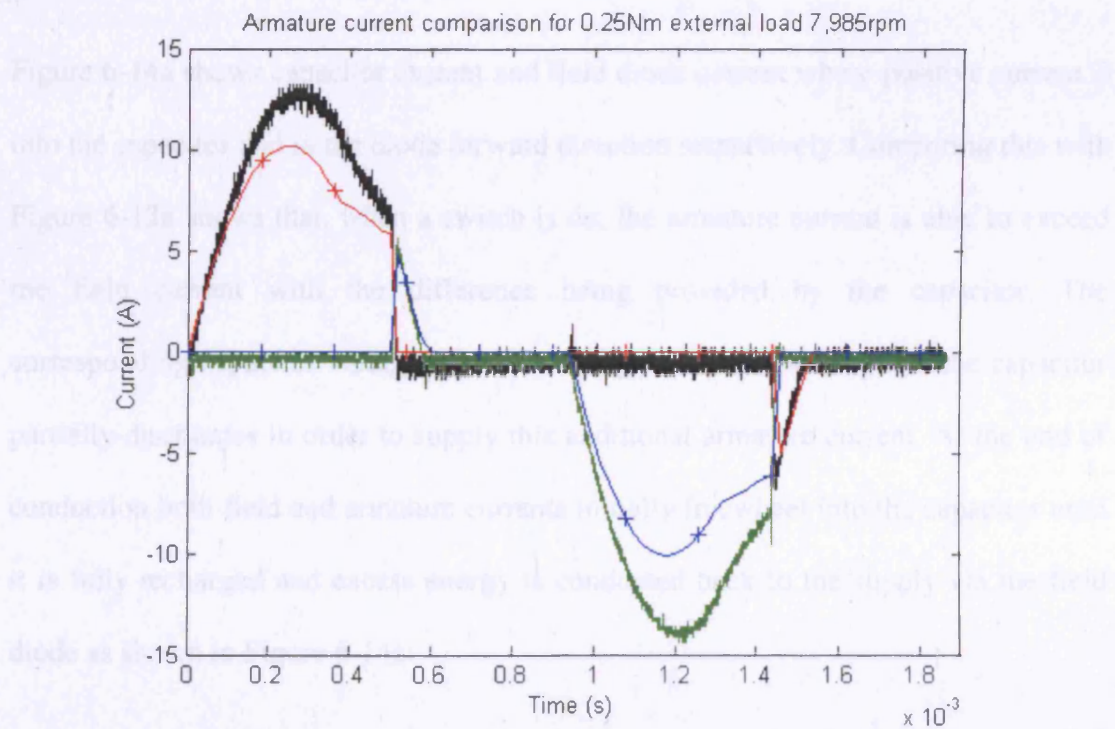


Figure 6-11 Comparison of simulated and experimental current waveforms for the 8/4 flux switching motor running at 8,075rpm with no externally applied load



(a) Field current



(b) Armature current

----- Experimental    +---+ Simulated

**Figure 6-12 Comparison of simulated and experimental current waveforms for the 8/4 flux switching motor running at 7,985rpm with 0.25Nm externally applied load**

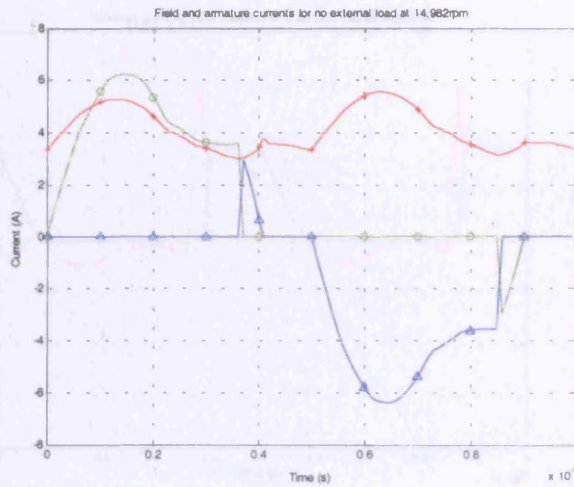
### 6.5.2.2 Illustrative set of comprehensive results

Figure 6-13 to Figure 6-15 shows a more comprehensive set of results obtained from simulation with no external applied load at 14,982rpm to illustrate the range of quantities which are available, many of which cannot be measured experimentally, and provide a further insight into the operation of the flux switching motor and drive under working conditions. This corresponds to the case shown in Figure 6-9. Figure 6-13a shows the field and armature currents which correspond to the switching signals shown in Figure 6-13c with the optical sensor signal. This shows that the switching angles are advanced with respect to the aligned positions. Figure 6-13b shows the current in the armature leg of the drive circuit, defined as  $i_{arm}$  in the model derivation, which instantaneously changes direction when a switch is turned off and current freewheels in the bifilar armature.

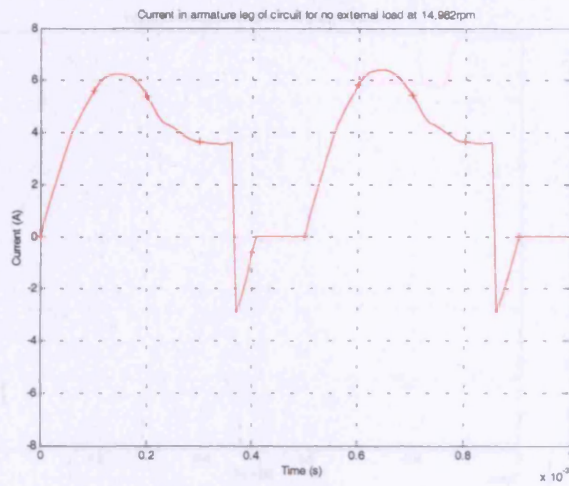
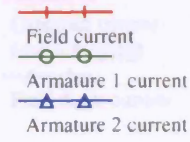
Figure 6-14a shows capacitor current and field diode current where positive current is into the capacitor and in the diode forward direction respectively. Comparing this with Figure 6-13a shows that, when a switch is on, the armature current is able to exceed the field current with the difference being provided by the capacitor. The corresponding capacitor voltage is shown in Figure 6-14b showing that the capacitor partially discharges in order to supply this additional armature current. At the end of conduction both field and armature currents initially freewheel into the capacitor until it is fully recharged and excess energy is conducted back to the supply via the field diode as shown in Figure 6-14a.

Figure 6-14c shows the instantaneous electromagnetic torque obtained by the Maxwell Stress method from finite element analysis. It can be seen that, although most torque is produced while the armature is energised, it is also positive during the times that there is no armature current. Hence main torque is produced by changing mutual coupling between the field and armature but there is also a contribution due to changing self coupling of the field.

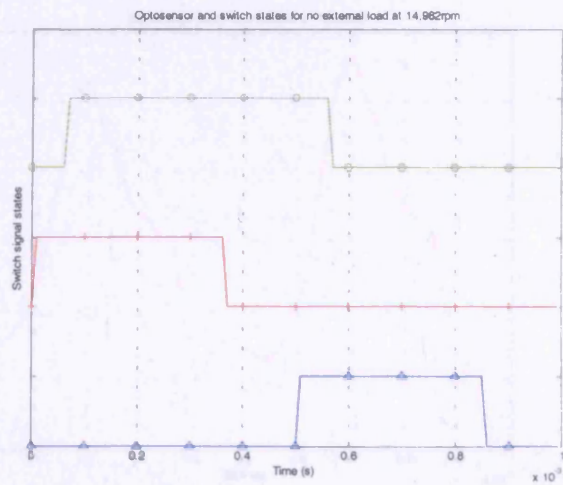
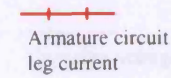
Figure 6-15a and Figure 6-15b show the winding flux linkages and emfs respectively. Field flux linkage remains relatively constant throughout the electrical cycle while armature flux linkage is ac. When a switch is on the armature flux linkage changes almost linearly. The switch is turned off as the rotor moves towards an aligned position and the mutual coupling between field and armature is approaching its peak. As armature current falls rapidly to zero its flux linkage falls only slightly before increasing again due entirely to mutual coupling with the field, showing that most armature flux linkage is due to the field current.



(a) Field and armature currents



(b) Current in armature leg of circuit ( $i_{arm}$ )



(c) Optical position sensor signal and switch states

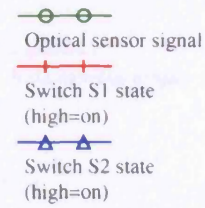
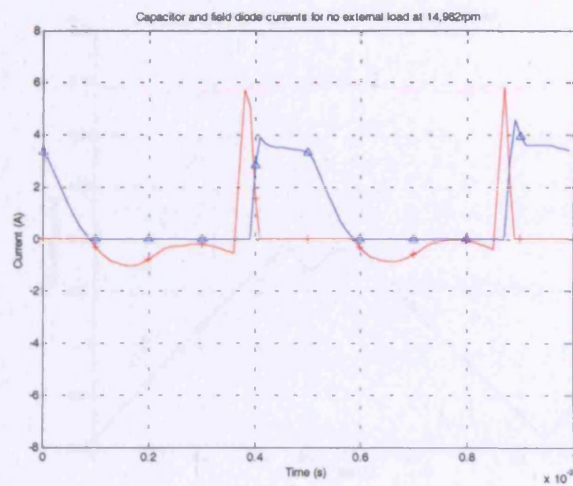
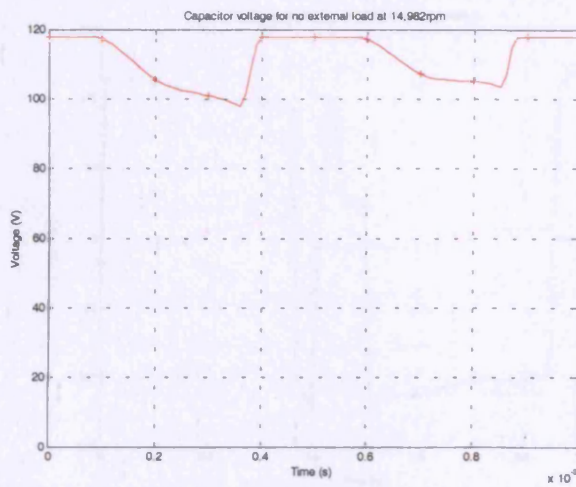


Figure 6-13 Sample comprehensive set of results from simulation (Part 1 of 3)



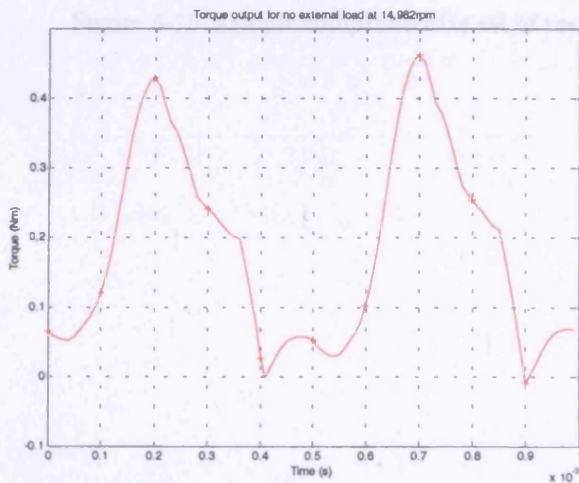
(a) Capacitor and field diode currents

Capacitor current  
(+ve=charging)  
Field diode current



(b) Capacitor voltage

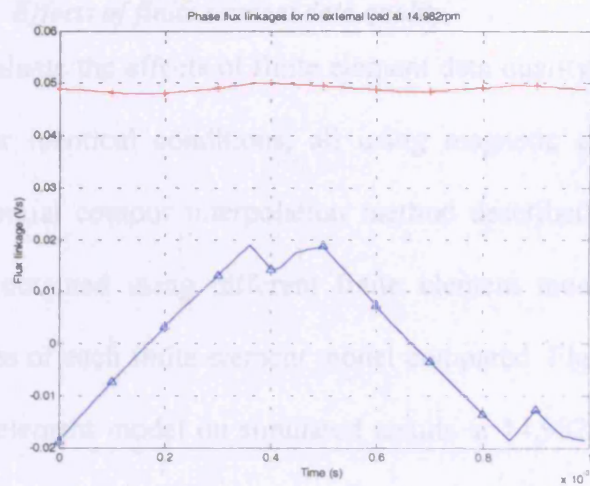
Capacitor voltage



(c) Instantaneous torque by Maxwell Stress method

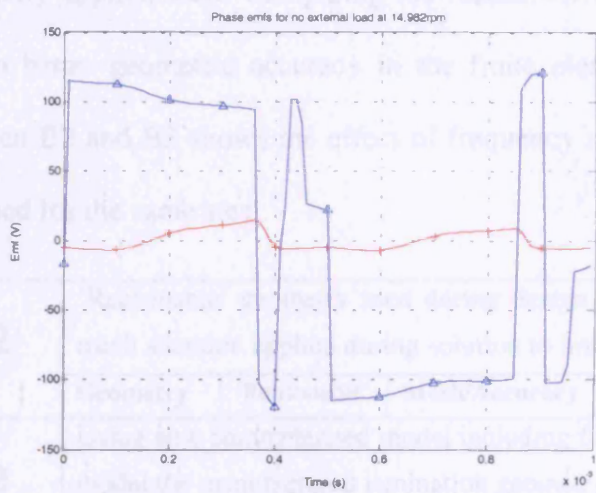
Instantaneous torque

Figure 6-14 Sample comprehensive set of results from simulation (Part 2 of 3)



(a) Field and armature flux linkages

Field flux linkage  
Armature flux linkage



(b) Field and armature emfs

Field emf  
Armature emf

Figure 6-15 Sample comprehensive set of results from simulation (Part 3 of 3)

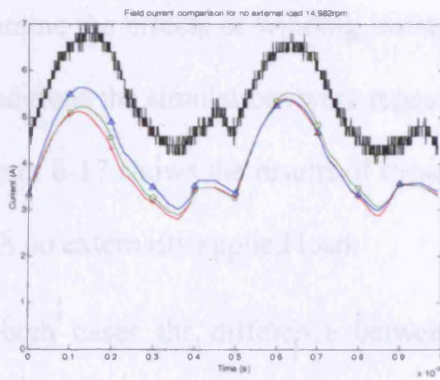
**6.5.3 Effects of finite element data quality**

To evaluate the effects of finite element data quality a set of simulations were carried out for identical conditions, all using magnetic data derived using the quadratic polynomial contour interpolation method described in chapter 4 but based on flux maps obtained using different finite element models. Table 6-4 recaps the main features of each finite element model compared. Figure 6-16 shows the effects of the finite element model on simulated results at 14,982rpm and 8,075rpm, both with no externally applied load. Comparing the results for B2 and A2 shows the difference due to better geometric accuracy in the finite element model while a comparison between B2 and B3 shows the effect of frequency at which the B-H characteristic is obtained for the same steel.

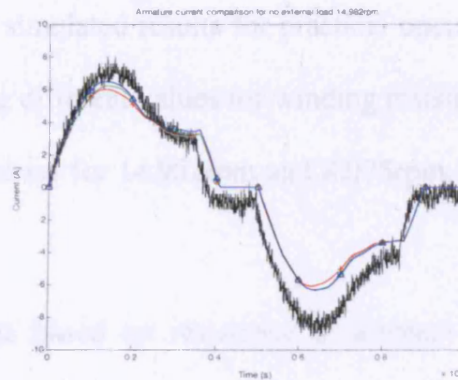
<b>A2</b>	'Reasonable' geometry used during design of the flux switching machine with mesh adaption applied during solution to improve numerical accuracy					
	<b>Geometry</b>	'Reasonable'	<b>Mesh/Accuracy</b>	Accurate	<b>Steel B-H</b>	540Hz
<b>B2</b>	Using new parameterised model including filleting and coil set back to precisely model the manufactured lamination geometry.					
	<b>Geometry</b>	Precise	<b>Mesh/Accuracy</b>	Accurate	<b>Steel B-H</b>	540Hz
<b>B3</b>	As B2 but using 20Hz steel B-H characteristic					
	<b>Geometry</b>	Precise	<b>Mesh/Accuracy</b>	Accurate	<b>Steel B-H</b>	20Hz

**Table 6-4 Summary of finite element models used to create flux maps**

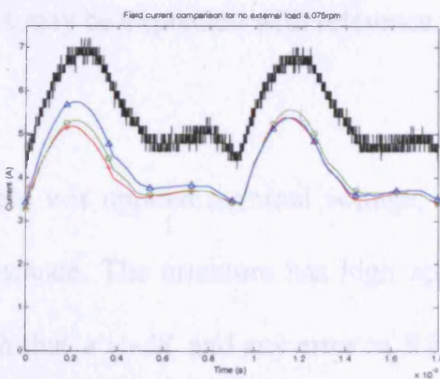
While there are small differences in the simulated results for each case the overall magnitude and shape of the waveforms obtained is similar. The greatest difference in results is due to improved geometric accuracy. In particular, the inclusion of filleting at the stator pole roots and setting the coils back from the airgap could cause the effects seen by changing the winding flux linkages for given currents and position. However, it can be seen that, provided the finite element model is 'reasonable', then the results obtained from simulation are not greatly affected by incremental increases in its complexity.



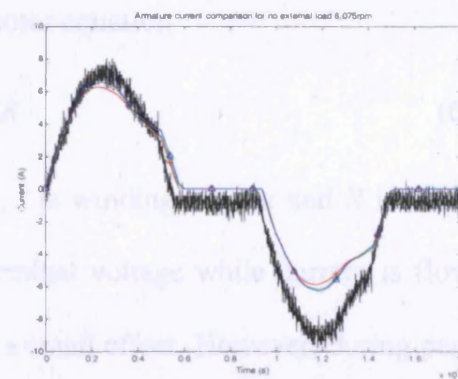
(a) Field current at 14,982rpm with no external load



(b) Armature current at 14,982rpm with no external load



(c) Field current at 8,075rpm with no external load



(d) Armature current at 8,075rpm with no external load

— Experimental  
 —○— Simulated using flux map B3  
 —+— Simulated using flux map B2  
 —△— Simulated using flux map A2

Figure 6-16 Effect of finite element model accuracy on simulated current waveforms

#### 6.5.4 *Effects of winding resistances*

For the case where the field is excited by a constant dc voltage and the motor rotated to obtain the armature induced emf, as modelled in chapter 5, the simulated results were shown to be very sensitive to errors in the winding resistance as this determines the mean current. However, during normal operation of the flux switching motor a high voltage is generally applied to the windings with current being controlled by the amount of time for which this voltage is applied rather than winding resistance. To examine the effects of winding resistance on simulated results for practical operating conditions the simulations were repeated using different values for winding resistance. Figure 6-17 shows the results of these simulations for 14,982rpm and 8,075rpm, both with no externally applied load.

In both cases the difference between results based on resistance at ambient and running temperature is extremely small. For results using doubled resistance values the armature currents are still very similar while field currents are reduced slightly. This may be explained with reference to the motor equation

$$v = e + iR \quad (6.41)$$

where  $v$  is applied terminal voltage,  $e$  is emf,  $i$  is winding current and  $R$  is winding resistance. The armature has high applied terminal voltage while current is flowing such that  $e \gg iR$  and any error in  $R$  has only a small effect. However, during periods when field current is freewheeling it has a low applied voltage and  $iR$  forms a larger proportion of  $v$  leading to more noticeable effects. *Hence, for practical working conditions the simulated output is relatively insensitive to errors in the value of winding resistance used.*

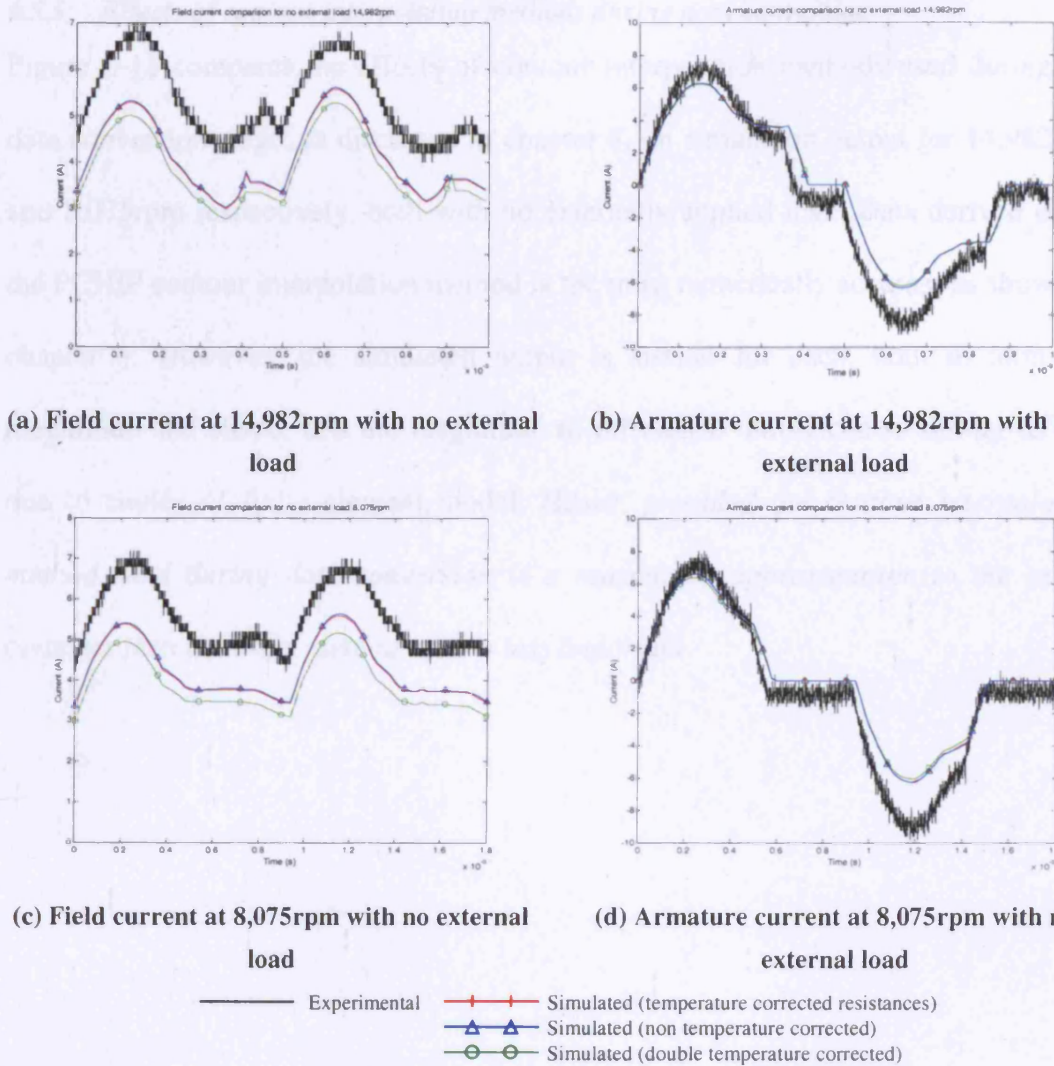


Figure 6-17 Effect of winding resistance on simulated current waveforms

### **6.5.5    *Effects of contour interpolation methods during data conversion***

Figure 6-18 compares the effects of contour interpolation methods used during the data conversion stage, as discussed in chapter 4, on simulation output for 14,982rpm and 8,075rpm respectively, both with no externally applied load. Data derived using the PCHIP contour interpolation method is the most numerically accurate as shown in chapter 4. However, the simulated output is similar for each, both in terms of magnitude and shape, and the magnitude of difference introduced is similar to that due to choice of finite element model. *Hence, provided the contour interpolation method used during data conversion is a reasonable approximation to the actual contours then the exact method used is less important.*

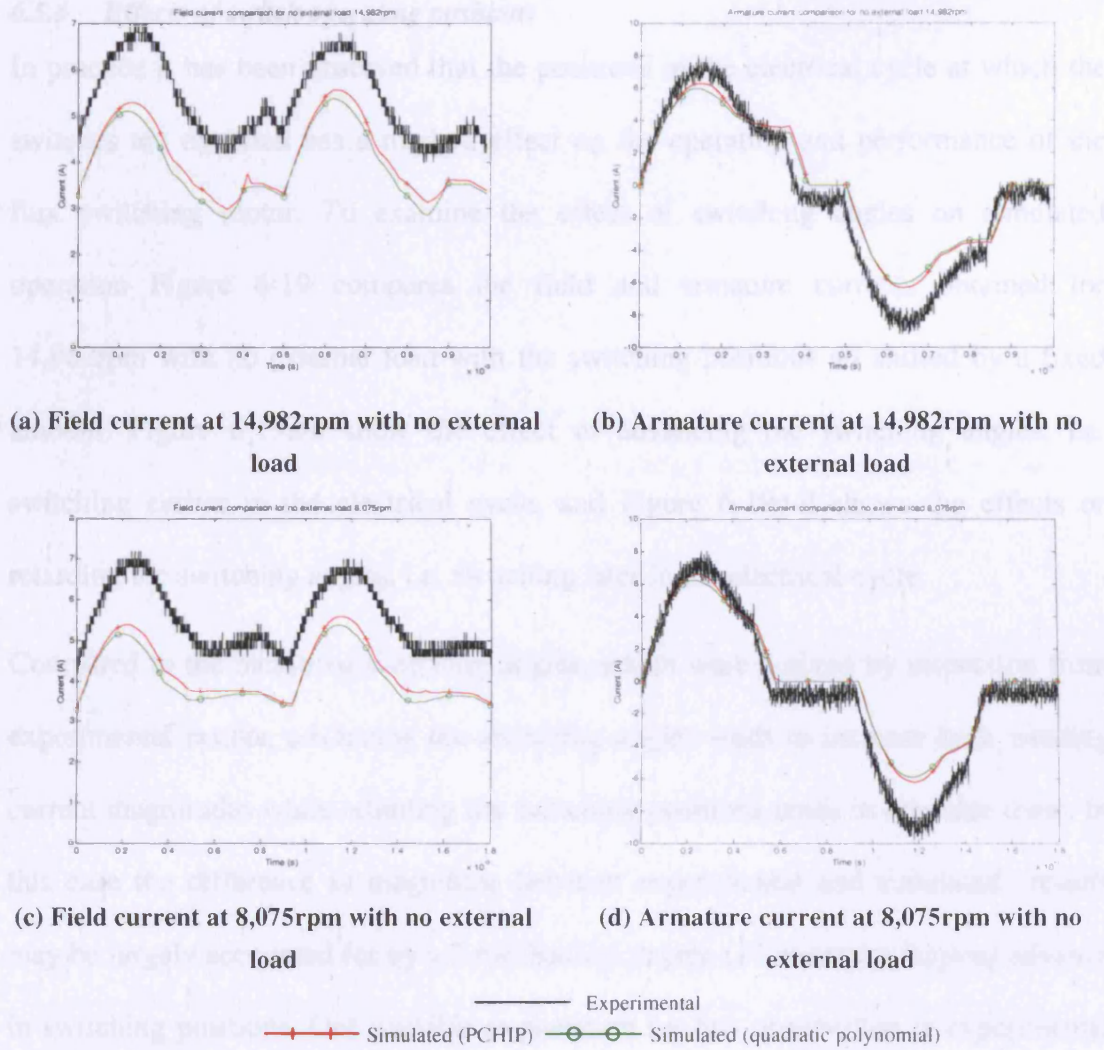


Figure 6-18 Effect of contour interpolation method used during data conversion on simulated current waveforms

### **6.5.6    *Effects of switch operating positions***

In practice it has been observed that the positions in the electrical cycle at which the switches are operated has a marked effect on the operation and performance of the flux switching motor. To examine the effect of switching angles on simulated operation Figure 6-19 compares the field and armature currents obtained for 14,982rpm with no external load with the switching positions all shifted by a fixed amount. Figure 6-19a-b show the effect of advancing the switching angles, i.e. switching earlier in the electrical cycle, and Figure 6-19c-d shows the effects of retarding the switching angles, i.e. switching later in the electrical cycle.

Compared to the measured switching angles, which were derived by inspection from experimental results, advancing the switching angles tends to increase both winding current magnitudes while retarding the switching positions tends to decrease them. In this case the difference in magnitude between experimental and simulated results may be largely accounted for by a 3 mechanical degree (12 electrical degree) advance in switching positions. One possible explanation for this observation is experimental error in determining switching angles. Experimentally, it was observed that the exact switching positions within successive cycles were not constant but tended to oscillate relative to the optical sensor signal due to asymmetry in the slotted disc and the feedback action of the controller. Such behaviour would tend to lead to a constant offset error in derived switch operating positions.

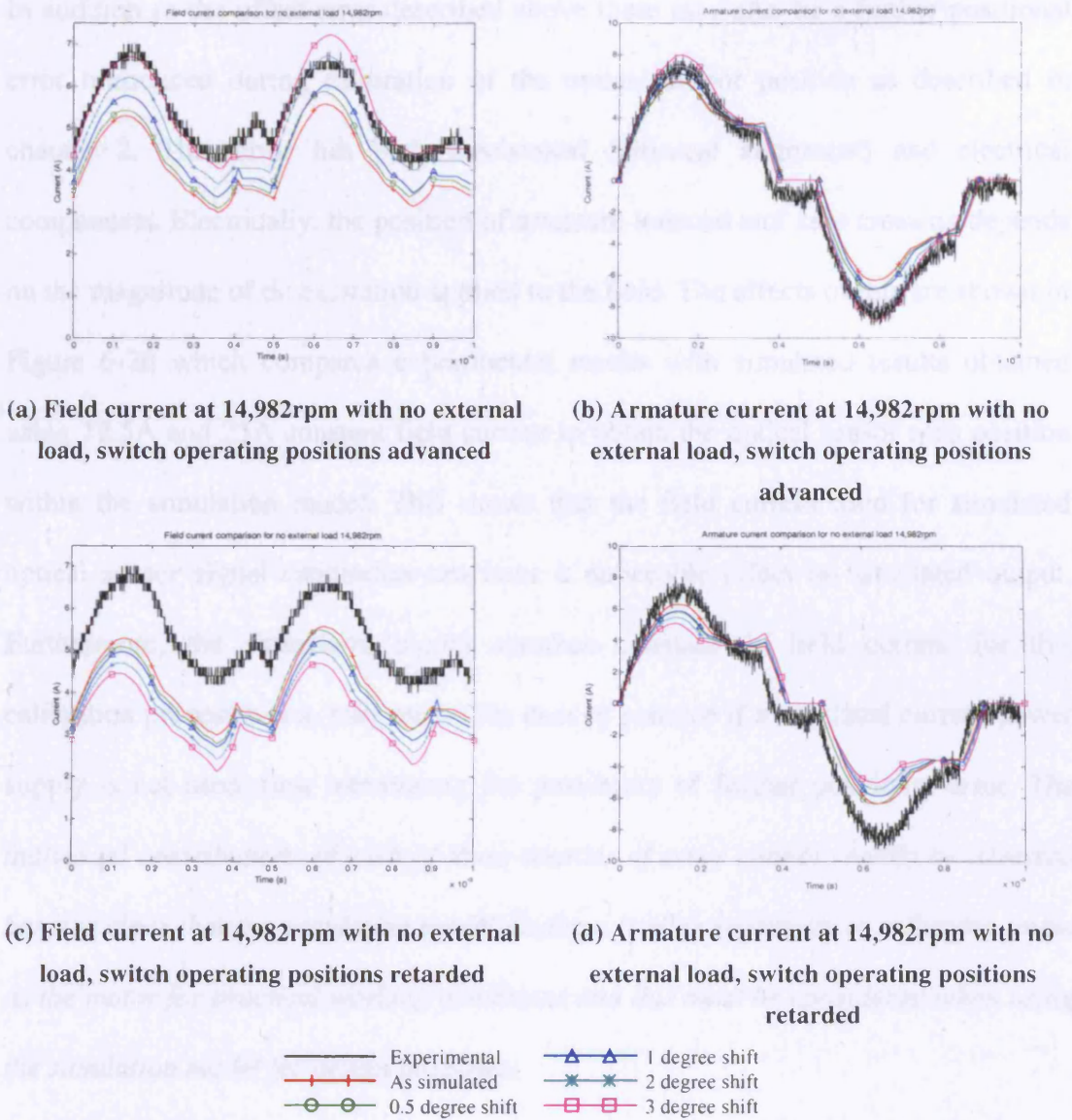
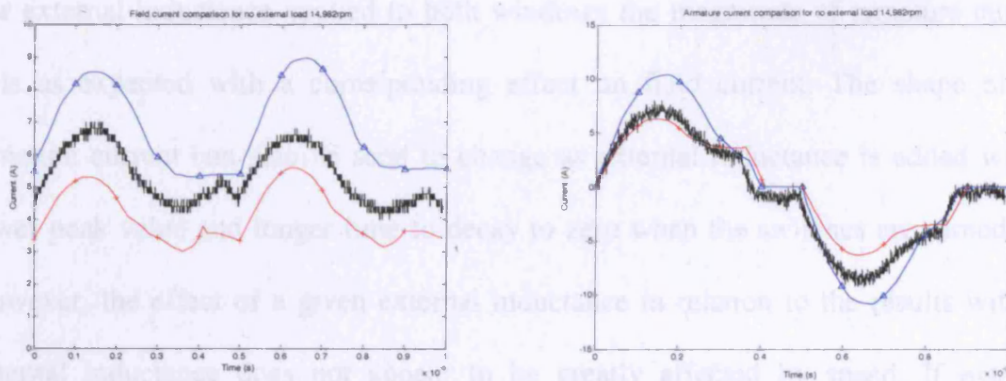


Figure 6-19 Effect of shifted switch operating positions on simulated current waveforms

In addition to the offset error described above there may also be a further positional error introduced during calibration of the optical sensor position as described in chapter 2. This error has both mechanical (physical alignment) and electrical components. Electrically, the position of armature induced emf zero crossing depends on the magnitude of dc excitation applied to the field. The effects of this are shown in Figure 6-20 which compares experimental results with simulated results obtained using 12.5A and 25A constant field current to obtain the optical sensor zero position within the simulation model. This shows that the field current used for simulated optical sensor signal calibration can have a noticeable effect on simulated output. Furthermore, the simulation model assumes constant dc field current for this calibration process which may not be the case in practice if a regulated current power supply is not used, thus introducing the possibility of further positional error. *The individual contributions of each of these sources of error cannot readily be assessed but it is clear that the simulation model displays similar sensitivity to switching angle as the motor for practical working conditions and this must be considered when using the simulation model for design purposes.*



(a) Field current at 14,982rpm with no external load (b) Armature current at 14,982rpm with no external load

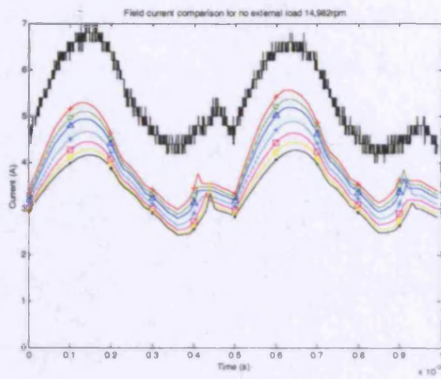
— Experimental  
 —+— Simulated (12.5A field current) —▲— Simulated (25A field current)

**Figure 6-20 Effect of field current used for optical position sensor signal calibration in the simulation model on simulated current waveforms**

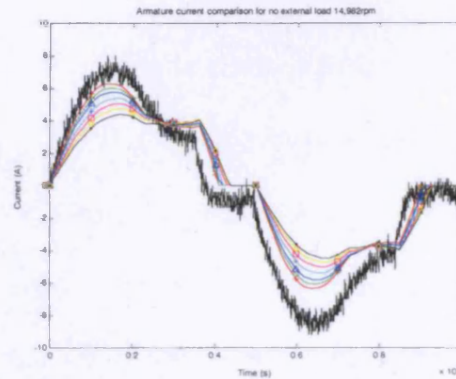
### 6.5.7 Effects of external inductances

As the flux map is obtained using 2-dimensional magnetostatic finite element analysis it does not include 3-dimensional effects such as end-winding inductances etc. Allowance may also be made for dynamic effects by adding an external inductance in series with the windings to reduce the rate of change of working flux and current which is implemented in the simulation model as a series linear inductance as described in section 6.3.3. The effects of adding various values of external inductance to the windings are shown in Figure 6-21 and Figure 6-22 for 14,982rpm and 8,075rpm, both with no externally applied load. Figure 6-21 shows the effect of adding the same series inductance to both windings while Figure 6-22 shows the effect of adding series inductance to only one winding at a time.

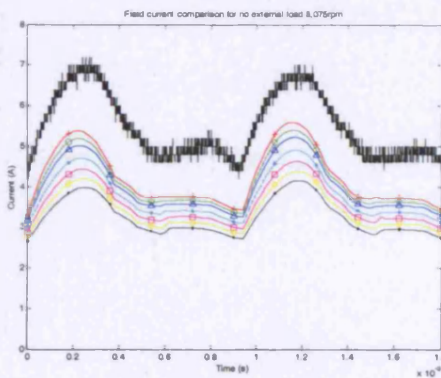
For external inductance applied to both windings the magnitude of armature current falls as expected with a corresponding effect on field current. The shape of the armature current can also be seen to change as external inductance is added with a lower peak value and longer time to decay to zero when the switches are turned off. However, the effect of a given external inductance in relation to the results without external inductance does not appear to be greatly affected by speed. If external inductance is applied to only one winding at a time then it can be seen that the simulation results are most sensitive to armature inductance, which has a noticeable effect on both armature and field currents, while field inductance has relatively little effect. This is because in operation the magnitude of field current is controlled mainly by the peak value of armature current which is reduced as series inductance is added. *Hence, the simulation results are more sensitive to additional armature inductance than field inductance although in this case additional inductance does not act to reduce the differences between experimental and simulated results.*



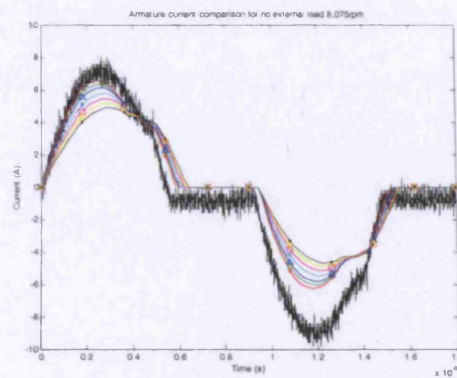
(a) Field current at 14,982rpm with no external load



(b) Armature current at 14,982rpm with no external load



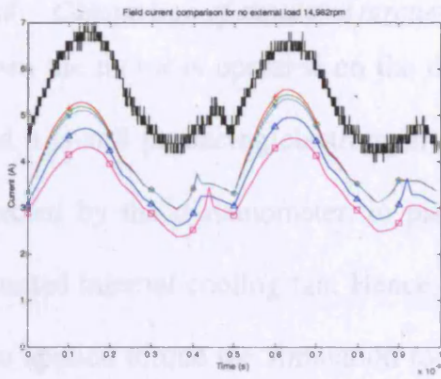
(c) Field current at 8,075rpm with no external load



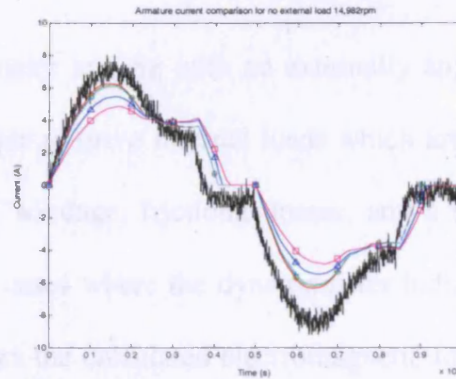
(d) Armature current at 8,075rpm with no external load

- Experimental
- +— No series inductance
- 0.1mH series inductance
- △— 0.2mH series inductance
- \*— 0.4mH series inductance
- 0.6mH series inductance
- ◇— 0.8mH series inductance
- 1.0mH series inductance

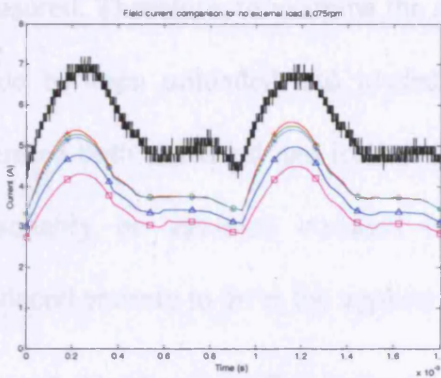
Figure 6-21 Effect of external series inductances applied to both windings on simulated current waveforms



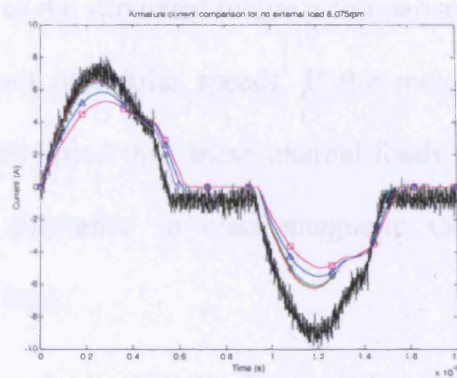
(a) Field current at 14,982rpm with no external load



(b) Armature current at 14,982rpm with no external load



(c) Field current at 8,075rpm with no external load



(d) Armature current at 8,075rpm with no external load

- Experimental
- +— No series inductance
- 0.4mH field series inductance
- △— 0.4mH armature series inductance
- \*— 0.8mH field series inductance
- 0.8mH armature series inductance

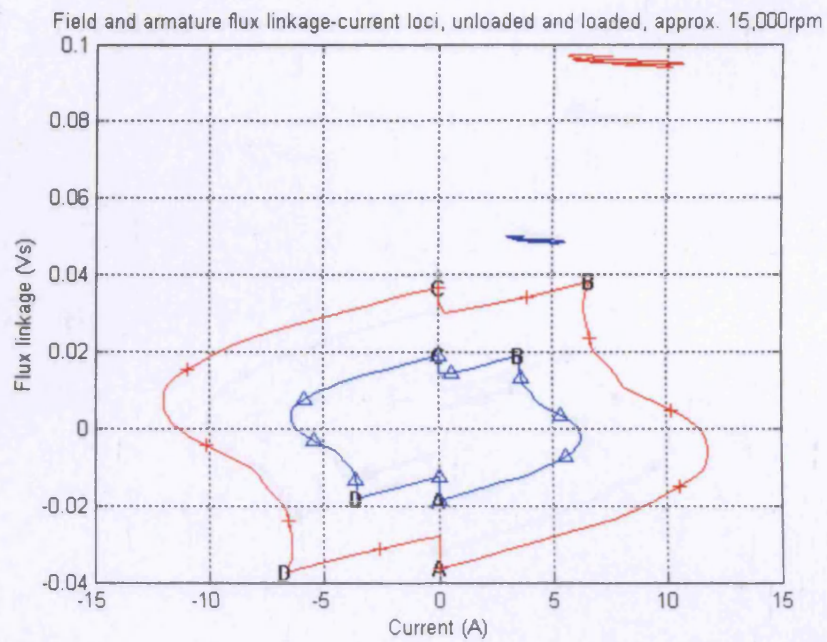
Figure 6-22 Effect of external series inductances applied to only one winding on simulated current waveforms

### 6.5.8 *Comparison of simulated torques*

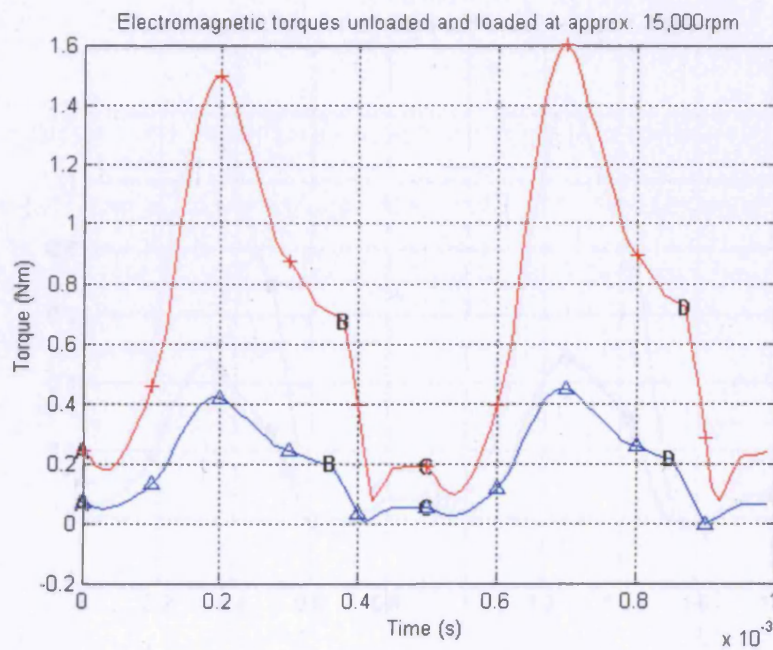
When the motor is operated on the dynamometer test rig with no externally applied load it is still producing electromagnetic torque to drive internal loads which are not detected by the dynamometer, in particular windage, frictional losses, and a shaft mounted internal cooling fan. Hence, for the cases where the dynamometer indicates zero applied torque the simulation model gives the calculated electromagnetic torque which is required to overcome these internal loads and losses which cannot readily be measured. Therefore, to examine the accuracy of the simulated torque a comparison is made between unloaded and loaded conditions at similar speeds. If the motor is operated both unloaded and loaded at a similar speed then these internal loads may reasonably be assumed constant and the difference in electromagnetic torque produced entirely to drive the applied external load.

Figure 6-23a shows the flux linkage-current loci obtained for the flux switching motor running at approximately 15,000rpm with no external load and 0.5Nm external applied load. Figure 6-23b shows the corresponding simulated instantaneous torques for the same conditions which are calculated using the Maxwell Stress method in finite element analysis. Figure 6-24 shows the same relationships for the flux switching motor running at approximately 8,000rpm unloaded and with 0.25Nm externally applied load. For the flux linkage-current loci the time instants of switch S1 turning on and off and switch S2 switching on and off are labelled A, B, C and D respectively.

In each case inspection of the flux linkage-current loci shows that the majority of mechanical energy is converted by the armature, as expected, although the work done by the field is not always negligible. For the armature loci shown in Figure 6-23a and Figure 6-24a from points A to B with switch S1 on positive current is flowing in the armature while its flux linkage is increasing to produce positive torque. At point B switch S1 is turned off and armature current falls rapidly to zero with a consequent reduction in armature flux linkage. However, as mutual coupling with the field is positive and still increasing, armature flux linkage rises again while there is zero armature current. At point C where switch S2 is turned on negative current is driven into the armature while its flux linkage is reducing, again producing positive torque and a similar process to above occurs after point D where switch S2 is turned off. The corresponding instantaneous torque waveforms obtained by the Maxwell Stress method shown in Figure 6-23b and Figure 6-24b also indicate that the majority of positive torque is produced by the armature but that there is a small positive torque produced by the field during periods of zero armature current. However, this is not immediately obvious from the complex path which the field flux linkage-current locus follows during an electrical cycle, a zoomed example of which is shown in Figure 6-25 for no external load at 14,982rpm.



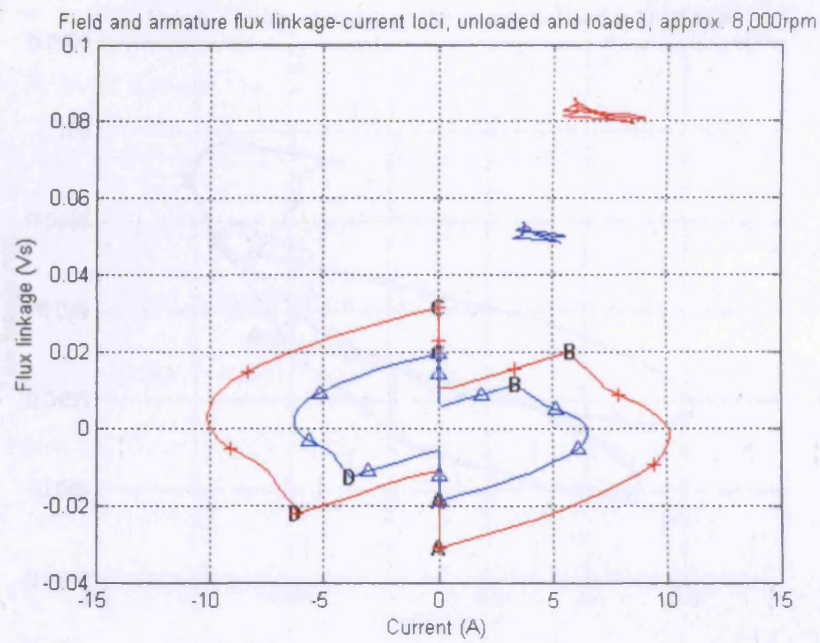
(a) Field and armature flux linkage-current loci for no externally applied load and 0.5Nm external load



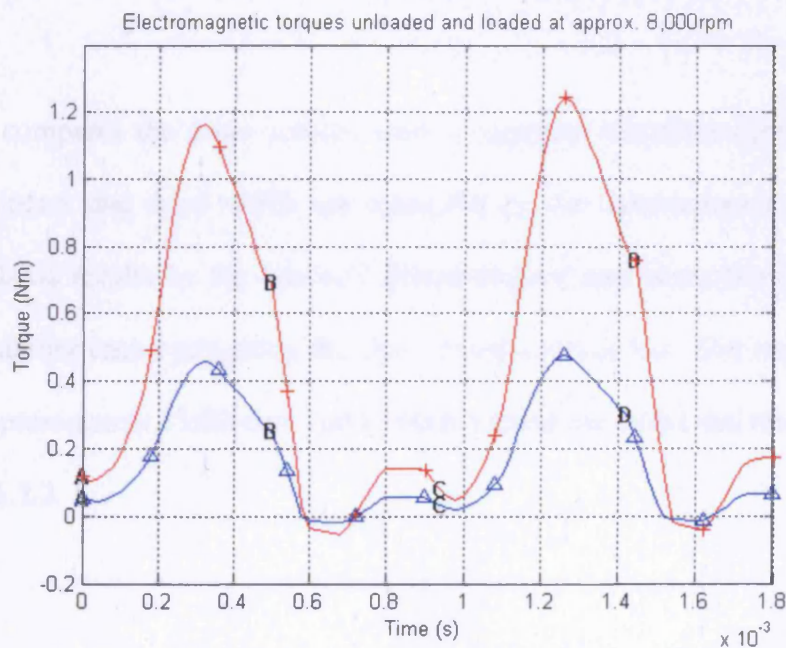
(b) Instantaneous torque by the Maxwell Stress method for no externally applied load and 0.5Nm external load

—▲—▲— No external load    —+—+— 0.5Nm external load

Figure 6-23 Flux linkage-current loci and instantaneous torque for the 8/4 flux switching motor running at approx. 15,000rpm unloaded and loaded



(a) Field and armature flux linkage-current loci for no externally applied load and 0.25Nm external load



(b) Instantaneous torque by the Maxwell Stress method for no externally applied load and 0.25Nm external load

—▲— No external load    —+— 0.25Nm external load

Figure 6-24 Flux linkage-current loci and instantaneous torque for the 8/4 flux switching motor running at approx. 8,000rpm unloaded and loaded

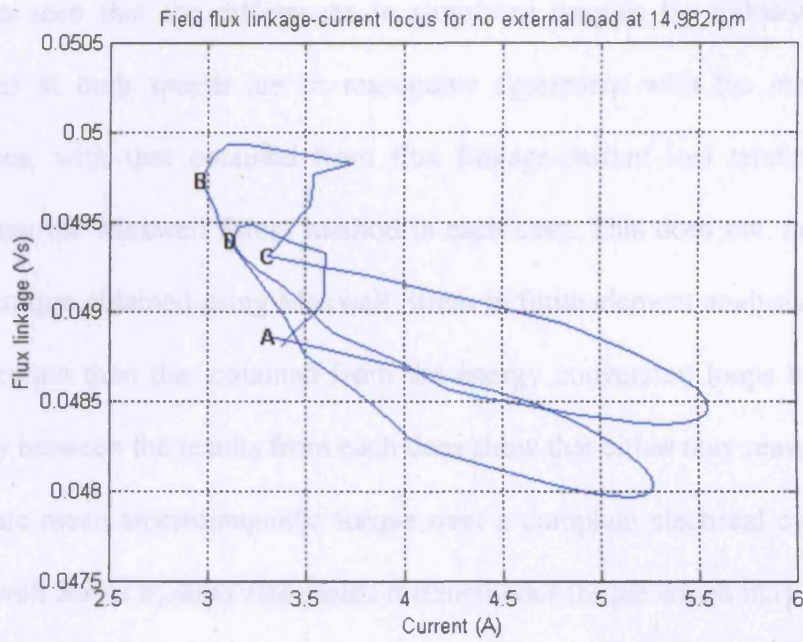


**Figure 6-25** Zoomed field flux linkage-current locus for the 8/4 flux switching motor running at 14,982rpm with no externally applied load

Table 6-5 compares the mean torques over a complete electrical cycle for the flux switching motor and drive which are measured by the dynamometer, and obtained from simulated results by the Maxwell Stress method and evaluation of the energy converted during each cycle using the flux linkage-current loci. The comparisons are made at approximately 15,000rpm and 8,000rpm using the simulated results presented in section 6.5.2.

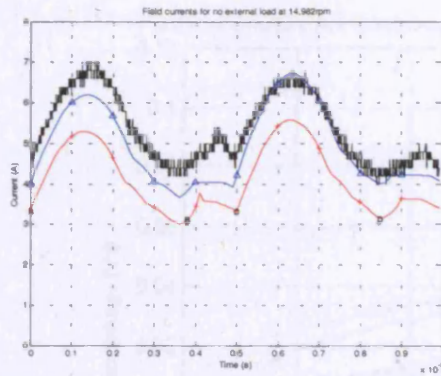
It can be seen that the differences in simulated torques for unloaded and loaded conditions at both speeds are in reasonable agreement with the measured torque differences, with that obtained from flux linkage-current loci tending to estimate higher than the Maxwell Stress method in each case. This does not, however, imply that the torque obtained using Maxwell Stress in finite element analysis is necessarily more accurate than that obtained from the energy conversion loops but the relative similarity between the results from each does show that either may reasonably be used to evaluate mean electromagnetic torque over a complete electrical cycle. However, the Maxwell Stress method also yields instantaneous torque which may be particularly useful for analysing the effects of varying control strategy etc.

Speed (rpm)	Measured torque from dynamometer (Nm)	Simulated torque from Maxwell stress (Nm)	Simulated torque from flux linkage-current loci (Nm)
15,022	0.5039	0.6804	0.7191
14,982	0.0231	0.1832	0.1934
Difference	0.4808	0.4972	0.5257
		(+3.4%)	(+9.3%)
7,985	0.2527	0.4207	0.4431
8,075	-0.0028	0.1586	0.1673
Difference	0.2555	0.2621	0.2758
		(+2.6%)	(+7.9%)

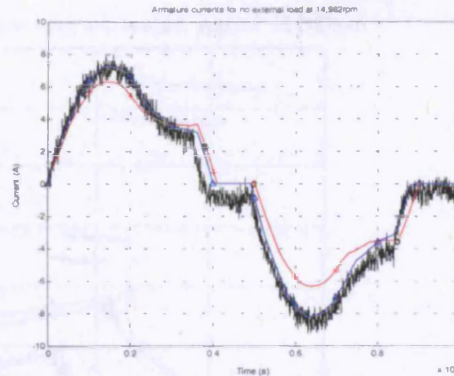
Table 6-5 Comparison of mean torque calculated by the Maxwell Stress and energy conversion loop methods

It was shown in section 6.5.6 that the simulated winding currents obtained for practical working conditions are sensitive to the positions at which the switched are turned on and off, as observed in practice. For the flux switching motor running at approximately 15,000rpm a 2 mechanical degree advance in switching positions can be seen to give the best correlation between simulated and experimental armature currents. As field current is controlled mainly by the peak value of armature current and most output power is created by the armature, it is reasonable to expect that the simulations which give the closest fit for armature current to experimental results may also give the closest simulated torque.

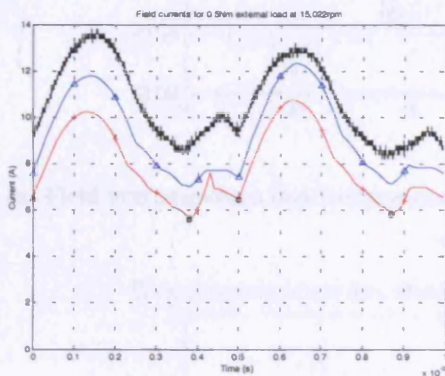
Figure 6-26 shows the differences in simulated field and armature currents for switching positions unadjusted and advanced by 2 mechanical degrees driving no external load and 0.5Nm external load. It can be seen that with the switching angles advanced the simulated armature currents are superimposed on the experimental results for much of the electrical cycle while field current is closer to experimental results but the agreement is not so close for both conditions.



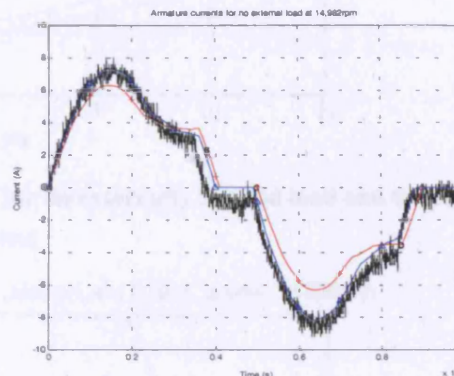
(a) Field current at 14,982rpm with no external load



(b) Armature current at 14,982rpm with no external load



(c) Field current at 15,022rpm with 0.5Nm external load

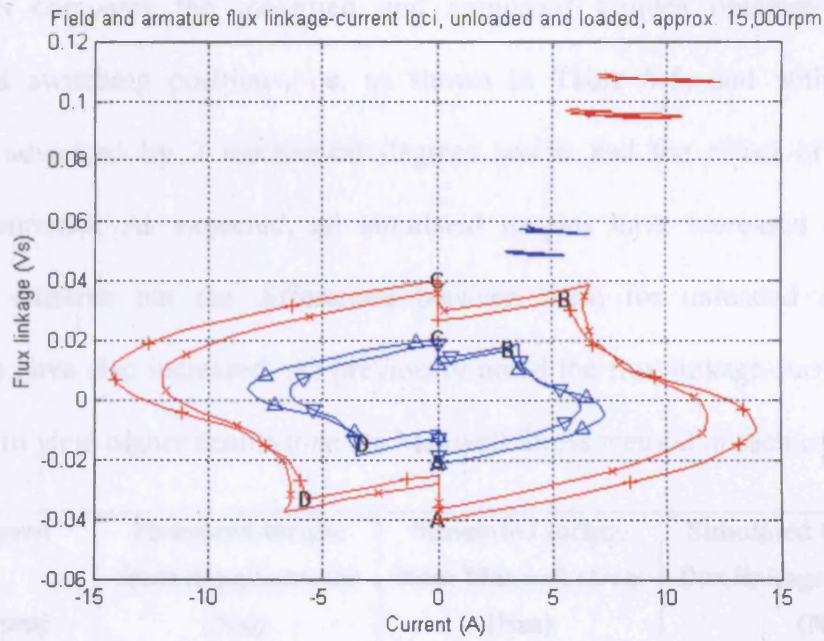


(d) Armature current at 15,022rpm with 0.5Nm external load

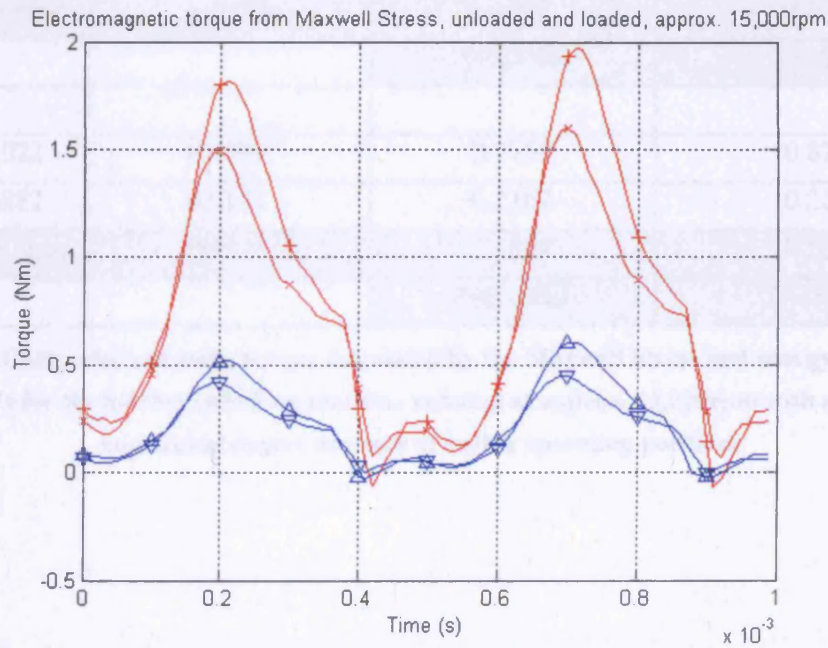
—●— Experimental    —■— As simulated  
 —▲— Simulated with 2°(mech) switching angle advance

Figure 6-26 Comparison of winding currents for the 8/4 flux switching motor running at approx. 15,000rpm with and without 2 mechanical degree advance of switch operating positions

Figure 6-27 shows the corresponding differences in simulated flux linkage-current loci and instantaneous torque for the unloaded case and with 0.5Nm external load. In each case the effects of larger field and armature currents due to the advanced switching positions are clear.



(a) Field and armature flux linkage-current loci for no externally applied load and 0.5Nm external load



(a) Instantaneous torque by the Maxwell Stress method for no externally applied load and 0.25Nm external load

▼▼ No external load(as simulated)     ×× 0.5Nm external load (as simulated)  
▲▲ No external load( $2^{\text{of(mech)}}$  advance)     + + 0.5Nm external load ( $2^{\text{of(mech)}}$  advance)

**Figure 6-27 Comparison of flux linkage-current loci and instantaneous torque for the 8/4 flux switching motor running at approx. 15,000rpm with and without 2 mechanical degree advance of switch operating positions**

Table 6-6 compares the measured and simulated torques obtained using the unadjusted switching positions, i.e. as shown in Table 6-5, and with switching positions advanced by 2 mechanical degrees which had the effect of increasing winding currents. As expected, all simulated torques have increased along with increased currents but the differences between them for unloaded and loaded conditions have also increased. As previously noted the flux linkage-current method continues to yield higher results than the Maxwell Stress method in each case.

	Speed (rpm)	Measured torque from dynamometer (Nm)	Simulated torque from Maxwell stress (Nm)	Simulated torque from flux linkage-current loci (Nm)
<b>Unadjusted</b>	15,022	0.5039	0.6804	0.7191
	14,982	0.0231	0.1832	0.1934
	Difference	0.4808	0.4972	0.5257
			(+3.4%)	(+9.3%)
<b>Advanced</b>	15,022	0.5039	0.7758	0.8213
	14,982	0.0231	0.2164	0.2286
	Difference	0.4808	0.5594	0.5927
			(+16.3%)	(+23.3%)

**Table 6-6 Comparison of mean torque calculated by the Maxwell Stress and energy conversion loop methods for the 8/4 flux switching machine running at approx. 15,000rpm with and without 2 mechanical degree advance of switch operating positions**

Hence, it can be seen that the simulation model of the flux switching motor and drive system for these conditions tends to overestimate the electromagnetic output torque. One explanation for some of this difference is that the switches are both switched on for slightly too long in simulation compared to experiment, which can be seen in Figure 6-9, thus extending the period of armature conduction and increasing mean torque. Another cause of difference between simulated and experimental results is the small cycle to cycle variation in switching positions and winding currents which are observed in practice due to non-symmetries and the feedback action of the controller. Hence, the quantities obtained from the dynamometer are averaged over several electrical cycles while the simulation is based on measured data collected for only one electrical cycle for each condition. These are both limitations of experimental technique and repeatability rather than the simulation model and their effects are not readily quantified.

Dynamic effects such as eddy currents and magnetic hysteresis are not included in the simulation model, which is based on 2-dimensional magnetostatic finite element data, and both will tend to have an effect on winding currents and system losses. However, the power losses associated with these effects may best be added to the input power rather than deducted from the output power, thus reducing efficiency rather than output for given operating conditions. This is also the case for electrical losses which are not explicitly accounted for in the model such as switching and diode losses while mechanical losses, such as friction and internal cooling fan, should be deducted from the gross electromagnetic output power.

*Hence, given these considerations, it can be seen that the dynamic simulation model for the flux switching motor, drive and control algorithm can yield results for winding currents and electromagnetic torque which both show reasonable agreement with experimental results. Allowances for the various losses which are not explicitly included in the simulation model may then be made using the simulated results and either added to the input power or deducted from the output power as appropriate.*

#### **6.5.9 Requirements for accurate dynamic simulation of the flux switching motor, drive and control strategy**

Unlike the back-emf test simulated in chapter 5, for practical operating conditions the current in the windings of the flux switching motor is controlled mainly by the action of the switches, hence the value of winding resistances used, even doubling the measured value, had relatively little effect on simulated results. However, in common with the results presented in chapter 5, it has been shown again that, provided the finite element model, flux map and data conversion process upon which the dynamic simulation is based are all 'reasonable' then the exact formulation or method used has only a relatively small effect on simulated results.

Adding a small amount of external inductance in series with the windings had a more noticeable effect on simulated output. It was observed that the simulated results are more sensitive to a change in armature inductance than field inductance and adding inductance affected both the magnitude and shape of simulated winding currents. However, for the simulation model of the complete motor, drive and control strategy it has been shown that the simulated results are very sensitive to changes in the positions at which the switches are operated. This sensitivity has also been observed experimentally. Hence, accurate determination of switch operating positions within the electrical cycle is the single most important requirement for obtaining good agreement between experimental and simulated results for the complete flux switching motor and drive system.

## **6.6      Summary and conclusions**

A dynamic simulation model for the flux switching motor, including power electronic drive circuit and switch control strategy was developed in this chapter. The normal and transient operation of the flux switching motor and drive circuit was also described, the behaviour of the bifilar wound armature was examined and a method for adding external series connected inductance to each winding was also introduced. The results of simulation were then compared to those obtained experimentally and the effects of several factors on the results obtained were examined.

Good agreement was demonstrated between simulated and experimental results. In particular the interaction of the field and armature and the behaviour of the bifilar armature are fully accounted for. Simulated results were shown to be very sensitive to the switch operating positions used, as is also the case in practice while the individual effects of different finite element model formulations was small. The simulated torques obtained by the Maxwell Stress and energy conversion loop methods were compared to experimental results and also shown to be in reasonable agreement. Examination of the energy conversion loops and instantaneous torque waveforms showed that, in practice, although most torque is produced by the armature there is a noticeable contribution made by the field.

Hence, these results fully support the position that, given a properly formulated finite element model which reasonably represents the machine to be simulated and provided 'reasonable' precautions are implemented during the data conversion process, good agreement between simulated and experimental results can be obtained for the operation of the flux switching machine. Furthermore, as the dynamic simulation model is relatively rapid at the point of use, the initial computational overhead is rapidly repaid and the overall dynamic simulation system is both accurate and efficient, hence suitable for detailed design use.

---

# **Chapter 7**

Electromagnetic design and  
optimisation using a genetic  
algorithm coupled with  
parameterised finite element  
analysis

---

## **7 ELECTROMAGNETIC DESIGN AND OPTIMISATION USING A GENETIC ALGORITHM COUPLED WITH PARAMETERISED FINITE ELEMENT ANALYSIS**

### **7.1 Introduction**

The electromagnetic design of new machine laminations generally involves the choice of multiple parameters from a very large design space, subject to constraints, in order to reach an optimal or acceptable design for a given application. This process is further complicated by non-linearity and the often strong interdependencies of the various parameters on each other and on performance. Hence, there is generally no readily derived analytic expression for the relationship between input parameters and machine performance, especially in the case of reluctance machines which offer a choice from several combinations of stator and rotor pole numbers, utilise electronic control and are generally driven heavily into saturation during normal operation.

The flux switching machine is particularly complex to design due to the mutual coupling between field and armature which must be taken into account as it is the main torque producing mechanism. Hence, design and optimisation of the flux switching machine is not readily amenable to traditional mathematical techniques and there is not a large body of design experience to guide the designer. Therefore, it is particularly appropriate to apply an automated design and optimisation technique which requires little or no prior knowledge or experience of a design problem yet is capable of yielding a near globally optimal solution. The genetic algorithm is one such technique which has been successfully applied to optimisation problems electrical engineering [64-66] and other areas [67-69].

This chapter describes the application of genetic algorithms to the design and optimisation of switched reluctance and flux switching machines, particularly the integration with parameterised finite element analysis which allows it to be readily applied to any problem which can be modelled in 2-dimensional magnetostatic finite element analysis. The genetic algorithm implemented is relatively simple and demonstrates the applicability and feasibility of the technique for this and other such design problems. Further work is currently being carried out as part of a separate research programme and the author would like to acknowledge the assistance of Mr Kao Siang Chai in programming the external genetic algorithm modules developed into the C++ language.

## 7.2 Genetic algorithms for optimisation

### 7.2.1 Background

The genetic algorithm for optimisation was initially proposed by Holland in 1975 [70]. Genetic algorithms attempt to mimic the process of Darwinian evolution [71], or 'survival of the fittest' in order to find a near globally optimal solution to a given problem [72-74]. Individuals are encoded into binary strings, or chromosomes, which mimic the function of DNA and completely describe a feasible candidate solution. An initial population of such individuals is created randomly, representing the well publicised 'primordial soup' from which life on Earth is widely believed to have evolved. The fitness of each individual in the population is evaluated with respect to the objective function being optimised, where the objective function is formulated to provide either a maximum or minimum value for the globally optimal solution. Once the fitness of each individual in the population has been evaluated, the next generation is created by allowing the fittest individuals to 'breed', creating offspring which generally combine and maintain desirable traits from the previous generation, while the weakest individuals simply die and are replaced with further random individuals, thus trying potentially new solutions. This cycle is repeated until either an optimal solution is found or the maximum allowable number of generations is reached. In general, the fitness of successive generations increases as evolution tends to favour the best, or fittest, individuals. Figure 7-1 illustrates the general operation of the genetic algorithm.

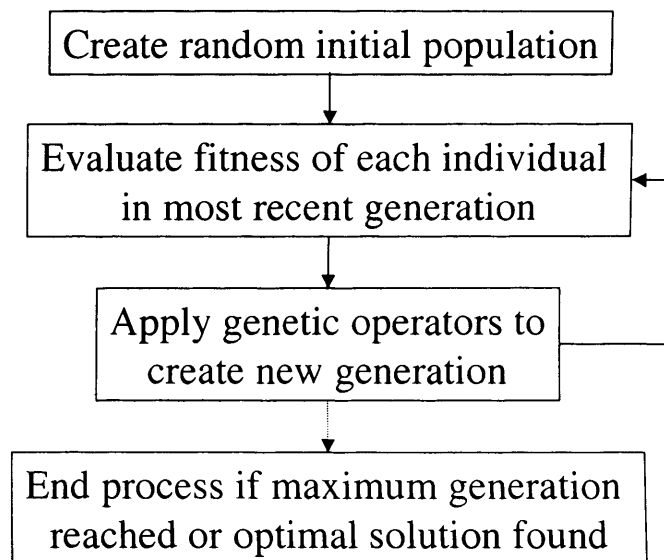
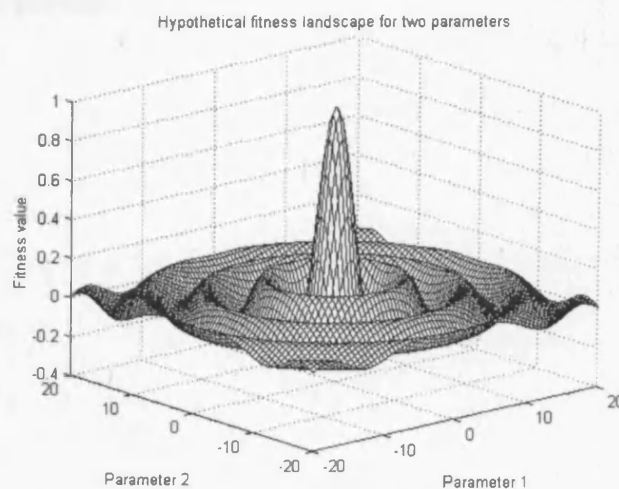


Figure 7-1 General operation of a genetic algorithm system

### 7.2.2 Comparison of genetic algorithms with other optimisation techniques

The concepts of ‘design space’ and ‘fitness landscape’ are central to the understanding of genetic algorithms. The design space is the complete range of feasible alternative solutions to a given problem, taking into account all constraints, i.e. every point in the design space corresponds to a unique feasible set of design parameters. For each feasible combination of parameters in the design space a numerical value may be derived which quantifies the goodness of that solution for a given purpose. The variation of this numerical value over the complete design space is the fitness landscape. For practical design and optimisation problems, the fitness landscape is generally large, multi-dimensional, discontinuous and/or contains several local maxima and minima.

Given no prior knowledge of the form of the fitness landscape an evaluative, or 'brute force' technique would seek to evaluate the fitness systematically for all, or a large number of, combinations of parameters and select the maximum value obtained. While such methods are likely to yield a near globally optimal solution, the amount of computation required for each evaluation makes them too expensive for many practical applications. A random search method would reduce the amount of computation required but the probability of locating the global maximum is directly proportional to the number of evaluations made. The effectiveness of analytic or 'hill-climbing' optimisation techniques often requires knowledge of the gradient of the fitness landscape in the vicinity of each evaluated solution and generally depends upon the choice of starting point. In cases where there are a number of local maxima such techniques are also likely to become trapped and return a locally optimal solution rather than the single global optimum. For example, Figure 7-2 shows a hypothetical fitness landscape for two parameters with a single global maximum and a number of local maxima which could be expected to 'trap' some optimisation techniques into returning only locally optimal solutions.



**Figure 7-2 Illustrative fitness landscape with multiple local optima**

Genetic algorithms begin with limited random search, the initial population, followed by the use of evolutionary strategies which also include some randomness and have been shown to have a good chance of finding a near globally optimal solution within a reasonable number of evaluations in such cases [72-74]. Genetic algorithms also require no knowledge of the form or gradient of the fitness landscape and by operating on complete populations of alternative solutions, the genetic algorithm may be considered inherently parallel, exploring several regions of the design space simultaneously within each population.

### *7.2.3 Enabling technologies for electromagnetic design using a genetic algorithm and finite element analysis*

As computer processor speeds have increased rapidly over the last decade and the 'usability' of commercially available software has improved, the use of finite element analysis for the electromagnetic design of machines has become more routine. Whereas it was once a costly tool requiring powerful computers and specialist analysts, practical only for detailed design and development work, it is now rapid enough to be used for comparison of a large number of alternative design options very early in the design process.

Alongside the improvement in finite element analysis solution times offered by increased computing power, the development of parameterised finite element analysis [46-48] has cut the effort required to create a large number of models for solving and automatic post processing as described in chapter 2. This is especially true for rotating machines where even simple analysis often requires a set of finite element solutions spanning a complete electrical cycle. Instead of having to manually create, mesh, solve and post-process a model for each position, parameterised finite element analysis allows the rapid creation, solution and post-processing of models with differing geometries and excitation conditions based on a generic model. This development greatly reduces the cost of finite element analysis while also making it readily amenable to automatic control for integration into an automated design and optimisation system.

### **7.3 Simple genetic algorithm implementation**

Referring to Figure 7-1, each of the major steps in implementing a simple genetic algorithm are treated in turn. The genetic algorithm acts on binary chromosomes which must be decoded into the parameters which describe the individual candidate solutions to be evaluated. The method used to analyse each candidate solution is external to the genetic algorithm but the objective function used to quantify the fitness of each is a key consideration in the implementation of genetic algorithms. Application of various genetic operators mimics the Darwinian evolutionary process while conditions are required for ending the genetic algorithm.

### 7.3.1 Encoding of individuals

In the same way as DNA completely describes the structure of living organisms, each potential solution in the design space is represented by a unique binary encoded string, or chromosome. The length of the binary string depends on the number of parameters being optimised and the resolution to which the range of each one is subdivided. For example, if there are 5 parameters available for optimisation and each is represented by 4 binary bits then the chromosome will be 20 bits long. With 4 binary bits per parameter, the continuous permissible range of each is divided into 16 discrete steps, thus giving a total of  $2^{20}$  or 1,048,576 possible unique chromosomes, each representing a feasible candidate design, making a complete search of the design space using finite element analysis unfeasible and a random search unlikely to locate the globally optimal design.

For solution of each individual, its chromosome must be decoded into values for each of the parameters which describe it. Knowing the number of parameters and number of bits representing each it is possible to divide the chromosome into a number of binary sub-strings, or genes, each of which describes one parameter. The value of the parameter can then be decoded by evaluating the binary sub-string and interpolating into the permissible range for that parameter. For example, if parameter 1 is represented by a 4 bit gene and its permissible range is 0 to 100 then the gene 0110, or 6 in decimal, represents the value 40, from the general relationship

$$value = \left[ \frac{(z_u - z_l)}{(2^n - 1)} \times gval \right] + z_l \quad (7.1)$$

where  $n$  is the number of bits representing the gene,  $z_l$  and  $z_u$  are lower and upper permissible limits respectively for the design parameter and  $gval$  is the decimal value of the gene to be evaluated. Table 7-1 shows an example of decoding an individual where 5 design parameters are encoded into a binary chromosome 18 bits long. For each gene the lower and upper limit is shown along with the corresponding evaluated parameter value.

Chromosome	010011010000111110 (length 18 bits)				
	Parameter 1	Parameter 2	Parameter 3	Parameter 4	Parameter 5
No. bits	4	4	4	4	2
Gene	0100	1101	0000	1111	10
Lower limit	0	10	-5	0.1	20
Upper limit	100	20	5	0.5	40
Value	26.67	18.67	-5	0.5	33.33

Table 7-1 Example of decoding design parameters from a binary chromosome

The choice of number of parameters optimised and number of bits per gene represents a compromise between speed of execution and resolution to which the design space is explored. For example, if there are five design parameters which may be optimised and each is represented by a 4-bit gene then there are 16 levels of discretisation for each parameter and a total of  $2^{20} = 1,048,576$  different feasible solutions in the design space. However, if each parameter is represented by 3-bit genes then each has 8 levels of discretisation and there are  $2^{15} = 32,768$  feasible alternatives in the design space, a reduction of almost 97%. Hence, a multi-stage approach with successively fewer parameters, but each with longer genes to maintain a given chromosome length, could be more efficient overall than a single very detailed search of a large design space.

### **7.3.2 Fitness evaluation of individuals**

The exact method used to analyse individuals is specific to each problem and is generally external to the genetic algorithm. For example, for design and optimisation of the flux switching machine, finite element analysis is used, either on its own or combined with additional analysis, to obtain relevant numerical indicators of performance. These results are then be read by the genetic algorithm for each individual to arrive at a single numerical fitness value for each evaluated candidate design. While the actual numeric values assigned to fitness need not be physical quantities, the fitness function must be formulated in such a way as to correctly compare between the ability of alternative solutions to meet the specified design objectives.

For example, in the initial design of the flux switching machine the peak to peak flux linking the armature for a fixed dc field mmf is one indicator of potential performance and may be used on its own as the fitness value. However, such a simple formulation may be susceptible to literal interpretation by which slot area could be minimised in order to achieve the lowest possible flux path reluctance in the steel but leading to unacceptably high current density in the coils. Although such a solution may give the best numerical value for fitness in this case it would not be a good solution in practice. A fitness function which includes a penalty for increasing current density would lead to 'better' designs being evolved, accounting correctly for the compromise between conflicting requirements. Hence, some caution is required in the formulation of fitness functions for electrical machine design and optimisation.

### **7.3.3 Genetic operators**

The mechanisms of Darwinian evolution for favouring survival of the fittest through successive generations are breeding among the fittest individuals, random genetic mutation and the deaths and replacement of the weakest individuals. These are implemented in the genetic algorithm optimisation scheme as crossover, mutation and replacement respectively.

#### **7.3.3.1 Crossover**

There are two aspects to the implementation of breeding, or crossover, between individuals to generate the next population. Firstly, the method by which parents' genetic information is combined to produce children and secondly the selection of which individuals will breed. These will be taken in turn.

Given two 'parent' chromosomes it may be generally expected that their offspring will exhibit some characteristics of each parent. Hence, genetic information is exchanged between the parents, known as crossing over. In this process, one or more points within the chromosomes are randomly selected and all binary bits within the selected range are exchanged between parents to create the offspring. Table 7-2 shows an example of single point and two point crossover [72-74] which are commonly implemented. The crossover points are denoted by dotted lines and it can be seen that some genes from each parent survive intact and are passed to the offspring, potentially carrying forward desirable features to the new generation, while some genes are destroyed if they span a crossover point, thus exploring new regions of the design space.

	Single point crossover		Two point crossover		
Parent 1	10011100101101	001011	1001100	11101010	11011
Parent 2	001100101110010	100111	0010011	01001110	01000
Child 1	10011100101101	100111	1001100	01001110	11011
Child 2	001100101110010	001011	0010011	11101010	01000

<sup>(1)</sup> Crossover points are denoted by a dotted line

Table 7-2 Examples of single and two point crossover of binary chromosomes

There are several alternative methods for selecting which individuals to breed with which others. However, in general the fittest individuals should generally have the best chance of their desirable genetic information surviving into the next generation. Three basic selection techniques are fit-fit breeding, random breeding and loaded roulette selection [72-74]. Fit-fit breeding requires all individuals to be ranked by fitness and, starting with the fittest, successively ranked individuals breed, i.e. 1st with 2nd, 3rd with 4th etc., with the expectation that two fit parents have the best chance of producing even fitter offspring. Random breeding represents the opposite extreme where parents are chosen randomly regardless of their relative fitness, thus implying that even poorly ranked individuals may contain some genes which, if combined with any other individual's genes, has an equally good chance of producing fit offspring as any other combination of parents.

In these ranked selection schemes each individual breeds once. Loaded roulette selection represents a compromise between these two extremes by semi-randomly selecting individuals, with the probability of selection for each individual being assigned in proportion to its fitness. Thus, breeding can occur between any combinations of individuals but, in general, the fittest will tend to breed more often than the weakest, which may not breed at all. Table 7-3 illustrates examples of these selection techniques for a hypothetical population of 10 individuals.

<b>Ranked individual</b>	1	2	3	4	5	6	7	8	9	10
<b>Evaluated fitness</b>	105	102	95	84	78	72	71	60	57	40
<b>Fit-fit selection</b>										
1&2	3&4		5&6			7&8		9&10		
<b>Random selection</b>										
4&7	9&1		8&5			6&3		10&2		
<b>Loaded roulette selection</b>										
<b>Individual</b>	1	2	3	4	5	6	7	8	9	10
<b>Breeding probability (%)</b>	13.7	13.4	12.4	11.0	10.2	9.4	9.3	7.9	7.5	5.2
10&2	5&4		9&7			4&1		8&4		

Table 7-3 Examples of selection strategies for breeding

### 7.3.3.2 Mutation

As in nature, random genetic mutation leads to new areas of the feasible design space being explored and helps to avoid the genetic algorithm becoming trapped in the vicinity of a locally optimal solution. Mutation is a bitwise operation applied to each new population before evaluation [72-74]. For example, if a mutation rate of 4% is specified then every bit in every individual has a 4 in 100 chance of being mutated. When a bit has been selected for mutation in this way its value may either be flipped, from 1 to 0 or vice versa, or randomly reselected. In the extreme, a 100% mutation rate is equivalent to a completely random search. Table 7-4 illustrates the mutation process for a hypothetical chromosome with a mutation rate of 25% using either the flip-bit or random reselection method.

<b>Chromosome</b>	1	0	0	1	1	0	1	0	0	0	1	0	1	1	0	1
<b>Mutate?</b>	N	N	Y	N	Y	N	N	N	N	N	Y	N	N	N	Y	N
<b>Flip-bit result</b>	1	0	1	1	0	0	1	0	0	0	0	0	1	1	1	1
<b>Reselection result</b>	1	0	0	1	0	0	1	0	0	0	1	0	1	1	1	1

Table 7-4 Example of bitwise mutation in a binary chromosome

### **7.3.3.3 Replacement**

In every population there are likely to be some individuals with very poor fitness evaluations which will die without breeding. This is implemented in the genetic algorithm by removing the weakest individuals before crossover and replacing them directly in the new generation with new randomly generated individuals. Thus, the genetic algorithm is able to continue exploring new regions of the design space while still evolving the best solutions. The proportion of individuals replaced at each generation must be chosen with caution as this could lead to the loss of weak individuals which, despite their poor fitness, possessed good genes which could have led to fit offspring if crossed over with another individual or with a small amount of mutation. In the extreme, 100% replacement rate is equivalent to a completely random search of the design space.

### **7.3.4 *Conditions for ending the genetic algorithm***

Although genetic algorithms are less likely to be trapped by local optima in the design space as some other optimisation techniques due to the presence of randomness in several of the operators, they do tend to converge, generally towards a near globally optimal solution. Under such conditions it may be more effective, both in terms of finding the global optimum and computational efficiency, to halt the present genetic algorithm and restart the process, either from a new random initial population or with updated genetic algorithm parameters to refine the search.

Due to the random nature of the genetic operators, successive executions of the genetic algorithm, even starting from the same initial population, will generally yield different results. If there is a single global optimum most instances of the genetic algorithm will tend to converge towards the same optimal solution. However, whether the genetic algorithm does converge towards the global optimum and the rate at which it does so is also affected by the choice of genetic algorithm parameters. Hence, to avoid abortive searches and limited benefit for computational investment, the first condition for ending the genetic algorithm is when the rate of fitness improvement between populations falls below a specified threshold.

To limit the amount of computational effort expended to a practical maximum, the second condition for ending a genetic algorithm is when a specified maximum number of generations, hence number of individuals evaluated, is reached. In general, if the genetic algorithm has had enough generations to have a 'reasonable' chance of converging then it may be more effective to restart the genetic algorithm from a new random initial population. It should be noted that the genetic operators are executed on each generation, hence evolution can only take place after each generation has been fully evaluated and a compromise is necessary between the number of individuals per population to maintain a sufficient 'gene pool' for breeding and the need to evaluate a sufficient number of generations to allow the evolutionary process to take effect within overall computational constraints.

If a specific performance target has been set but it is less important precisely how it is achieved then the genetic algorithm may also be ended after the first generation where this criterion has been met by one or more individuals. This method produces an acceptable design in terms of performance. However, a number of better alternative solutions may be expected to lie in the vicinity of the solution in question which could be found relatively rapidly by the genetic algorithm if it were allowed to continue. Hence, caution is required when exercising this condition for ending the genetic algorithm not to forfeit better alternative solutions which could have been found for little additional computational effort.

If a genetic algorithm has been stopped for any reason at the end of a generation it can be readily restarted from that point, either to allow more generations to be evaluated or using different genetic algorithm parameters. For example, for early generations it may be desirable to include a high degree of randomness in order to allow a relatively rapid exploration of the design space, by high mutation and/or replacement rates. However, as the genetic algorithm converges towards optimal solutions it may be more efficient to reduce the amount of randomness and/or change the number and resolution of design parameters to allow a more focused search in the region of design space of interest.

## 7.4 Integration of the genetic algorithm with parameterised finite element analysis

### 7.4.1 Software control

The genetic algorithm system implemented consists of four separate modules, with communication between them by means of formatted text files. These communication files may be retained to provide a full record of the activity of the genetic algorithm and allow any population or individual to be recreated for further analysis. Vector Fields Opera 2-dimensional parameterised finite element analysis software [46-48] was used in this case and overall control of the genetic algorithm is carried out by the control module which was written in the Opera scripting language. The external modules are the genetic algorithm engine module, which implements the genetic operators, decoding module, to convert binary chromosomes into input scripts for parameterised finite element analysis, and fitness evaluation module, to read the post processed output from finite element analysis and yield a fitness value for each individual tested. Figure 7-3 shows the structure of the overall system.

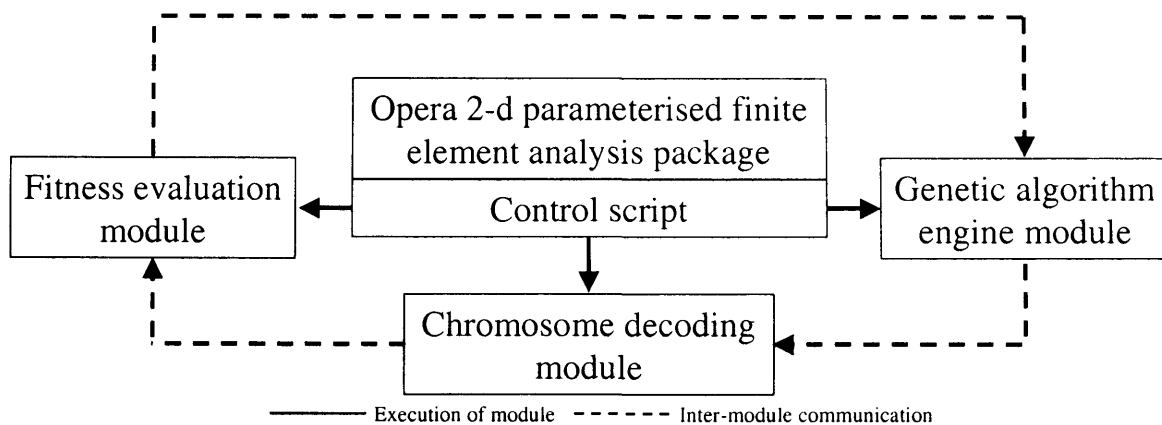


Figure 7-3 Schematic of genetic algorithm/parameterised finite element system implemented

#### ***7.4.2 Translation of decoded parameters into finite element models***

The parameters decoded from each individual chromosome completely describe a feasible candidate solution in the parameterised finite element model. However, this data must be entered and the model solved and post-processed for the necessary range of conditions, for example a range of positions spanning a complete electrical cycle. Design parameters are entered via script files created by the decoding module while the common operations carried out for each candidate design are defined in the control script and finite element model.

Each genetic algorithm parameter may also be set to correspond to more than one design parameter, for example to keep slot shapes symmetric etc. Once the parameter input script files for the entire population have been created by the decoding module, the control module instructs the finite element package to read them in turn to be solved and post-processed for the appropriate conditions.

#### ***7.4.3 Fitness evaluation using finite element analysis output***

After solving, each finite element solution for a given individual is automatically post-processed and the numerical results are placed into a text file. After each complete generation has been solved and post-processed, the fitness evaluation module is executed. It reads the relevant results files for each individual and computes their fitness values using the specified fitness function, for example mean torque, peak to peak flux etc.

The fitness function is formulated to reward desirable properties of the design and penalise undesirable ones using various weightings. Table 7-5 illustrates the process for calculating the fitness value for an individual using an extract from a results file. In this example the fitness function forms a compromise between slot area, hence field mmf, and flux path reluctance.

Fitness function $f = \frac{\Phi_{a\max} - \Phi_{a\min}}{F_f} \times A_{slot}$ where $f$ is fitness value, $\Phi_a$ is armature flux, $F_f$ is field mmf and $A_{slot}$ is slot area			
Extract from finite element results file		Fitness evaluation	
Solution file:	G006I0014_1.ST	$\Phi_{a\max}$	0.014938
Rotor angle:	0	$\Phi_{a\min}$	-0.013324
Field mmf:	349.645	$F_f$	349.645
Field flux:	0.0183486	$A_{slot}$	80.0869
Armature mmf:	0.0	$f$	<b>0.00647</b>
Armature flux:	0.014938		
Slot area:	80.0869		
Solution file:	G000I0014_2.ST		
Rotor angle:	45		
Field mmf:	349.645		
Field flux:	0.017532		
Armature mmf:	0.0		
Armature flux:	-0.013324		
Slot area:	80.0869		

Table 7-5 Example of obtaining individual fitness from finite element analysis text results file

#### 7.4.4 Progress logging

The genetic algorithm has the potential to generate and evaluate a very large number of candidate solutions automatically, most of which are likely to be of little interest. Hence, a record is required which allows the user to examine which options have been tried, examine progress of the genetic algorithm and select any individuals which are of particular interest for more detailed examination. In particular, after the genetic algorithm has finished the fittest few individuals may be more closely examined, regardless of the generations in which they occurred. Hence, general observations may be made of the ranges of parameters which yield good designs, either as the basis for a more focused genetic algorithm search or as the starting point for a conventional manual design process.

All text files generated by the genetic algorithm modules for communication and generation of individuals in finite element analysis are retained. The text files used for communicating between the fitness evaluation module and genetic algorithm engine module are especially informative as they contain a record of all evaluated chromosomes and their evaluated fitness in a known format, allowing examination in a spreadsheet package, as illustrated in Table 7-6, to search for common features etc. Thus, the genetic algorithm may be regarded as automatically 'keeping its own log book'.

Chromosome	Fitness
1011010001010100010	,0.0425
0101111010100100101	,0.0532
0101110101011101010	,0.0273
1101000101110101001	,0.0791
0101001111101010000	,0.0547
...	

Table 7-6 Extract from fitness evaluation module output file

## 7.5 Results

The operation of the complete genetic algorithm and parameterised finite element system is demonstrated, and the performance compared, for a variety of genetic algorithm parameter settings and three test problems. In each case the results of the genetic algorithm are presented as fitness plotted against generation for the fittest and weakest individual within each population and the mean population fitness. Linear least squared error fitted trend lines for each show the overall effects of evolution process and it is shown that implementation of the simple genetic algorithm with 'reasonable' parameter settings generally leads to an upward trend in fitness of both the fittest individual and population mean with successive generations.

### 7.5.1 *Effects of genetic algorithm parameter settings*

The operation of the genetic algorithm coupled to parameterised finite element analysis was initially tested by application to a test problem involving optimisation of four design parameters in the 8/4 flux switching machine described in chapter 2. Three tests, each a separate genetic algorithm optimisation, were carried out for optimisation of the geometric parameters summarised in Table 7-7. For tests 1 and 2 each parameter was described by a gene 8 bits in length (256 possible values) while for test 3 each parameter was described by a 4 bit gene (16 possible values). Hence, the discretised design space for tests 1 and 2 comprised  $2^{32}$  possible feasible solutions while the discretised design space for test 3 comprised  $2^{16} = 65536$  possible solutions, a 99.99% reduction in design space. For each test a total of 250 evaluations are made of candidate solutions, representing only a small portion of the design space. Hence, the genetic algorithm is unlikely to yield the globally optimal solution for any of the test cases and a reasonable comparison between the evolutionary performance of each, i.e. tendency to increase the fitness of individuals in successive generations, can be made.

As slot area available for windings is not greatly affected by the choice of parameters being optimised, a constant field mmf was used and the resulting geometry was solved in both aligned positions to obtain maximum peak to peak armature flux. Fitness was evaluated as

$$f = \Phi_{a(\max)} - \Phi_{a(\min)} \quad (7.2)$$

where  $f$  is evaluated fitness and  $\Phi_a$  is armature flux.

Description of geometric parameter	Length of gene			Lower limit	Upper limit
	Test1	Test2	Test3		
Field slot opening (% pitch)	8	8	4	0	70
Armature slot opening (% pitch)	8	8	4	0	70
Rotor grading length (% pitch)	8	8	4	20	50
Rotor grading depth (% thickness)	8	8	4	85	98

**Table 7-7 Design parameters and discretisation for tests 1-3**

The genetic algorithm parameters used for the tests were selected to give a 'reasonable' compromise between the ability of the genetic algorithm to probe new regions of the design space and to allow improvements due to evolution. For all the tests the size and number of generations, replacement rate, crossover method and mutation rate were kept the same. Table 7-8 summarises the genetic algorithm parameter settings used for each. Comparison between tests 1 and 2 shows the effect of ranked order and random order crossover selection while comparison between tests 1 and 3 shows the effects of gene length for each design parameter. Although the effects of genetic algorithm parameter settings are not fully evaluated using such a small number of tests due to the probabilistic nature of the process, the results obtained show that the genetic algorithm system works and some observations may be made of its effectiveness for each of the conditions.

Genetic algorithm parameter	Value		
	Test 1	Test 2	Test 3
Number of individuals per generation	10	10	10
Number of generations	25	25	25
Replacement rate (Individuals per generation)	2	2	2
Crossover ranking	Ranked	Random	Ranked
Crossover method	Single	Single	Single
Mutation rate (%)	5	5	5
Mutation method	Flip bit	Flip bit	Random

**Table 7-8 Genetic algorithm parameters used for tests 1-3**

Figure 7-4 shows the progress of the genetic algorithm for tests 1 to 3. In each case there is a clear upward trend in both maximum and mean population fitness with successive generations. The large fluctuation in minimum fitness for each population is largely due to the insertion of random individuals by the replacement process, which also affects the population mean values.

The maximum values for test 1 using rank order selection follow the linear trend line closely while for test 2 using random order selection the maximum fitness values vary about the trend line. *This observation indicates that, in general, fit individuals tend to breed to create fitter offspring but that randomly selected less fit chromosomes also have a good chance of producing fit offspring.*

As the gene lengths in test 3 are shorter, a single bit difference in each represents up to 16 times the difference in the associated geometric parameter value. Hence, the evolutionary process is affected more by random mutation and crossover effects, giving a more rapid search of the continuous design space and potentially more rapid evolution. The gradient of maximum fitness with generation for test 3 is over 9 times greater than test 1 and tends to support this. Hence, a coarse search appears most efficient for the genetic algorithm to rapidly locate the region of design space containing the globally optimal solution but a finer search may be necessary to better locate it.

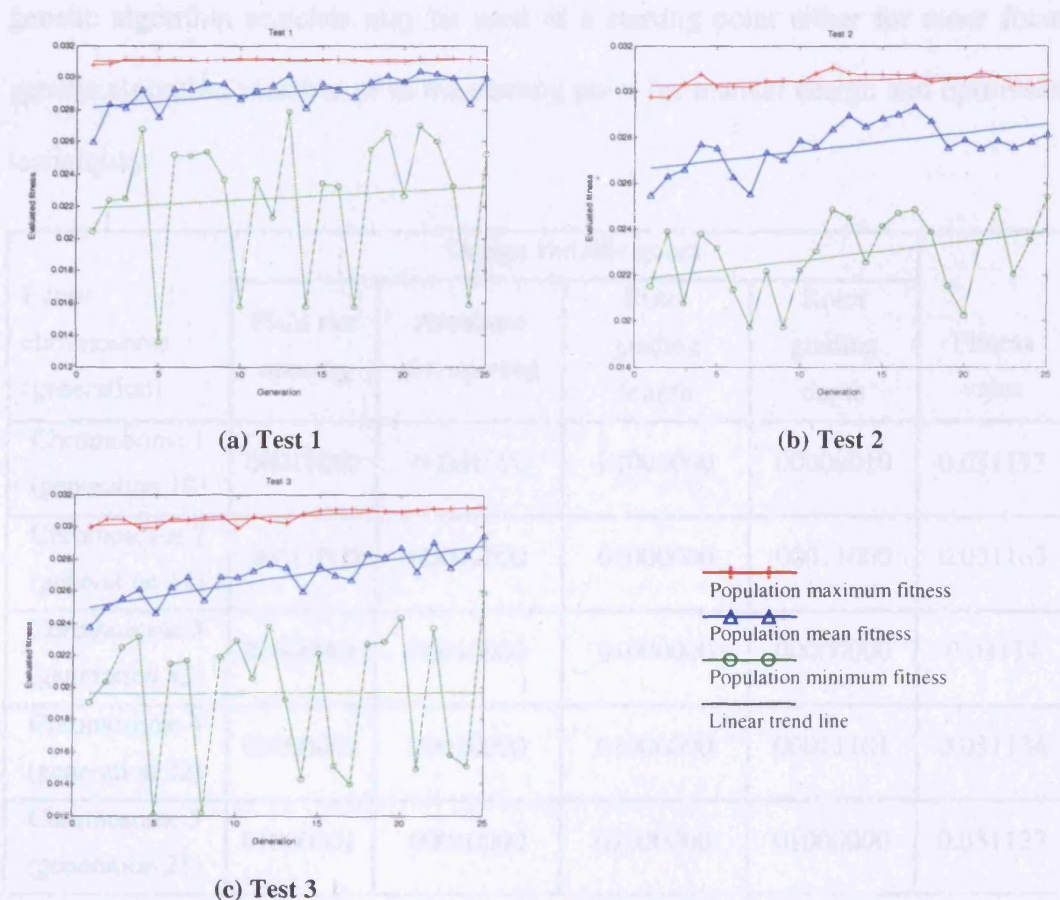


Figure 7-4 Evolutionary progress of genetic algorithm tests 1-3

Table 7-9 shows the chromosomes from test 1 which yield the highest fitness values and the generations in which they occurred. Inspection of the generations from which these chromosomes were obtained illustrates the effectiveness of evolution for carrying good traits forward into future generations as they occurred in two sets of successive generations. Comparing the genes for each design variable shows that in each case the gene for rotor grading length is identical while the genes for armature slot opening are similar. The value for field slot opening has less effect while the gene for grading depth varies greatly, hence implying that it has little effect on fitness compared to the other parameters. This example illustrates how data obtained from genetic algorithm searches may be used as a starting point either for more focused genetic algorithm searches or as the starting point for manual design and optimisation techniques.

Fittest chromosome (generation)	Design variable genes				Fitness value
	Field slot opening	Armature slot opening	Rotor grading length	Rotor grading depth	
Chromosome 1 (generation 10)	00011000	00001000	01000000	00000010	0.031173
Chromosome 2 (generation 11)	00011000	00001000	01000000	00011000	0.031163
Chromosome 3 (generation 23)	01000001	00010000	01000000	00000000	0.03114
Chromosome 4 (generation 22)	01000001	00010000	01000000	00011101	0.031134
Chromosome 5 (generation 21)	01000001	00010000	01000000	01000000	0.031127

**Table 7-9 Comparison of parameters between the fittest individuals found in test 1**

**7.5.2 Effects of population size and number of generations**

To evaluate the effects of population size and number of generations the genetic algorithm was applied to the optimisation of 8 design parameters describing slot and rotor shape for a switched reluctance machine geometry with symmetric rotor and stator poles, each represented by genes 3 bits long, i.e. each parameter has 8 possible values and the design space comprises  $2^{24} = 16,777,216$  feasible solutions. Table 7-10 summarises the genetic algorithm parameters used for each case with tests 4 to 6 comprising 800, 600 and 1500 candidate solution evaluations respectively. Replacement rate is selected to be between 15 and 25% in each case while all other genetic algorithm parameters are the same for each.

Genetic algorithm parameter	Value		
	Test 4	Test 5	Test 6
Number of individuals per generation	16	30	50
Number of generations	50	20	30
Replacement rate (Individuals per generation)	4	6	8
Crossover ranking	Ranked	Ranked	Ranked
Crossover method	Single point	Single point	Single point
Mutation rate (%)	5	5	5
Mutation method	Random	Random	Random

**Table 7-10 Genetic algorithm parameters used for tests 4-6**

A fixed mmf is used for each case and the finite element models for each candidate solution were solved in the aligned and unaligned positions. Fitness was defined as

$$(\Phi_{al} - \Phi_{un}) \times A_{slot} \tag{7.3}$$

where  $\Phi_{al}$  and  $\Phi_{un}$  are phase flux in the aligned and unaligned positions respectively and  $A_{slot}$  is slot area, thus encouraging a large change in flux between aligned and unaligned positions, i.e. high electromagnetic torque, combined with large slot area, i.e. low copper losses.

Figure 7-5 shows the results obtained for tests 4-6. In each case there is an upward trend in mean population fitness and also for maximum fitness in tests 4 and 5. The linear trend in maximum fitness for test 6 is downwards although this may be partly due to the high maximum fitness of the early generations as mean population fitness still shows an upward trend.

For the test case used the range of potential fitness values for feasible candidate solutions is very large and the gene length for each design parameter comparatively short. Hence, a single bit change in genes can lead to a large change in corresponding geometric parameter, thus helping to explain the large fluctuation in maximum fitness values observed. In this instance it can be seen that test 4 produced the greatest number of individuals with high evaluated fitness values despite only half the finite element evaluations of test 6. *This implies that, for cases where there is a large number of parameters to optimise, it is most effective for a given number of finite element evaluations to spread them over a larger number of smaller generations, thus giving the evolutionary operators the best chance to create good solutions by successive breeding.*

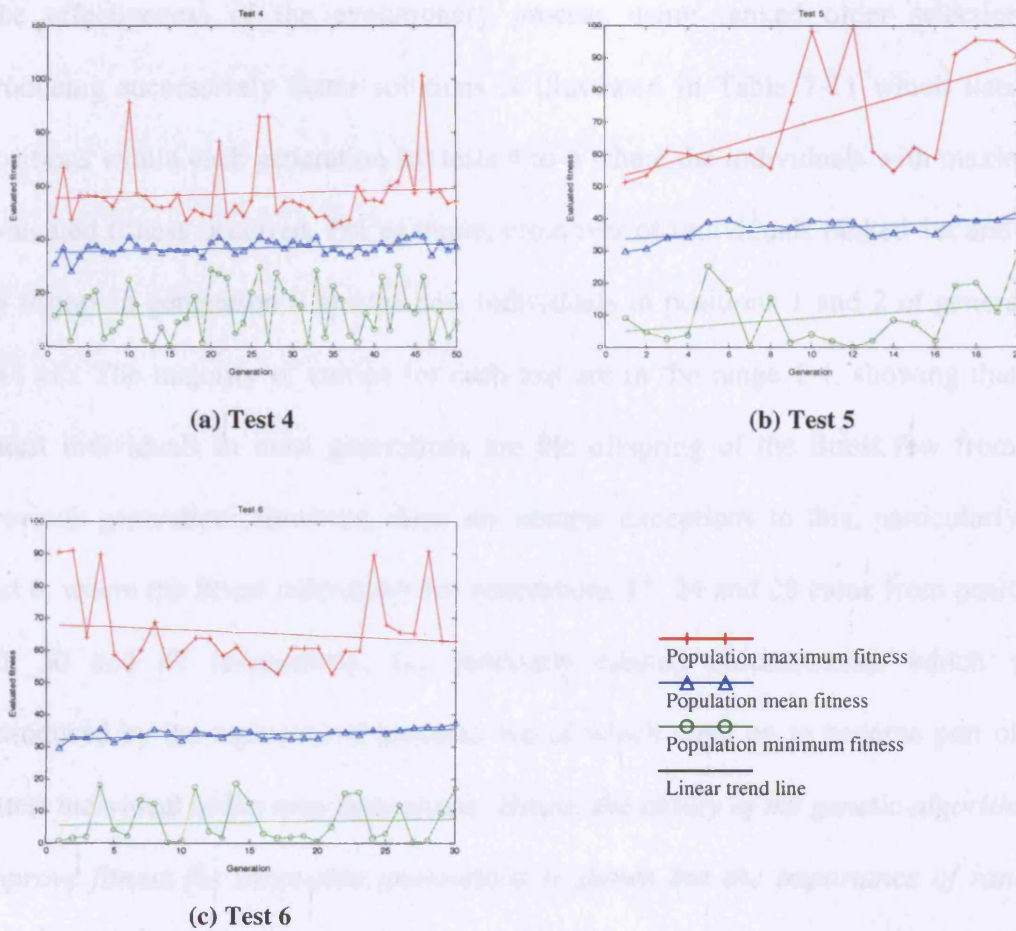


Figure 7-5 Evolutionary progress of genetic algorithm tests 4-6

Test	Gen	Max	Mean	Min
Test 4	0	45	35	15
	5	45	35	15
	10	90	35	15
	15	45	35	15
	20	45	35	15
Test 5	0	50	35	10
	5	60	35	10
	10	95	35	10
	15	60	35	10
	20	90	35	10
Test 6	0	90	35	5
	5	90	35	5
	10	65	35	5
	15	65	35	5
	20	65	35	5

The effectiveness of the evolutionary process using ranked order selection in producing successively better solutions is illustrated in Table 7-11 which lists the positions within each generation for tests 4 to 6 where the individuals with maximum evaluated fitness occurred. For example, crossover of individuals ranked 1st and 2nd by fitness in generation  $n$  creates new individuals in positions 1 and 2 of generation  $n+1$  etc. The majority of entries for each test are in the range 1-4, showing that the fittest individuals in most generations are the offspring of the fittest few from the previous generation. However, there are notable exceptions to this, particularly for test 6, where the fittest individuals for generations 17, 24 and 28 came from positions 50, 50 and 47 respectively, i.e. randomly created chromosomes which were introduced by the replacement process, two of which went on to become part of the fittest individual in the next generations. *Hence, the ability of the genetic algorithm to improve fitness for successive generations is shown but the importance of random replacement in exploring new regions of the design space is also demonstrated.*

Test	Position of fittest individual in each generation
Test 4	10, 12, 3, 1, 1, 1, 1, 2, 1, 1, 2, 5, 4, 4, 2, 2, 6, 3, 1, 2, 5, 2, 4, 4, 2, 2, 1, 3, 7, 3, 4, 2, 15, 3, 2, 14, 14, 2, 2, 2, 14, 2, 1, 11, 16, 2, 1, 1, 1, 11
Test 5	2, 6, 1, 1, 2, 2, 2, 3, 9, 2, 26, 2, 1, 1, 14, 2, 5, 10, 1, 1
Test 6	36, 1, 1, 5, 1, 1, 4, 2, 46, 4, 2, 2, 2, 1, 1, 3, 50, 2, 1, 1, 1, 4, 1, 50, 12, 2, 2, 47, 1, 1

Table 7-11 Positions of fittest individuals in each generation of tests 4-6

### 7.5.3 Genetic algorithm applied to initial design

During the initial design stages of the flux switching machine a large number of design parameters describing lamination geometry are available for selection. To show the effectiveness of the genetic algorithm for such cases it has been applied to the initial design of a flux switching machine with 24 parameters available for optimisation describing field and armature slot shapes, rotor shape and rotor diameter within a fixed stator outer diameter. Each variable is described by a gene 3 bits long, giving 8 possible values for each and a total discretised design space of  $2^{72}$  possible candidate solutions. The ranges for each parameter describing geometry are selected such that they do not overlap and every chromosome yields a feasible candidate solution.

As slot area is affected strongly by the selected geometry a fixed field slot current density is specified and the fitness is specified as

$$f = \Phi_{a(rms)} \times 100 \quad (7.4)$$

where  $f$  is evaluated fitness and  $\Phi_{a(rms)}$  is the rms value of armature flux over a complete electrical cycle. Thus, larger slots are rewarded by a higher field mmf and the fitness function directly rewards higher armature flux, whether obtained by improved coupling or higher field mmf. Table 7-12 summarises the genetic algorithm parameter settings used. As a relatively rapid search of the design space is required for such initial design a replacement rate of 8 individuals per generation is specified. Two-point crossover is also used in this case to potentially increase the exploration of new areas of design space as the genes are short compared to chromosome length.

Genetic algorithm parameter	Value
Number of individuals per generation	20
Number of generations	34
Replacement rate (Individuals per generation)	8
Crossover ranking	Ranked order
Crossover method	Two-point
Mutation rate (%)	2
Mutation method	Random reselection

Table 7-12 Genetic algorithm parameters used for test 7

Figure 7-6 shows the fitness results obtained from the genetic algorithm at each generation. There is a clear upward trend in both maximum individual and population mean fitness values which may reasonably be expected to continue for further generations.

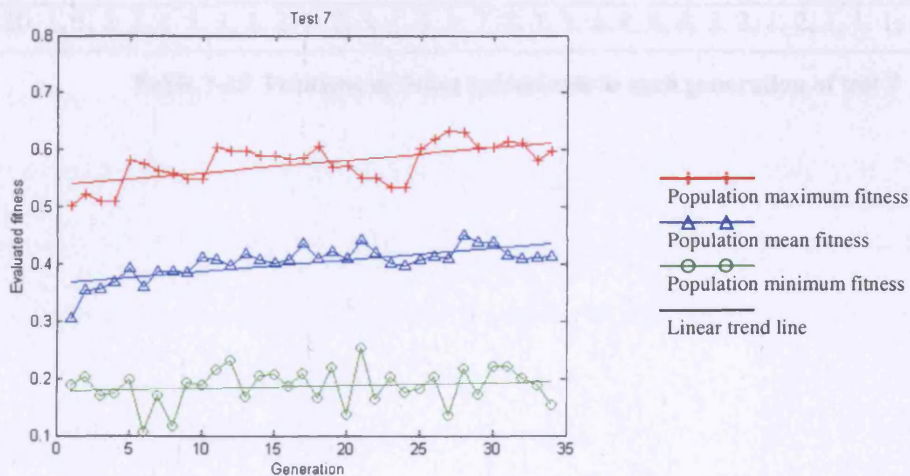


Figure 7-6 Evolutionary progress of genetic algorithm test 7

Table 7-13 shows from the positions of the fittest individuals in each population that most of this improvement is due to progressive evolution among the fittest groups of individuals in each population. This implies that, despite the high replacement rate, many areas of the design space yield poor solutions, as expected, but if a good solution is found in a new area of design space then it has a good chance of being combined with existing fit individuals to yield still fitter solutions. Thus, a comparison of the chromosomes of the fittest few individuals obtained from such a general genetic algorithm would yield common factors which strongly affect fitness and those which do not, which may be eliminated from successive genetic algorithm searches. *Hence, the applicability of the genetic algorithm for initial design with a large number of design parameters is demonstrated.*

Positions of highest individuals in fitness files
9, 20, 1, 1, 2, 1, 1, 1, 1, 1, 2, 1, 2, 3, 1, 5, 1, 2, 2, 1, 3, 1, 4, 4, 4, 2, 2, 1, 2, 1, 1, 1, 1, 2

**Table 7-13 Positions of fittest individuals in each generation of test 7**

#### *7.5.4 Summary of results*

The tests carried out on the simple genetic algorithm coupled with parameterised finite element analysis show that, in general, an upward trend in both maximum individual and population mean fitness with successive generations is obtained using 'reasonable' genetic algorithm parameters, although this is not necessarily guaranteed in every case. In particular, the genetic algorithm has been shown to lead to an upward trend in tests representing both initial design and detailed optimisation, making the technique applicable throughout the design process. Furthermore, successful operation has been demonstrated for both flux switching and switched reluctance machines, indicating that the system developed may be applied to the design and optimisation of other electromagnetic devices which can also be described and modelled using parameterised finite element analysis.

Therefore, genetic algorithms coupled with parameterised finite element analysis have been shown to work in practice. However, the fitness functions used in the tests presented were relatively simple and the fittest individuals produced in the tests may not necessarily be the best solutions in practice. Hence, further investigation and development is continuing as part of a separate research project.

## 7.6 Summary and conclusions

This chapter has described the implementation of a simple genetic algorithm system coupled with parameterised finite element analysis for the design and optimisation of electromagnetic problems. In particular, the operation of genetic algorithms and their integration with parameterised finite element analysis was described. Application of the system to test optimisation problems representing both initial design and detailed optimisation phases of the design process led in each case to successively better solutions. Hence, the effectiveness and applicability of the system developed as part of a semi-automated electromagnetic design process was demonstrated. However, the practical effectiveness of the system was also shown to be dependent on the formulation of the objective function and it is, therefore, suggested that such a technique is best applied as an aid alongside the manual design process rather than as a replacement for it.

---

# **Chapter 8**

Image processing method for iron  
loss visualisation in electrical  
machines

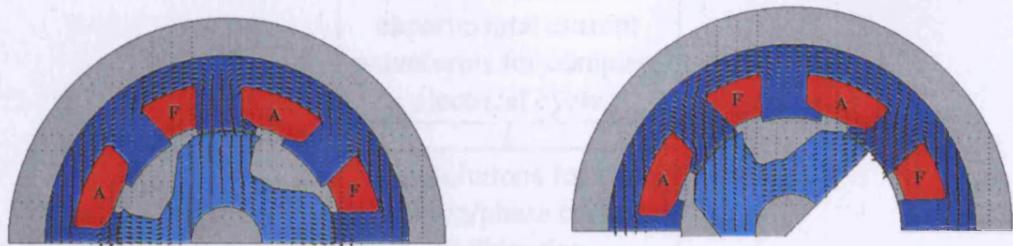
---

## **8 IMAGE PROCESSING METHOD FOR IRON LOSS VISUALISATION IN ELECTRICAL MACHINES**

### **8.1 Introduction**

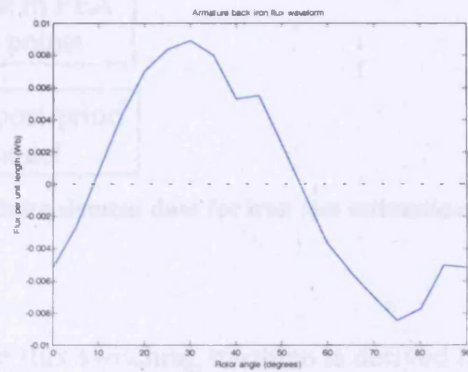
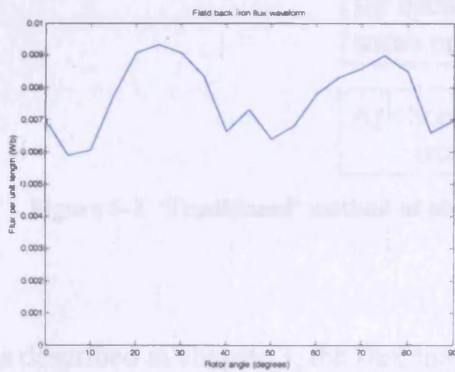
Any part of the magnetic circuit in an electrical machine which is subject to time varying magnetic flux will experience heating due to power losses, the main mechanisms being hysteresis loss, due to domain wall movement [75], and resistive loss, due to induced eddy currents. The instantaneous magnitudes of these power losses depends on the magnitude and the rate of change of flux. Measures taken in practical machines to mitigate these losses include the use of electrical steel, with a narrow hysteresis loop and higher electrical resistivity than pure iron, and the magnetic circuit is often built from a stack of thin laminations electrically insulated from each other to reduce the magnitude of eddy currents which are able to flow in the steel. Despite these measures, iron losses can account for a significant proportion of total power losses, particularly in reluctance machines as they are often operated at high speeds and the magnetic circuit is driven well into saturation during each cycle with non-sinusoidal waveforms, the effects of which are not readily quantified [76,77].

In the flux switching machine the stator back iron behind the field slots experiences a dc flux with ripple at twice the commutation frequency while the steel behind the armature slots experiences ac flux at the commutation frequency. Figure 8-1a and b shows the orientation of flux at each aligned position for the 8/4 flux switching machine. Field and armature slots are labelled  $F$  and  $A$  respectively. Figure 8-1c and d show the corresponding flux waveforms in the stator back iron behind the field and armature respectively using experimental winding currents as the input to finite element analysis. Hence, for the same average power loss in each back iron section, the field back iron may be made thinner than behind the armature slots, allowing current density in the field, hence copper losses, to be reduced and/or the stator poles to be wider, for example. This qualitative analysis does not require accurate quantification of the iron loss magnitudes but simply their relative spatial and temporal distribution over an electrical cycle. Hence, a technique is developed to visualise iron loss distribution using data obtained from 2-dimensional finite element analysis and image processing. Although it has been applied here to the flux switching machine it is applicable to the design and analysis of a wide range of electrical machines.



(a) Flux orientation in aligned position 1

(b) Flux orientation in aligned position 2



(c) Unipolar field current

(d) Bipolar armature current

Figure 8-1 Example of 8/4 flux switching motor flux orientation and currents during operation

The magnetostatic finite element analysis applied to the simulation model for the flux switching machine does not include dynamic effects. However, an estimate can be made post-priori for the power dissipated in the steel due to dynamic effects [78-82]. Such post-priori iron loss models generally require that the flux in each section of the steel is known for a complete electrical cycle. To obtain this data generally requires finite element data for the machine in every simulated position and winding current combination [83,84]. However, such a methodology as that illustrated in Figure 8-2 would generally be impractical for routine use due to the computational expense involved in creating and solving the set of finite element models required.

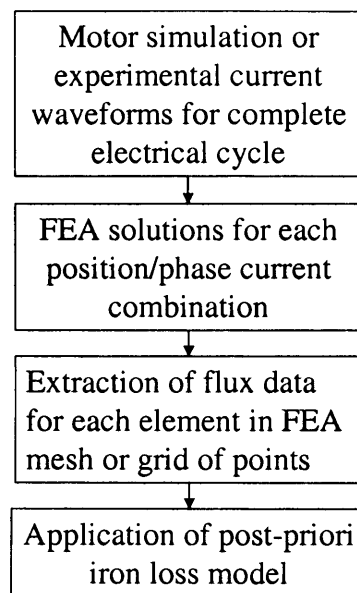


**Figure 8-2** ‘Traditional’ method of obtaining finite element data for iron loss estimation

As described in chapter 3, the flux map for the flux switching machine is derived from finite element solutions for a grid of winding mmf combinations at a variety of positions spanning a complete electrical cycle, half of which are solved explicitly by finite element analysis and the other half inferred due to anti-symmetry. As these finite element models must be solved to generate the flux map used as the basis for dynamic simulation, flux data is available for the discrete mmf-position combinations described in the flux map in either numerical or graphical format for relatively little further computational effort. Hence, a method is presented in this chapter which takes advantage of the existing finite element solutions used to create the flux map to inexpensively obtain the required flux data for post-priori iron loss estimation for the modelled lamination geometry under any operating condition within the mmf range of the flux map.

## **8.2 Obtaining graphical magnetic field data from finite element analysis**

The finite element solutions used to generate the flux map for the flux switching machine are solved for a grid of field mmf, armature mmf and position values. However, to obtain results for any mmf-position combination, interpolation between these data points is generally required. Furthermore, the movement of the rotor makes direct comparison between the finite element solutions difficult, particularly if the mesh is not identical in each case. Hence, the required flux data must be obtained from every finite element solution in a position-independent way which can then be pre-processed, to make the results obtained from each finite element solution directly comparable, and stored in such a way that interpolation is possible to yield flux data for any mmf and position combination within the modelled range. The finite element meshes for the iron regions in each finite element solution are generally not the same if automatic mesh generation is used so it is not possible to obtain data for each element for direct comparison. This is especially the case where automatic mesh adaption is implemented to improve numerical accuracy as described in chapter 2.

Most commercially available finite element analysis software packages have the facility to create filled zone plots of various field quantities with magnitude represented by colour for output to graphics file [45]. Figure 8-3 shows an example of such a plot for the flux switching machine showing spatial distribution of flux density for given winding mmfs. The graphical appearance of the output is independent of the finite element mesh and, in conjunction with the scale relating colour to field quantity, contains a complete description of the spatial distribution of that field quantity within the geometry. Such images can then be manipulated to allow for physical movement and obtain directly comparable, position and mesh independent results corresponding to each entry in the flux map. This data may then be interpolated to yield field spatial distribution for any mmf combination and position within the modelled range.

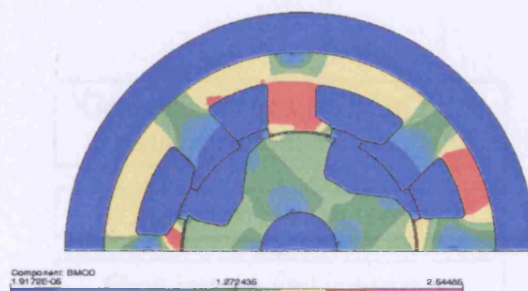


**Figure 8-3** Example graphical output from finite element analysis showing spatial distribution of flux density

### 8.3 Image processing method for obtaining magnetic field data from finite element analysis

In order to obtain magnetic field data from finite element analysis graphical output and store it in an accessible way for iron loss estimation, a number of pre-processing operations are required. Figure 8-4 illustrates the processes which needs to be carried out only once to yield data in the necessary format for any number of iron loss visualisations based on the modelled geometry. The required images are each exported from finite element analysis before being converted into bitmap graphic file format, from which the area of interest is extracted and image matrices are derived for subsequent manipulation. Rotor images are also rotated such that they are all aligned, making them directly comparable with each other in both visual and numerical terms. Finally the derived matrices are collated into arrays to facilitate rapid access and interpolation.

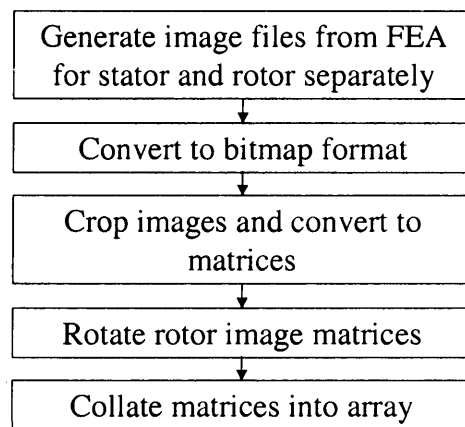


Figure 8-4 Methodology for iron loss visualisation method developed

### 8.3.1 Image generation in finite element analysis

#### 8.3.1.1 Derivation of position independent magnetic field components

The flux components generally available in Vector Fields and other 2-dimensional finite element analysis are  $B_x$ ,  $B_y$  and  $B_{MOD}$  [45] which represent the components of flux in the  $x$  and  $y$  Cartesian axis directions and the magnitude of the resultant flux respectively. However,  $B_x$  and  $B_y$  components are not directly comparable for regions where there is rotation between solutions. Hence, position independent flux components are required such as  $B_{RAD}$  and  $B_{TAN}$  which represent radial and tangential flux components respectively as shown in Figure 8-5.

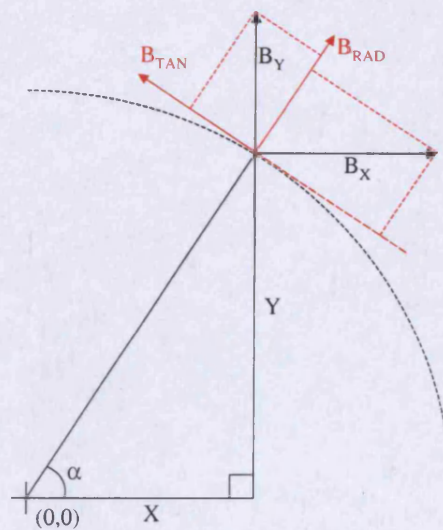


Figure 8-5 Derivation of position independent flux components

Given the flux components directly available from finite element analysis,  $B_x$  and  $B_y$ , along with the coordinates relative to the centre of rotation of the point at which they are evaluated  $(X, Y)$  the position independent components  $B_{RAD}$  and  $B_{TAN}$  may be derived where positive  $B_{RAD}$  is outwards from the origin and positive  $B_{TAN}$  is anti-clockwise. The angle  $\alpha$  of the vector from the origin to  $(X, Y)$  is given by

$$\tan \alpha = \frac{Y}{X} \quad (8.1)$$

The contributions of components  $B_x$  and  $B_y$  to the components  $B_{RAD}$  and  $B_{TAN}$  are found by taking projections as shown in Figure 8-5. Thus,

$$B_{RAD} = B_{XRAD} + B_{YRAD} \quad (8.2)$$

and

$$B_{TAN} = B_{YTAN} - B_{XTAN} \quad (8.3)$$

where

$$B_{XRAD} = B_x \cos \alpha \quad (8.4)$$

$$B_{YRAD} = B_y \sin \alpha \quad (8.5)$$

$$B_{XTAN} = B_x \sin \alpha \quad (8.6)$$

and

$$B_{YTAN} = B_y \cos \alpha \quad (8.7)$$

It can be seen that

$$\cos \alpha = \frac{X}{\sqrt{X^2 + Y^2}} \quad (8.8)$$

and

$$\sin \alpha = \frac{Y}{\sqrt{X^2 + Y^2}} \quad (8.9)$$

Hence, substituting equations (8.8) and (8.9) into (8.4) to (8.7) yields the position independent components which must be specified and plotted in finite element analysis for all  $X$  and  $Y$  within the stator and rotor steel regions.

$$B_{RAD} = \frac{B_x \cdot X + B_y \cdot Y}{\sqrt{X^2 + Y^2}} \quad (8.10)$$

and

$$B_{TAN} = \frac{B_y \cdot X - B_x \cdot Y}{\sqrt{X^2 + Y^2}} \quad (8.11)$$

For example, Figure 8-6a shows the orientation of magnetic flux within the flux switching machine at an aligned position. Figure 8-6b and c show the spatial distribution of the components  $B_x$  and  $B_y$  respectively and Figure 8-6d and e show the spatial distribution of the derived components  $B_{RAD}$  and  $B_{TAN}$  respectively.

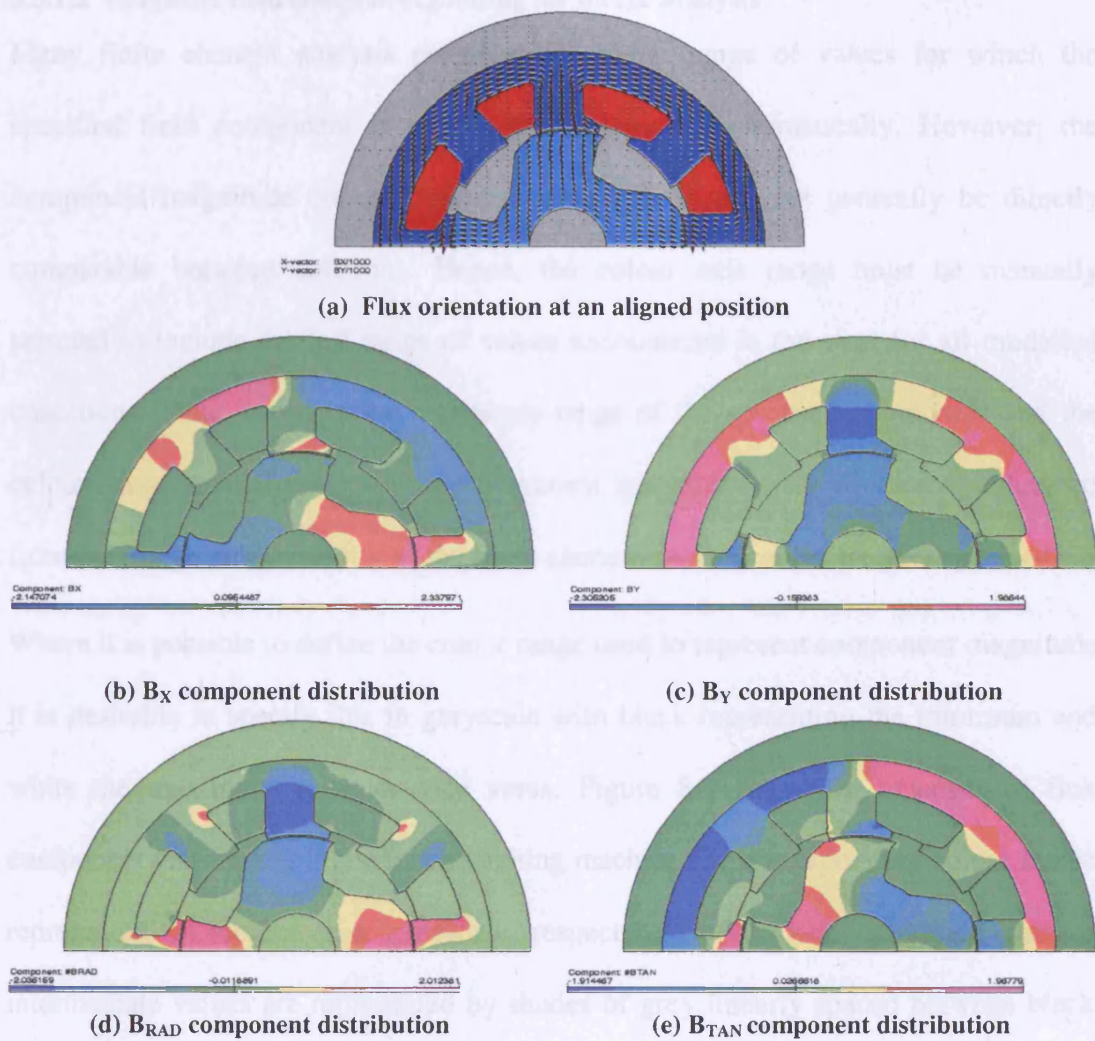


Figure 8-6 Comparison of Cartesian and polar flux components

### 8.3.1.2 Magnetic field component plotting for image analysis

Many finite element analysis packages allow the range of values for which the specified field component is plotted to be selected automatically. However, the component magnitude corresponding to each colour will not generally be directly comparable between solutions. Hence, the colour axis range must be manually selected to include the full range of values encountered in the steel for all modelled conditions. Thus, knowing the magnitude range of the specified component and the colour range representing it, flux component magnitude may be directly obtained from the image independently of the finite element mesh or software package used.

Where it is possible to define the colour range used to represent component magnitude it is desirable to specify this in greyscale with black representing the minimum and white the maximum value or vice versa. Figure 8-7 shows an example of flux component distribution in the flux switching machine and corresponding colour scales represented in colour and greyscale respectively. For such greyscale images intermediate values are represented by shades of grey linearly spaced between black and white. Thus, flux component magnitude may be readily derived at any point in the lamination from only a knowledge of the specified range and whether black represents the maximum or minimum. However, if a colour scale is used the magnitude range and corresponding sequence of colours must both be known.

In red, green and blue (RGB) definition black is [0,0,0], white is [1,1,1] and any shade of grey in between is described by the RGB triplet  $[x,x,x]$  where  $0 \leq x \leq 1$ . For example, if the specified range for the field component is 0 to +3 and black represents 0 then the grey shade described by the RGB triplet [0.5,0.5,0.5] corresponds to a component magnitude of 1.5. The general relationship relating field component magnitude to greyscale value is

$$C_x = x(C_{\max} - C_{\min}) + C_{\min} \quad (8.12)$$

where  $C_x$  is the magnitude represented by RGB triplet  $[x,x,x]$ ,  $C_{\max}$  and  $C_{\min}$  are the range maximum and minimum respectively and  $0 \leq x \leq 1$  is greyscale value.

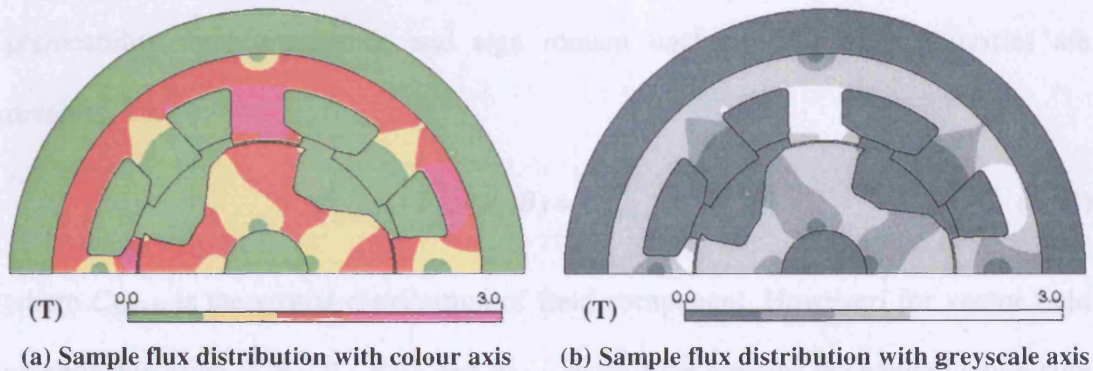


Figure 8-7 Comparison of colour and greyscale component axes

### 8.3.1.3 Image view axes

To ensure that each image plotted is directly comparable it is essential that the same view is specified for each plot. The view specified in finite element analysis must be able to contain the entire lamination geometry even if only a section of it is actually solved and displayed. This ensures that the rotor remains within the limits of the image for all rotational angles.

### 8.3.1.4 Treatment of finite element analysis solutions which are inferred

As described in chapter 3, finite element solutions are required for only half of the mmf and position combinations contained in the flux map to fully describe the electromagnetic characteristics of the flux switching machine lamination geometry, the other half being inferred, due to anti-symmetry, i.e.

$$\Phi_x(-F_f, -F_a, \theta) = -\Phi_x(F_f, F_a, \theta) \quad (8.13)$$

where  $\Phi$  is flux per unit stack length,  $F$  is winding mmf,  $\theta$  is rotor angle and the subscripts  $f$ ,  $a$ , and  $x$  denote field, armature and either winding respectively. Similarly, the magnitudes of the flux components visualised may be inferred when both mmf polarities are reversed. For scalar field components, such as resultant flux density and permeability, both magnitude and sign remain unchanged if mmf polarities are reversed, i.e.

$$C_{Scalar}(-F_f, -F_a, \theta) = C_{Scalar}(F_f, F_a, \theta) \quad (8.14)$$

where  $C_{Scalar}$  is the spatial distribution of field component. However, for vector field components, such as  $B_X$ ,  $B_Y$ ,  $B_{RAD}$  and  $B_{TAN}$ , magnitude remains unchanged while sign is reversed, i.e.

$$C_{Vector}(-F_f, -F_a, \theta) = -C_{Vector}(F_f, F_a, \theta) \quad (8.15)$$

Hence, for cases where sign must be reversed either the negative quantities, e.g.  $-B_{RAD}$  and  $-B_{TAN}$ , may be plotted using the same colour axis definitions or the positive components, e.g.  $B_{RAD}$  and  $B_{TAN}$ , may be plotted but with the corresponding sequence of axis colours reversed to yield the same result, provided the specified axis limits are symmetric, i.e.  $C_{max} = -C_{min}$ . Hence, spatial field distribution may also be inferred for those finite element solutions which are not solved explicitly. However, a further advantage of using greyscale values for the colour axis is that only the component distributions for positive mmfs need to be obtained from finite element analysis and the corresponding images for opposite mmf polarities may be obtained by inverting the entire image, a process which is readily carried out in most image manipulation software packages or numerically on the image matrices.

### 8.3.2 Image conversion to bitmap format

The format in which images are exported from finite element analysis will differ between software packages- for the Vector Fields Opera suite images are saved in Adobe® postscript format [85]. However, the images are required in greyscale bitmap format, i.e. the greyscale value of each picture element (pixel) is stored individually, for later manipulation. Although not as compact as some other image file formats, the file size of bitmap images can be determined from a knowledge of the pixel dimensions of the image while the compression techniques applied to some image formats such as jpeg [86] are 'lossy', i.e. some image information is lost in the compression/decompression process. If storage space is limited then the bitmap images may be compressed individually using a variety of freely available tools without loss of image data.

For the flux switching machine lamination shown in Figure 8-8, it is known from finite element analysis that the outside diameter of the stator is 89mm. Inspection of the bitmap image representing this lamination shows that this linear physical dimension is spanned by 305 pixels. Similarly, the 53mm rotor diameter is spanned by 183 pixels. Hence, each pixel in the bitmap image represents a square of the lamination with approximate side length 0.291mm. Hence, the volume of steel represented by each pixel is  $(0.291 \times 10^{-3})^2 \times l \text{ m}^3$ , where  $l$  is stack length.

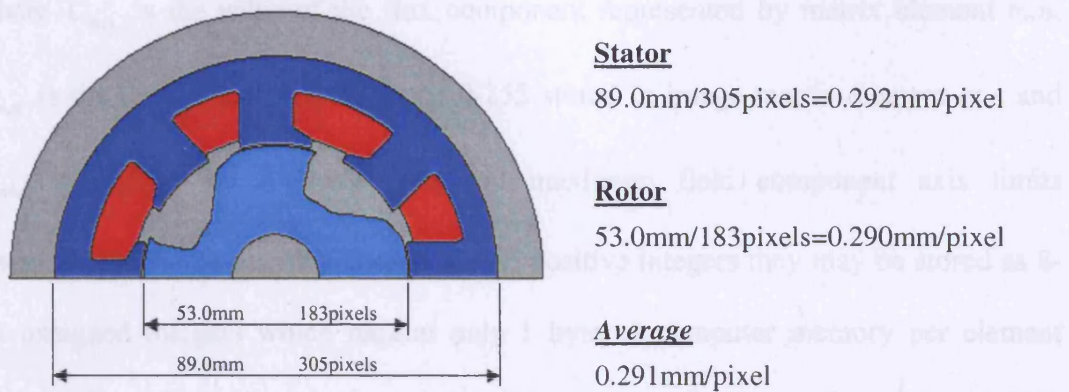


Figure 8-8 Example of deriving pixel dimensions by inspection of the bitmap image

### 8.3.3 Bitmap image to matrix conversion

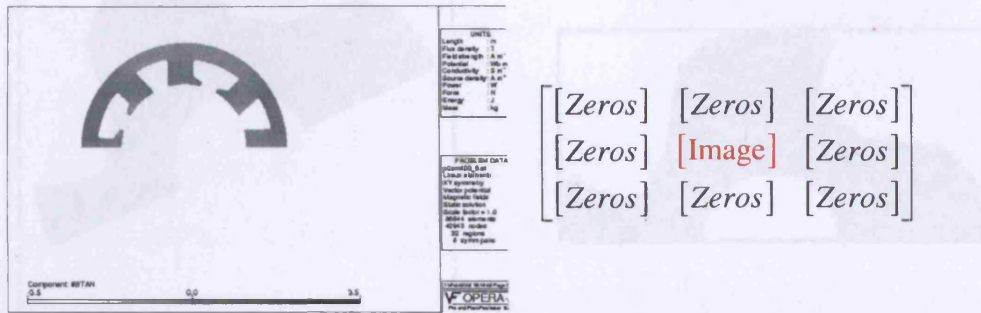
To allow mathematical manipulation, comparison and collation of the magnetic component distribution data, the bitmap image files are loaded into MATLAB [61] and stored as matrices. At this stage any parts of the image outside the region of interest may be removed to reduce the storage requirements.

Each image is read into MATLAB and stored as a matrix of integer values in the range 0-255 with each matrix element corresponding to one pixel in the bitmap image. A colour map is also obtained which relates the RGB pixel colour in the image to the corresponding matrix numerical value. For greyscale images of the format used these colours are RGB triplets  $[x,x,x]$  linearly spaced in the range  $0 \leq x \leq 1$ , i.e. matrix value 0 represents black  $[0,0,0]$ , matrix value 255 represents white  $[1,1,1]$  and intermediate values represent the various shades of grey in between. Hence, the integer values stored in the image matrix are related to field component magnitude by the relationship

$$C_{m,n} = \frac{x_{m,n}}{255} (C_{\max} - C_{\min}) + C_{\min}$$

where  $C_{m,n}$  is the value of the flux component represented by matrix element  $m,n$ ,  $x_{m,n}$  is the integer value in the range 0-255 stored in image matrix element  $m,n$  and  $C_{\min}$  and  $C_{\max}$  are the minimum and maximum field component axis limits respectively. As the matrix elements are all positive integers they may be stored as 8-bit unsigned integers which require only 1 byte of computer memory per element compared to 8 bytes for the storage of double precision floating point numbers which is the default format in MATLAB [61].

By inspection of any of the image matrices and the original image the rectangular sub-matrix which completely contains the region of interest can be found and all elements outside this range may be deleted. This process is carried out for both stator and rotor images as, in the case of an internal rotor machine, the rotor will be contained within a smaller sub-matrix and vice versa. In both cases the rectangular matrix will generally have an odd number of rows and columns, thus the central element coincides with the centre of the machine. Figure 8-9a shows an example stator image with white background from finite element analysis and Figure 8-9b shows the matrix pattern by which the region of interest may be recognised where [*Zeros*] represents a null sub-matrix and [*Image*] represents the non-zero sub-matrix containing the region of interest.



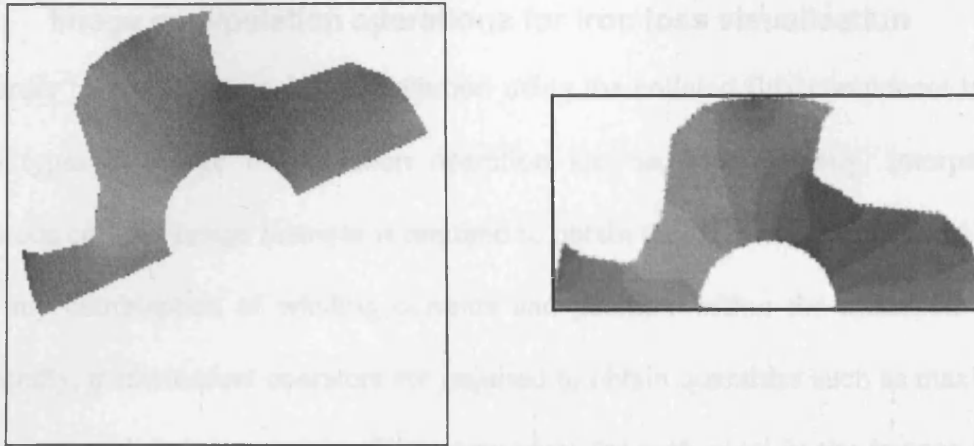
(a) Sample bitmap image from finite element analysis

(b) Characteristic pattern of sub-matrices in bitmap image

Figure 8-9 Example of finding region of interest within bitmap image by inspection

### 8.3.4 Rotation of image matrices

To make rotor images directly comparable with each other they must be rotated about the shaft centre such that the rotor is moved to a specified position. After this process has been carried out the rotor appears stationary over the complete electrical cycle. During the rotation process any elements which were previously outside the matrix are filled with the same value as the background. After this rotation has been carried out it is possible to further crop the image matrices to include only the required part of the resulting image, for example half a rotor or stator, to further reduce storage requirements. Figure 8-10a shows a square rotor image containing a half rotor before rotation and Figure 8-10b shows the rotated and trimmed image showing the half rotor in the specified position.



(a) Rotor image before rotation and cropping

(b) Rotor image after rotation and cropping

**Figure 8-10** Example of rotor image rotation and cropping

### 8.3.5 Image matrix collation

For calculation and visualisation of the change in flux component distribution over a complete electrical cycle for given winding current waveforms, the image matrices must be collated and stored in such a way that they can be readily retrieved and interpolated. To achieve this in MATLAB they are stored in multi-dimensional cell arrays [61] which have a similar structure to the numerical arrays used to store the flux map except that each element may in turn contain a matrix. Hence, the arrays used to store the flux component images have the same mmf and position axes as the flux map which may be de-normalised to give winding currents as described in chapter 3, with numerical flux values replaced by corresponding image matrices. One such multi-dimensional cell array is required for each type of image, i.e. stator and rotor images for each field component.

#### **8.4 Image manipulation operations for iron loss visualisation**

In order to visualise iron loss distribution using the collated flux component images two types of image manipulation operation are necessary. Firstly, interpolation between collated image matrices is required to obtain the field component distribution for any combination of winding currents and position within the modelled range. Secondly, mathematical operators are required to obtain quantities such as maximum, minimum and derivative of the field component for each pixel in the images over a complete electrical cycle.

Given winding currents and position over a complete electrical cycle, either from simulation or experiment, image interpolation yields a sequence of image matrices describing the corresponding spatial and temporal distributions of field component. From this sequence of images either another sequence or a single image may be derived using mathematical operators to visualise iron loss distribution or as the input data for a more detailed post-priori iron loss estimation algorithm.

Although the images from finite element analysis and subsequent manipulation have used greyscale images, it is not easy for the human eye to distinguish between very similar shades of grey. Hence, for visualisation purposes each image matrix may be displayed using a more readily interpreted colour map, for example blue through green to red is commonly used and understood.

#### 8.4.1 Image interpolation

To obtain the equivalent flux component images for corresponding to any winding current and position combination within the modelled range, interpolation between images representing several data points is required. As the cell array elements are matrices, generally containing several thousand elements each, special treatment is required for their interpolation. The images may either be interpolated linearly, which requires only arithmetic sums of entire matrices to be calculated, or using higher order interpolation algorithms.

To perform linear image interpolation between data points requires only a knowledge of the independent axis values for which data is known and the values at which it is required. If the point required is coincident with a known data point then the result is obtained directly without further calculation. If the required data falls between data points then the result is a linear sum of the values at the known axis values between which it falls, the weighting factors being determined by relative proximity to each known data point. In the case of 3-dimensional arrays this is a linear sum of 8 data points of the form

$$a[C_1]+b[C_2]+c[C_3]+d[C_4]+e[C_5]+f[C_6]+g[C_7]+h[C_8] \quad (8.16)$$

where  $a-h$  are calculated linear weighting factors and  $C_1$  to  $C_8$  are the known image matrices adjacent to the desired interpolated image.

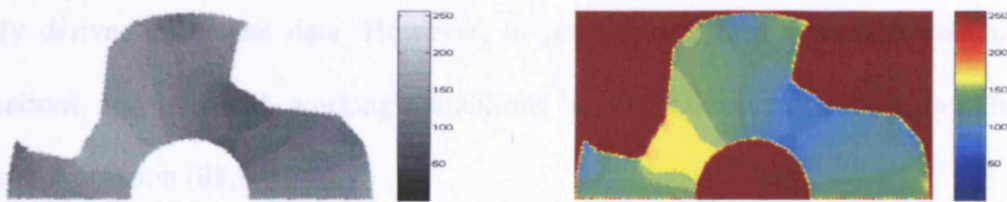
Although more potentially accurate interpolation methods are available, linear interpolation has the advantage of being simple to implement and rapid in use with only first order arithmetic operations on entire matrices required throughout. As the size of each image matrix increases the computation time will tend to increase approximately linearly with the number of pixels per image. This method is generally sufficient for visualisation of iron loss distribution while more accurate interpolation may be necessary for accurate post-priori iron loss analysis.

#### ***8.4.2 Image operators for visualisation of iron loss distribution***

To extract iron loss distribution information from a sequence of interpolated images describing the spatial and temporal variation of magnetic field components in the machine over a complete electrical cycle, arithmetic operators are required which accept such an image sequence as inputs and return either a sequence or a single image as outputs. The most relevant arithmetic operators to implement for iron loss visualisation are maximum, minimum, mean and derivative. Each is implemented to give resulting images of the same dimensions as the input images, hence, information on the spatial and temporal distribution of the required quantity is obtained. Further operators may be implemented in a similar way to derive more detailed information from the image sequence as required.

### 8.4.3 Image results display

Given an image, or sequence of images, in greyscale format as generated by finite element analysis and subsequent numerical operations, it is difficult for the human eye to correctly distinguish between similar shades of grey and it is not practical to manually read and comprehend the numerical element values for an image containing thousands of pixels. To overcome these difficulties the images may be displayed using a colour axis which is selected for better differentiation between values. A typical example widely used and understood is a smooth transition from blue, representing the minimum value, through green to red, representing the maximum value. For this example, the value 0 in an image matrix is displayed as blue while 255 is displayed as red with a smooth transition in between, although any other sequence of RGB triplets may be defined to correspond to the numerical values 0-255 to highlight particular details [61]. Figure 8-11 shows an example of how visualisation is aided by the use of such a colour map by showing the same image matrix displayed using black-to-white and blue-to-red colour maps respectively.



(a) Sample rotor image in greyscale

(b) Sample rotor image in colour

Figure 8-11 Comparison of greyscale and colour axes for data visualisation

## 8.5 Results

To illustrate the application of the image processing technique for iron loss visualisation a range of results are obtained using simulated running currents, obtained in chapter 6, with the flux switching motor running at approximately 15,000rpm driving an unloaded dynamometer and with the dynamometer loaded to 0.5Nm. By comparing the results obtained in each case it is possible to visualise the effect that this applied external load has on the relative magnitude and distribution of iron losses under practical operating conditions.

The Steinmetz equation [87,88], which gives a post-priori estimate of the power losses due to hysteresis and eddy currents for sinusoidal flux density, is

$$P = C_h f B_{pk}^n + C_e f^2 B_{pk}^2 \quad (8.17)$$

where  $P$  is power loss in W/kg,  $f$  is frequency in Hz,  $B_{pk}$  is peak flux density,  $C_h$  and  $C_e$  are hysteresis and eddy current loss coefficients respectively and the exponent  $n$  is often assumed to be in the range 1.6-1.8. These coefficients and the exponent are usually derived from test data. However, in practice the flux density in machine laminations for practical working conditions is not sinusoidal and a modified Steinmetz equation [88,89]

$$P = C_h f B_{pk}^{a+bB_{pk}} + C_{e1} \left[ \frac{dB}{dt} \right]^2 \quad (8.18)$$

may be used where  $B$  is instantaneous flux density,  $a$  and  $b$  are experimentally determined exponents and  $C_{e1}$  is a modified eddy current loss coefficient.

Although a detailed post-priori iron loss calculation is not performed in this case, relevant qualitative and comparative information may readily be obtained after inspection of the form of equation (8.18). In particular it can be seen that the magnitude of hysteresis loss is related to the peak to peak flux density while eddy current loss is related to the rate of change of flux density, the spatial and temporal distributions of which are readily available by interpolation of the image processed data.

All the results presented for visualising iron loss are single images showing the spatial distribution of various derived quantities over a complete electrical cycle. However, further detailed information on the temporal variation of these and other quantities is also readily available for further examination in the form of image sequences and animations. These results may then be examined to gain an insight into the complex interaction between operating speed, external load, control strategy, and iron losses.

### 8.5.1 Results relating to hysteresis loss visualisation

Referring to the modified Steinmetz equation, magnetic hysteresis power loss is related to the peak-to-peak flux density variation over a complete electrical cycle at a given frequency. Hence, for visualisation of the distribution of such losses under working conditions the maximum  $B_{MOD}$  within each complete electrical cycle is instructive. Figure 8-12 shows the distribution of maximum  $B_{MOD}$  within the steel of the flux switching motor running at approximately 15,000rpm with no externally applied load and driving 0.5Nm. As expected, it can be seen that hysteresis losses are higher for the loaded case, particularly in the stator, with high localised losses near the stator pole tips and very low losses on the outer periphery of the stator back iron directly behind the poles. However, while this simple analysis gives a rapid impression of the spatial distribution of hysteresis losses it must be noted that, for the flux switching machine, the flux density waveform in each section of steel is generally non-sinusoidal and may be either ac or dc with differing fundamental frequencies.

14,982rpm, no externally applied load

Maximum BMOD for 0Nm external load at 14,982rpm

(a) Stator maximum  $B_{MOD}$  distribution

Maximum BMOD for 0Nm external load at 14,982rpm

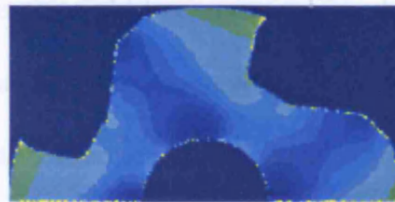
(c) Rotor maximum  $B_{MOD}$  distribution

15,022rpm, 0.5Nm external load

Maximum BMOD for 0.5Nm external load at 15,022rpm

(b) Stator maximum  $B_{MOD}$  distribution

Maximum BMOD for 0.5Nm external load at 15,022rpm

(d) Rotor maximum  $B_{MOD}$  distribution

Scale

(T) 0 0.5 1 1.5 2 2.5 3

Figure 8-12 Spatial distribution of maximum flux density in the stator of the 8/4 flux switching motor operating at approx. 15,000rpm unloaded and loaded

To obtain more detailed information about the spatial distribution of hysteresis losses in the flux switching machine it is necessary to consider the flux density waveform including direction in each section of the steel. The radial and tangential flux components,  $B_{RAD}$  and  $B_{TAN}$  respectively, are useful in this respect and a more instructive visualisation of hysteresis power loss distribution is obtained if the mean and peak-to-peak values of each are plotted, as shown in Figure 8-13 and Figure 8-14 for the stator and rotor respectively for the same operating conditions as Figure 8-12. In this example  $B_{RAD}$  is most applicable to the poles while  $B_{TAN}$  is most applicable in the stator and rotor back iron sections and the two may be read in conjunction to obtain a full appreciation of the time varying flux in each section of steel during a complete electrical cycle.

Examining the results for  $B_{RAD}$  in the stator it can be seen that the mean flux in the pole teeth is not zero, which follows from the fact that the stator poles carry pulsating dc flux, and the peak-to-peak variation over an electrical cycle increases with load as expected. A similar examination of  $B_{TAN}$  in the stator back iron shows that the mean behind armature slots is approximately zero, because the armature back iron carries ac flux, while it is non-zero behind the field slots as the field back iron carries dc flux with ripple as discussed in chapter 2. *An examination of the range of  $B_{TAN}$  shows that hysteresis loss is greatest in the armature back iron and relatively low behind the field slots, although it should be noted that the flux frequency is higher behind the field slots. Furthermore, the potential for additional filleting at pole roots to reduce iron losses is illustrated by the high localised losses at the base of the armature slots. A similar analysis yields hysteresis loss distribution in the rotor, again illustrating the potential for filleting to reduce localised hysteresis losses at the pole roots [90].*

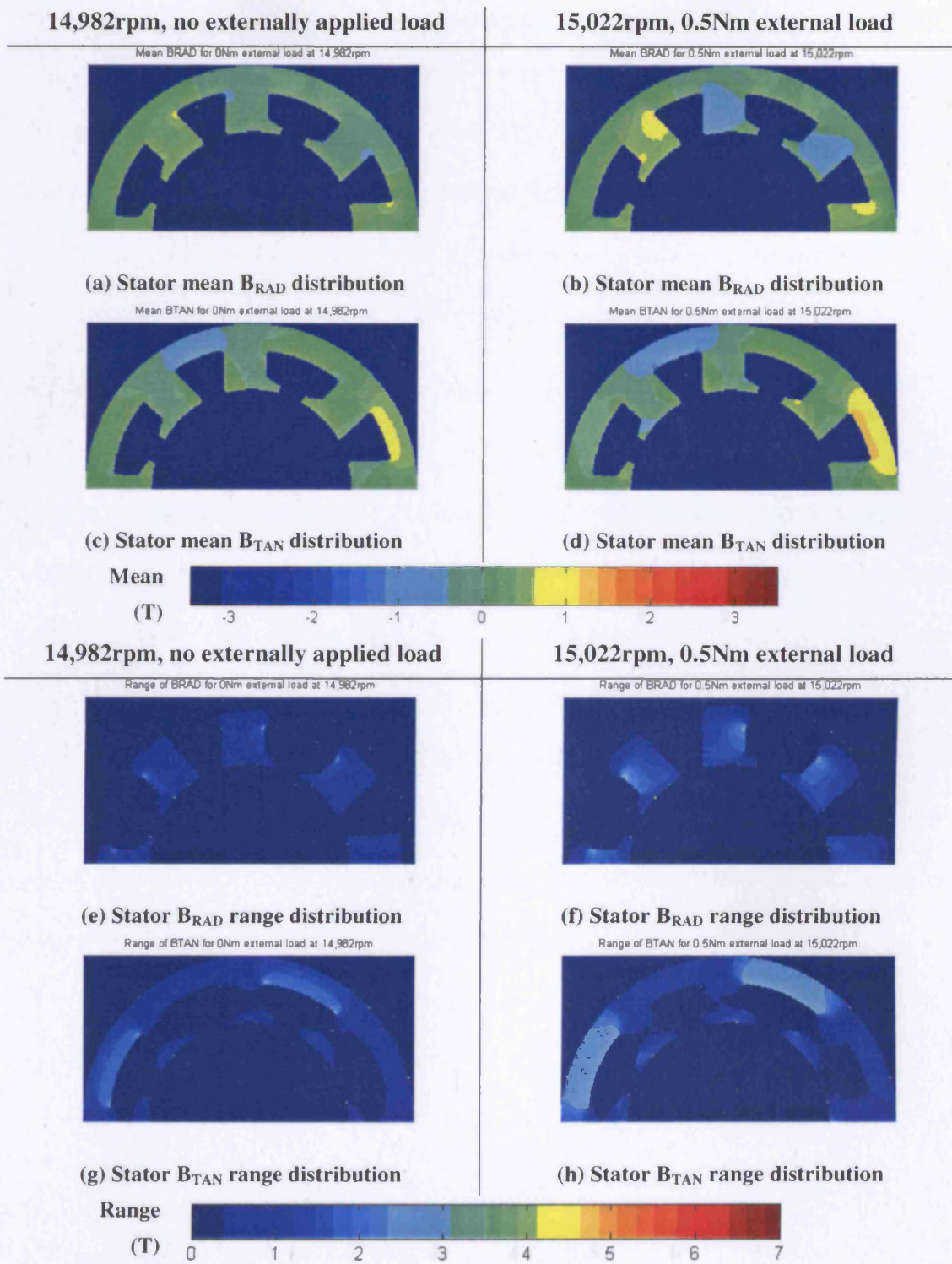


Figure 8-13 Spatial distribution of mean and range of flux in the stator of the 8/4 flux switching motor operating at approx. 15,000rpm unloaded and loaded

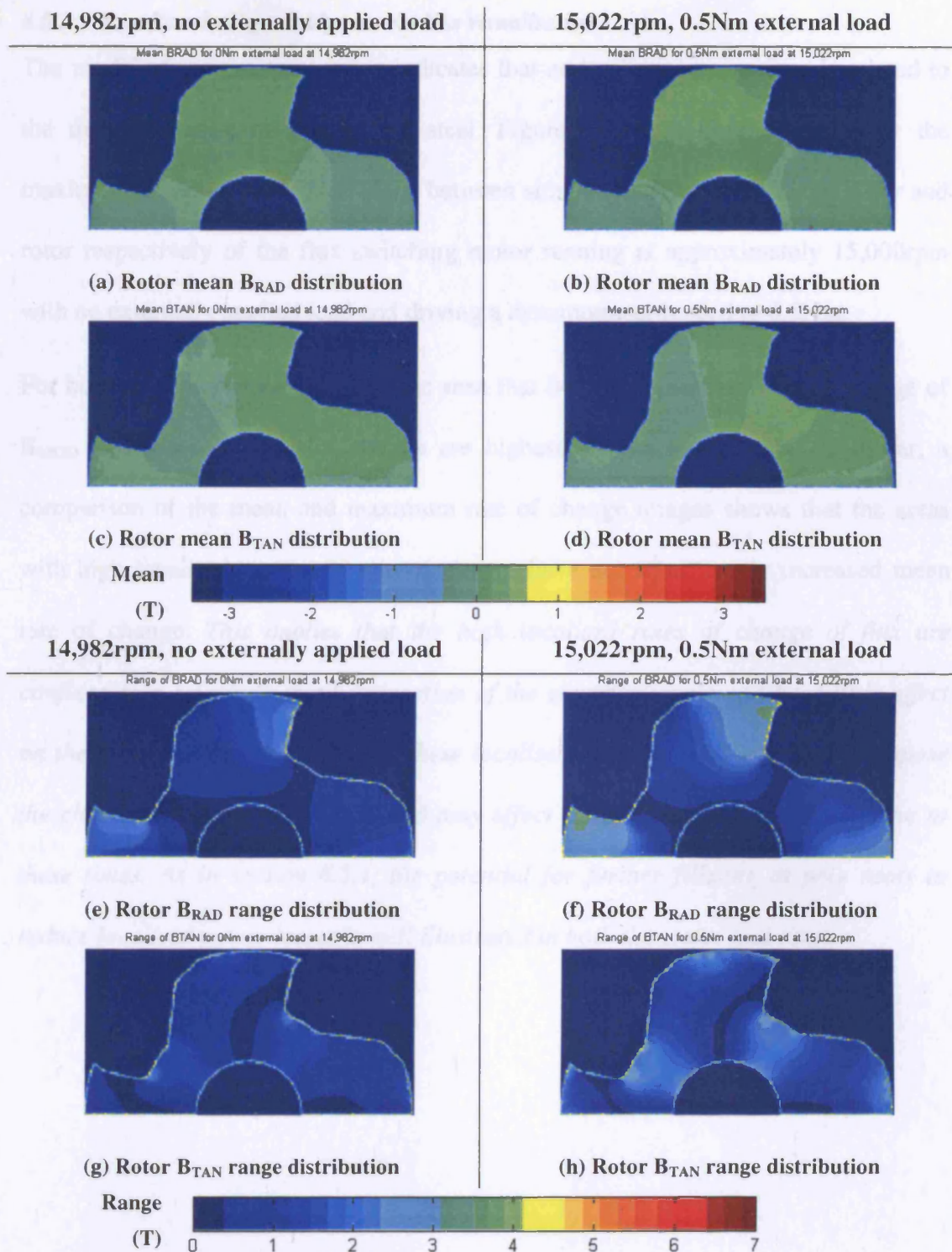


Figure 8-14 Spatial distribution of mean and range of flux in the rotor of the 8/4 flux switching motor operating at approx. 15,000rpm unloaded and loaded

### 8.5.2 Results relating to eddy current loss visualisation

The modified Steinmetz equation indicates that eddy current power loss is related to the time derivative of flux in the steel. Figure 8-15 and Figure 8-16 show the maximum and mean change in  $B_{MOD}$  between simulation time steps for the stator and rotor respectively of the flux switching motor running at approximately 15,000rpm with no externally applied load and driving a dynamometer loaded to 0.5Nm.

For both the stator and rotor it can be seen that both the maximum rate of change of  $B_{MOD}$  and the mean rate of change are highest for the loaded case. However, a comparison of the mean and maximum rate of change images shows that the areas with high localised maximum rate of change have not significantly increased mean rate of change. *This implies that the high localised rates of change of flux are confined to a relatively small proportion of the electrical cycle and have little effect on the mean power loss. However, these localised eddy currents will tend to oppose the change in flux being applied and may affect the performance of the machine at these times. As in section 8.5.1, the potential for further filleting at pole roots to reduce localised power losses is well illustrated in both the stator and rotor.*

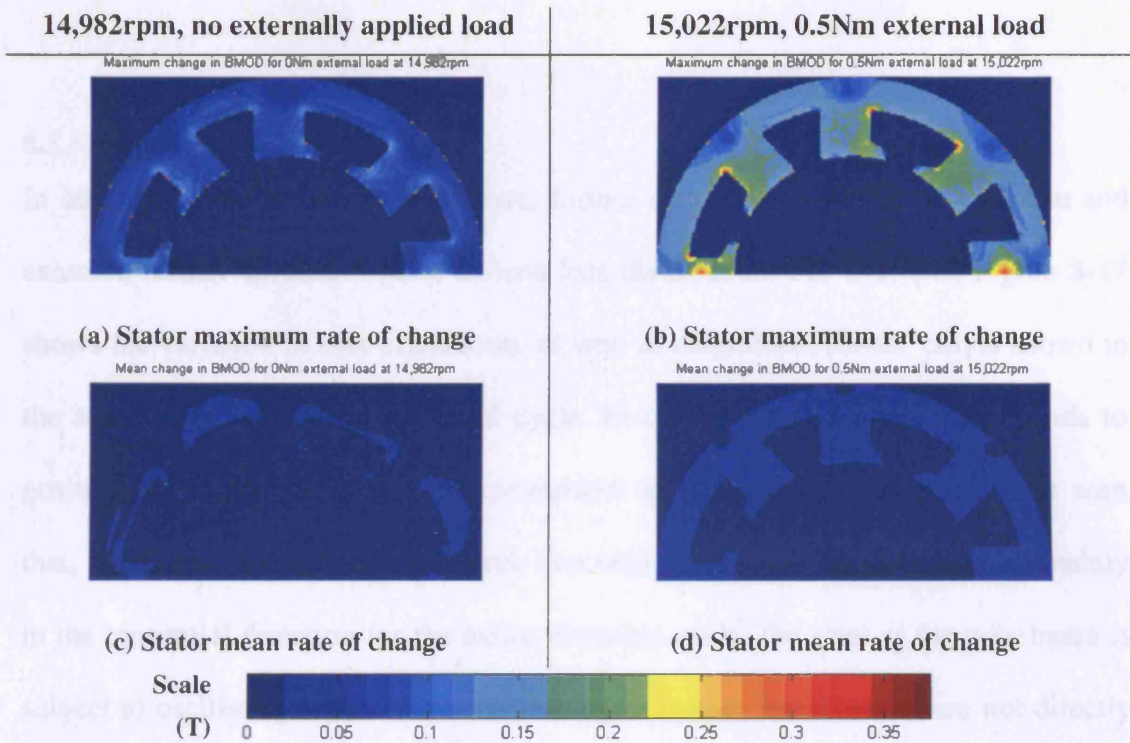


Figure 8-15 Spatial distribution of maximum and mean rate of change of flux in the stator of the 8/4 flux switching motor operating at approx. 15,000rpm unloaded and loaded

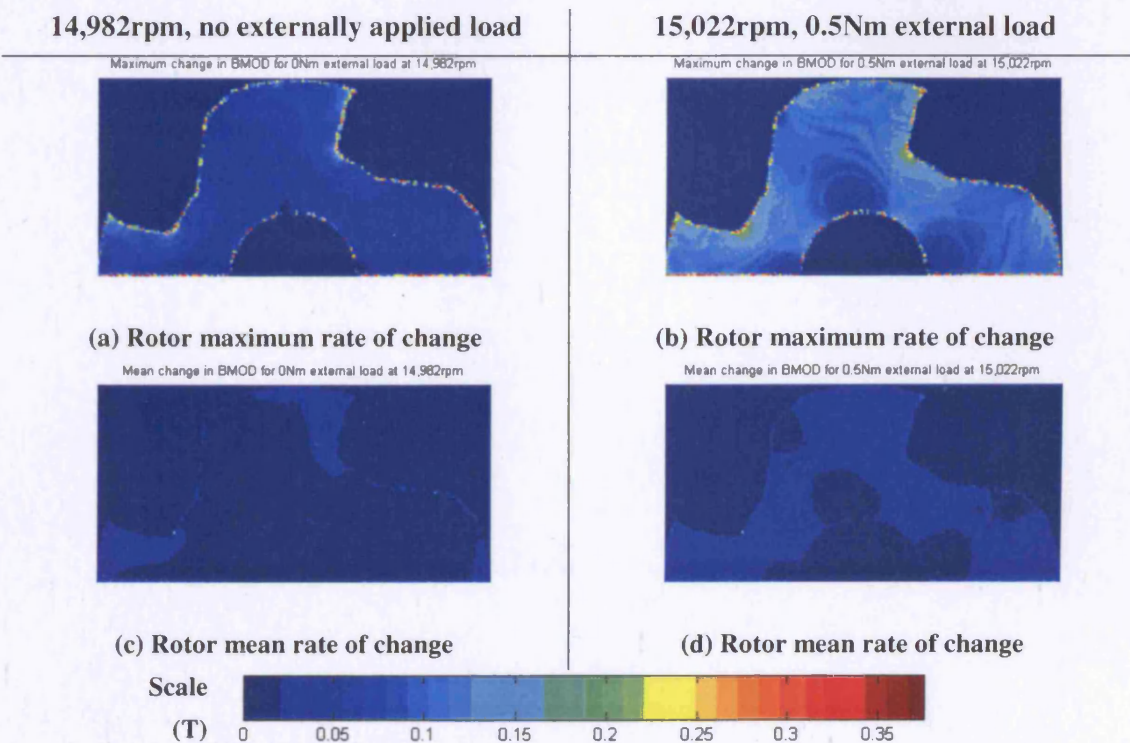


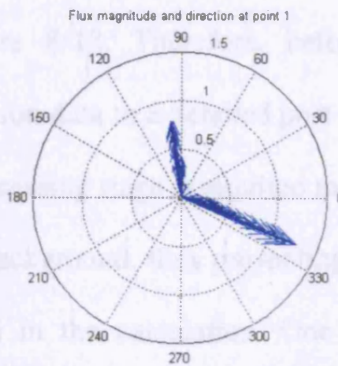
Figure 8-16 Spatial distribution of maximum rate of change of flux in the rotor of the 8/4 flux switching motor operating at approx. 15,000rpm unloaded and loaded

### 8.5.3 *Further results available*

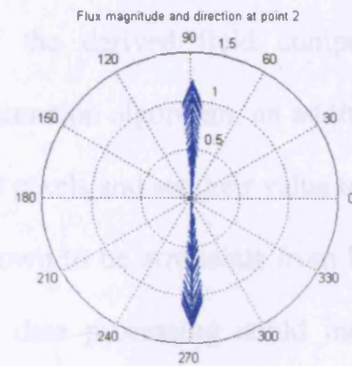
In addition to the results shown above, further results are available to visualise and examine further specific aspects of iron loss distribution. For example, Figure 8-17 shows the variation in flux orientation, as well as magnitude, for the points shown in the stator over a complete electrical cycle. In these plots 0 degrees corresponds to positive  $B_{RAD}$  only and 90degrees corresponds to positive  $B_{TAN}$  only. It can be seen that, while flux in the sections of back iron behind the winding slots remains mainly in the tangential direction for the entire electrical cycle, the steel at the pole bases is subject to oscillating flux orientation, leading to further losses which are not directly accounted for in the Steinmetz equation. However, the distribution of such losses may be visualised, for example, by plotting mean and/or peak-to-peak directional oscillation and magnitude.



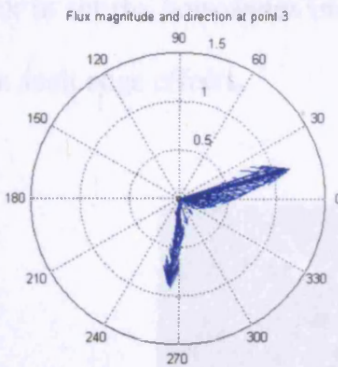
(a) Positions in stator for which flux orientation is compared



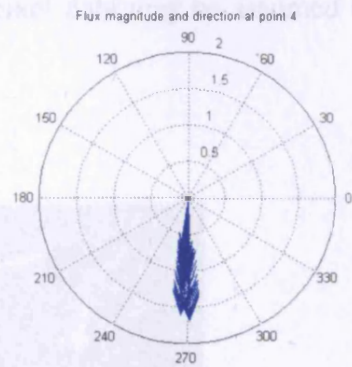
(b) Flux orientation at position 1



(c) Flux orientation at position 2



(d) Flux orientation at position 3



(e) Flux orientation at position 4

Figure 8-17 Example of oscillating flux in regions of the stator back iron

#### 8.5.4 Application of data obtained to post-priori iron loss estimation formulae

The data obtained by the image processing technique may be used as the input data for post-priori iron loss estimation formulae including the modified Steinmetz equation. However, some caution and further data processing is required in order to obtain consistently reliable results due to artefacts in the data images caused by bitmap discretisation effects. These effects may be observed at the periphery of both rotor and stator regions in the derived data as pixels with colours which, by inspection, obviously do not match their surroundings, as highlighted in the example of Figure 8-18. Therefore, before application of the derived field component distribution data to a detailed post-priori iron loss estimation algorithm, an additional data processing stage is required to detect the affected pixels and set their value to that of the background, thus preventing data which is known to be erroneous from being included in the calculation. One method for such data processing could include obtaining an outline plot of the geometry from finite element analysis and using this as a mask to set the boundaries inside of which all pixel data may be assumed to be free from such edge effects.

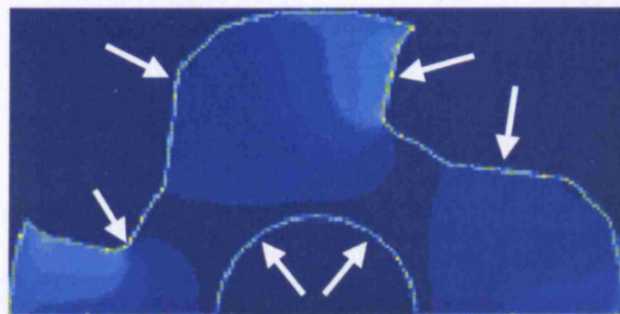


Figure 8-18 Example of edge effects due to bitmap image discretisation and interpolation

## 8.6 Summary and conclusions

A simple image processing method was developed in this chapter for the visualisation of iron loss distribution within electromagnetic devices using data obtained from finite element analysis. The method is entirely independent of the software package and finite element meshes used to obtain this data. The technique was demonstrated for the flux switching motor using simulated winding currents for unloaded and loaded conditions and the relative distributions of eddy current and hysteresis losses within the machine were shown.

Although the results obtained from the method developed in this chapter are presently only qualitative, the operation of the technique and its applicability in the design process for further optimisation of the lamination design for iron loss reduction were both demonstrated. However, with minor additional development the method is also applicable to the detailed quantitative analysis of iron losses.

---

# **Chapter 9**

Conclusions and further work

---

## 9 CONCLUSIONS AND FURTHER WORK

### 9.1 Conclusions

The flux switching machine in its present form is a relatively new class of reluctance machine which has shown considerable potential for commercial application due to its high power density, simple construction, high material utilisation and simple electronic drive circuit, although the inductor alternator and limited motion actuators of similar construction predate it. Chapter 2 of this thesis described the construction and method of operation of the flux switching machine and showed that its operation may be considered analogous to that of the brushed dc machine. Parameterised 2-dimensional finite element analysis of the finite element machine was also introduced along with methods for ensuring numerical accuracy while reducing the associated computational expense. A new parameterised finite element model of the flux switching machine was also developed which is highly flexible for design and physically accurate for simulation.

The flux map developed in chapter 3 is a coupled extension to the flux-mmF characterisation of switched reluctance machines where mutual coupling is neglected and fully describes the electromagnetic characteristics a given flux switching machine geometry. Two methods were introduced for reducing the computational overhead associated with obtaining the flux map by finite element analysis and the differences between various finite element models were compared. A comparison was also made between winding self inductances obtained from finite element analysis and experimentally, using a variety of techniques and it was shown that it was not appropriate to use the experimental results obtained to calibrate the flux map.

Chapter 4 developed a new technique for deriving the complete set of electromagnetic relationships from the flux map data by contour analysis and the detection of intersections between relevant contour lines. The implementation of the technique was described in detail and an algorithm was also developed for estimating and reducing the numerical error introduced by it. It was shown that errors are generally greatest for all flux maps in positions of strong mutual coupling and geometric accuracy of the finite element model was shown to have the greatest individual effect on converted data.

Chapter 5 then developed a dynamic simulation model for the flux switching machine, either stationary or running at constant speed, with arbitrary voltage excitation on both windings or with one winding open circuit. Simulated and experimental results were compared for the 8/4 flux switching machine running at constant speed with steady dc voltage field excitation and the armature open circuit, i.e. a standard back-emf test. Good agreement was shown between experimental and simulated results with winding resistance estimate having the largest individual effect on simulated results. It was also shown that the simulated results are relatively insensitive to the exact geometric and numerical accuracy of the finite element model used to create the flux map and the techniques used during data conversion.

A dynamic simulation model for the flux switching motor, including power electronic drive circuit and switch control strategy was developed in chapter 6. The normal and transient operation of the flux switching motor and drive circuit was described and the behaviour of the bifilar wound armature was examined. A method for adding external series connected inductance to each winding was also introduced. Good agreement was demonstrated between simulated and experimental results. In particular the interaction of the field and armature and the behaviour of the bifilar armature are fully accounted for. Simulated results were shown to be very sensitive to the switch operating positions used, as is also the case in practice. The simulated torques obtained by the Maxwell Stress and energy conversion loop methods were compared to experimental results and shown to be in reasonable agreement. Examination of the energy conversion loops and instantaneous torque waveforms showed that, in practice, although most torque is produced by the armature there is a noticeable contribution made by the field.

The results obtained in chapters 5 and 6 showed that, provided that the finite element model used to create the flux map and the data conversion techniques used are 'reasonable', then good agreement between experimental and simulated results can be achieved. The simulations were also relatively rapid at the point of use, hence repaying the earlier computational investment and providing a complete simulation process overall which is computationally efficient overall.

Chapter 7 described a genetic algorithm system coupled with parameterised finite element analysis for the design and optimisation of electromagnetic problems. The operation of genetic algorithms and their integration with parameterised finite element analysis was described. Application of the system to several optimisation problems led in each case to successively better solutions and the effectiveness of the system developed as part of a semi-automated electromagnetic design process was demonstrated.

Chapter 8 developed a simple image processing method for the visualisation of iron loss distribution within electromagnetic devices using data obtained from finite element analysis but which is entirely independent of the software package and meshes used to obtain it. The technique was demonstrated for the flux switching motor and the relative distributions of eddy current and hysteresis losses within the machine were shown. The operation of the technique and potential for further optimisation of the lamination design for iron loss reduction were both demonstrated

The development of parameterised finite element analysis was an enabling factor in the development and implementation of the simulation and design tools developed for the flux switching machine. By allowing a large number of different finite element models based on a common topology to be automatically created, solved and post-processed, both the creation of the flux map and operation of the genetic algorithm optimisation system require very little user input. Hence, although the computational investment is still not trivial, the overall cost is drastically reduced. Furthermore, the development of an accurate and flexible parameterised finite element model for the flux switching machine facilitates the rapid semi-automated design of new and novel machines which was not previously possible.

The flux map and data conversion algorithm provide a complete characterisation of the electromagnetic characteristics of the flux switching machine and are an extension to the flux-mmF characterisation widely used for switched reluctance motors. Although developed primarily for the flux switching machine, the techniques are more widely applicable to any reluctance machine where mutual coupling between two windings must be accounted for. The techniques developed for reducing the associated computational overhead along with rapid execution of the simulation models at the point of use make the overall simulation system computationally efficient and practical for design use.

Comparison of the flux maps, converted data and simulation results using a variety of finite element models and data conversion implementations has shown that, provided the models and numerical operations are properly formulated at each stage, then the individual effects of each on the simulated results of interest are relatively small. Hence, given a properly formulated finite element model which reasonably represents the machine to be simulated, good agreement with experimental results can be obtained for the operation of the flux switching machine, both with and without its power electronic drive and switch control strategy, using the models developed in this thesis.

Given that the a number of finite element solutions are required to create the flux map, the additional post-processing operations for implementation of the image processing method for iron loss visualisation may be added at relatively little additional cost and is rapid at the point of use. Hence, it is applicable alongside dynamic simulations for examination of the complex relationships between the machine, its drive circuit, the switch control strategy and iron losses. The value added to the design process by visualisation of iron loss distribution is potentially great, particularly in the case of the flux switching machine where performance benefits may be readily obtained through prudent lamination design with respect to iron losses. However, the technique is also more widely applicable to any electromagnetic system with time varying fluxes and the results obtained may be used for a detailed iron loss estimation algorithm with minor further development.

The integration of a genetic algorithm and parameterised finite element analysis makes possible the semi-automated design and optimisation of almost any electromagnetic system which may be modelled using 2-dimensional finite element analysis, theoretically producing a near globally optimal design for the given specification. However, the practical effectiveness of the system was also shown to be dependent on the formulation of the objective function and it is best applied as an aid alongside the manual design process rather than a replacement for it. Having developed the methods of integrating parameterised finite element analysis with external software modules there is also new scope for implementing further automated design and optimisation tools.

## **9.2 Areas for further work**

The dynamic simulation models developed for the flux switching machine are both implemented in MATLAB and are applicable only to the specific circuits for which the models are written. Hence, the application of the dynamic models to new power electronic circuits or winding connections is not trivial and would require significant reprogramming. However, if the data structures and simulation model could be integrated into a module for inclusion in a system simulator such as Saber then complete machine, drive, control and mechanical systems could be readily assembled and simulated. This would both widen the applicability of the simulation models developed and speed up the design and optimisation process for new applications in addition to allowing verification of the models and observations made for a range of flux switching machine sizes, configurations and drive circuits.

As the simulation models developed are based entirely on 2-dimensional magnetostatic finite element analysis, it is accepted that end effects are not modelled and only machines for which a 2-dimensional approximation is valid may be simulated. However, as available computing power and ease of use of 3-dimensional finite element software packages both continue to increase, the range of motors which may be simulated would be increased by the use of 3-dimensional finite element models for creating the flux map. It may also be possible to use both 2- and 3-dimensional finite element analysis results in conjunction to improve accuracy while maintaining flexibility.

The simple method developed in chapter 8 for visualising the distribution of iron losses is useful during the design process for qualitative comparisons and may also be used as the basis for quantitative post-priori iron loss estimation with limited further development. This would be particularly applicable to the design of future flux switching machines in order to take full advantage of the benefits offered by regions which carry predominantly steady dc flux. In the longer term the simulation of hysteresis and eddy current effects, along with their effects on the operation of electromagnetic systems, is a very important area for development. However, the mechanisms involved are very complex and, although there is great research interest in the topic, there is still a lot of research required in this area.

Genetic algorithms coupled with parameterised finite element analysis have been shown, in principle, to be effective for the design and optimisation of a wide range of electromagnetic problems. With reference to the flux switching machine it was noted that the formulation of the fitness function was very important. Hence, further investigation is warranted in developing suitable numerical measures of performance and fitness functions for this application. In particular, it may be necessary to include a more detailed model for the flux switching machine, possibly including iron losses, in addition to the results obtained directly from finite elements. Furthermore, the genetic operators implemented were relatively simple and the implementation of more complex operators may be beneficial. At the time of writing research in these areas is progressing as part of a separate research programme.

---

# References

---

## REFERENCES

- [1] M.Eshani, "Switched reluctance motor drives- recent advances", *Sadhana*, Vol. 22, Pt. 6, pp821-836, Dec. 1997
- [2] J.Faiz, J.W.Finch, H.M.B.Metwally, "A novel switched reluctance motor with multiple teeth per stator pole and comparison of such motors", *Electric Power Systems Research*, Vol. 34, No. 3, pp197-203, Elsevier Sciences, 1995
- [3] C.E.B.Green, J.M.Stephenson, "A sensorless switched reluctance drive", *EMD 1997*, IEE conference 444, pp64-68, 1997
- [4] G.Gallegos-Lopez, P.C.Kjaer, T.J. E.Miller, "A new sensorless method for switched reluctance motor drives", *IEEE IAS annual meeting 1997*, Vol. 1, pp564-570, 1997
- [5] C.Pollock, M.Wallace, "Flux switching motor: a DC motor without magnets or brushes", *IEEE IAS annual meeting 1999*, Vol. 3, pp1980-1987, 1999
- [6] T.J.E.Miller, "Brushless permanent magnet and reluctance motor drives", Oxford university press, 1989
- [7] T.J.E.Miller, "Switched reluctance motors and their control", Magna Physics publishing, 1993
- [8] S.K.Mondal, S.N.Saxena, S.N.Bhandra, "Effects of saturation on performance of SRM and controller during starting", *IEEE Trans. Magnetics*, Vol. 33, No. 2, pp2105-2108, 1997
- [9] H.Lin, T.S.Low, S.X.Chen, "Investigation on magnetic saturation in switched reluctance motor using 2-d hybrid finite element method", *IEEE Trans. Magnetics*, Vol. 32, No. 5, pp4317-4319, 1996

- [10] L.Chang, "Design procedures of a switched reluctance motor for automobile applications", *Canadian conference on electrical and computer engineering*, Vol. 2, pp950-954, IEEE, 1996
- [11] Y.Ohdachi et al, "Optimum design of switched reluctance motors using dynamic finite element analysis", *IEEE Trans. Magnetics*, Vol. 33, No. 2, Pt. 2, pp2033-2036, 1997
- [12] T.W.Preston, A.B.J.Reece, P.S.Sangha, "Analysis of switched reluctance drives by the finite element time-stepping method", *EMD 1991*, Vol. 1, pp81-85, 1991
- [13] N.Sadowski, Y.Lefevre, C.G.C.Neves, R.Carlson, "Finite elements coupled to electrical circuit equations in the simulation of sqwitched reluctance drives: Attention to mechanical behaviour", *IEEE Trans. Magnetics*, Vol. 32, No. 3/1, pp1086-1089, 1996
- [14] A.Michaelides, C.Pollock, C.Jolliffe, "Analytical computation of minimum and maximum inductances in single and two-phase switched reluctance motors", *IEEE Trans. Magnetics*, Vol. 33, No. 2, Pt. 2, pp2037-2040, 1997
- [15] J.M.Kokernak, D.A.Torrey, "Magnetic circuit model for the mutually coupled reluctance machine", *IEEE IAS annual meeting 1997*, Vol. 1, pp302-309, 1997
- [16] Y.Li, J.D.Lloyd, G.E.Horst, "Switched reluctance motor with DC assisted excitation", *IEEE IAS annual meeting 1996*, Vol. 2, pp801-807, 1996
- [17] F.Ismail, S.Wahsh, A.Z.Mohamed, "High-performance prediction for variable-speed switched reluctance drives", *Intersociety energy conversion engineering conference 1997*, Vol. 1, pp348-352, 1997
- [18] J.R.Suriano, C.M.Ong, "Variable reluctance motor structures for low-speed operation", *IEEE Trans. Industry Applications*, Vol. 32, No. 2, pp345-353, 1996
- [19] H.Ertan, "Analytical prediction of torque and permeance-displacement characteristics of asymmetrical tooth pairs", *ICEM '86*, pp97-100, 1986
- [20] M.Hassanin et al, "Flux density models for the switched reluctance machine", *IEEE IAS annual meeting 1996*, Vol. 2, pp745-752, 1996

- [21] Y.Tang, "Characterization, numerical analysis and design of switched reluctance motors", *IEEE Trans. Industry Applications*, Vol. 33, No. 6, pp1544-1552, 1997
- [22] B.Fahimi, G.Suresh, J.Mahdavi, M.Eshani, "A new approach to model switched reluctance motor drive Application to dynamic performance prediction, control and design", *IEEE PESC '98*, Vol. 2, pp2097-2102, 1998
- [23] J.Mahdavi, G.Suresh, B.Fahimi, M.Eshani, "Dynamic modelling of non-linear SRM drive with PSPICE", *IEE IAS annual meeting 1997*, Vol. 1, pp661-667, 1997
- [24] D.A.Staton, R.P.Deodhar, W.L.Soong, T.J.E.Miller, "Torque prediction using the flux-mmf diagram in AC, DC, and reluctance motors", *IEEE Trans. Industry Applications*, Vol. 32, No. 1, pp180-188, 1996
- [25] Fitzgerald, Kingsley, Umans, "Electric Machinery", 5th ed., McGraw Hill, 1992
- [26] W.F.Ray, F.Erfan, "A new method of flux or inductance measurement for switched reluctance motors", *IEE conf. Proceedings, No. 444, pp137-140*, Volume, Page, Year
- [27] W.M.Chan, W.F.Weldon, "Development of a simple nonlinear switched reluctance motor model using measured flux linkage data and curve fit", *IEEE IAS annual meeting 1997*, Vol. 1, pp318-325, 1997
- [28] S.Gotovac, "Mathematical model of switched reluctance motor", *International journal for engineering modelling*, Vol. 8, pp15-20, 1995
- [29] A.M.Omekanda, C.Broche, M.Renglet, "Calculation of the electromagnetic parameters of a switched reluctance motor using an improved FEM-BIEM- Application to different models for the torque prediction", *IEEE Trans, Industry Applications*, Vol. 33, No. 4, pp914-918, 1997
- [30] L.Chang, "Modelling of switched reluctance motors", *Canadian conference on electrical and computer engineering 1997*, Vol. 2, pp866-869, IEEE, 1997
- [31] T.J.E.Miller, et al, "Ultra-fast model of the switched reluctance motor", *IEEE IAS annual meeting 1998*, Vol. 1, pp319-326, 1998

- [32] M.Barnes, A.Michaelides, C.Pollock, "The design and performance of a self-starting 2-phase switched reluctance drive", *IEE PEVD '96*, pp419-423, 1996
- [33] A.Michaelides, C.Pollock, "Modelling and design of switched reluctance machines with two phases simultaneously excited", *IEE Proc. Electric Power Applications*, Vol. 143, No. 5, pp361-370, 1996
- [34] S.H.Li, F.Liang, Y.Zhao, T.A.Lipo, "A doubly salient doubly excited variable reluctance motor", *IEEE Trans, Industry Applications*, Vol. 31, No. 1, pp99-106, 1995
- [35] B.C.Mecrow, "New winding configurations for doubly salient machines", *IEEE Trans. Industry Applications*, Vol. 32, No. 6, pp1348-1356, 1996
- [36] F.Liang, Y.Liao, T.A.Lipo, "A new variable reluctance motor utilizing an auxiliary commutation winding", *IEEE Trans. Industry Applications*, Vol. 30, No. 2, pp423-432, 1994
- [37] B.C.Mecrow, "Fully-pitched switched-reluctance and stepping-motor arrangements", *Proc. IEE Part B*, Vol. 140, No. 1, pp61-70, 1993
- [38] T.A.Lipo, F.Liang, "Variable reluctance drive system", *US Patent No. 5,459,385*, Oct. 17 1995
- [39] J.Worotynski, M.Turowoski, W.Worotynska, "Generation of an optimal reluctance network model for fast 2-d and 3-d simulations of electromagnetic devices", *2<sup>nd</sup> International conference on computation in electromagnetics*, IEE conference publication 384, pp116-119
- [40] K.F.Raby, "Inductor alternators for 10kc/s", *British Thomson Houston technical monograph*, TMS755, 1950
- [41] "Medium-frequency motor-alternator systems", Source unknown
- [42] B.C.Mecrow, A.C.Clothier, P.G.Barrass, "High performance switched reluctance drives using novel windings", *IEE colloquium (digest)*, No 152, pp6/1-6/5, 1996
- [43] Y.Li, Y.Tang, "Switched reluctance motor drives with fractionally-pitched winding design", *IEEE PESC 1997*, Vol. 2, pp875-880, 1997

- [44] "Opera 2-d user guide", Vector Fields Ltd., Oxford, U.K.
- [45] "Opera 2-d reference manual", Vector Fields Ltd., Oxford, U.K.
- [46] C.S.Biddlecombe, C.F.Parker, J.K.Sykulski, S.C.Taylor, "The design environment for electromagnetics", *Proc. ELECTROSOFT '96*, pp157-166, 1996
- [47] "Design environment user guide", Vector Fields Ltd., Oxford, U.K.
- [48] "Design environment reference manual", Vector Fields Ltd., Oxford, U.K.
- [49] A.F.L.Nogueira, "Computation of cogging torques in permanent-magnet machines using the finite elements method", *PhD thesis, University of Wales, Cardiff*, 1992
- [50] S.J.Salon, "Finite element analysis of electrical machines", *Kluwer Academic Publishers*, 1995
- [51] K.J.Binns, P.L.Lawrenson, C.W.Trowbridge, "The analytical and numerical solution of electric and magnetic fields", Wiley, 1992
- [52] C.W.Trowbridge, "An introduction to computer aided electromagnetic analysis", Vector Fields Ltd., 1993
- [53] A.B.J.Reece, T.W.Preston, "Finite element methods in electrical power engineering", Oxford science publications, 2000
- [54] P.P.Silvester, R.L.Ferrari, "Finite elements for electrical engineers", Cambridge university press, 1983
- [55] C.S.Biddlecombe, J.Simkin, C.W.Trowbridge, "Error analysis in finite element models of electromagnetic fields", *IEEE Trans. Magnetics*, Vol. 22, No. 5, pp811-813, Sept. 1986
- [56] L.Chang, G.E.Dawson, T.R.Eastham, "Finite element analysis of electric machines: Post-processing methods", *Intl. Journal of applied electromagnetics in materials*, Vol. 5, pp321-330, 1994

- [57] N.J.Nagel, R.D.Lorenz, "Modelling of a saturated switched reluctance motor using an operating point analysis and the unsaturated torque equation", *IEEE Trans. Industry Applications*, Vol. 36, No. 3, pp714-721, 2000
- [58] M.J.DeBertoli, S.J.Salon, "Computation of forces and torque in electromagnetic devices using the finite element method", *ICEM '90*, pp699-705, 1990
- [59] Private communication from Black and Decker Ltd.
- [60] J.M.Reeve, C.Pollock, "Dynamic simulation model for two-phase mutually coupled reluctance machines", *IEE IAS annual meeting 2001*, Vol. 1, pp40-47, 2001
- [61] "MATLAB Release 12 reference manuals", Mathworks Inc.
- [62] P.W.Lee, C.Pollock, "Measurement of flux linkage in the hybrid stepping motor drive", *IEE colloquium (Digest)*, No. 17, pp4/1-4/4, 1994
- [63] Bajpai, Calus, Farley, "Numerical methods for scientists and engineers", *Wiley*, 1978
- [64] J.K.Lahteemaki, "Optimisation of high-speed motors using a genetic algorithm", *EMD 1997*, IEE conference publication 444, pp26-30, 1997
- [65] S.Palko, "Structural optimisation of an induction motor using a genetic algorithm and a finite element method", *Acta Polytechnica Scandinavica*, No. 84, , Finnish Academy of Technology, 1996
- [66] B.Benedicic, T.Kmecl, G.Papa, B.Korousic, "Evolutionary optimisation of a universal motor", *Proc. IECON '01*, pp19-24, 2001
- [67] S.Bureerat, J.E.Cooper, "Evolutionary methods for the optimisation of engineering systems", *IEE colloquium digest*, No. 521, pp1/1-1/10, 1998
- [68] F.Boschetti, M.Dentith, R.List, "Inversion of potential field by genetic algorithms", *Geophysical prospecting*, Vol. 45, pp461-478, 1997
- [69] E.Kita, H.Tanie, "2D shape optimisation using genetic algorithm", *Computer assisted mechanics and engineering sciences*, Vol. 5, pp311-321, 1998

- [70] J.Holland, "Adaptation in natural and artificial systems", University of Michigan press, 1975
- [71] C.Darwin, "On the origin of species by means of natural selection", Thompson and Thomas, 1906
- [72] D.E.Goldberg, "Genetic algorithms in search, optimization and machine learning", Addison Wesley, 1988
- [73] L.Davis, "Handbook of genetic algorithms", Van Nostrand Rheinhold, 1991
- [74] L.Chanmers, "Practical handbook of genetic algorithms", CRC press, 1995
- [75] D.C.Jiles, D.L.Atherton, "Theory of ferromagnetic hysteresis", *Journal of magnetism and magnetic materials*, Vol. 61, pp48-60, 1986
- [76] L.G.Grainger, K.E.Bollinger, "Measurement of frequency of non-sinusoidal waveforms", *Canadian conference on electrical and computer engineering 1996*, Vol. 2, pp675-678, IEEE, 1996
- [77] J.Conrad, F.Ossart, A.Foggia, "Investigation of soft magnetic material behaviour under non-symmetrical excitation", *Journal de Physique, IV*, Vol. 8, No. 2, pp673-676, EDP Science, 1998
- [78] M.S.N Al-Din, A.F.Kader, J.Al-Samarai, "A new method to compute eddy current losses by the finite element method", *IEEE IAS annual meeting 1997*, Vol. 1, pp3-9, 1997
- [79] S.P.Lou, J.Ye, "Flux distribution and core losses of switched reluctance motors", *Canadian conference on electrical and computer engineering 1996*, Vol. 2, pp935-938, IEEE, 1996
- [80] Y.Hayashi, T.J.E.Miller, "A new approach to calculating core losses in the SRM", *IEEE Trans. Industry Applications*, Vol. 31, No. 5, pp1039-1046, 1995
- [81] I.Mayergoyz, "Mathematical models of hysteresis", *IEEE Trans. Magnetics*, Vol. 22, No. 5, pp603-608, 1986

- [82] I.Mayergoz, "Mathematical models of hysteresis", Springer-Verlag, 1991
- [83] A.A.Arkadan, H.H.Shehadeh, R.H.Brown, N.A.O.Demerdash, "Effects of chopping on core losses and inductance profiles of SRM drives", *IEEE Trans. Magnetics*, Vol. 33, No. 2, pp2105-2108, 1997
- [84] F.Leonardi, T.Matsuo, T.A.Lipo, "Iron loss calculation for synchronous reluctance machines", *Proc. PEDES 1*, pp307-312, 1996
- [85] Adobe Systems Inc., [www.adobe.com](http://www.adobe.com)
- [86] Joint photographic experts group, [www.jpeg.org](http://www.jpeg.org)
- [87] C.P Steinmetz, "On the law of hysteresis", *AIEE Transactions*, Vol. 9, pp3-64, 1892 (reprinted by J.E.Britten, "A Steinmetz contribution to the ac power revolution", *Proc. IEEE*, Vol. 72, No. 2, pp196-221, 1984
- [88] T.J.,E.Miller, "WinSPEED 2 manual", SPEED laboratory, University of Glasgow, p68
- [89] J.Reinert, A.Brockmeyer, R.W.DeDoncker, "Calculation of losses in ferro- and ferrimagnetic materials based on the modified Steinmetz equation", *IEEE IAS annual meeting 1999*, Vol. 3, pp2087-2092, 1999
- [90] H.Lee, S.Park, I.Park, S.Hahn, "Core shape design of electrical devices for iron loss reduction", *Int. journal of applied electromagnetics and mechanics*, Vol. 6, pp331-338, 1995
- [91] P.N.Materu, R.Krishnan, "Estimation of switched reluctance motor core losses", *IEEE Trans. Industry Applications*, Vol. 28, No. 3, pp668-679, 1992
- [92] J.L.Tasker, "Law's relay actuators", *Proc. 2<sup>nd</sup> Int. Conf. On small and special electrical machines 1981*, pp69-73, 1981
- [93] C.V.Jones, "The unified theory of electrical machines", *Butterworths*, 1967